Impact Parameter-Gated Two-Proton Intensity Interferometry in Intermediate Energy Heavy Ion Collisions

By

Michael Annan Lisa

A DISSERTATION

Submitted to
Michigan State University
in partial fulfillment of the requirements
for the degree of

DOCTOR OF PHILOSOPHY

Department of Physics and Astronomy

1993

ABSTRACT

Impact Parameter-Gated Two-Proton Intensity Interferometry in Intermediate Energy Heavy Ion Collisions

By

Michael Annan Lisa

Impact parameter gated two-proton intensity interferometry is employed to probe the space-time structure of emitting sources created in intermediate energy heavy ion collisions.

The Koonin-Pratt formalism relating the single-proton phase space population density to the two-proton correlation function is discussed. Schematic calculations illustrate the sensitivity of the correlation function to source size and lifetime.

Single- and two-proton yields, used to construct the two-proton correlation function, were measured with a high-resolution 56-element hodoscope for the reaction $^{36}Ar+^{45}Sc$ at E/A=80 MeV. Coincident measurement of charged particle yields in a 4π detector array provided information about the impact parameter of the collision. For both central and peripheral events, proton correlations are larger (indicative of a smaller space-time extent for the source) for proton pairs with larger total momentum. For central events, the total

momentum dependence is stronger than for peripheral events, indicating a distinct reaction evolution for events with different impact parameter.

Methods for comparing impact parameter-gated data to theoretical predictions are discussed, and predictions of a model based upon the Boltzmann-Uehling-Uhlenbeck (BUU) equation are compared to experimental correlation functions. For central collisions, the total momentum dependence of the correlations is well reproduced. For peripheral collisions, this dependence is underpredicted, suggesting that the model may be deficient in its description of peripheral heavy ion collisions.

Differences between longitudinal and transverse correlation functions allow independent extraction of source size and lifetime. Potential difficulties in the search for such differences are discussed. For intermediate energy protons emitted from central $^{36}Ar+^{45}Sc$ collisions at E/A=80 MeV, a source with a Gaussian radius and lifetime of about 4.5 ± 1.0 fm and 30 ± 10 fm/c is indicated. For the reverse kinematics reaction $^{129}Xe+^{27}Al$ at E/A=31 MeV, we observe lifetimes of about 1700 fm/c and 1200 fm/c for proton pairs with total momentum $P \geq 480$ MeV/c and $P \geq 580$ MeV/c, respectively; this behaviour is consistent with emission from a cooling system.

Dedicated, with love, to

my mother, Claire Marie Annan Lisa

and

my father, Charles Pasquale Lisa

ACKNOWLEDGMENTS

I have enjoyed extraordinarily good fortune in my brief scientific career so far. During my graduate studies, many scientists and friends (non-exclusive sets) have taught and supported me. I wish to thank a few of them here, for despite claims of the title page, a thesis is rarely the work of one person.

Firstly, I would like to thank Dr. Claus-Konrad Gelbke. His support has been crucial to me at every step, from my transition to MSU from Stony Brook, to my thesis experiment, to our European experiments, to the writing of this dissertation. The energy, integrity, and insight which he brings to his work leads to my utmost respect, and will inspire me through my career. Without him, this work would have been impossible.

I would also like to thank Dr. Pawel Danielewicz, Dr. S.D. Mahanti, Dr. Bernard Pope, and Dr. Gary Westfall, who gave generously of their time to serve on my thesis committee. Their cheerful and patient efforts make my degree attainable.

As an undergraduate, I was introduced to scientific research through the REU program at the University of Notre Dame and was fortunate to work with two fine scientists, Dr. Gerald Jones and Dr. James Kolata, who impressed me with their ability to work with developing physicists at all stages.

During my second of two years of graduate study at the State University of New York at Stony Brook, I was privileged to work in the group of Dr. Peter Braun-Munzinger and Dr. Johanna Stachel. Their friendly instruction style combined with a strong grasp of important physical issues made for an

impressive introduction to the field of high energy nuclear physics. Particularly, I wish to thank Dr. Stachel for serving on my committee at Stony Brook and Dr. Braun-Munzinger for his kind recommendation as I began my studies at MSU.

The enthusiasm and intelligence of the students and postdocs at Stony Brook impressed me from the start. For infecting me with enthusiasm and for their valuable friendship, I especially thank Mark Bellermann, Rene Bellwied, Dave Coker, Jimmy Dee, Anindita Ghosh, Rajeev Gupta, Chris Kendsiora, Claus Koestler, Dennis LaFosse, Steve Riemersma, Mark Widmer, and Christof Wunderlich.

My training in experimental nuclear physics at Michigan State has been quite enjoyable, due to skilled scientists at the lab who love their work. I was privileged to learn the fine art of designing, optimizing, and debugging an acquisition electronics system while working alongside Dr. David Bowman and Dr. Skip Vander Molen. I am grateful to Dr. Betty Tsang for constantly reminding me to take nothing for granted and for showing me that computer control of an experiment *can* be done in a systematic manner. Thanks also to Dr. Romualdo de Souza, who taught me not to lose sight of the physics when conducting an experiment.

My work in two-proton interferometry builds largely on the foundation laid by Dr. Wen Gong. His patient instruction in the theoretical and experimental aspects of this field during the time that he was preparing to write his dissertation is much appreciated. I am also indebted to Dr. Scott Pratt, correlation guru, for many patient and insightful explanations of the subtleties of interferometric physics and for the use of his correlation code. I was privileged also to work with Dr. Bill Lynch, who can as easily discuss an involved theoretical issue as a tricky technical one.

I would also like to thank Dr. Wolfgang Bauer and Dr. Catherine Mader for providing me with the results of their BUU calculations, and for fruitful discussions.

The lab staff is the largest asset of the NSCL. In particular, I would like to thank Jim Vincent for help with nuclear electronics problems, and Len Morris, Renan Fontus, and Steve Bricker for help with the design and "field engineering" aspects of the mechanical apparatus used in my experiment. Barb Pollack and Ron Fox were there to help when I had computer problems, and Dennis Swan always seemed to know some trick to deal with a detector problem I was having. Finally, the entire operations group deserves my thanks for a steady, well-tended beam during my experiment.

I am fortunate to count among my friends many fellow graduate students and postdocs at the NSCL. I am indebted to the friendship of James Dinius, Thomas Glasmacher, Gene Gualtieri, Damian Handzy, Stefan Hannuschke, Rick Harkewicz, Wen Chien Hsi, Yeonduk Kim, Roy Lacey, Tong Li, Mike Mohar, Raman Pfaff, Larry Phair, Don Sackett, Carsten Schwarz, Cornelius Williams, Bo Zhang, and Fan Zhu. From them and with them, I learned a lot.

The greatest thanks must go to my family. My brother Greg and my sisters Shawna and Jennifer are a restless lot, and their energy and achievements remind me never to get too lazy. Similarly, tales of the Irish Annans and McCabes and the Italian Boninos and Lisas remind me that any of our accomplishments stem from the sacrifices and efforts of those who have gone before. Closest to me are my parents, whose own achievements serve as both example and inspiration. Their loving support has meant everything to me.

Finally, the greatest gift I have received in Michigan has been to meet and get to know Laura. Her love has supported me through trying times and has made the future look like a pretty nice place to be.

Table of Contents

List of Tables

List of Figures

Chapter 1 - Introduction

1.1 Intensity Interferometry

The importance of interferometric measurements in the development of modern physics can hardly be overstated. A crucial element in what was to become a unified electromagnetic theory was revealed when Young's double slit experiment firmly established the wave nature of light. Then, the existence of waves in otherwise empty space naturally led to the question of 'what was waving?' and the concept of a universal medium through which massive bodies move freely— the aether— was born. In 1881, Michelson built an interferometer sensitive enough to disprove the existence of the aether, and the fundamental basis for special relativity was laid. Finally, the essence of the third great development of modern physics— quantum mechanics— is contained in an interferometric experiment: Feynman states that truly quantum mechanical effects can always be summarized by saying, 'You remember the case of the experiment with the two holes? It's the same thing!' [Feyn 65]. Indeed, in Feynman's path integral formalism, any physical phenomenon may be viewed as an interference pattern to which all possible paths contribute.

The cases mentioned above are all examples of amplitude interferometry. In amplitude interferometry, schematically illustrated in the upper panel of Figure 1.1, the waves emitted from the source O are split by two slits. The probability amplitude at detection point D is the sum of the amplitudes associated with the two paths O-S_1-D and O-S_2-D. The dark fringe spacing may

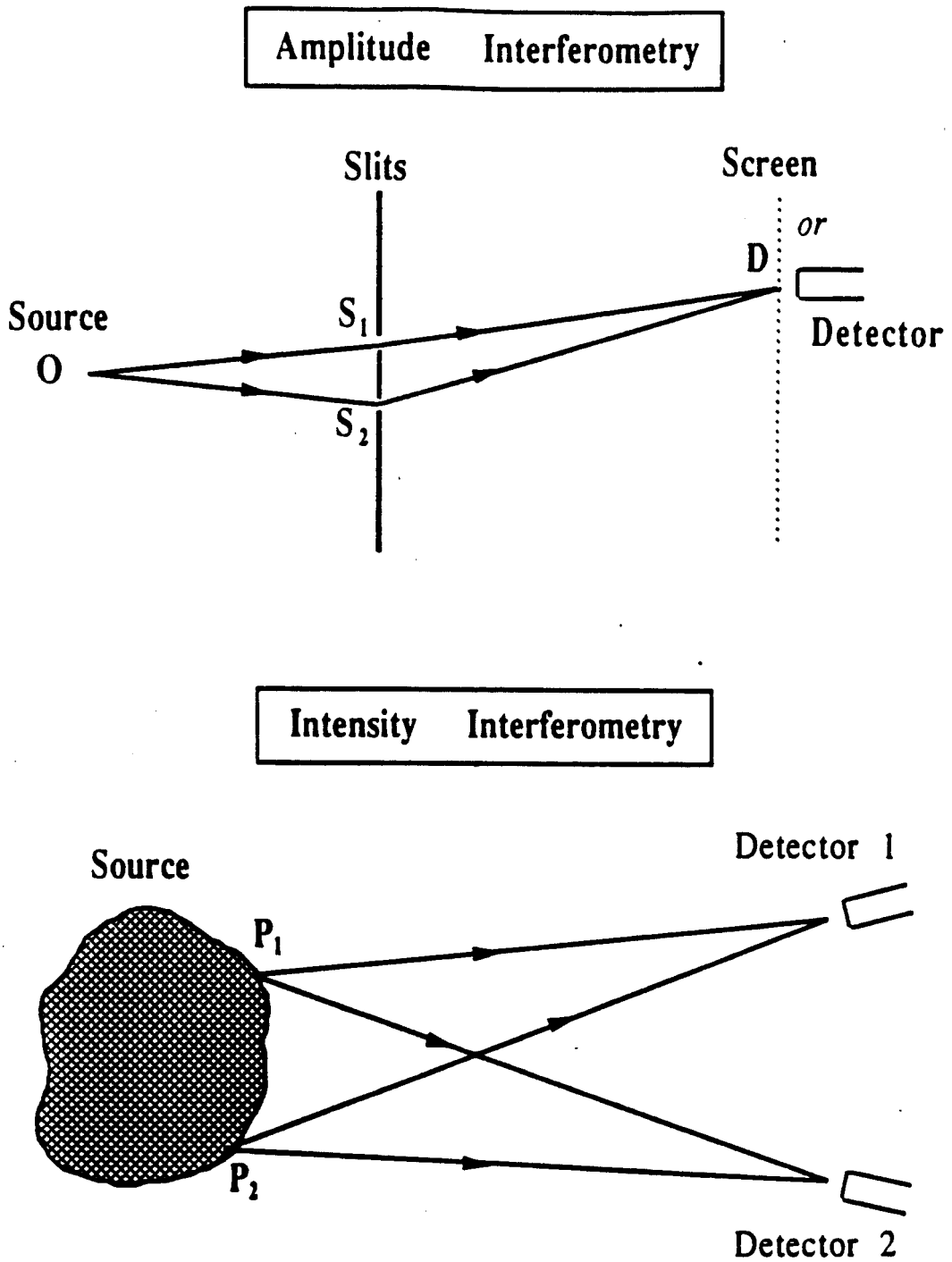

Figure 1.1. The operation of the two types of interferometer is schematically shown. In the upper panel, an amplitude (Michelson) interferometer measures the single-body detection probability. The lower panel shows an intensity (HBT) interferometer which measures the two-particle yield. (From [Gong 91c]).

be studied as a function of slit separation, and information on the angular size of the source O may be extracted.

A Michelson interferometer may be based on this principle (employing a beam splitter instead of a plate with two slits) to measure stellar sizes. In 1920, the angular diameter of the red giant Betegeuse in the shoulder of Orion was measured with such a technique [Swen 87]. However, measurement of significantly smaller sources proved difficult with the Michelson interferometer. Improving the resolving power meant increasing the baseline, and distances of 100 km or more involved more elaborate equipment [Hanb 54]. More importantly, as the path lengths sample less and less common air volume, atmospheric disturbances impose random relative phase shifts, destroying the interference signal.

In response to this problem, Hanbury Brown and Twiss (HBT) proposed an interferometer that operated on a different principle. The operation of their intensity interferometer is schematically shown in the lower panel of Figure 1.1. As opposed to the amplitude (Michelson) interferometer, which measures the single-particle detection probability, the intensity (HBT) interferometer records the two-particle probability. Information about the relative phase of wavefronts impinging on Detectors 1 and 2 is lost (and is unnecessary), but the time-structure of the measured probability at each detector is recorded. The two-particle coincidence yield n_{12} and the single-particle yields n_1 and n_2 are measured. A correlation function $C(\mathbf{p}_1,\mathbf{p}_2)$ is constructed according to:

$$C(\mathbf{p}_1,\mathbf{p}_2) = 1+R(\mathbf{p}_1,\mathbf{p}_2) = \langle n_{12}\rangle / \langle n_1\rangle\langle n_2\rangle. \qquad (1.1)$$

Source size information may be extracted from the two-particle correlation function.

The correlation function depends only on the correlations present in the coincidence yield. For a photon measurement, such correlations arise due to their bosonic nature. The presence of one photon in a particular momentum state increases the likelihood that another will be emitted into the same state. The strength of such correlations depends on the average space-time separation of the photon emission points— that is, the source size.

The use of intensity interferometry in subatomic physics followed a few years later in a study of angular correlations of pions emitted from antiproton-proton annihilation reactions at about 1 GeV. Goldhaber, Goldhaber, Lee, and Pais (GGLP) [Gold 60] found that the statistical model described well the correlations between pion pairs of unlike charge, but that distributions for like-charge pions contained additional correlations. Assuming that these arose from wavefunction symmetrization effects (or so-called Bose-Einstein correlations), GGLP were able to reproduce the additional correlations with an assumed source radius on the order of 5 fm. Today, pion correlations are used extensively as a tool to probe the space-time extent of sources created in high energy nuclear collisions [Boal 90] and are to be the subject of major experimental efforts in the search for the quark-gluon plasma at the Relativistic Heavy Ion Collider (RHIC).

In 1977, Koonin [Koon 77] proposed the use of proton correlations as a means of studying intermediate-energy nuclear reactions. As fermions, protons should show an *anti-correlation* in the two-particle yields, in contrast to photons or pions. Dominating the correlations, however, are final-state interactions due to the strong nuclear force and Coulomb repulsion. When correctly incorporated into the theoretical formalism, these too may be used as probes into the space-time extent of the source. Two-proton correlation functions have been studied extensively in intermediate-energy heavy ion collisions (for references, see, e.g.

[Boal 90]) and may eventually pinpoint the elusive liquid-gas phase transition of nuclear matter [Prat 87].

1.2 Geometrical Measurements with Two-Proton Correlation Functions

Two protons emitted from an excited region of nuclear matter will mutually interact through the strong nuclear and Coulomb forces. These final-state interactions, along with the quantum mechanical requirement of wavefunction antisymmetrization, will alter the measured two-proton distribution, compared to a scenario in which the protons are distinguishable and do not interact. The magnitude of these effects depends on the phase space separation of the two protons upon emission. By dividing the coincidence yield by the single-particle yields, the correlation function measures the amount of distortion in the final state, revealing information about the initial space-time separation of the pair, while dividing out single-particle phase space effects.

An attractive S-wave component of the strong interaction leads to a pronounced maximum in the correlation function at a relative momentum $q \approx 20$ MeV/c. Smaller emitting sources lead to more pronounced bumps. The Coulomb repulsion and the Pauli antisymmetrization principle suppress the correlation function at small q values. The amount of suppression increases with decreasing source size. The interplay between these three effects, along with the initial proton phase space distribution, determines the shape of the correlation function.

Protons emitted with an average velocity $\mathbf{v}$ from a source with radius r and an emission timescale characterized by τ, will have an initial spatial separation on the order of $d = |\mathbf{r} + \mathbf{v}\cdot\tau|$. In Figure 1.2, the spatial distributions of protons emitted toward a detector system to the right are shown. It is qualitatively clear that an increase in the source radius (panel *b*) or in the

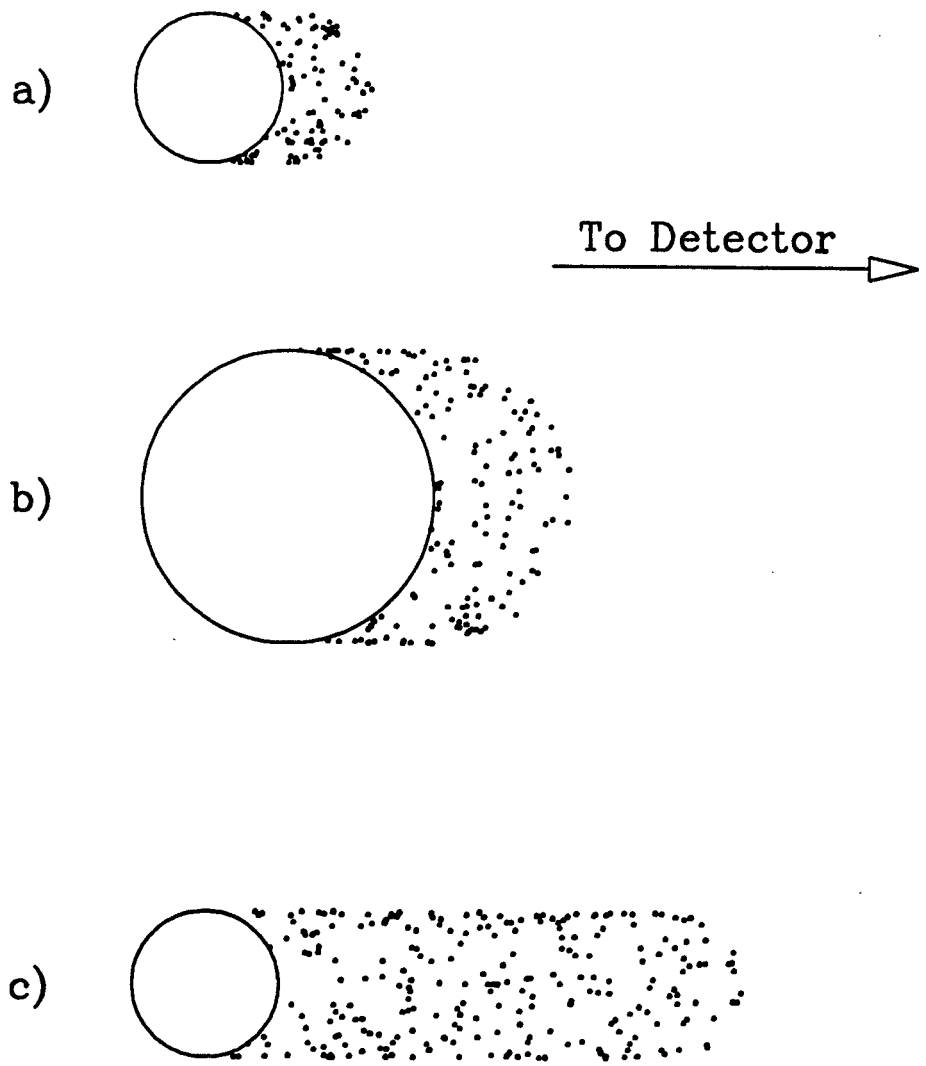

Figure 1.2. Spatial distributions of emitted protons originating from a source with a small spatial and temporal extent (a), with a large spatial extent (b), and with a large temporal extent (c).

emission timescale (panel *c*) leads to a more extended phase space distribution than is shown in panel *a*.

The resonance in the strong interaction is S-wave in nature, and, for spatial separations less than the Bohr radius of 58 fm, the long-range Coulomb repulsion is dominated by the $\ell=0$ partial wave. Therefore, the magnitude of these final-state interactions depends upon the average separation d only; the distributions in panels *b* and *c* are not distinguishable through final-state interactions.

However, information about the shape of the distribution may be extracted through quantum mechanical effects. The antisymmetrization requirement suppresses the correlation function over the range $q_x \lesssim 1/R_x$, where q_x and R_x are the component of the relative momentum and the spatial separation of the phase space distribution in the x-direction, respectively. Therefore, if the phase space distribution resembles that shown in panel *b*, a correlation function constructed from proton pairs whose relative momentum is oriented along the short dimension of the distribution will be suppressed as compared to a correlation function constructed from pairs with the relative momentum oriented along the long dimension. Through such cuts, both the size and lifetime of the source may be extracted.

1.3 Sources Created in Intermediate-Energy Heavy Ion Collisions

The study of heavy ion collisions is currently an active area of research, pushing existing accelerators to the limits of their design and prompting the construction of a new machine able to accelerate heavy ions to energies not currently attainable. The system under study is finite, quantum mechanical, strongly interacting, and quickly evolving. Furthermore, the behaviour of the system depends on variables that elude direct measurement. The complexity of heavy ion collisions presents a true challenge to theorists and experimentalists

alike because both statistical and dynamical effects play a role in the evolution of the collision, the relative importance of each being determined by the bombarding energy and impact parameter.

At low bombarding energies ($E/A \lesssim 10$ MeV), the evolution of a heavy ion collision is largely determined by mean field effects and one-body dissipation. Central collisions are understood in terms of the creation and statistical decay of a long-lived, equilibrated compound system which is formed through complete fusion and which decays by particle evaporation. Proton-emitting sources created in such a scenario may be expected to have a spatial extent comparable to that of the compound nucleus, and a lifetime on the order of hundres to thousands of fm/c [Frie 83].

Heavy ion collisions that occur at relativistic energies ($E/A \gtrsim 1$ GeV) are largely understood in terms of individual nucleon-nucleon interactions. The geometrical participant-spectator model applies, and the energy density is greatest in the reaction zone, defined by the spatial overlap of the target and projectile density distributions. The binding energies are negligible compared to the energy deposited in the reaction zone, and the system explodes into its constituents. A "source" in this case may be difficult to envision, and lifetimes are expected to be on the order of the time required for a nucleon to traverse the nuclear region– roughly 10 fm/c.

Intermediate bombarding energies constitute the realm of the transition between the statistical decay of an equilibrated compound system and the dynamical explosion of nuclei into constituent components. Highly excited composite systems may be created on very short timescales, allowing dynamical and statistical processes to compete as the distinction between pre-equilibrium and thermal emission from a "hot spot" blurs. After the early emission of high-energy nucleons, an equilibrated hot residue is expected to remain, which then

undergoes statistical decay. At low excitation energies, the compound system resembles a hot liquid drop which evaporates nucleons as it cools. At higher excitation energies, thermal pressure may push the residue to the limits of stability and cause it to expand to low density where disintegration into nucleons and bound clusters may occur.

The transition to a mixture of nucleons and bound clusters is similar to a liquid-gas phase transition. Although current heavy ion accelerators are capable of creating nuclear systems hot enough to leave the liquid state, no definitive experimental signature for the liquid-gas phase transition has been found in the single-particle spectra. Kinetic energy "temperature" parameters vary smoothly with projectile energy [West 82, Chit 86b], and no sudden "jump" in the fragment multiplicities indicative of a phase transition is observed as a function of bombarding energy or impact parameter [de So 91, Ogil 91, Bowm 91, Peas 93, Tsan 93].

A saturation in the temperature of a statistical system as the excitation energy is increased may signal a phase transition. Indeed, temperatures extracted by comparing relative yields of particle-unstable states emitted from heavy ion collisions show surprisingly little sensitivity to projectile energy [Chen 87c]. (A small systematic dependence is, however, observed [Schw 93].) At present, it is not yet certain whether the relative population of states is determined by the temperature of the emitting system or whether it is determined by the reaction dynamics [Fuch 90].

As discussed by Pratt and Tsang [Prat 87], an experimental determination of the timescale of particle emission could give essential information about the phase of the decaying nuclear system. The decay of nuclear matter in the liquid phase would be characterized by lifetimes on the order of several thousand fm/c [Frie 83, Prat 87], with longer lifetimes for less energetic particles, since the

temperature drops more slowly as the system cools [Boal 86b]. A nuclear gas, on the other hand, should exhibit emission timescales on the order of 100 fm/c or less [Aich 85, Aich 86, Prat 87], as spontaneous expansion of the system follows compression.

1.4 Motivation for This Study

The dependence of the correlation function on the total momentum of the proton pair $P = |\mathbf{p}_1 + \mathbf{p}_2|$ has been studied previously for many systems [Lync 83, Chen 87c, Poch 86, Poch 87, Awes 88, Gong 90b, Gong 90c, Gong 91b, Lisa 91]. Stronger correlations have been observed for pairs with larger total momentum, qualitatively indicating a tendency towards sources of larger space-time extent as the reaction evolves. Recently, this dependence was successfully reproduced by a dynamical model based upon the Boltzmann-Uehling-Uhlenbeck (BUU) equation [Gong 90c, Gong 91b, Baue 92], suggesting that the BUU may reliably describe the evolution of the reaction zone. However, the P-dependence of the correlation function predicted by the BUU was quite different for central and peripheral collisions [Gong 91a], indicating a distinct reaction evolution for central and peripheral collisions. In the past, such detailed predictions were inaccessible to experimental tests, since high-statistics proton coincidence measurements lacked experimental impact parameter filters. Those measurements which did have impact parameter filters lacked sufficient statistics to gate simultaneously on P. Experimental tests of the impact parameter and total momentum dependence of predicted correlations may isolate those impact parameters for which the BUU adequately describes the reaction evolution and indicate areas in which further theoretical work is needed.

As discussed in Section 1.2, proton emission from a long-lived source should be evident through cuts on the relative orientation of the total and relative momenta of the proton pair, $\psi = \mathrm{Cos}^{-1}(\mathbf{P}\cdot\mathbf{q}/P\,q)$. Comparison of the longitudinal

($\psi \approx 0°$) and transverse ($\psi \approx 90°$) correlation functions should eliminate the ambiguity between space and time effects and thus allow the determination of expansion and emission timescales in a relatively model-independent way. Previous searches for a directional dependence in two-proton correlation functions have produced null results [Zarb 81, Awes 88, Ardo 89, Gong 90b, Gong 91b, Gouj 91, Rebr 92]. Recently, it was suggested [Rebr 92] that incorrect assumptions about the rest frame of the emitting source due to incomplete knowlege of the impact parameter could wash out the expected directional dependence.

It was the aim of this thesis to measure the total momentum and directional dependence of the two-proton correlation function for $^{36}Ar+^{45}Sc$ collisions at E/A=80 MeV as a function of impact parameter. This required a high-resolution, high-statistics measurement of proton yields, with coincident information on the violence of the collision from the yields of other charged particles emitted in the reaction. Coincidence and single proton yields were measured in a high-resolution detector array at $\langle\theta_{lab}\rangle=38°$. The MSU 4π Detector Array, covering about 85% of the remaining solid angle, provided information about the violence of the collision. Two-proton correlation functions were constructed from the proton yields and impact parameter selection was performed with cuts on global observables measured in the 4π Array.

1.5 Organization of This Work

This work concentrates on a study of the nearly symmetric system $^{36}Ar+^{45}Sc$ at E/A=80 MeV. Full details of this study are presented here. Also presented are some results from a re-analysis of data previously taken by Gong et al. for the systems $^{14}N+^{27}Al$ at E/A=75 MeV [Gong 90c, Gong 91b] and $^{129}Xe+^{27}Al$ at E/A=31 MeV [Gong 90b, Gong 91b]. Experimental details for

these data have been previously reported [Gong 91c]; we do not reproduce them here.

Chapter 2 discusses the technical details of the Ar+Sc experiment, including descriptions of the 56-element hodoscope and 4π Array detector systems and electronic logic used. Chapter 3 presents the details of the data reduction, including particle identification, time walk correction, and energy calibration techniques.

Chapter 4 deals with experimental determination of the centrality of an event. Impact parameter selection based on global observables is discussed, as well as a method to experimentally determine the experimental resolution for centrality determination. Also described are two methods for comparing centrality-cut data to predictions of a dynamical model.

Chapter 5 discusses the two-proton correlation function. The theoretical framework in which the correlation function is usually understood– the Koonin-Pratt formalism– is presented, and specific application of the formalism to two-proton data is discussed. Sensitivity of the correlation function to the space-time structure of the source is illustrated by schematic calculations. Two commonly-used methods for constructing the experimental correlation function are discussed and compared for the system $^{14}N+^{27}Al$ at E/A=75 MeV. Finally, a discussion of the effects on the correlation function from finite experimental resolution is presented; the $^{36}Ar+^{45}Sc$ data measured with the 56-element hodoscope is used as an example.

Chapter 6 presents the centrality-cut proton data measured for $^{36}Ar+^{45}Sc$ at E/A=80 MeV. Predictions of a Boltzmann-Uehling-Uhlenbeck transport model are compared to the single-particle energy spectra and to the two-proton correlation functions.

Chapter 7 discusses the use of longitudinal and transverse correlation functions to independently determine the source size and lifetime for a short-lived hot source created in central $^{36}Ar+^{45}Sc$ collisions at E/A=80 MeV, and for an evaporative source created in $^{129}Xe+^{27}Al$ collisions at E/A=31 MeV. The importance of proper source frame identification is discussed.

Finally, in Chapter 8, we present a summary and some brief conclusions.

Most of the results presented in this work have been submitted to refereed journals for publication [Lisa 91, Lisa 93a, Lisa 93b, Lisa 93c, Lisa 93d].

Chapter 2 - Experimental Details

The experiment was performed at the National Superconducting Cyclotron Laboratory at Michigan State University using particle beams provided by the K1200 cyclotron. Two charged particle detector arrays were combined to measure reaction products. A schematic diagram of the set-up is shown in Figure 2.1. The energy and emission direction of light charged particles were measured with high precision in a 56-element hodoscope, which was centered at a laboratory angle of 38°. Information about the centrality or violence of the collision was determined by measuring charged particles in the MSU 4π Array [West 85], which surrounded the target. Event information from each collision was digitized on an event-by-event basis and written to tape to be analyzed off-line.

Here, we discuss the major subsystems of the experiment, concentrating first on the detectors themselves, and then discussing the electronics. Finally, we discuss our choice of nuclear system under study.

2.1 The 56-Element Hodoscope

Light particles (p,d,t,^{3}He,α) were measured in a 56-element hodoscope, comprised of a closely-packed array of 56 ΔE-E telescopes [Gong 91b]. The mechanical structure of the hodoscope and 37 of the 56 detector elements had already been constructed for the thesis experiment of W.G. Gong [Gong 91b]. In preparation for the measurements discussed in this work, we constructed the remaining detector elements and the mechanical support/vacuum chamber to couple the hodoscope to the 4π Array.

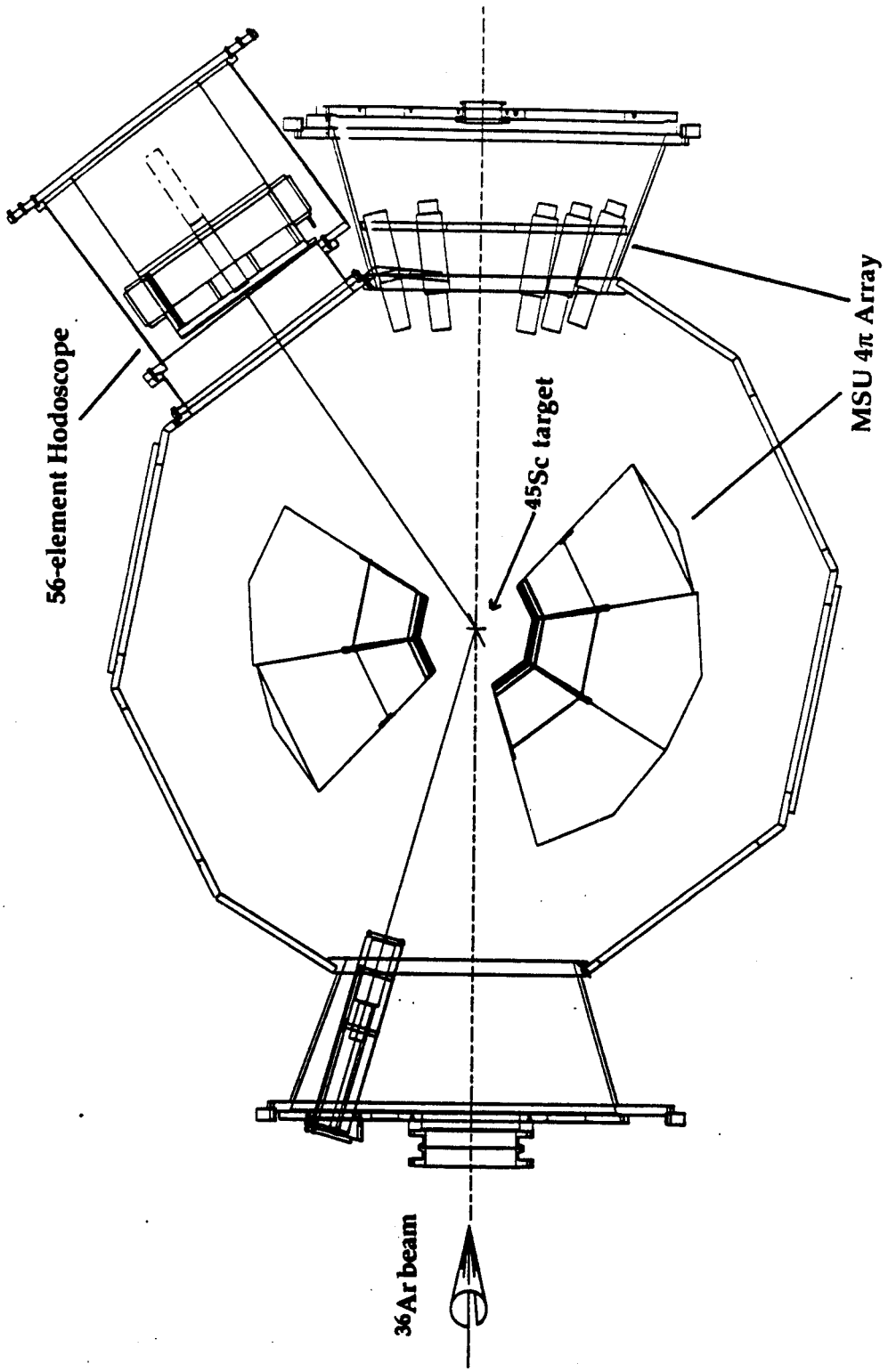

Figure 2.1. Schematic diagram showing the arrangement of the 56-element hodoscope and the MSU 4π Array.

2.1.1 Detector Elements

The ΔE component of the telescope consisted of a 300-μm-thick planar surface barrier detector with an active area of 450 mm^2 (Ortec models TB-024-450-300-S and TD-024-450-300-S). A positive voltage (typically ~ 100 V) across the face of the detector allows the collection of free charge generated when ionizing radiation (e.g. a charged particle) passes through the detector. The signal is then passed to a preamplifier and sent out to the electronics system to be discriminated and digitized.

The E component of the telescope consisted of a CsI(Tl) detector [Gong 88, Gong 90a, Gong 91c]. A schematic of this detector is shown in Figure 2.2. The CsI(Tl) crystal is a 10 cm long cylinder with a diameter of 38 mm. The crystals used for the original telescopes were manufactured by BICRON corporation. For the completion of the hodoscope, we purchased crystals of identical dimensions from Hilger corporation of France.

The crystals arrived unpolished. Following the "standard" crystal processing developed in the construction of the original detectors, we sanded the (vertical) sides of the crystal with fine sandpaper (#320) with strokes parallel to the cylinder axis. The two end faces were first polished with fine sandpaper in a circular motion; the crystal was held vertically over the sandpaper which sat on a flat glass plate. Ethyl alcohol was liberally applied to the sandpaper to help the crystal glide smoothly, avoiding "jumps" which can deeply scratch the surface. Next, a silk cloth with polishing compound (National Diagnostics ND-706) was used to polish the surfaces, and finally, a tissue that had been very slightly dampened with water was used. CsI is hygroscopic, so it is important to avoid contact with water; however, a very small amount will "melt" a surface slightly, greatly improving the polish. Although we eventually would roughen one end of the crystal with #320 sandpaper, first polishing both ends allowed us to see

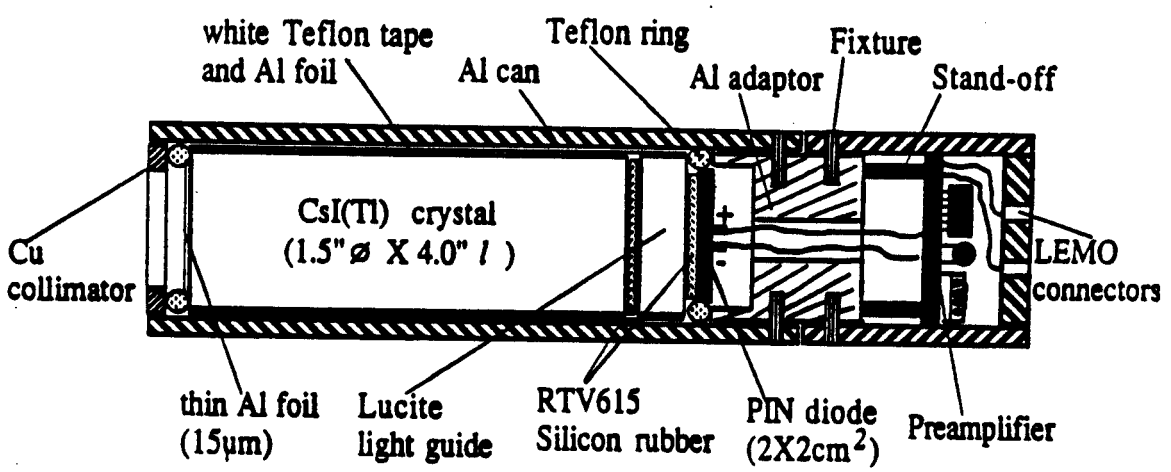

Figure 2.2. Schematic anatomy of the CsI(Tl)-PIN diode assembly used as the E detector in the light particle telescope.

through the crystal. Most crystal interiors were uniformly clear. Two of the crystals had small visible defects; these did not affect performance as determined by resolution bench tests [Gong 90a]. When coupling the crystal to the light guide with optical cement, bubbles of air can form which may interfere with the detector performance. These were easily identified visually through the crystal. When such defects were discovered, coupling was re-done.

The crystal was coupled at the back end to a clear Lucite light guide with RTV 615 silicon rubber. It is relatively easy to couple two surfaces without air bubbles using this compound, and good optical coupling as well as mechanical stability is achieved. The sides of the light guide were sanded like the sides of the crystal. Finally, to prevent light loss, the sides and back of the light guide (where not coupled to the PIN diode) were painted with reflective paint.

A square PIN diode (Hamamatsu model S1790-02) of 2 cm X 2 cm active area was coupled to the back end to the light guide. The photodiode has an operating voltage of about 50 V and a leakage current of about 3 nA at room temperature. Operation of the diode in vacuum can result in increased leakage currents due to heating both from the diode and associated preamplifiers. Therefore, it was necessary to actively cool the hodoscope in vacuum; details are discussed below.

The crystal/light guide/PIN diode assembly was next wrapped in Teflon to further decrease light loss and nonuniformity along the detector edge. Long strips of thick Teflon tape were laid overlapping along the axis of the crystal. Next, thinner Teflon tape was wrapped around the assembly. Thin (15 μm), light-opaque aluminum foil covered the front face of the detector, and thick aluminum foil was wrapped outside the Teflon tape.

The wrapped assembly was placed into the "front" portion of an aluminum detector can, which provided mechanical rigidity. A copper ring in

the front of the can shielded the outer edges of the detector, giving a collimated diameter of 2.5 cm. Teflon rings held the crystal assembly firmly in the front portion of the can.

The signal from the PIN diode was sent by short leads (3-4 cm long) to the back portion of the can, where the preamplifier was mounted. This preamplifier, shown schematically in Figure 2.3, was developed by Michael Maier at the NSCL. The low power dissipation of this preamplifier (0.5 W) is nicely suited for operation in vacuum; a large array of these preamps can be handled by our cooling system. The rise time of the preamp (τ_r =0.2 μs) is less than both of the decay components of the CsI(Tl) (0.4 and 7 μs). For an input impedance of 130 pF, corresponding to that of our PIN diodes, the full width at half maximum (FWHM) noise of the preamplifier corresponds to a charge of 2000 electrons. For a typical CsI(Tl) detector, this corresponds to a resolution of about 300 keV for α particles of 5.5 MeV. To monitor possible gain drifts (either in the preamplifier or the amplifier that follows), a pulser test input was provided. In our experiment, gains were found to drift by less than 1% over the week-long experiment. Since both preamplifier gain and crystal light output depend on temperature, active temperature stabilization was important to steady gains.

2.1.2 Mechanical Support

The 56 detector elements were mechanically mounted in the hodoscope structure. A schematic of the front face of the structure is shown in Figure 2.4. Silicon detectors are securely held in removable brass mounts on the front face of the structure. Covering the front face of each mount is a thin (~10 μm) Ta foil to suppress unwanted signals from electrons and X-rays. Preamplifiers for these detectors surrounded the main structure. They were in good thermal contact with copper bars cooled by flowing alcohol to about 15° C.

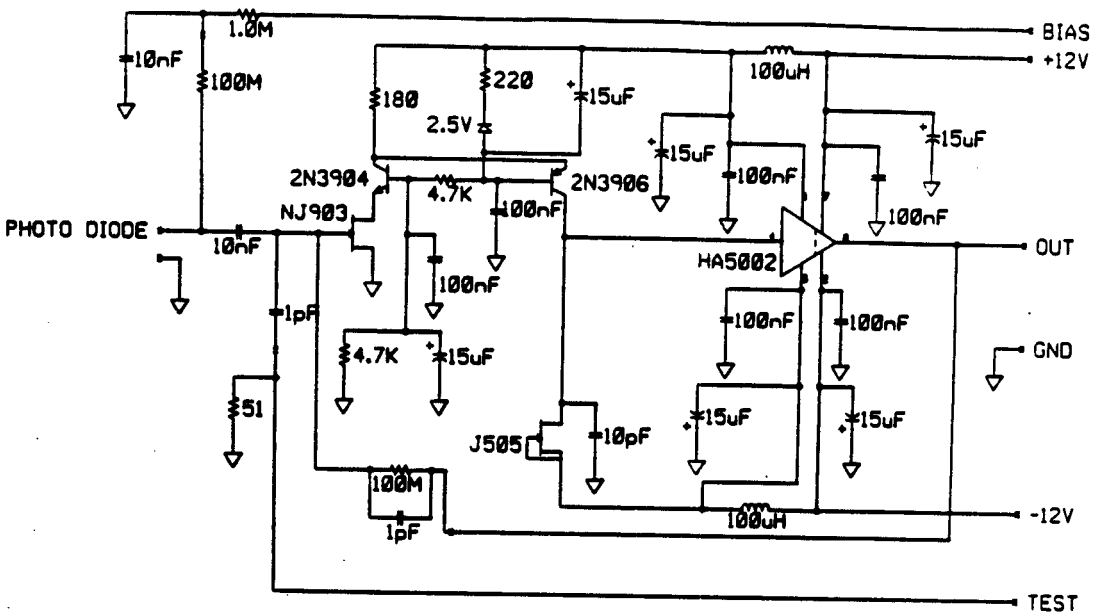

Figure 2.3. Schematic of the preamplifier for the PIN diode used to read out the CsI(Tl) detector.

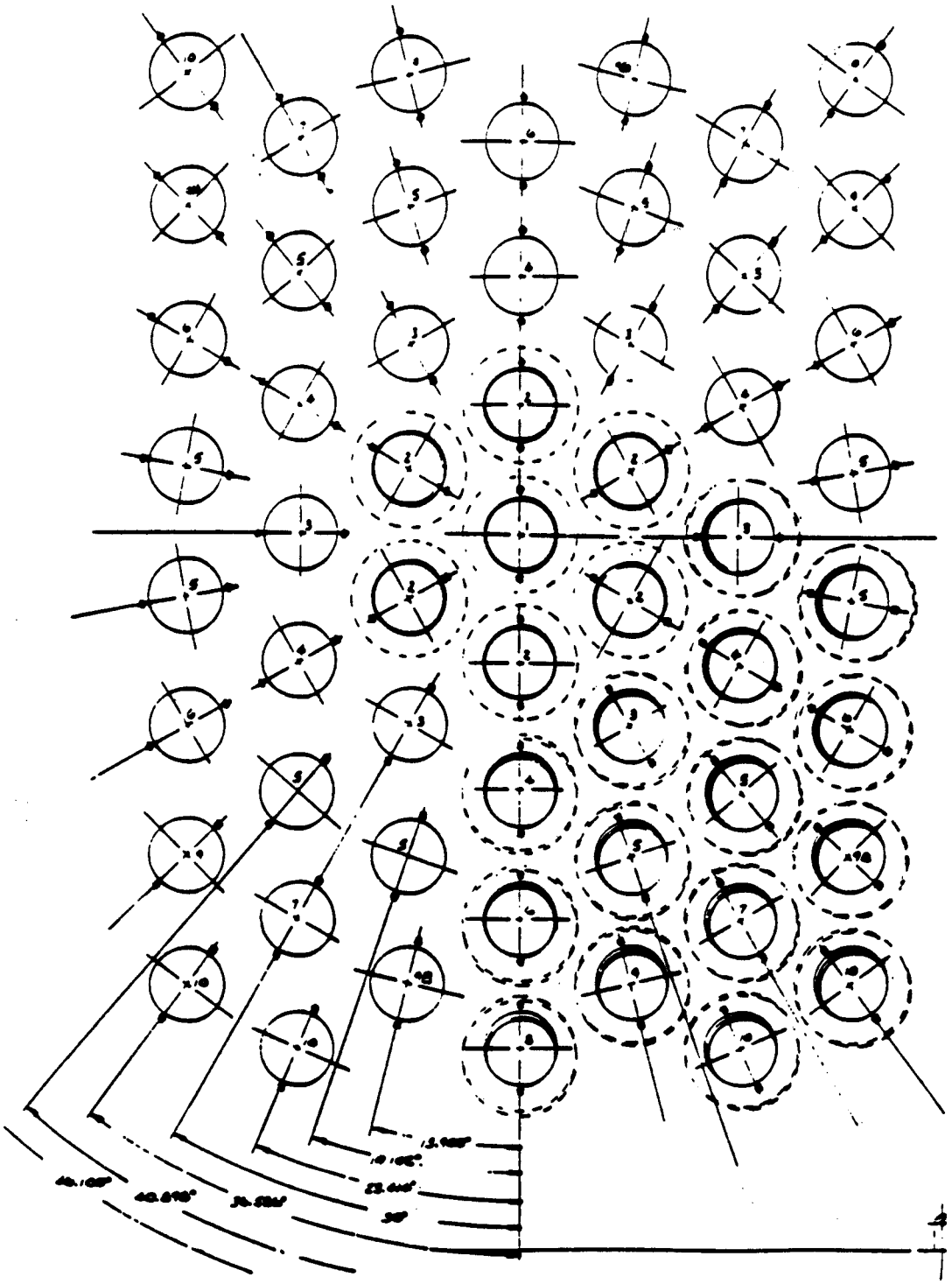

Figure 2.4. Schematic of the front face of the 56-element hodoscope structure.

Each CsI(Tl) detector is centered behind a Si detector. The back end fits snugly into a hole in a square aluminum back plate, and the front end fits into a recess in the back of the front plate. Cooling liquid flows through a copper tube embedded in the back plate to remove heat from the CsI(Tl) preamplifiers.

Telescopes mounted in the hodoscope structure face the center of a sphere with a radius of about 1 meter; this was well suited to our target-to-detector separation of 105 cm.

The hodoscope structure was housed in a vacuum chamber attatched to a hexagonal port of the 4π Array vacuum chamber, positioning the hodoscope at an average polar angle of about 38°. Figure 2.5 shows the angular coverage provided by the 56-element hodoscope.

2.2 The NSCL 4π Detector Array

The NSCL 4π Array [West 85] is a closely-packed array of plastic phoswich detectors which covers approximately 84% of the solid angle surrounding the target. Although many measurements at the NSCL are performed using the "standard" 4π set-up, a primary consideration in the design of the 4π Array was the flexibility to perform coincidence experiments with other detector systems. This consideration led to the use of interchangeable detector modules with nearly identical particle response, for ease of analysis. It is customary to distinguish between two groups of detectors in the 4π Array, the forward array and the main ball. Although in operation and response these detectors are similar, their geometries differ.

2.2.1 Detector Elements

All detectors in the 4π Array are phoswich telescopes. A thin layer of "fast" scintillating plastic is optically coupled to a larger piece of "slow" scintillating plastic, which is then optically coupled to a phototube. The fast and

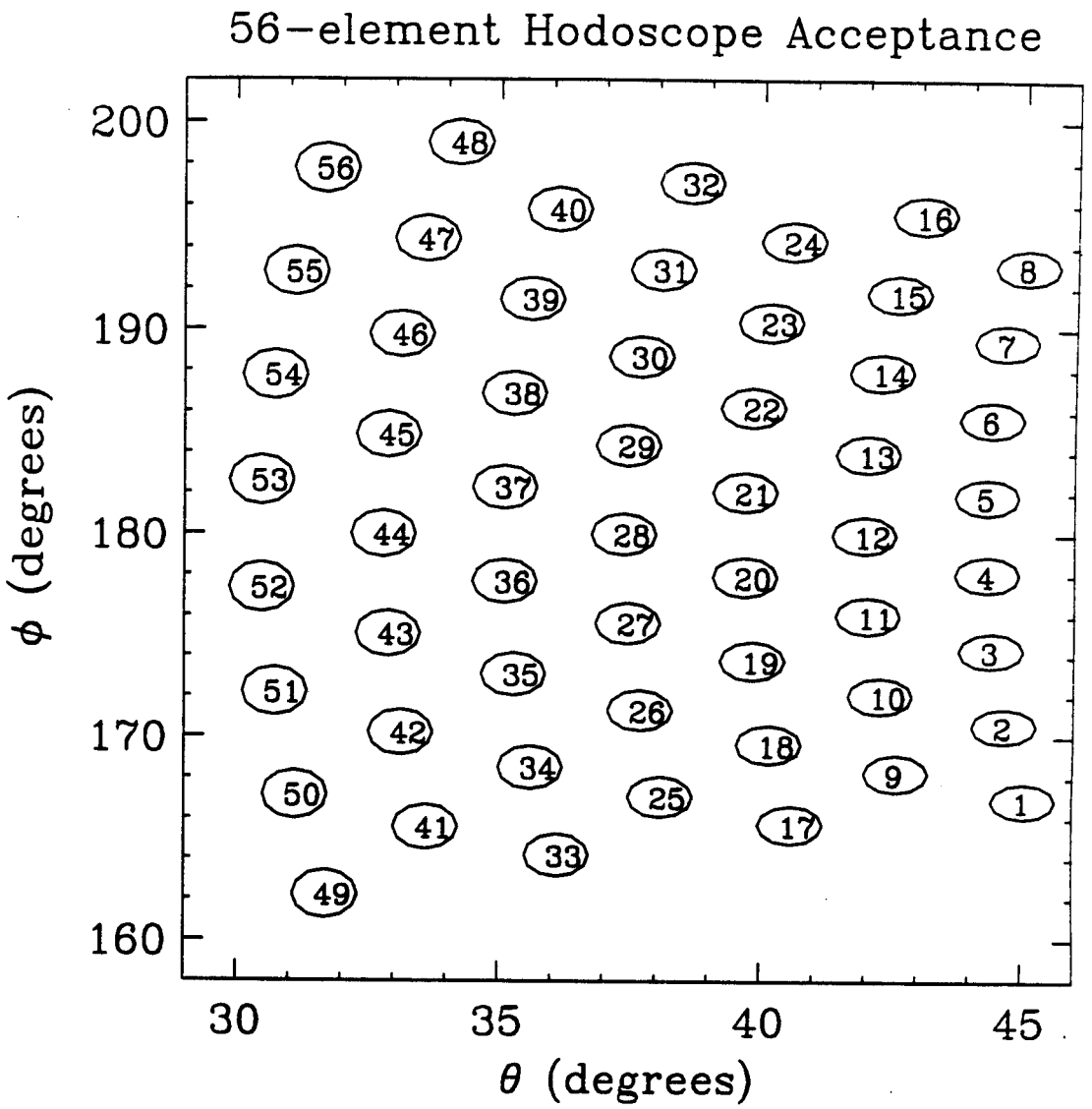

Figure 2.5. Angular coverage provided by the 56-element hodoscope.

slow plastic have different rise and fall times, as shown in Table 2.1. Figure 2.6 schematically shows the principle of operation. A charged particle entering the detector through the front face loses energy in the fast plastic, causing a brief flash of light. The particle then stops in the slow plastic and the light emitted with the slower time scales is proportional to the remaining energy.

Table 2.1. Time constants for fast and slow scintillating plastics

BICRON plastic	rise time (ns)	fall time (ns)
BC-412 (fast)	1.0	3.3
BC-444 (slow)	19.5	179.7

The signal read from the photomultiplier tube is a linear sum of the fast and slow components. Electronically, the components are approximately separated by integrating the signal over different time windows, as shown in Figure 2.6.

A typical detector response is shown in Figure 2.7, where a raw "fast" vs. "slow" spectrum from a main ball element is shown. Particles of a given species define a curve in the fast-slow space as a function of energy. Two features of the spectrum deserve mention.

Particles with energy below the so-called punch-in energy stop in the fast plastic and the signal has no slow component. The punch-in energy varies with particle type; values for the ball and forward array detectors are given in Tables 2.2 and 2.3. Although no light is generated in the slow plastic, residual light from the fast plastic appears in the slow gate. In this case, the slow signal is proportional to the fast signal, and the "punch-in line" is defined; see Figure 2.7.

A similar situation occurs for particles which do not lose energy in the fast plastic, but lose energy in the slow plastic. Examples of such particles are gamma rays, neutral particles, and cosmic rays that enter the detector from the

Table 2.2. Punch-in Energies for Ball detectors

Particle Type	Punch-in Energy (MeV)	Particle Type	Punch-in Energy (MeV)
p	17	Li	140
d	24	Be	214
t	28	B	287
He	70	C	380

Table 2.3. Punch-in Energies for Forward Array detectors

Particle Type	Punch-in Energy (MeV)	Particle Type	Punch-in Energy (MeV)	Particle Type	Punch-in Energy (MeV)
p	12	C	259	Al	816
d	16	N	328	Si	927
t	19	O	403	P	1009
He	47	F	472	S	1124
Li	95	Ne	570	Cl	1216
Be	146	Na	636	Ar	1403
B	195	Mg	737		

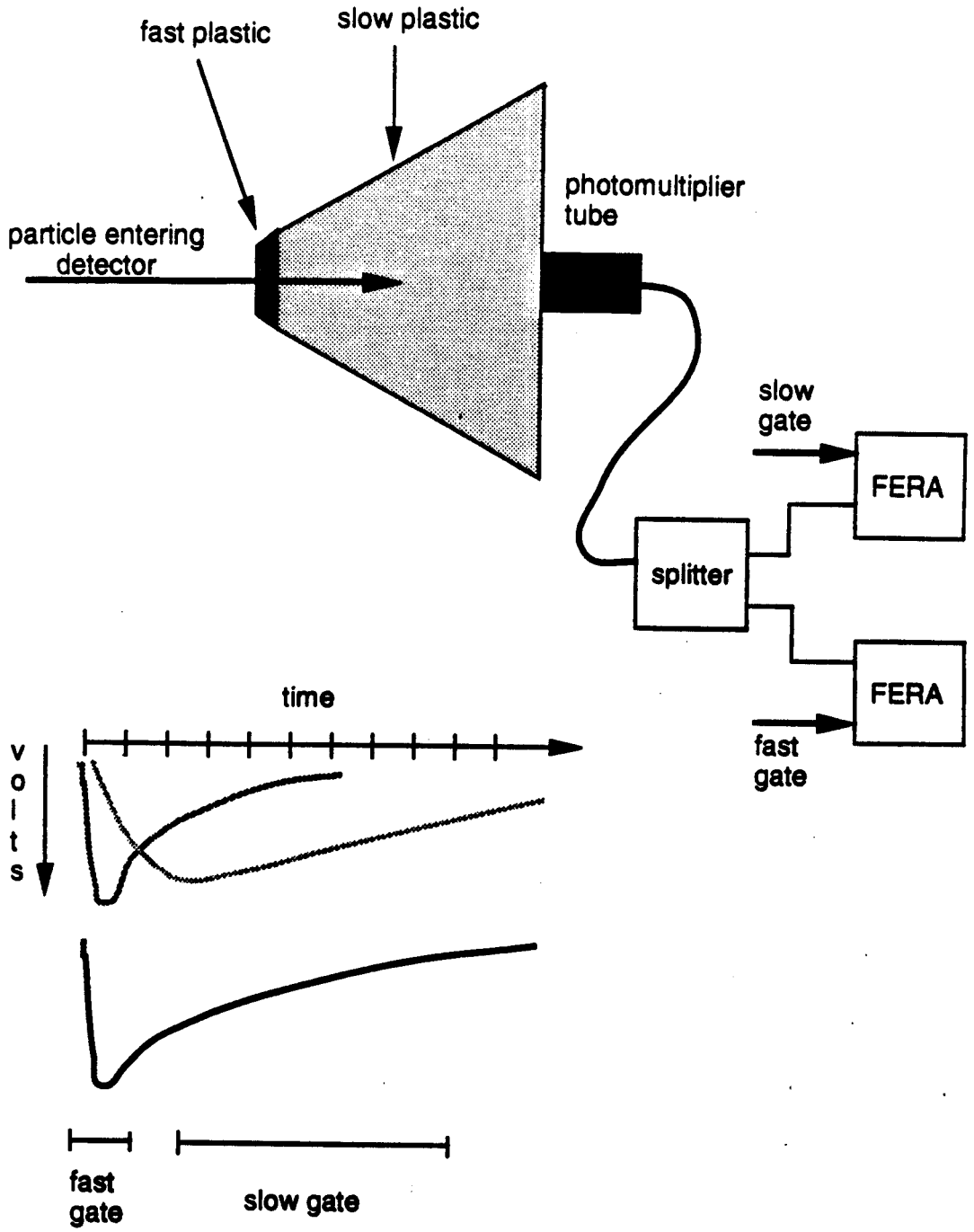

Figure 2.6. Schematic of phoswich detector operation. The signal from the phototube is split and the light components from the "fast" and "slow" plastic are separately integrated.

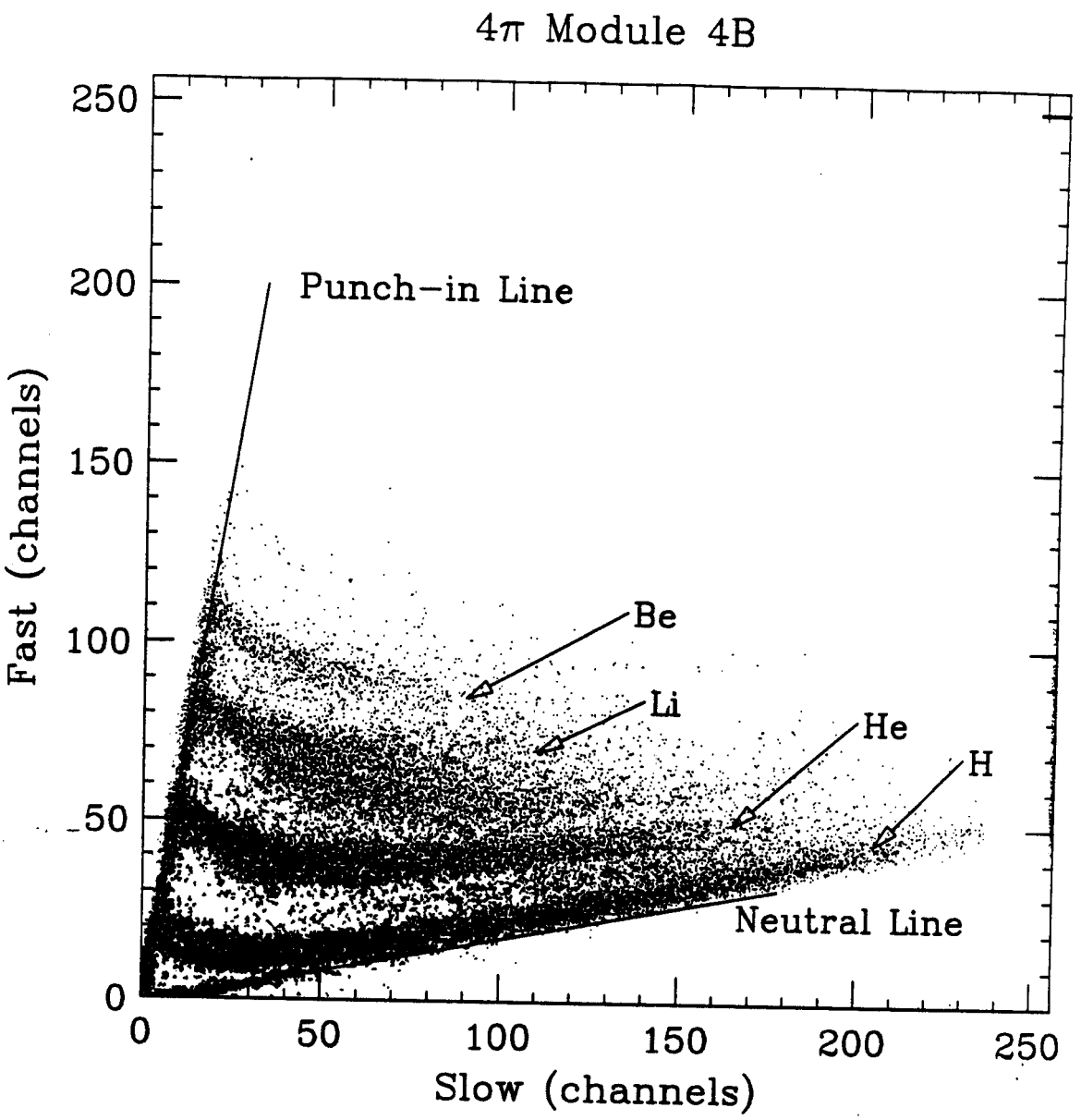

Figure 2.7. A "fast" vs. "slow" spectrum from a detector element from the main ball. The punch-in line and neutral line frame signals from identifiable particles.

side. The fast-slow curve of these particles defines the "neutral line," also shown on Figure 2.7.

2.2.2 Mechanical Set-up

The basic geometry of the 4π Array is that of a 32-faced truncated icosahedron, giving it the appearance of a soccer ball with twenty hexagonal and twelve pentagonal faces, as shown in Figure 2.8. The beam enters through one pentagonal face and exits through another. The entrance face is the only face not covered by detectors, allowing space for target insertion. The exit face contains the forward array, a set of 45 phoswich detectors with polar angles less than about 18°. A forward array element has either a square or circular front face; these shapes are not amenable for close-packing in a pentagonal geometry, so the solid angle coverage is about 54% for the exit face. The arrangement of forward array elements is shown in Figure 2.9.

The remaining faces are covered with ball modules. The pentagonal and hexagonal modules are divided into five and six wedges, respectively. Each of the 170 wedges is an independent phoswich detector.

2.3 Electronics

In this experiment, we measured two-proton correlation functions as a function of impact parameter. The correlations were measured in the 56-element hodoscope, while the impact parameter was determined by charged particle measurements in the 4π Array. All two-particle hits in the hodoscope were recorded along with the corresponding information in the 4π Array.
Because of the much faster rise time of the 4π detector elements as compared to those of the hodoscope, the 4π Array had to self-trigger its ADC's and the digitized information had to be read into the computer, or it had to be cleared, depending on whether the slower hodoscope satisfied the trigger condition.

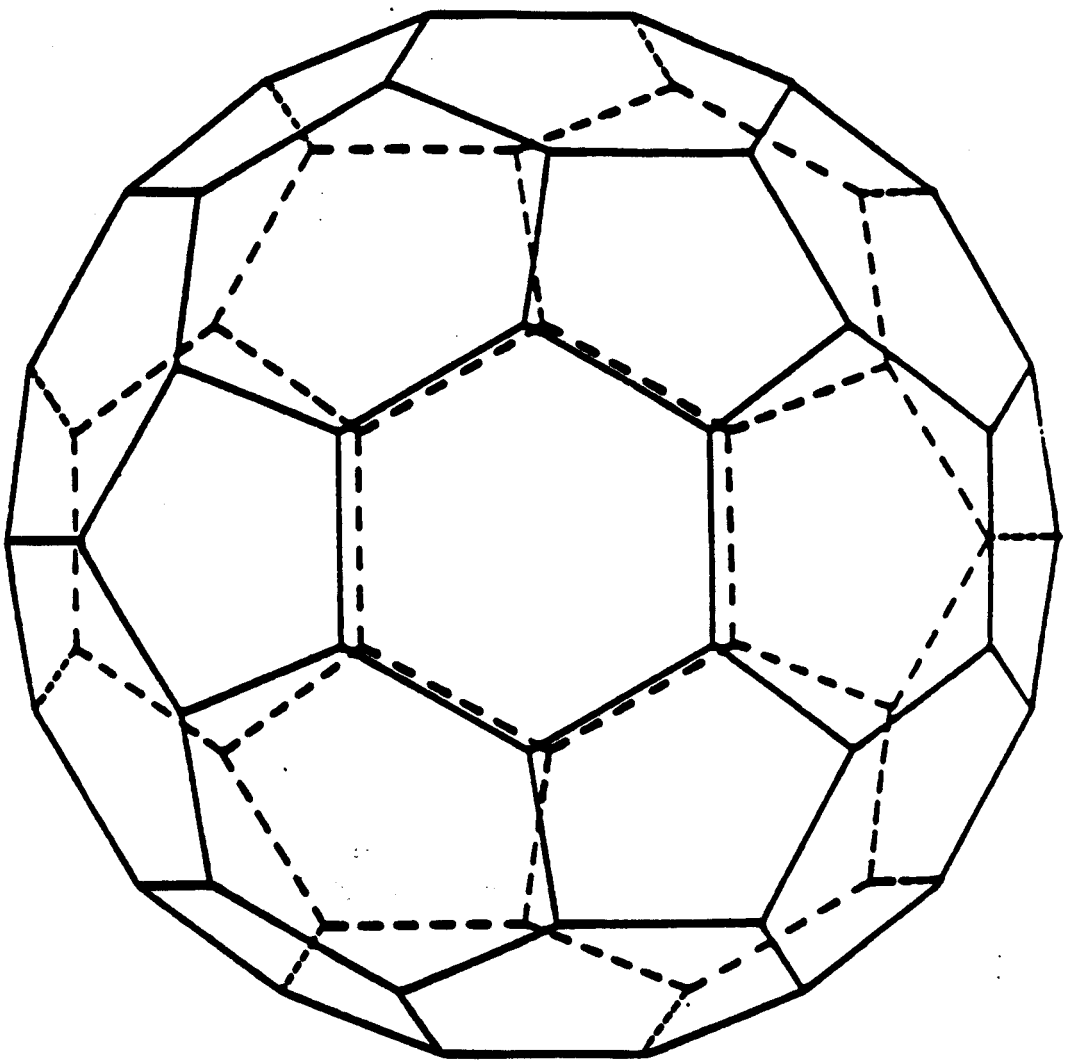

Figure 2.8. A 32-faced truncated icosahedron, the underlying geometry of the MSU 4π Array.

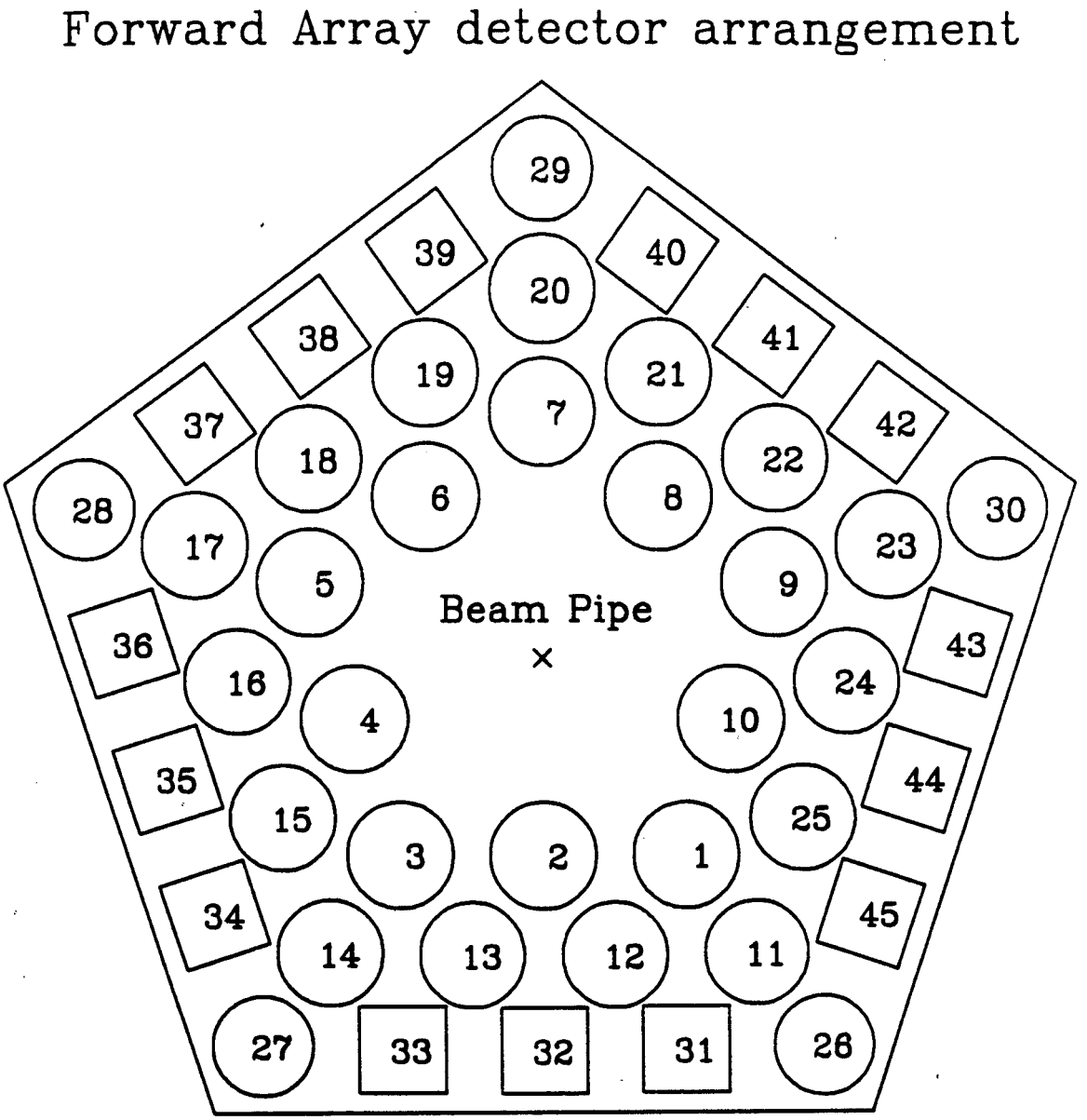

Figure 2.9. Spatial arrangement of phoswich detectors in the forward array.

In this situation, two distinct trigger conditions operated in parallel. The first condition is generated by the 4π to gate its ADC's. The second "master" condition is generated by the hodoscope to start the readout of the event. Events with a hodoscope trigger but without a 4π trigger contain no information about the impact parameter for the event. Clearly, it is important that there be a 4π trigger present every time there is a hodoscope (master) trigger, although the reverse need not be true. Therefore, we set the 4π trigger condition at "minimum bias" settings– usually at multiplicity 2 or 3 in the array. Due to the much greater geometric coverage of the 4π Array as compared to the hodoscope and to the fact that the hodoscope was positioned at a relatively large polar angle, trigger rates in the 4π Array were much larger than the master (hodoscope) trigger rates.

Three master trigger conditions were used in this experiment. For most of the 5-day data-taking period, we ran with a coincidence trigger in the hodoscope. At regular intervals, we took data under a singles trigger in the hodoscope to have data with which to construct the denominator of the correlation function, and also to be able to compare coincident and singles spectra. Finally, we took a short run with the 4π Array as the master with the trigger condition set at multiplicity 1. This last set of data was important in construction of an impact parameter scale; see Chapter 4.

Figure 2.10 shows a schematic block diagram of the electronics setup used. It is seen that the electronics for the two detector subsystems, the 56-element hodoscope and the 4π Array, are largely independent. Below, we discuss the two main branches of the electronics setup, and then how they work together.

2.3.1 56-Element Hodoscope

Preamplifier signals from the Si and CsI(Tl) detectors were sent to shaping amplifiers. The "slow" output of the amplifier, operated with a differentiating

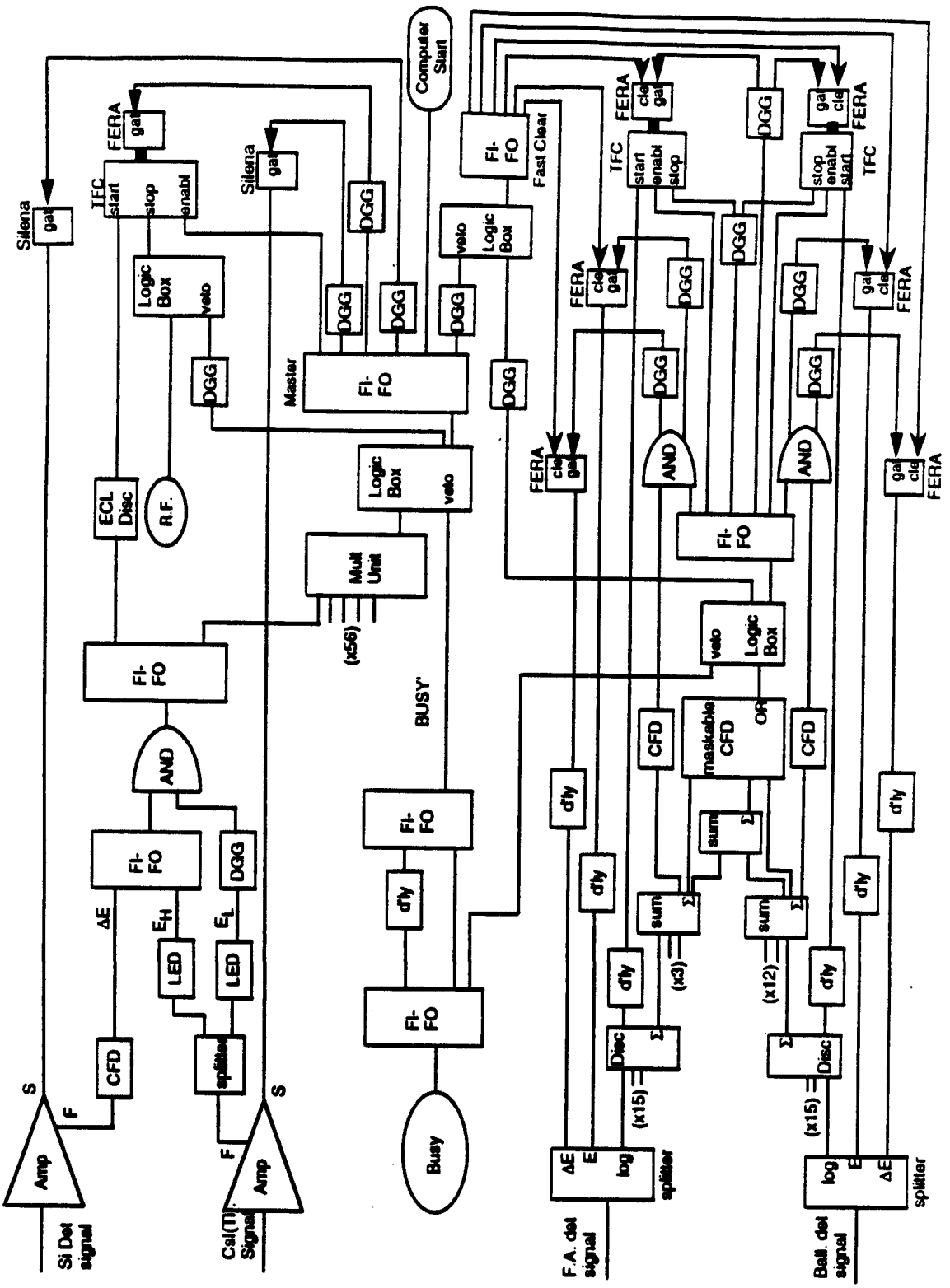

Figure 2.10. Electronics used to digitize data and trigger the computer.

and integrating time constant τ~3.5 μs, was sent directly to a peak-sensing ADC, Silena model 4418/V. The "fast" outputs from the amplifiers, with a time constant τ~100 ns, were used to build the trigger logic. The logic for one ΔE-E telescope is shown in the upper third of Figure 2.10.

The fast output from the silicon detector amplifier was sent to a constant-fraction discriminator (CFD) with a relatively low threshold. We will refer to the logic signal generated by this component as "ΔE". The fast output from the CsI(Tl) detector amplifier was passively split and sent to two leading edge discriminators (LEDs). One LED was set with a very low threshold, so that it fired somewhat in the noise; this logical signal we shall call E_L. The E_L signal was then delayed and stretched by a delay and gate generator (DGG). The other LED was set with a higher threshold; its signal we call E_H.

The trigger for the 56-element hodoscope consisted of either one (singles trigger) or two (coincidence trigger) detectors firing in an event. A telescope is considered to have "fired" when it satisfies a logical condition E_L*(E_H+ΔE), where E_L, E_H, and ΔE are considered as Boolean variables. A schematic indication of the meaning of these conditions is seen in Figure 2.11, where a ΔE-E plot from a typical detector element is shown, along with the threshold conditions E_L, E_H, and ΔE. For real particles, a small signal in the CsI(Tl) detector (E component) is accompanied by a large signal in the silicon detector (ΔE component). To reduce experimental energy thresholds, we set the discriminator level for E_L into the noise. Therefore, any real particle in the telescope must at least fire E_L. To reduce the frequency of triggering on the noise, however, we required one of two additional conditions to be satisfied. We set the ΔE threshold just above the noise, so most particles deposit sufficient energy in the silicon detector to fire this logical component; a E_L*ΔE trigger condition is sufficient for these particles. However, high energy (180 MeV) protons leave a very small signal in our

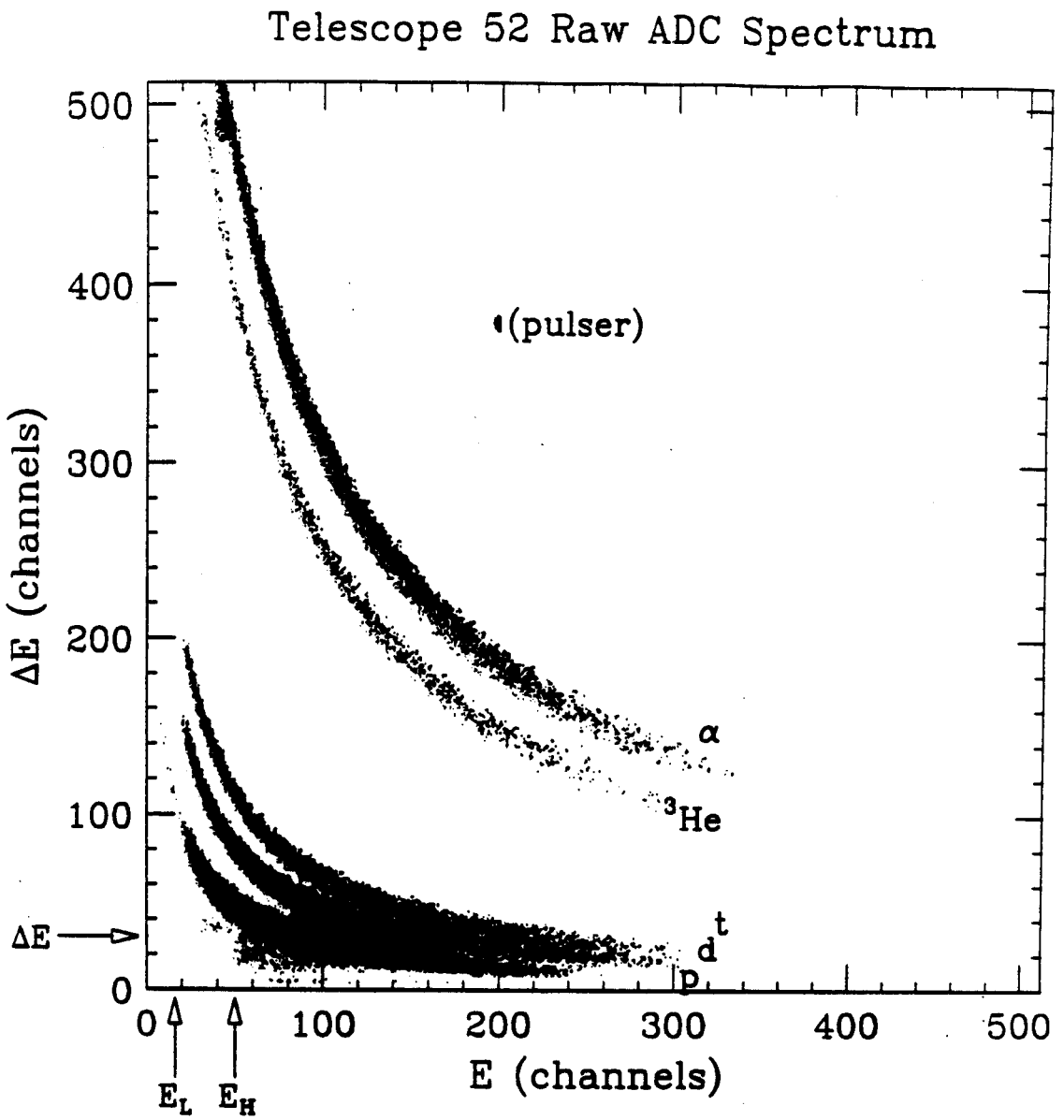

Figure 2.11. Raw spectrum of signals of the Si and CsI(Tl) detectors is shown for a typical ΔE-E telescope from the 56-element hodoscope. Note the effect of the various discriminator thresholds in eliminating coincident noise from the two components.

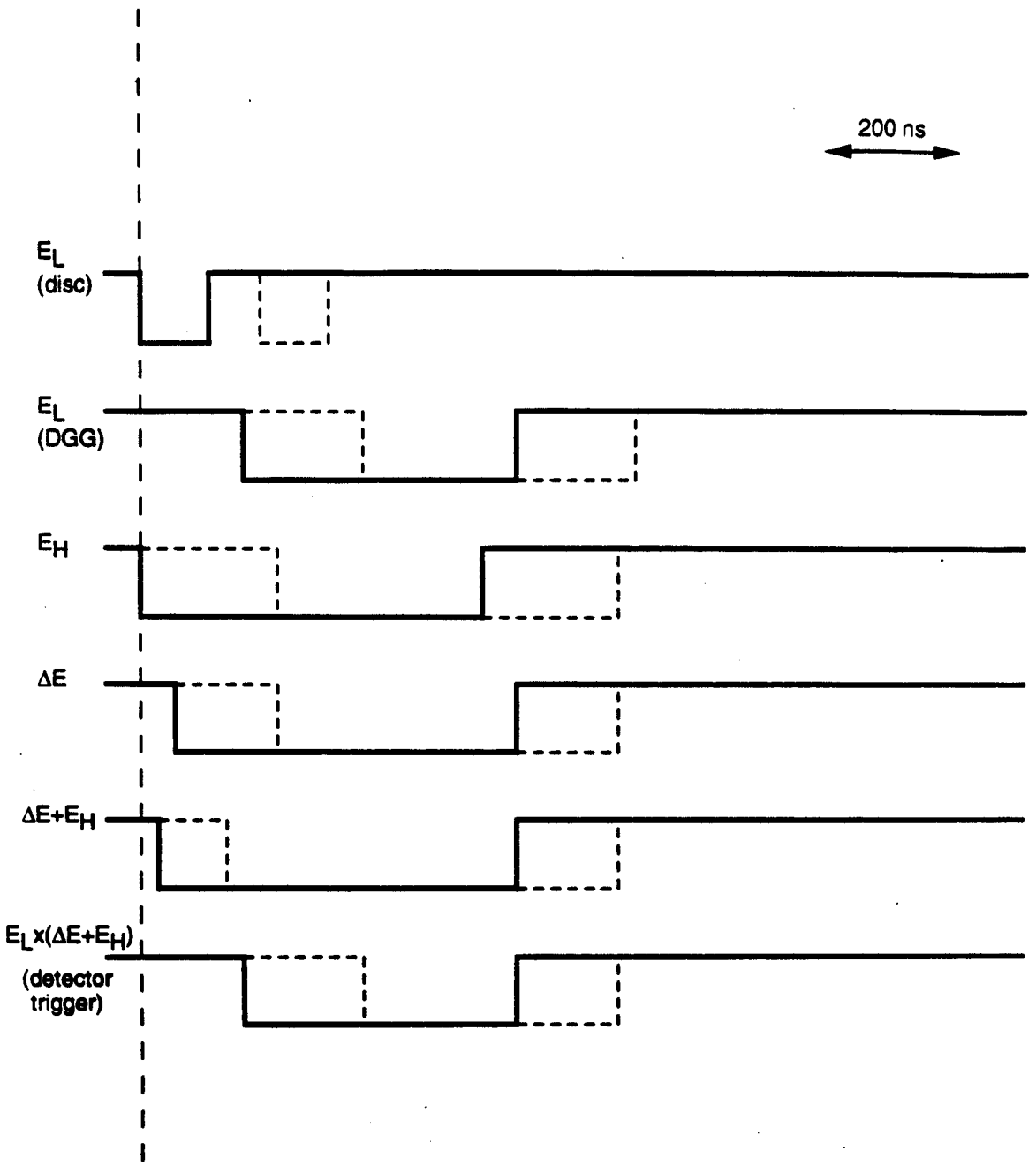

Figure 2.12 Signal timing for the internal logic of a detector trigger. Solid lines correspond to timing for large signals, while dashed lines indicate timing for signals at threshold. The "E_L" signal always determines the overall timing.

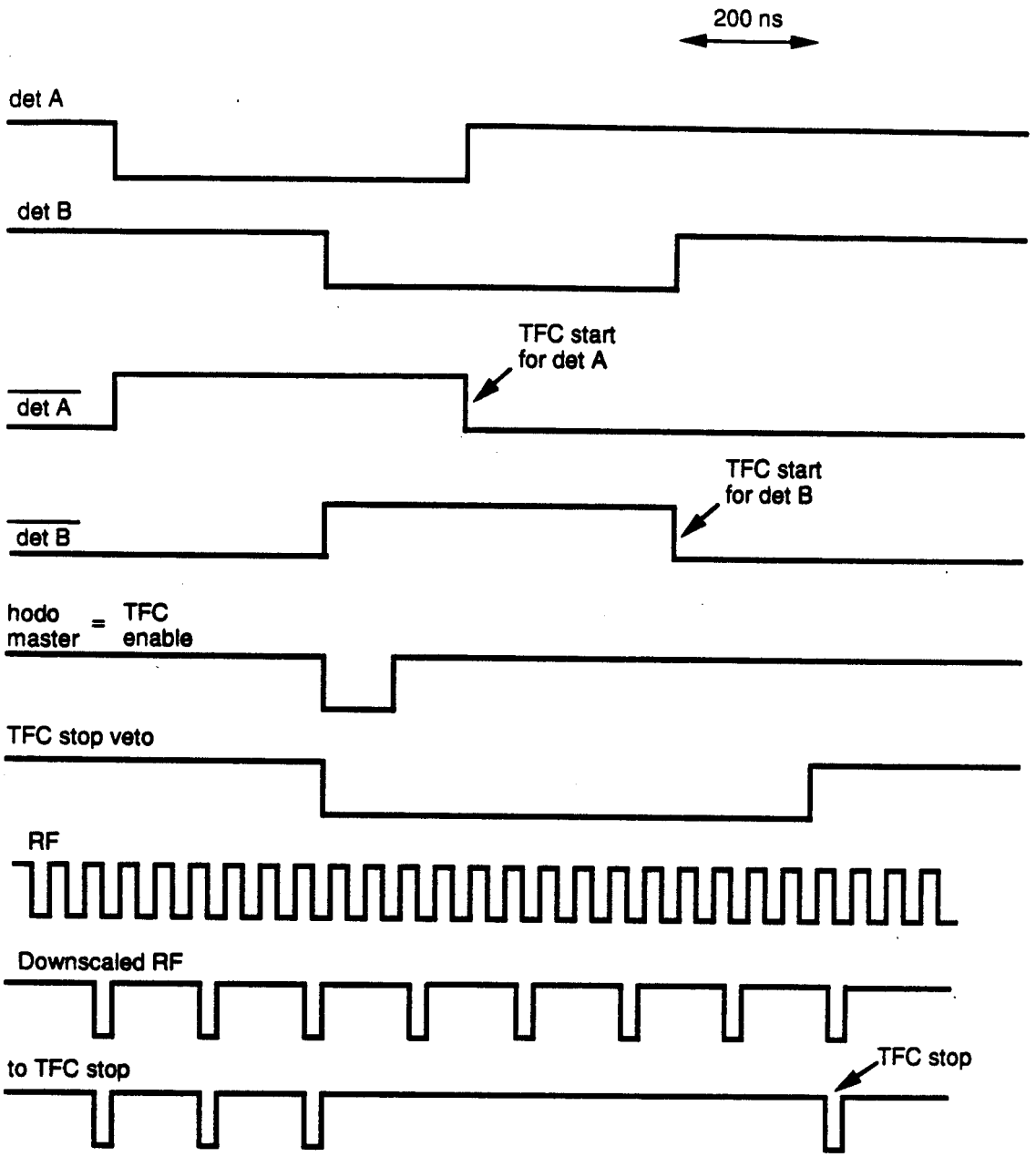

Figure 2.13. Signal timing for the determination of the time that a detector element fired.

300-μm-thick silicon detectors (~250 keV) which may not fire our ΔE discriminator. Therefore, we also accept a condition of E_L*E_H.

The timing of the detector trigger signals is shown in Figure 2.12. All of our discriminators show a time walk (or "slewing") effect; the timing of the discriminated signal depends on the pulse height. The solid lines in the figure show the timing for large pulses, while the dashed lines indicate the timing for signals just above threshold. The overall timing of the detector trigger is determined by the walk of E_L; since E_L is generated by a LED, this has the advantage of exhibiting a well-defined time walk function which can be corrected off-line (see Chapter 3).

Besides reading out ΔE and E signals through the Silena 4418/v's, we also read out the time that a detector fired relative to the RF cycle of the cyclotron. Therefore, the "detector trigger" for a given element served two main purposes: to go into the overall "hodoscope trigger", and to act as a time marker. We used LeCroy TFC-FERA combinations to digitize this information. This system requires three signals in time-order, an enable, a start, and a common stop. Figure 2.13 shows the timing of these signals.

The enable signal was provided in our case by the master. The start signals were generated by the individual "detector triggers." However, the start must arrive after the enable, and the master is determined by coincident detector triggers. Due to time walk, the master may be generated as much as 200 ns after the first detector fires. In this case, then, the individual starts should arrive about 500 ns after the detector triggers. Instead of creating this delay using cable delay or DGGs, which would add considerable hardware to our electronics setup, we used a somewhat unconventional technique. The detector triggers passed through an Phillips 7106 ECL discriminator with an adjustable output signal width. We adjusted this width so that the "trailing edge" of the signal came 500

ns after the detector trigger. Then, since physical inversion of an ECL signal conjugates the logical signal, we used modified cables that flipped the signal from the ECL discriminators. Therefore, the trailing edge acts as a leading edge to the TFC, and the start is delayed. The common stop to the TFC was generated by the discriminated RF signal from the cyclotron. This signal, which had a frequency of about 1/(50 ns), was downscaled by a factor of 3 in order to evaluate the timing resolution on-line.

2.3.2 The 4π Detector Array

Signals from the photomultiplier tubes of the ball and forward array elements are sent to specially-made splitter boxes which passively divide the signal into three components: "logic," "fast," and "slow."

The "fast" and "slow" signals are passed through a cable delay and into a FERA for charge integration and digitization. Figure 2.6 shows a typical phoswich signal and the FERA gate timing used to digitize the fast and slow signal components.

The "logic" signal is simply the raw phototube signal passed to a Phillips 7106 discriminator. The individual discriminator outputs were then delayed and sent to TFC starts for timing measurement.

The Phillips discriminator also has a "sum" output that generates a linear signal with a magnitude of 50 mV for each firing channel. The sum output of a discriminator, then, could be used to determine the hit multiplicity for 15 detectors. The 45 forward array elements passed to 3 discriminators, whose sum outputs were summed in a summing module; the output of this module was then the event multiplicity in the forward array. Similarly, the multiplicity from the 170 ball detectors was determined in a separate summing module. One output from each of these summing modules was sent to a third summing module, whose output was the device multiplicity. The outputs from each of the three

summing modules was sent to a maskable CFD. This device, a commercial module produced by EG&G, can be programmed through the CAMAC system. Any or all of the input channels can be masked off-- allowing one to fire on ball multiplicity, forward array multiplicity, or device multiplicity. The multiplicity level is selected by setting the discriminator threshold.

The output of this module, then, is the "4π trigger." The 4π master is generated by vetoing this signal with the Computer Busy signal. The 4π master enables the TFCs, provides the TFC stops (after a delay), and sets the gates for the time FERAs. The timing for the FERA gates for the E and ΔE phoswich signal components are determined separately for the main ball and the forward array. This is done by requiring a coincidence between the 4π master and a delayed logical signal generated by the forward array and main ball separately. In this way, timing jitter of the gates, which can degrade resolution, is reduced.

2.3.3 Master Circuitry

For the majority of the experiment, the hodoscope trigger condition determined whether to record digitized information from both the 4π Array and the hodoscope. As explained above, this required the use of a fast clear circuit to allow the 4π Array to self-gate and store digitized signals in the FERAs for every event, and then either erase those signals (fast clear) if the hodoscope trigger condition was not met, or read them out via CAMAC if the hodoscope trigger condition was satisfied. The signal timing for the master circuit is shown in Figure 2.14.

If both the hodoscope and the 4π Array fired in an event, the hodoscope trigger was generated about 1.1 μs later, with a jitter of about 200 ns. The fast clear signal is generated by delaying the 4π trigger by about 1.5 μs. Dashed lines in the figure indicate the effect of jitter. If the hodoscope triggered, then a fast

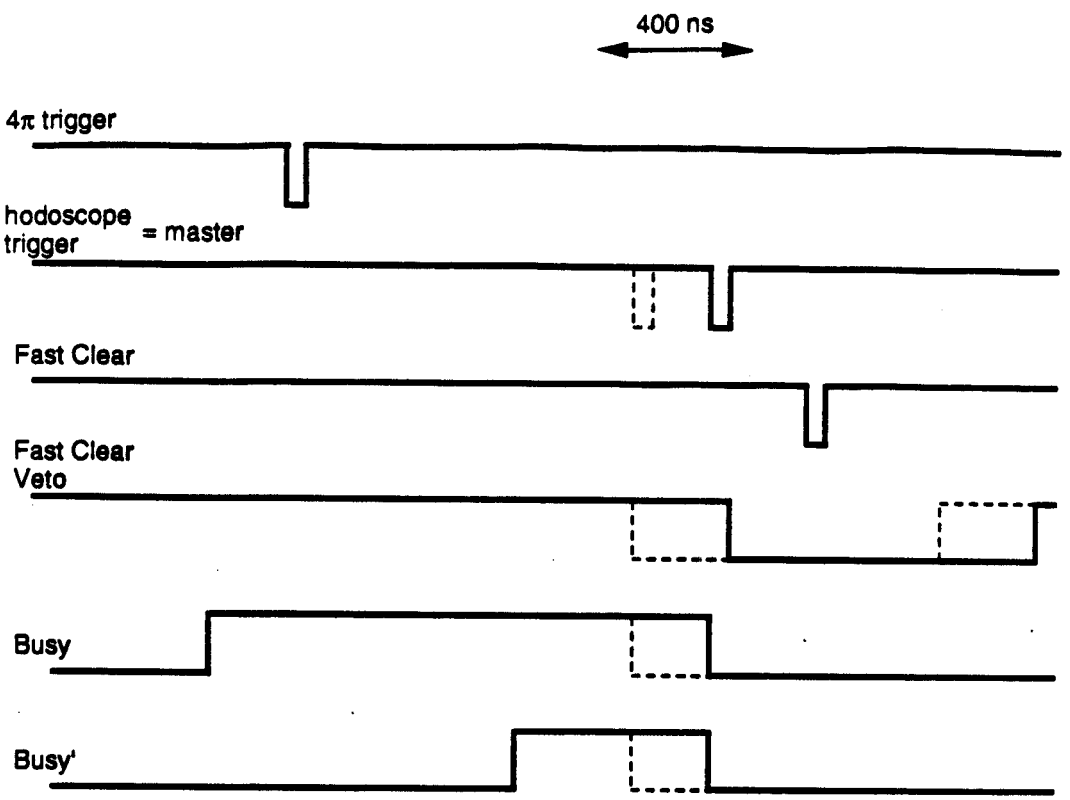

Figure 2.14. Signal timing for the master circuit.

clear veto is generated to disable the fast clear, and a "computer start" is given to the system.

When vetoing the triggers with the computer busy, it was appropriate to account for the relatively large time delay between the 4π and hodoscope triggers. Therefore, we employed the true computer busy to veto 4π masters and the so-called busy' to veto hodoscope masters. Simple use of two fan-in/fan-outs and an appropriate cable delay made a signal whose leading edge coincided with that of the busy, but whose trailing edge lagged that of the busy by 800 ns. (In the figure, the computer has become "live" (not busy) just before the 4π fires, and then becomes busy again due to the new master.) The reason for such a signal follows. If the computer is busy when a 4π trigger occurs, then no 4π gates will be set, and the event should not be read. However, if the computer becomes live again immediately after the 4π trigger, then use of the busy to veto the hodoscope trigger would allow the event to be read. Vetoing with the busy', on the other hand, largely eliminated the readout of these useless events; if the busy signal was set when the 4π trigger fired, then the busy' would be set when the hodoscope fired, and the event would not be read out.

2.4 Nuclear System Studied

The system we chose to study with the set-up described above was $^{36}Ar+^{45}Sc$ at E/A=80 MeV. The choice of this system was the result of many considerations.

As discussed in Chapter 1, a high-statistics measurement of the two-proton correlation function had been made by Gong [Gong91b, Gong91c] on the relatively light system $^{14}N+^{27}Al$ at E/A=75 MeV. Correlations for this system showed a very strong dependence on the total momentum of the proton pair, and BUU simulations were largely successful in reproducing this dependence. The simulations also showed that the total momentum dependence was a strong

function of impact parameter; such predictions, of course, could not be tested by Gong's data. We wished to perform our measurement in the energy region for which the BUU is relatively well-understood and could explain impact-parameter-averaged measurements.

We attempted to extract the impact parameter from global observables, such as event multiplicity and transverse energy. In a naïve participant-spectator model, such global variables depend on the volume of overlap between the projectile and target nuclei. As is shown schematically in Figure 2.15, this overlap volume reaches a maximum when the smaller nucleus fits inside the larger. For a very asymmetric system, then, global observables are expected to be rather insensitive to impact parameter for central collisions. Our choice of a nearly symmetric system was designed to maximize sensitivity to impact parameter.

Correlation functions corresponding to emission from a very large system are suppressed, and the effect of any cut, such as in impact parameter or total momentum, is difficult to see. Therefore, we did not want to study a very large system.

On the other hand, the search for impact parameter effects with a very light system is difficult, since fluctuations in impact parameter may dominate the centrality filter. Also, smaller systems are less sensitive to bulk-compressional effects, which may be important in the difference between peripheral and central collisions.

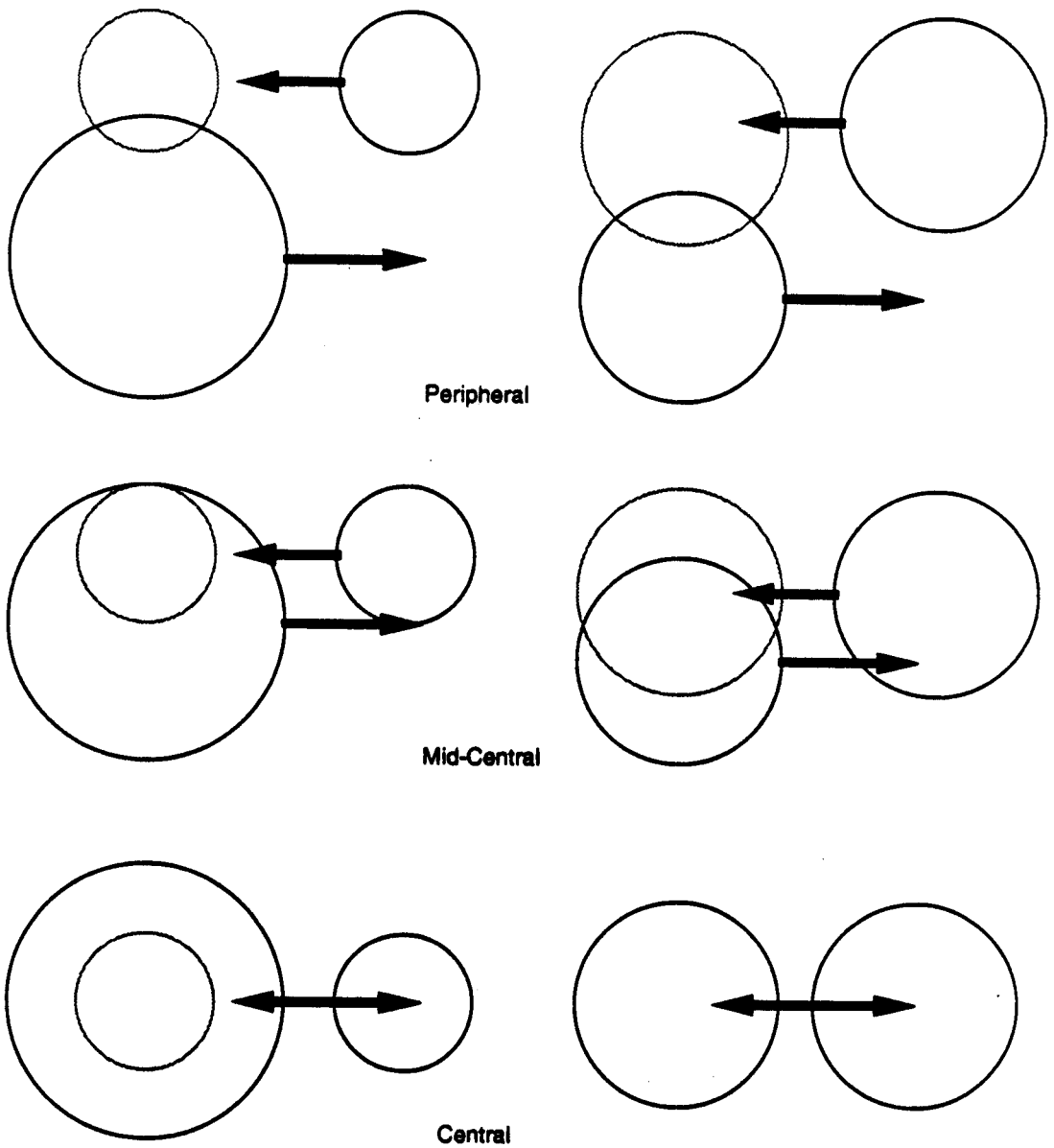

Figure 2.15. Schematic illustrating, in a purely geometric picture, the reduced sensitivity of global observables to the impact parameter for very asymmetric systems.

Chapter 3 - Data Reduction

In the experiment, electronic signals from the detectors were digitized and recorded on magnetic tape on an event-by-event basis. In this chapter, we discuss our procedures for obtaining particle identification, energy, and time signals from the raw data. We concentrate first on the 56-element hodoscope, and then on the 4π Array.

3.1 56-Element Hodoscope

One of the attractive features of the correlation function is its relative insensitivity to complicated experimental distortions, such as position-dependent energy thresholds, for example. However, one must still exercise care in the treatment of correlation data. Contamination from deuterons in proton data, for example, is not "corrected for" by the correlation function. Likewise, inclusion of a large number of "random," or uncorrelated, pairs in the construction of the correlation function will suppress true correlations.

Below, we discuss our procedure to determine particle identification, energy, and relative time with precision. Although we discuss them separately, we note that the extraction of each of these quantities is not independent. To determine particle identification, for example, we used the proton energy calibration, the extraction of which, in turn, required a rough proton identification.

3.1.1 Particle Identification

Particle lines can be identified in a two-dimensional map of the energy deposited when punching through the silicon detector (ΔE) vs. the energy

deposited while stopping in the CsI(Tl) detector (E); see Figure 2.10. However, the channel resolution required to cleanly separate particle lines and set gates in this map demands large amounts of computer memory. Therefore, we transformed the ΔE-E map into a so-called PID-E map, where PID is a linearizing function of ΔE and E [Shim 79].

The advantages of using a linearizing PID function are twofold. Firstly, the two-dimensional channel space is more efficiently utilized, decreasing "wasted" computer memory spent on unoccupied ΔE-E bins. Secondly, in regions in which there is less resolution between particle lines, it is easier to extrapolate the gate from regions with good resolution.

We found that our PID-E maps were most linear with the parametrization:

$$PID = (E+\Delta E)^{1.73} - E^{1.73}. \qquad (3.1)$$

The PID-E map for a typical detector is shown in Figure 3.1 as a logarithmic density plot. Particle species are identified by relatively straight curves. An exception is the low-energy behavior of the helium isotopes, where the nonlinearity of the PID function for nearly-stopped particles in the Silicon detector is evident.

Two-dimensional gates on particle type were set in these maps, and clear identification is achievable for ^{1}H, ^{2}H, ^{3}H, ^{3}He, and ^{4}He. Particle identification resolution is a function of energy. At low kinetic energies, where a considerable signal is observed in the ΔE component, the distinction between particle types is excellent. Separation is most difficult, however, for the lightest particles with high (~ 100 MeV) kinetic energy. In Figure 3.2, we show one-dimensional PID projections for various gates on E. The proton and deuteron peaks are absolutely separated at low energy, while the peak-to-valley ratio is typically 7:1 in the

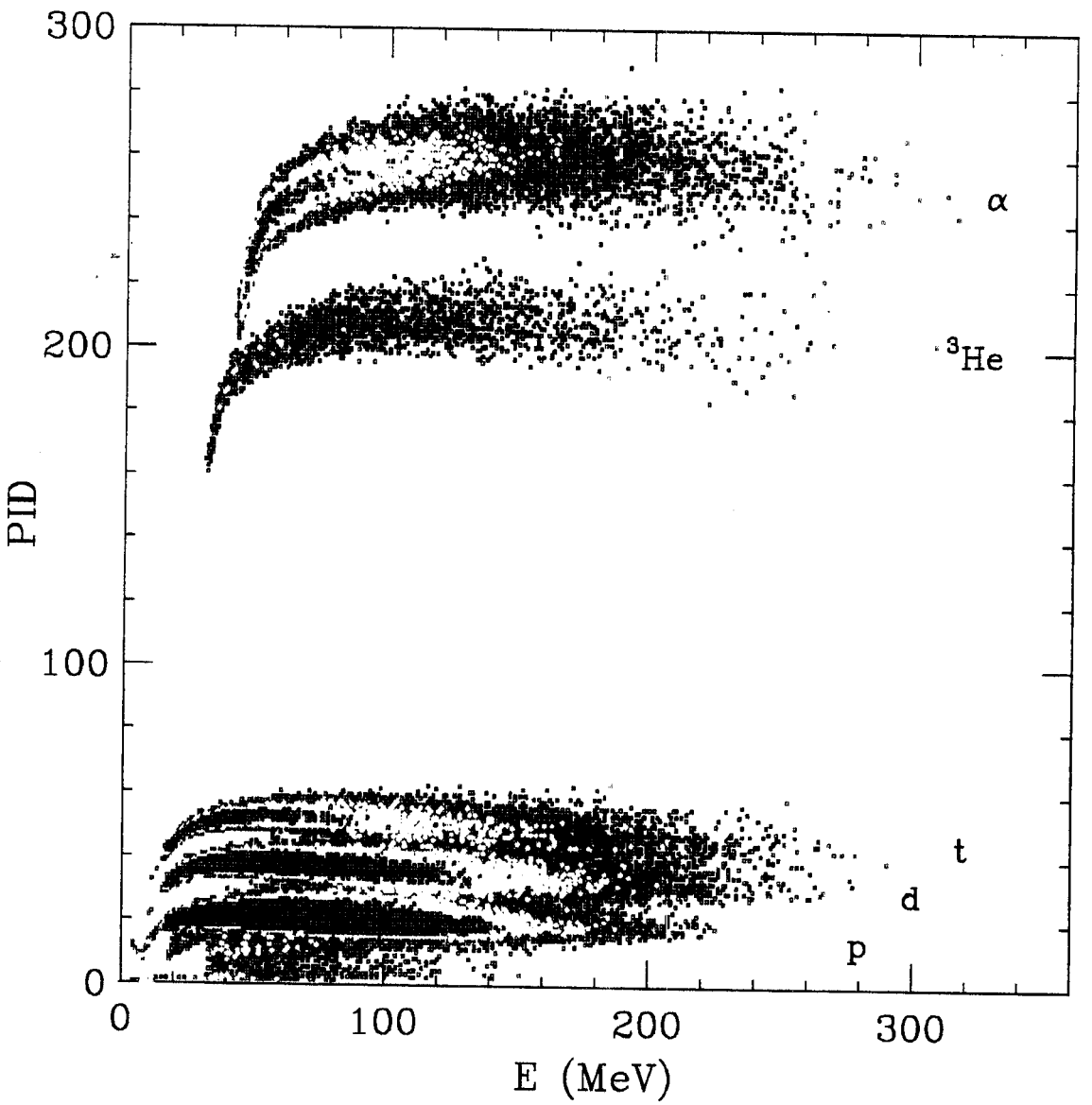

Figure 3.1. Two-dimensional density plot of the PID function vs. the particle energy. The z-axis has a logarithmic scale.

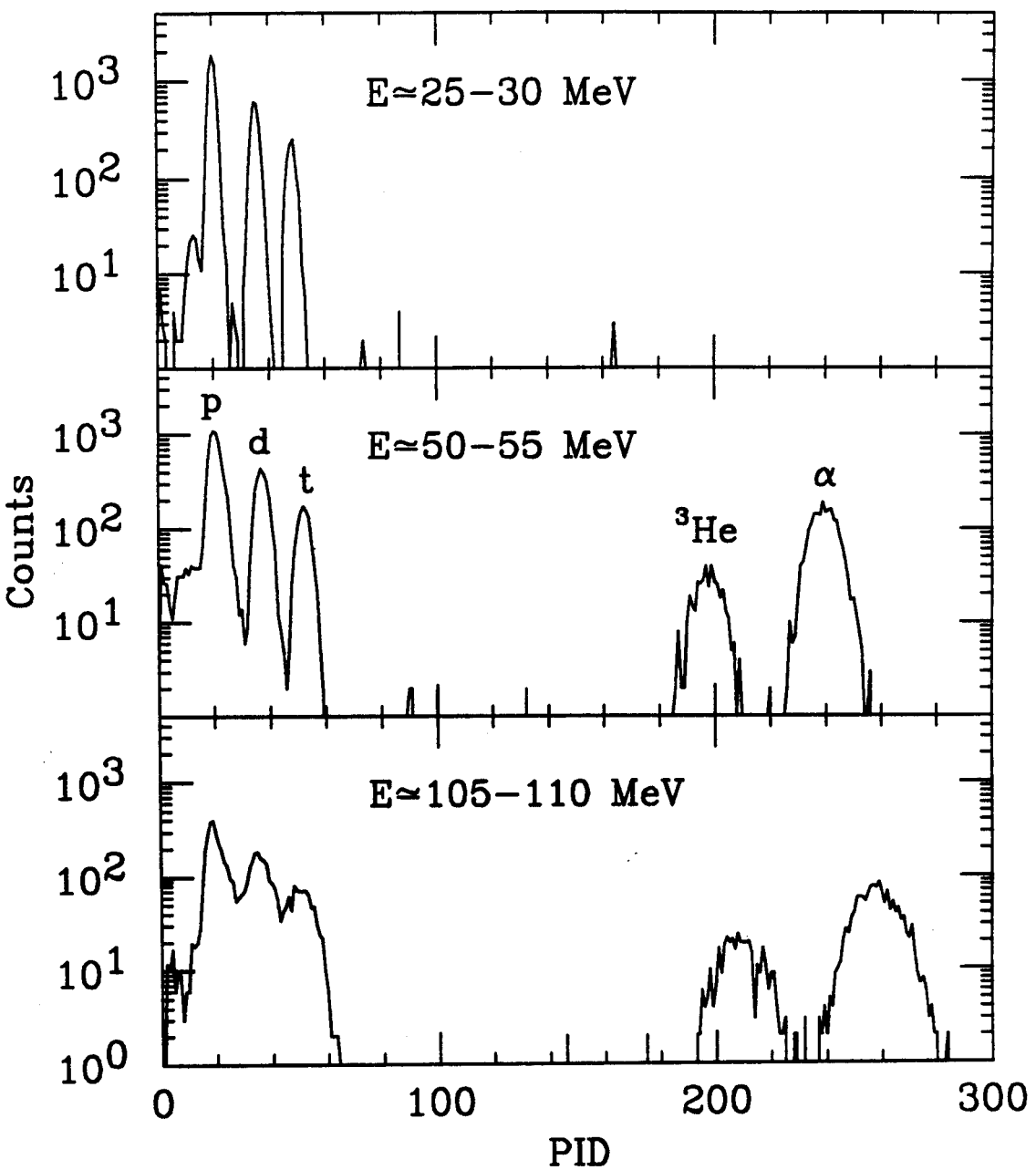

Figure 3.2. One-dimensional projections of PID for thin cuts in particle energy, showing particle identification resolution as a function of energy.

worst region, at a proton energy of about 100 MeV. Estimated deuteron contamination in this energy region is of the order of 0.5%.

3.1.2 Silicon Detector Calibration

The ΔE components of our telescopes were relatively easy to calibrate because of the well-known linearity of silicon detectors. A precision capacitor and pulser system was calibrated with alpha particles of known energy from the following radioactive isotopes stopping in one of our silicon detectors:

^{228}Th	E_α=5.423 MeV.
^{224}Ra	E_α=5.686 MeV.
^{220}Rn	E_α=6.288 MeV.
^{216}Po	E_α=6.779 MeV.
^{212}Bi	E_α=8.784 MeV.
^{241}Am	E_α=5.486 MeV.

The pulser calibration resulted in a proportional relationship between voltage on the capacitor (equivalent to charge injected into the preamplifier) and energy deposited in the silicon detector. This allowed us to "dial in" any ΔE signal with the pulser system.

Charge was injected into each silicon preamplifier with the pulser at several settings ΔE_i, and the corresponding peaks in the ΔE ADC spectrum at channels N_i provided a calibration

$$\Delta E(N) = b + m \cdot N. \tag{3.2}$$

for each detector.

3.1.3 CsI(Tl) Detector Calibration

A $(CH_2)_n$ target of about 20μm thickness was bombarded by α particles of 160, 120, and 100 MeV kinetic energy. The CsI(Tl) detectors were calibrated by

measuring monoenergetic particles emitted from the following elastic, inelastic, and transfer reactions:

$p(^4He,p)^4He$		(3.3)
$^{12}C(^4He,d)^{14}N^*$	E^*=8.96 MeV	(3.4)
$^{12}C(^4He,t)^{13}N^*$	E^*=0.0, 3.51, 6.89 MeV	(3.5)
$^{12}C(^4He,^3He)^{13}C^*$	E^*=0.0, 3.86 MeV	(3.6)
$^{12}C(^4He,^4He)^{12}C^*$	E^*=0.0, 4.44 MeV	(3.7)

For each detector angle and particle species, two-body kinematics were used to calculate the kinetic energy associated with each peak in the energy spectrum. Energy loss in the Ta foil and ΔE detector was accounted for. Because of the finite solid angle of each ΔE-E telescope, the widths of calibration peaks are greater than the intrinsic energy resolution of the detectors. In all cases, the energy was calculated for a particle hitting the center of the detector, and the peak centroid was extracted to establish the energy calibration.

Raw energy spectra of a typical detector for a calibration run with E_α=120 MeV are shown in Figure 3.3. Clear peaks for all light particle species are observed. In Figure 3.4, we show the calibrated E+ΔE spectra for protons and alpha particles. The widths of the calibration peaks in both cases are dominated by kinematic broadening, as indicated by the energies of particles entering the detector at the most forward and backward edges. The intrinsic energy resolution of the detector is of the order of 1%.

Previous energy calibrations of the CsI(Tl) detectors with a larger set of calibration points than was available to us have demonstrated a highly linear response for light charged particles [Gong 91c]. Therefore, we assumed linearity in our energy calibrations and observed no deviations from this assumption.

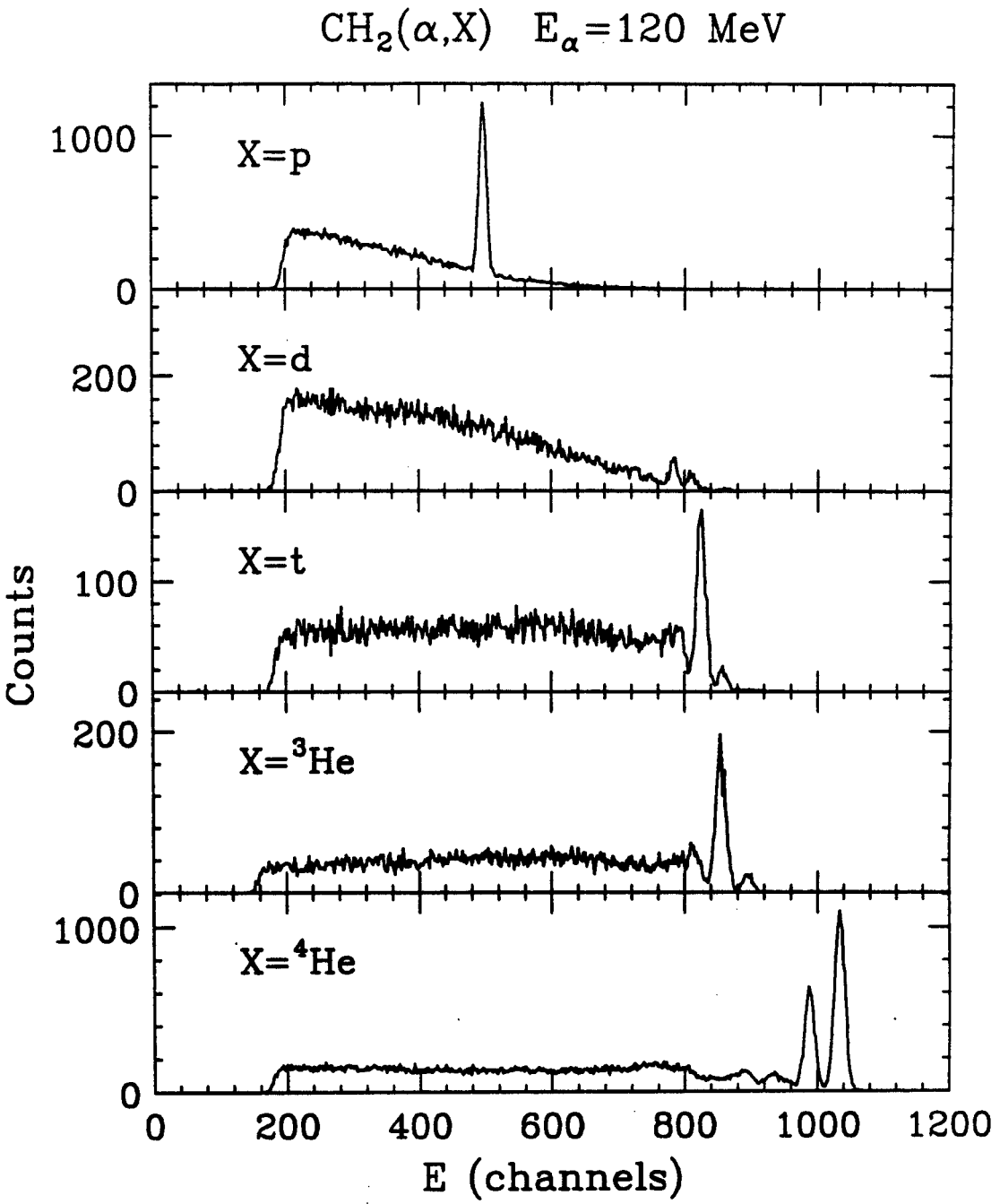

Figure 3.3. Raw energy spectra measured in a typical detector for light particles emitted when 120 MeV alpha particles bombarded a polypropylene target.

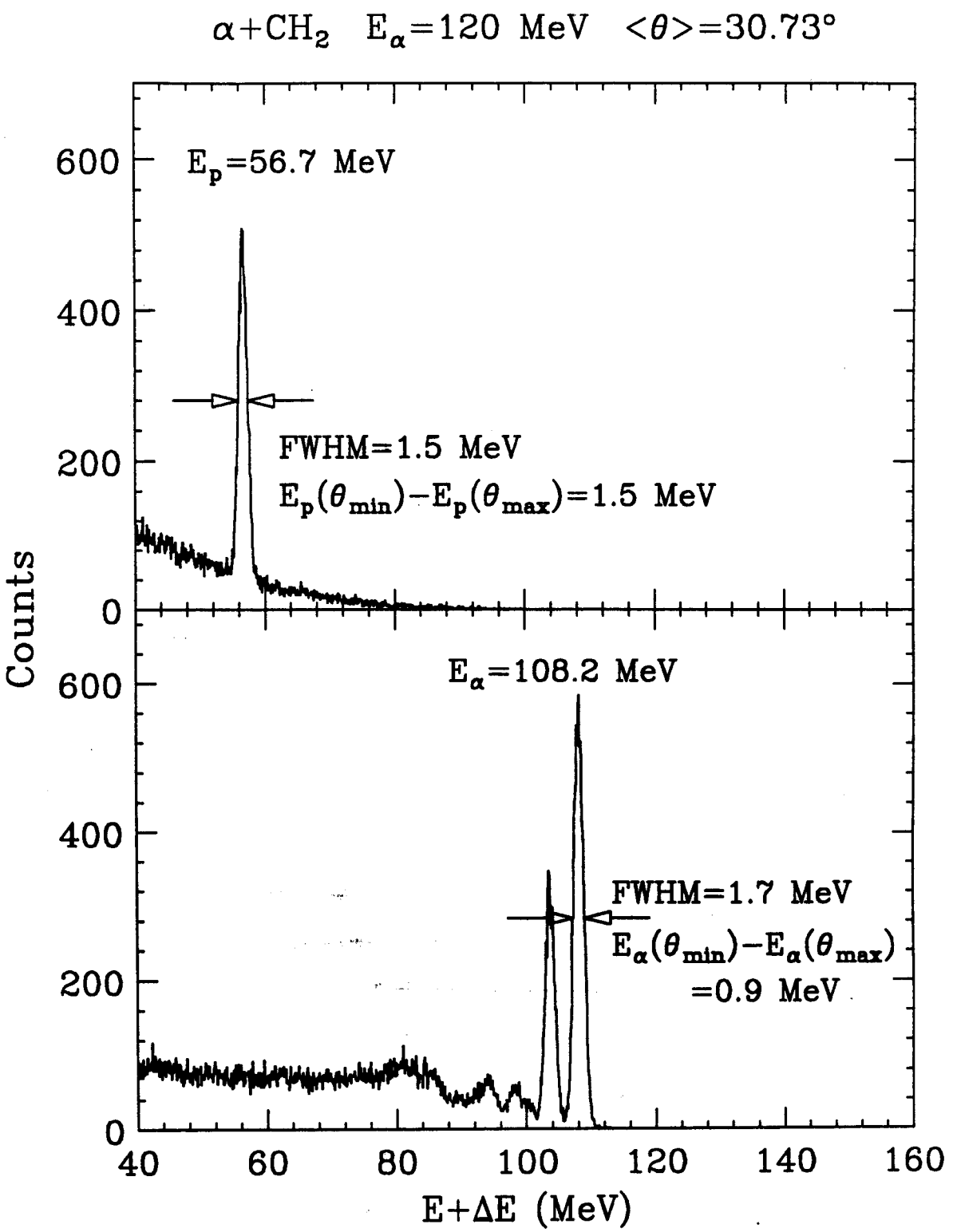

Figure 3.4. Calibrated proton and alpha energy spectra from 120 MeV α+CH_2 reactions. The widths of the measured peaks are dominated by kinematic broadening, indicating an intrinsic energy resolution on the order of 1%.

The determination of the excited states which were populated in the direct reactions (3.4), (3.5), and (3.6) required interpolation. Proton and alpha calibrations were straight-forward; only the well-known lowest excited state of ^{12}C (E^*=4.44 MeV) was excited. The previous detector calibrations by Gong indicated that energy calibrations of the other light particles (d,t,^{3}He) would lie between the proton and alpha calibrations. With this assumption, it became clear which states were populated. An example is shown in Figure 3.5. The energy of a deuteron emitted from the direct reaction $^{12}C(^4He,d)^{14}N^*$ is calculated as a function of lab angle, assuming the excitation of selected low lying states in ^{14}N. Also indicated is the measured deuteron energy in our detectors, using the proton and triton calibrations as an approximation. With the knowledge that the deuteron calibration lies between the proton and triton calibrations, it is clear that the population of the E^*=8.96 MeV state in ^{14}N is consistent with our observations. Previous reports of the strong dominance of this state in this reaction [Ajze 86, Harv 62] confirmed this assumption.

Calibration curves for a typical detector are shown in Figure 3.6. In the most backward detectors, for which deuteron peaks were not available, we averaged the proton and triton calibrations to provide the deuteron calibration. This procedure was performed also for the forward detectors, and calibrations were in good agreement with observed peaks.

3.1.3 Slewing Correction

The construction of a correlation function or any other two-particle observable from experimental data requires the separation of real coincident pairs from so-called "random" coincidences, which contain particles emitted from two separate nuclear collisions. In our measurement, we recorded the time that each hodoscope detector element fired relative to the (downscaled) RF time from the cyclotron, T_i-T_{RF}. In principle, then, if detector i and detector j fire in an

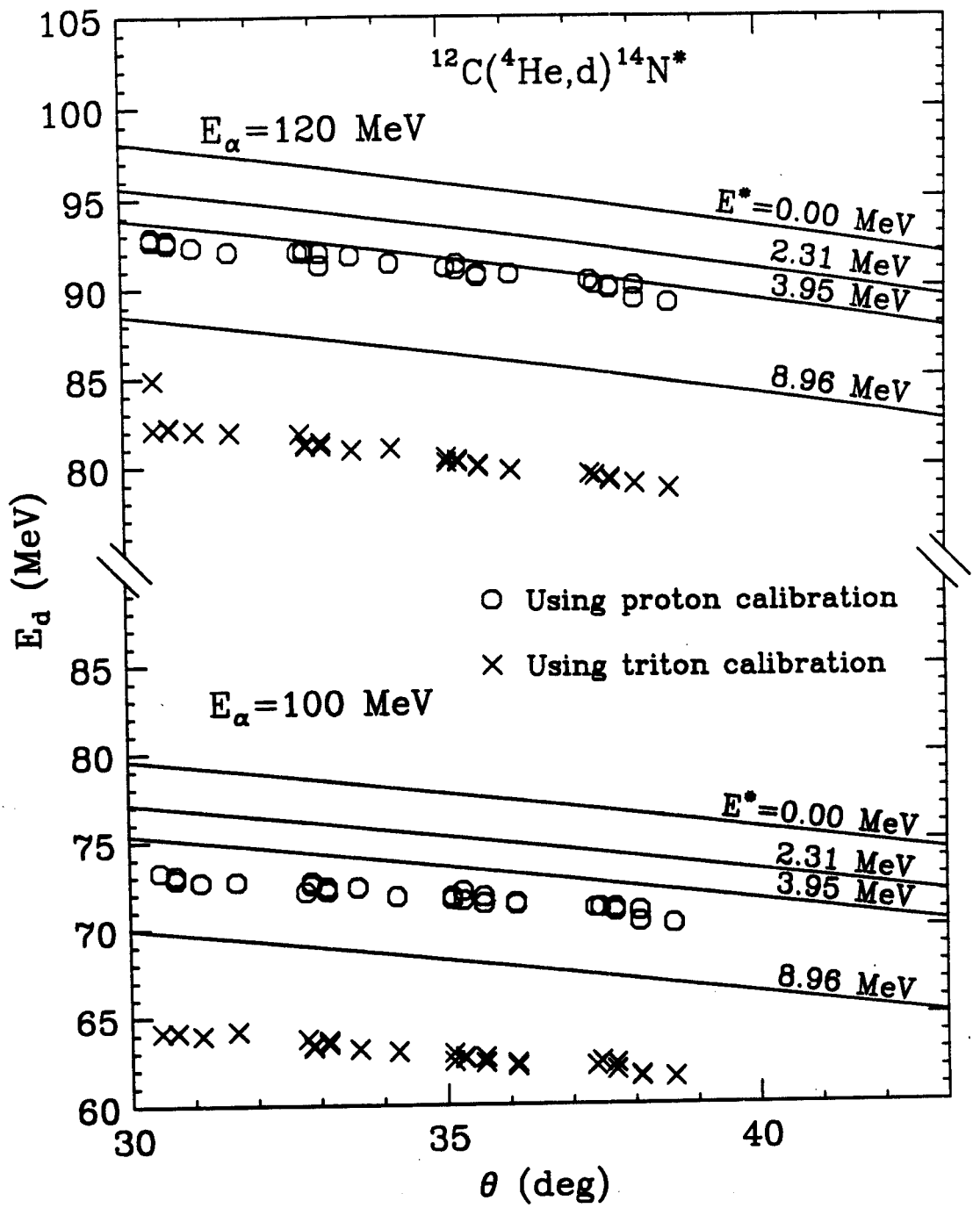

Figure 3.5 Lines indicate calculated deuteron energies from $\alpha(^{12}C,d)^{14}N^*$ for E_α=120 and 100 MeV . Measured deuteron energies assuming a deuteron energy calibration identical to the proton and triton calibrations are shown as circles and x's, respectively.

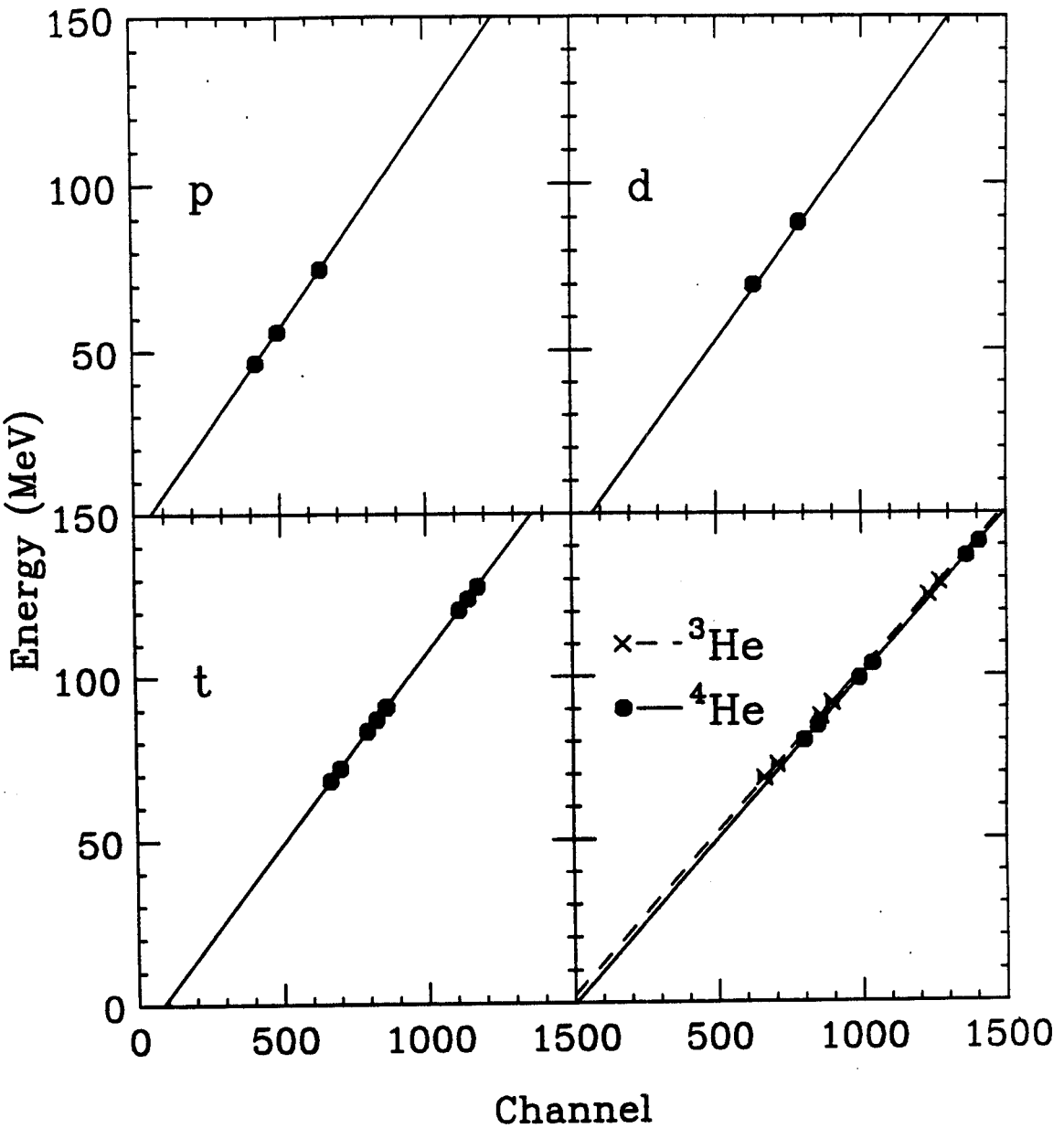

Figure 3.6. Energy calibration curves for a typical CsI(Tl) detector from the 56-element hodoscope.

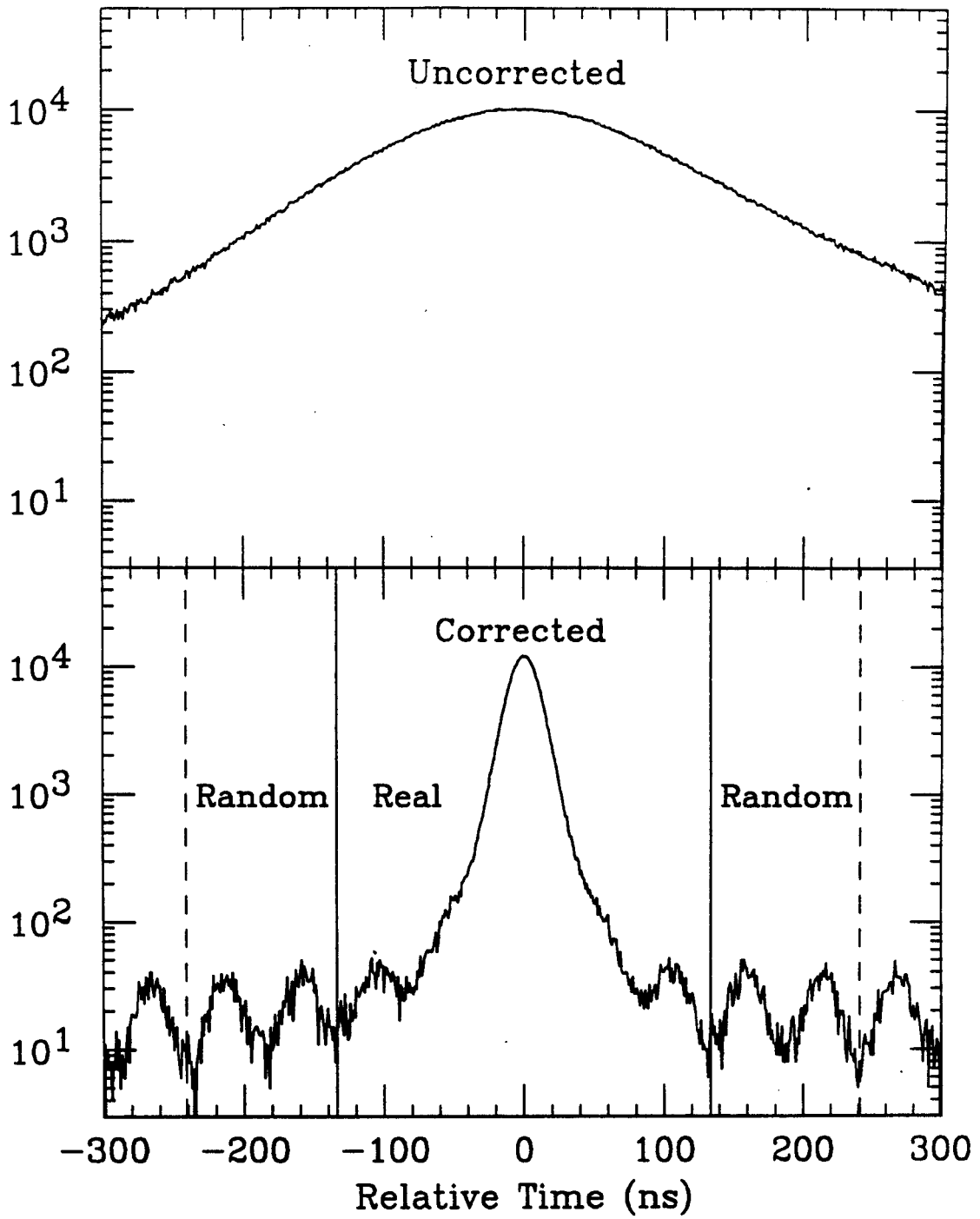

Figure 3.7. Relative timing spectrum for two particles recorded in coincidence in the 56-element hodoscope. The upper and lower panels show the spectrum before and after slewing correction, respectively. Also shown are the relative timing regions defining a "real" and a "random" coincidence in the correlation analysis.

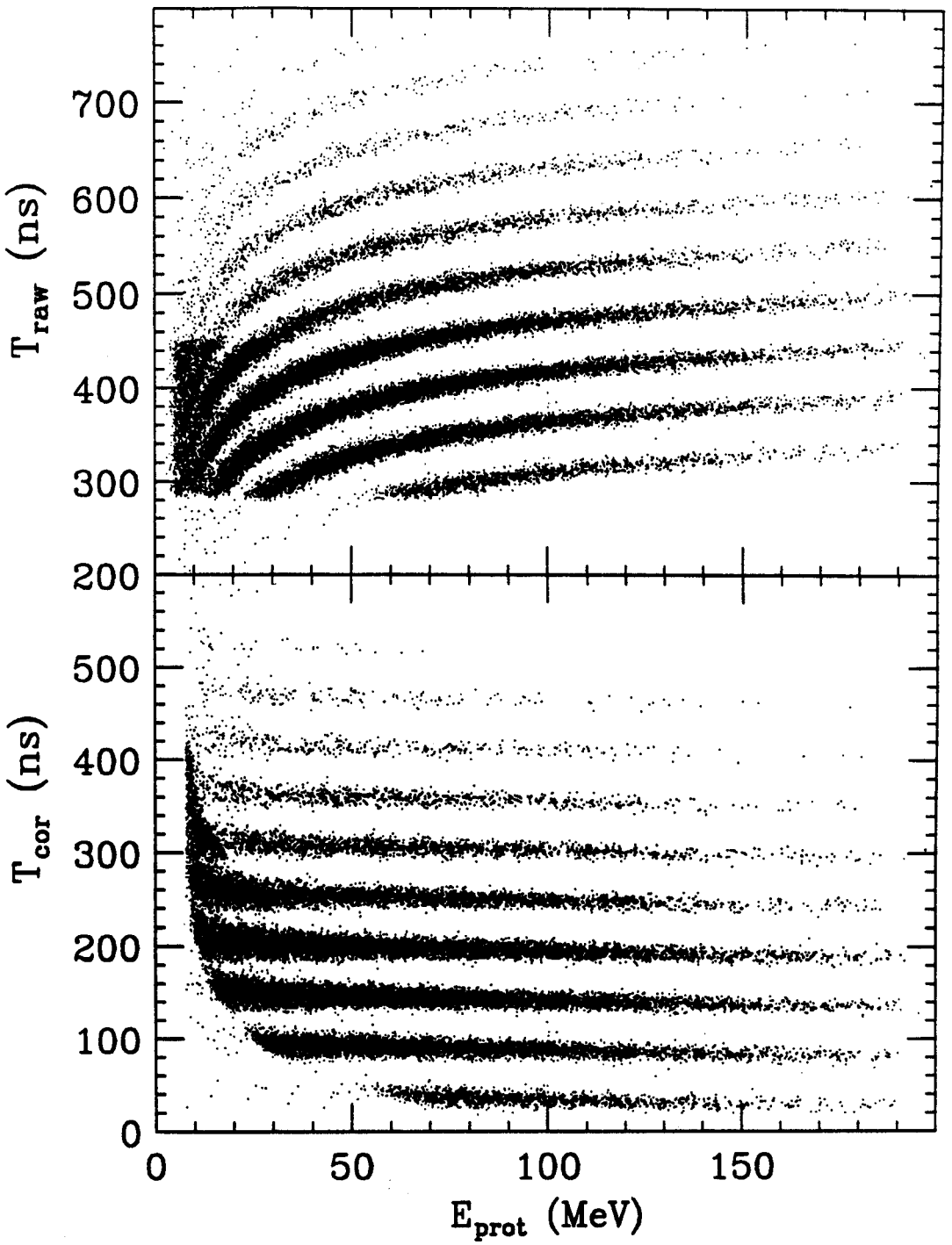

Figure 3.8. The time when a detector fired relative to the cyclotron RF signal vs. the energy is shown for protons measured in a typical ΔE-E telescope. The raw spectrum (top panel) shows the effects of slewing or time-walk. Slewing effects are absent in the corrected timing signal (bottom panel) Different bands in both spectra reflect the RF structure of the cyclotron beam.

event, the variable $|(T_i-T_{RF})-(T_j-T_{RF})| = |T_i-T_j|$ should indicate whether the pair constitutes a real or a random coincidence. The upper panel of Figure 3.7 is a histogram of the variable T_i-T_j, summed over all particle types and all detector pairs (i,j). A broad smear in the relative timing spectrum is observed, and no obvious distinction between real and random coincidences is visible. The cause of such a smear becomes apparent when we examine a spectrum of the time vs. the energy of the particle, shown for protons measured in a typical detector in the top panel of Figure 3.8. There, it is seen that no unique relationship exists between a detector's firing time and the RF signal. The relatively slow risetime of the CsI(Tl) detector and the use of leading edge discriminators to construct the logic signal for the hodoscope detectors gives rise to a large energy-dependent "walk" or "slewing" effect in the timing signal.

In order to obtain a clean measure of the relative time signals between coincident particles, the energy dependence of the time signal must be corrected for. Moreover, since the slewing curve shows a dependence on particle type, this correction must be performed separately for each particle type.

The detector timing signal was determined only by the E_L signal, which was generated by a leading edge discriminator (LED) (see Section 2.3.1). We modeled the slewing effect by assuming a Gaussian-like leading edge from the fast output of the shaping amplifier. If we may assume a proportional relationship between the pulse height and the energy of the particle, then the fast output as a function of time is

$$V(t) = m \cdot E \cdot e^{-(t-t_0)^2/\tau^2} \tag{3.8}$$

where τ is a characteristic rise time which depends on the particle type, E is the energy of the particle, m is the energy calibration constant, and t_0 may be considered the "true" firing time of the detector. The LED fires when the signal

reaches the threshold voltage $V_{th}=m \cdot E_{th}$. Therefore, the slewing-corrected firing time t_0 may be written in terms of the recorded firing time t as

$$t_0 = t - \tau\sqrt{\ln(E) - \ln(E_{th})}. \tag{3.10}$$

A spectrum of t_0 vs. E for protons in one detector is shown for protons in the lower panel of Figure 3.8, where it is seen that the effect of slewing has been removed. The threshold energies used in Equation (3.10) were determined for each detector from the energy spectra.

Table 3.1. Rise times used to correct for slewing effect for light particles

Particle Type	τ (ns)
p	173.8
d	181.3
t	185.6
^{3}He	111.6
α	94.5

It is important to adjust τ for each particle type. The characteristic rise times τ were determined by trial and error and are given in Table 3.1.

After correcting for slewing and adjusting the zero-time offset of each detector relative to the others, relative timing spectra were constructed. The bottom panel of Figure 3.7 shows such the spectrum when all detector pairs and all particle species are summed over. The cyclotron RF structure of the Ar beam is apparent through random coincidences between particles from different beam bursts. Clearly, all real coincidences have both particles emitted in the same RF burst. However, since our time resolution was not perfect, we included pairs with a relative timing difference of up to two RF bursts in our definition of a "real" coincidence.

Four representative "random" peaks are indicated in the figure. Particle pairs in these peaks were used to correct the correlation function for the effects of random coincidences (see Chapter 5). It is clear from the relative sizes of the real and random peaks in Figure 3.7, however, that the effect of randoms will be small. In the construction of coincidence spectra, we use the schematic algorithm:

$$\text{"True"} = \text{"Real"} - (5/4) \cdot \text{"Random"} \tag{3.11}$$

3.2 4π Detector Array

Particle identification and energy calibration for the detector elements of the 4π Array proceeded through what has become the "official" 4π algorithm [Wils 91]. The fast-slow map is transformed through a number of operations onto a standard pallet in which all detectors appear similar. Then, PID gates and energy calibrations are performed.

In the first step, the neutral and punch-in lines (see Section 2.2.1 and Figure 2.6) are identified for each detector. The position at which they intersect corresponds to zero light output from both the fast and the slow plastic. Therefore, this fast-slow value is defined as the origin of the new map by subtracting its fast-slow value from every point; this corrects for offsets in the FERA QDCs.

Next, the coupling between fast and slow signals that allow finite slope of the punch-in and neutral lines was corrected for. For a given slow-value, the fast-value of the neutral line was subtracted from every point. This operation transformed the neutral line into the x-axis. In a similar fashion, the punch-in line was transformed into the y-axis by subtracting the slow-value associated with the punch-in line from every point according to its fast-value.

Multiplicative factors further transform the new fast and slow variables in order to match the spectrum to a calibrated template [Cebr 90]. This template contains gates for particle identification, and every point on the template has an associated particle energy.

Therefore, six numbers are associated with each detector: the fast and slow positions of the QDC offset point, the slopes of the punch-in and neutral lines, and the multiplicative factors for the fast and slow variables. The "standard 4π physics routine" uses these numbers to transform the fast and slow values for a particle measured in a detector. The position of the transformed point relative to the calibrated pallet indicates particle type and energy. Energy calibrations obtained by this gain-matching procedure are estimated to be good to about 10%.

3.3 Physics Tapes

To decrease the processing time involved with physical analyses, we created so-called "physics tapes," which contain recorded events in terms of the calibrated data. Although in principle the use of physics tapes makes no difference to a physical analysis, in practice the increase in speed encourages the scientist to optimize the analysis and sample the data in more ways.

Simple histogramming of calibrated data from "raw," or unprocessed, tapes required about 24 cpu hours per 2.2 GB (exabyte) tape on a VAX model 76. Such a procedure also required almost all of the 32 MB of memory, rendering the machine virtually useless for other purposes.

Such a procedure using our physics tapes required less than 2 cpu minutes and less than 4 MB on the same machine. However, limited tape I/O speed caused this process to take about 2 hours of real time, with a low cpu load. Construction of correlation functions with impact parameter calculations did not increase the real time of the analysis, only the cpu load.

The details of our raw and physics tape formats are given in Appendix A.

Chapter 4 - Impact Parameter Selection

The two-proton correlation function provides a measure of the space-time extent of the proton source created in a nuclear collision. Dynamical calculations with a Boltzmann-Uehling-Uhlenbeck model indicated that the source would evolve differently in central and peripheral collisions, and that the correlation function could reveal this difference [Gong 91a, Baue 92].

In order to investigate in detail the behaviour of the proton source separately for central and peripheral collisions, cuts on global observables were employed. Two-proton coincidences were measured in the hodoscope to construct the correlation function. In order to avoid the effects of "self-cut" biasing the impact parameter selected correlation functions, the "global" observables used were constructed from particles measured in the 4π Array only.

Below, we define the global observables used in this analysis. Next, we discuss the average reduced impact parameter which provides a common scale for the comparison of different global observables. Finally, we discuss two possible methods to compare impact parameter cut data to theoretical predictions.

4.1 Variables Used for Centrality Selection

We studied three commonly used global observables, each of which are assumed to provide a measure of the violence of the collision. To what degree this assumption is true for each is examined in the next section. Here, we define and present spectra of each observable for each of three trigger conditions (see

Section 2.3): inclusive (4π multiplicity ≥ 1), singles (hodoscope multiplicity ≥ 1), and coincidence (hodoscope multiplicity ≥ 2).

The charged particle multiplicity, N_C, is defined as the number of 4π detector elements that recorded a valid particle in an event. A "valid" particle is defined as at least one charged particle in the detector; unidentified charged particles that stopped in the fast plastic and double hits were counted as one particle.

The charged particle multiplicity spectrum is shown for three different event triggers in Figure 4.1. Open circles, squares, and filled circles show dP/dN_C for events measured with the inclusive, singles, and coincidence triggers, respectively. Presumably, a larger multiplicity indicates a more central event. Therefore, we see from Figure 4.1 that even without explicit centrality cuts, the requirement of measuring two protons in the hodoscope already preferentially selects more central events.

The second global observable we studied was the midrapidity charge, Z_y, defined as:

$$Z_y = \sum_{i=1}^{N_c} Z_i \cdot \Theta(y_i - 0.75y_{targ}) \cdot \Theta(0.75y_{proj} - y_i) \tag{4.1}$$

with

$$\Theta(x) = \begin{cases} 1 \text{ if } x > 0 \\ 0 \text{ if } x \leq 0 \end{cases}. \tag{4.2}$$

In Equation 4.1, and y_{targ}, y_{proj}, and y_i are respectively the rapidity of the target, projectile, and i^{th} charged particle in the center-of-momentum frame of the system.

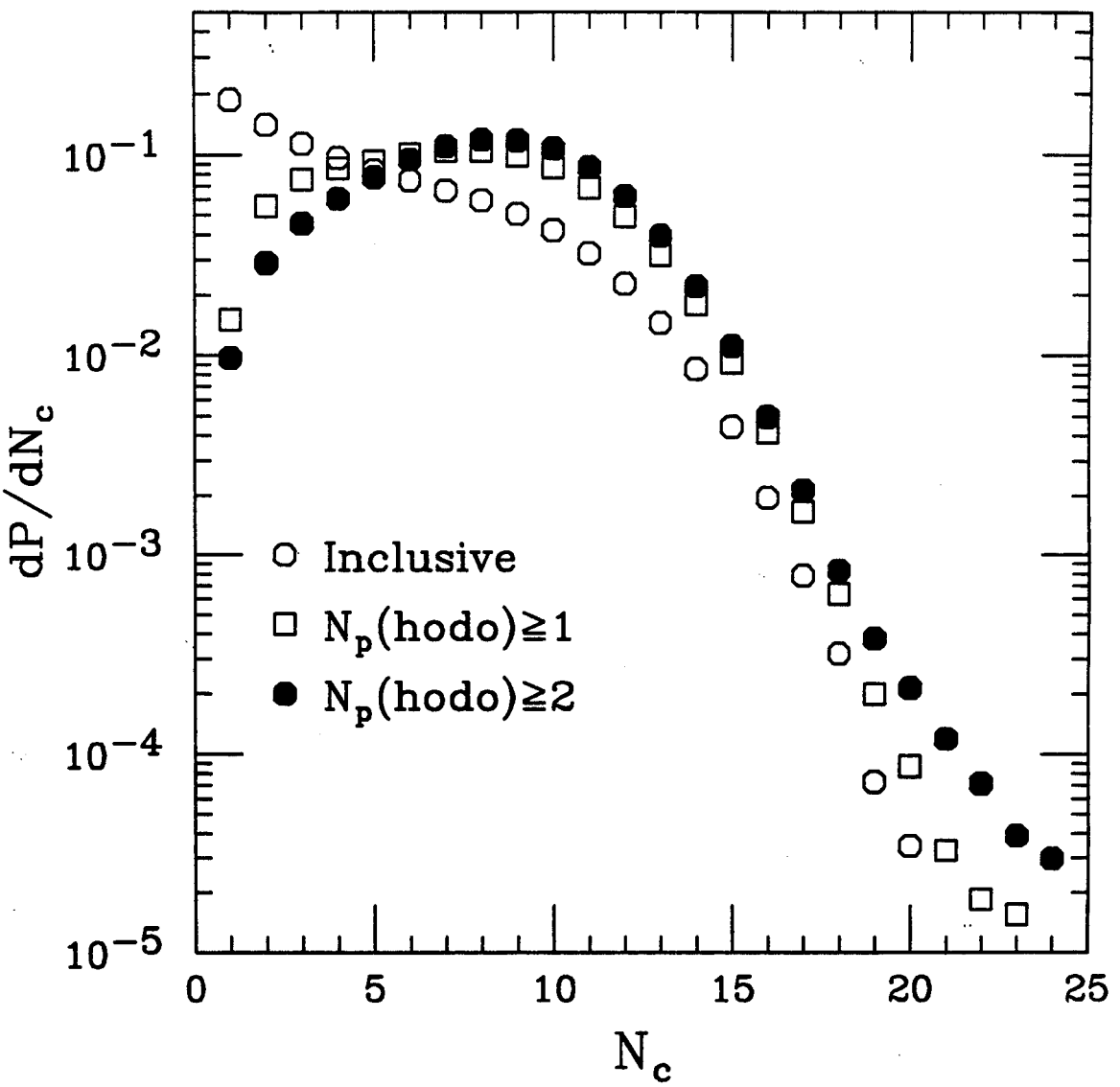

Figure 4.1. Charged particle multiplicity distributions measured in the 4π Array under 3 separate triggering conditions. Open circles, open squares, and filled circles indicate dP/dN_C for inclusive, hodoscope singles, and hodoscope coincidence triggers, respectively.

Figure 4.2 shows the midrapidity charge distributions dP/dZ_y for our three triggering conditions. Qualitatively, a trend towards more central events (as characterized by large values of Z_y) is again observed as the trigger varies from inclusive (open circles), to coincidence (filled circles).

Finally, centrality cuts were based on the total transverse energy of the event, defined as:

$$E_t = \sum_{i=1}^{N_c} E_i \cdot \sin^2 \theta_i , \tag{4.3}$$

where E_i and θ_i are respectively the energy and laboratory angle of the i^{th} particle measured in the event.

The spectra dP/dE_t are shown in Figure 4.3 for our three trigger conditions. Once again, the requirement of measuring two protons in the hodoscope appears to bias our event distribution toward more violent collisions.

The distributions of all three of the global observables display similar trends as the trigger condition varies. The assumption that a large value of any one signals a central collision leads to the reasonable conclusion that measuring two protons in our hodoscope at 38° in the lab frame biases the event sample toward more central collisions.

If the value of one of our global observables indicates a central collision, what is the likelihood that another will do likewise? This issue is addressed in Figure 4.4, in which the correlations between E_t, Z_y, and N_c are shown. On average, the values of the other two global observables increase when the value of any one increases. If any global observable is a measure of the centrality, they all are.

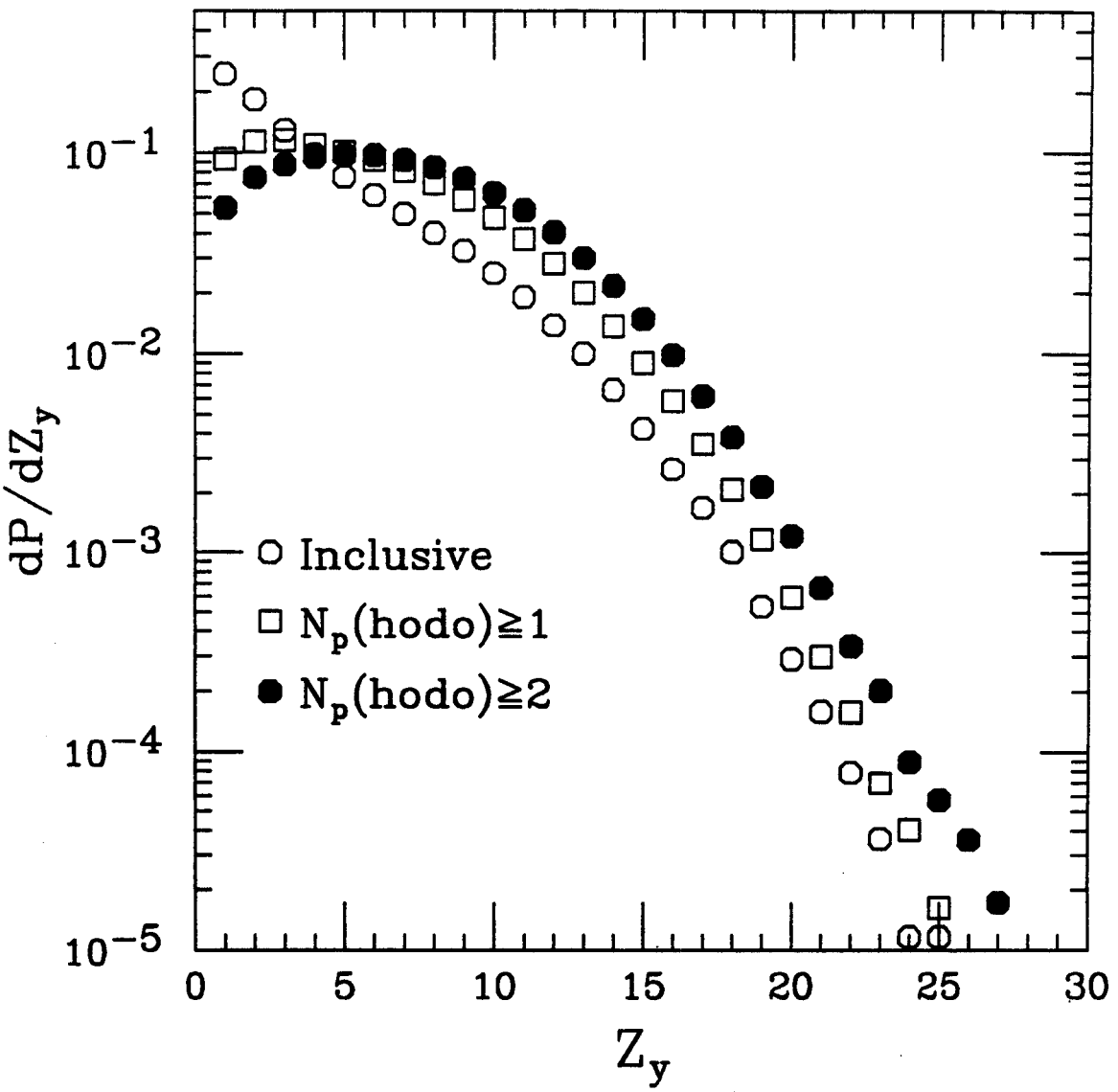

Figure 4.2. Midrapidity charge distributions measured in the 4π Array are shown for the same triggering conditions as for Figure 4.1.

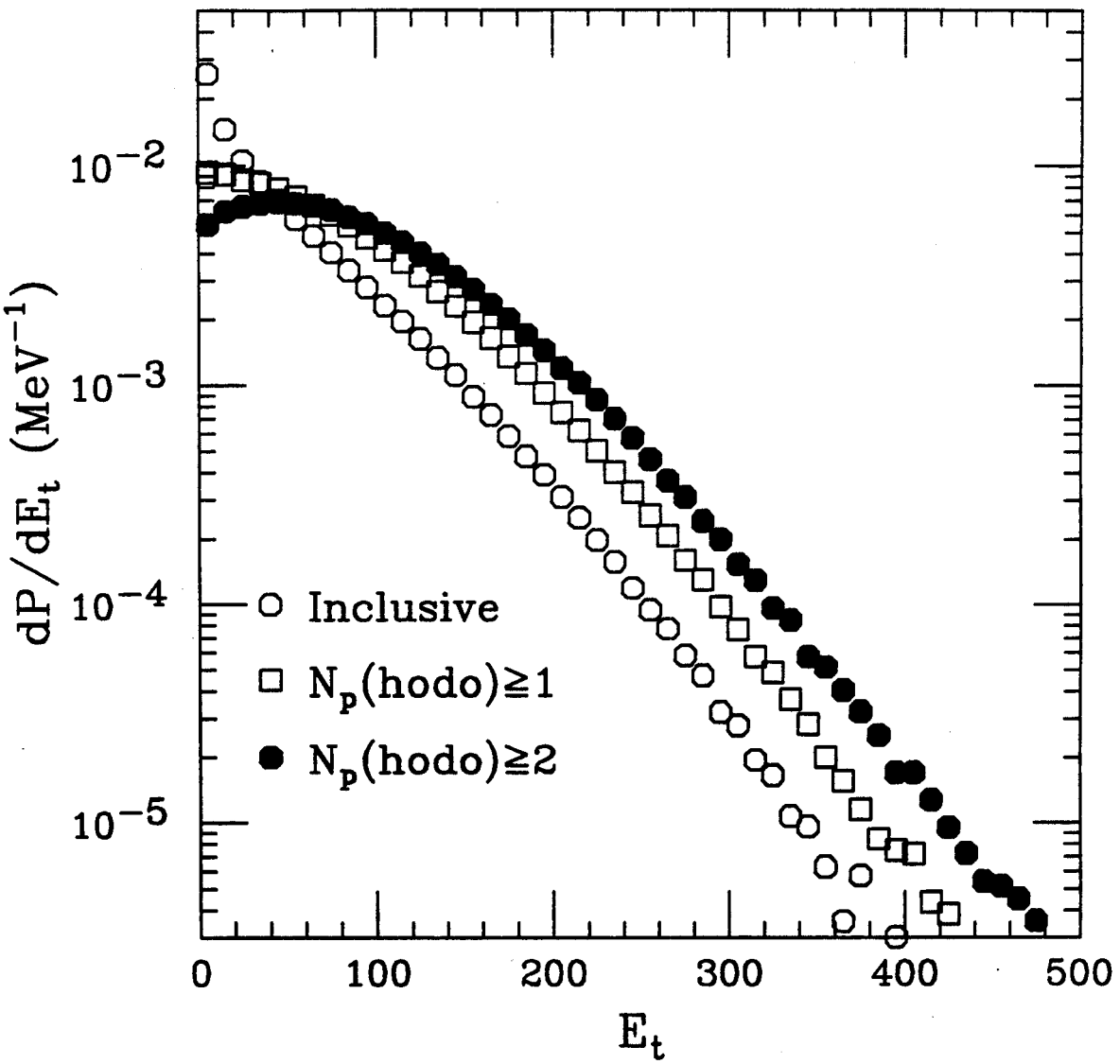

Figure 4.3. Total transverse energy distributions measured in the 4π Array for the same triggering conditions as for Figures 4.1 and 4.2.

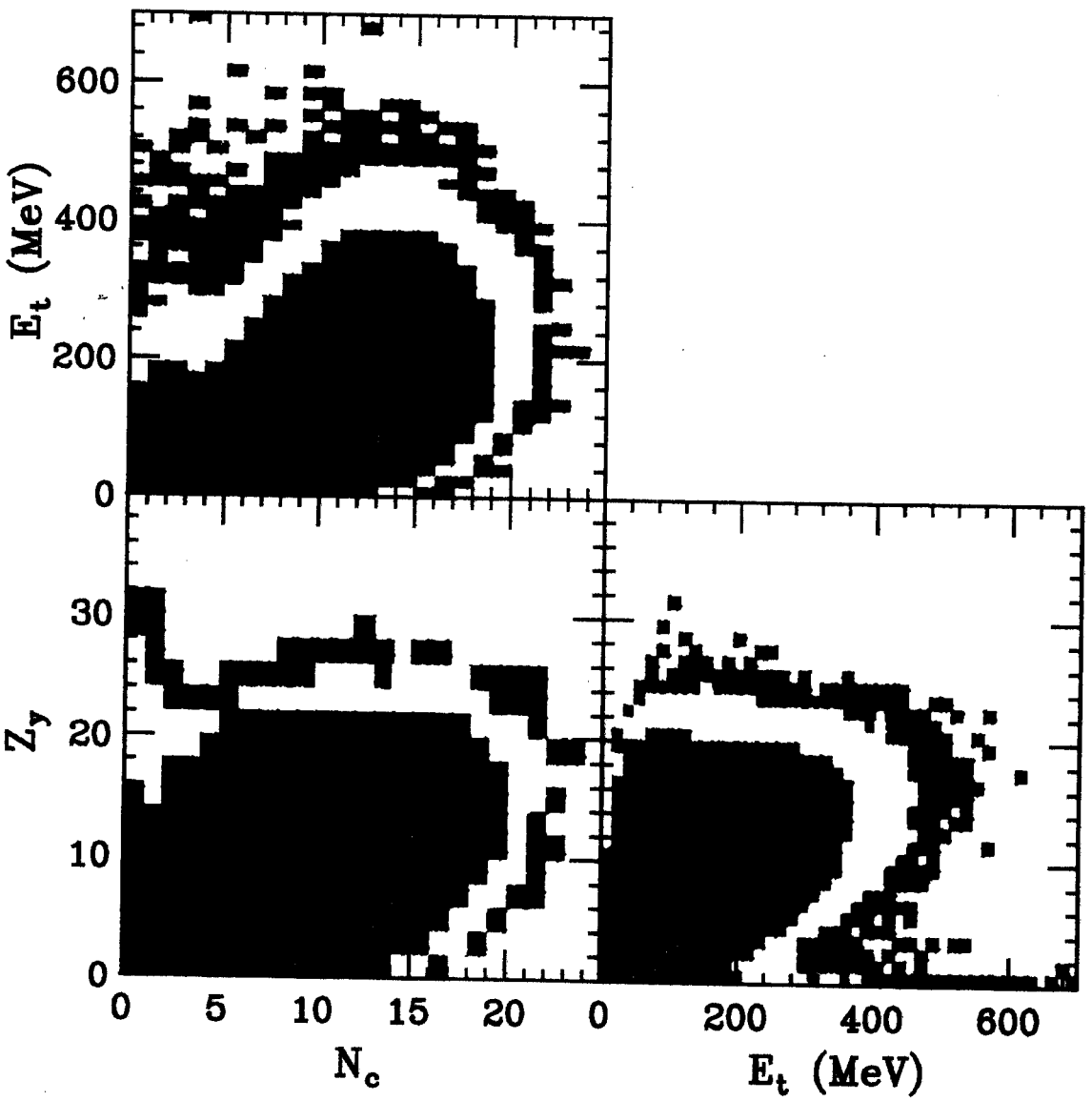

Figure 4.4. Logarithmic two-dimensional probability distributions are shown for pairs of global observables. The values of the three observables shown, the charged particle multiplicity (Nc), the mid-rapidity charge (Zy), and the transverse energy (Et) are highly correlated. If one observable is a good measure of event centrality, they all are.

4.2 Construction of the Reduced Impact Parameter Scale

In this and the following section, we follow closely the technique described by Phair [Phai 92].

A uniform scale indicating the event centrality may be based on any global observable, which we generically label X. The validity of this scale as an average impact parameter scale is based on three assumptions, which we list below. The first two assumptions are quite feasible, while the last is only an approximation for a non-ideal detector system.

We assume a strictly monotonic relationship between the average value of X and the impact parameter of the event. Then the relationship between the probability of measuring an event with impact parameter b and the probability of measuring the observable with the value X may be written:

$$\frac{dP}{db} \cdot db = \frac{dP}{dX} \cdot dX. \tag{4.4}$$

If we assume that the largest values of X are associated with the most central collisions, we obtain:

$$\int_0^b \frac{dP}{db'} \cdot db' = \int_X^\infty \frac{dP}{dX'} \cdot dX'. \tag{4.5}$$

Finally, we assume that the detector system has unit efficiency, regardless of impact parameter. Therefore, with an inclusive event trigger, the probability of observing an event with impact parameter b follows the geometric distribution $dP/db \sim b$. Then, defining the average reduced impact parameter $\hat{b}$, we have:

$$\hat{b}(X) = \frac{\langle b(X) \rangle}{b_{max}} = \sqrt{\int_X^\infty \frac{dP}{dX'} \cdot dX'}. \tag{4.6}$$

Thus the centrality of an event may be quantified by the average reduced impact parameter, which takes on a value of zero for the most central events and unity for the most peripheral.

An example of such a scale based on the total transverse energy ($X=E_t$) is shown in Figure 4.5. The inclusive distribution dP/dE_t is shown in the upper panel, while the bottom panel shows $\hat{b}(E_t)$, calculated through Equation 4.6.

Through such scales, distributions of global variables may be transformed into average reduced impact parameter distributions through

$$\frac{dP}{d\hat{b}(X)} = \frac{dP}{dX} \Big/ \frac{d\hat{b}}{dX}. \tag{4.7}$$

When cuts are made on X, extraction of the impact parameter distribution becomes more involved. We discuss this in Section 4.4.2.

Figure 4.6 shows the distributions $dP / d\hat{b}(E_t)$ corresponding to our three event triggers. These curves correspond to those shown in Figure 4.3, and illustrate more quantitatively the shift toward centrality as we require the observation of protons in the 56-element hodoscope.

4.3 Comparison of Variables

The average reduced impact parameter, discussed in the previous section, is an approximate measure of the event centrality, based on the value of some global observable X. Clearly, however, there exist fluctuations in the relationship between impact parameter and any global observable on an event-by event basis. The relationship $\hat{b}(X)$ describes only the average behaviour of this relationship. In this section, we discuss how to estimate the magnitude of the fluctuations in the relationship between the "true" reduced impact parameter $b_r=b/b_{max}$, and a global observable X.

The utility of such an exercise is twofold. It determines which global observable provides the most precise measure of event centrality. Also, as we

discuss in Section 4.4.2, the extracted widths may be convoluted with the average reduced impact parameter distributions and used as input for dynamical models.

In Figure 4.7 the reduced impact parameter distribution $dP/d\hat{b}(E_t)$ is shown for narrow cuts on $\hat{b}(X)$, where $X=N_C$ (dashed lines) and Z_y (dot-dashed lines) for central and mid-central values of $\hat{b}$. Also shown is the distribution with a narrow double cut on both $\hat{b}(N_c)$ and $\hat{b}(Z_y)$ (solid lines). All probability distributions are normalized to unit area for ease of comparison.

For the midcentral cut $\hat{b}(X)=0.35$-0.4 (bottom panel), the width of the distribution $dP/d\hat{b}(E_t)$ is roughly the same for $X=N_C$ and $X=Z_y$. The fact that this width does not significantly decrease when a double cut is performed indicates that the extracted width ($\sigma \approx 0.15$) approaches the magnitude of the intrinsic fluctuations between the impact parameter and E_t.

For narrow cuts centered at very small values of the average reduced impact parameter (top panel), an edge effect-- due to the fact that $\hat{b}$ takes on only positive values-- distorts the distribution, moving its centroid to larger values of $\hat{b}$.

Distributions similar to those shown in Figure 4.7 are shown in Figures 4.8 and 4.9 for $dP/d\hat{b}(N_c)$ and $dP/d\hat{b}(Z_y)$, respectively. Somewhat smaller values of $\sigma(\hat{b})$ were extracted from the distributions of $dP/d\hat{b}(E_t)$, indicating that E_t is the best measure of centrality. This is consistent with a similar study of other nuclear systems [Phai 92].

4.4 Impact Parameter Distributions as Inputs to Models

Dynamic models of nuclear collisions simulate the evolution of a nuclear system as it undergoes a collision. This evolution can depend strongly on impact parameter, and experimental cuts on global observables may be used to test the details of theoretical predictions.

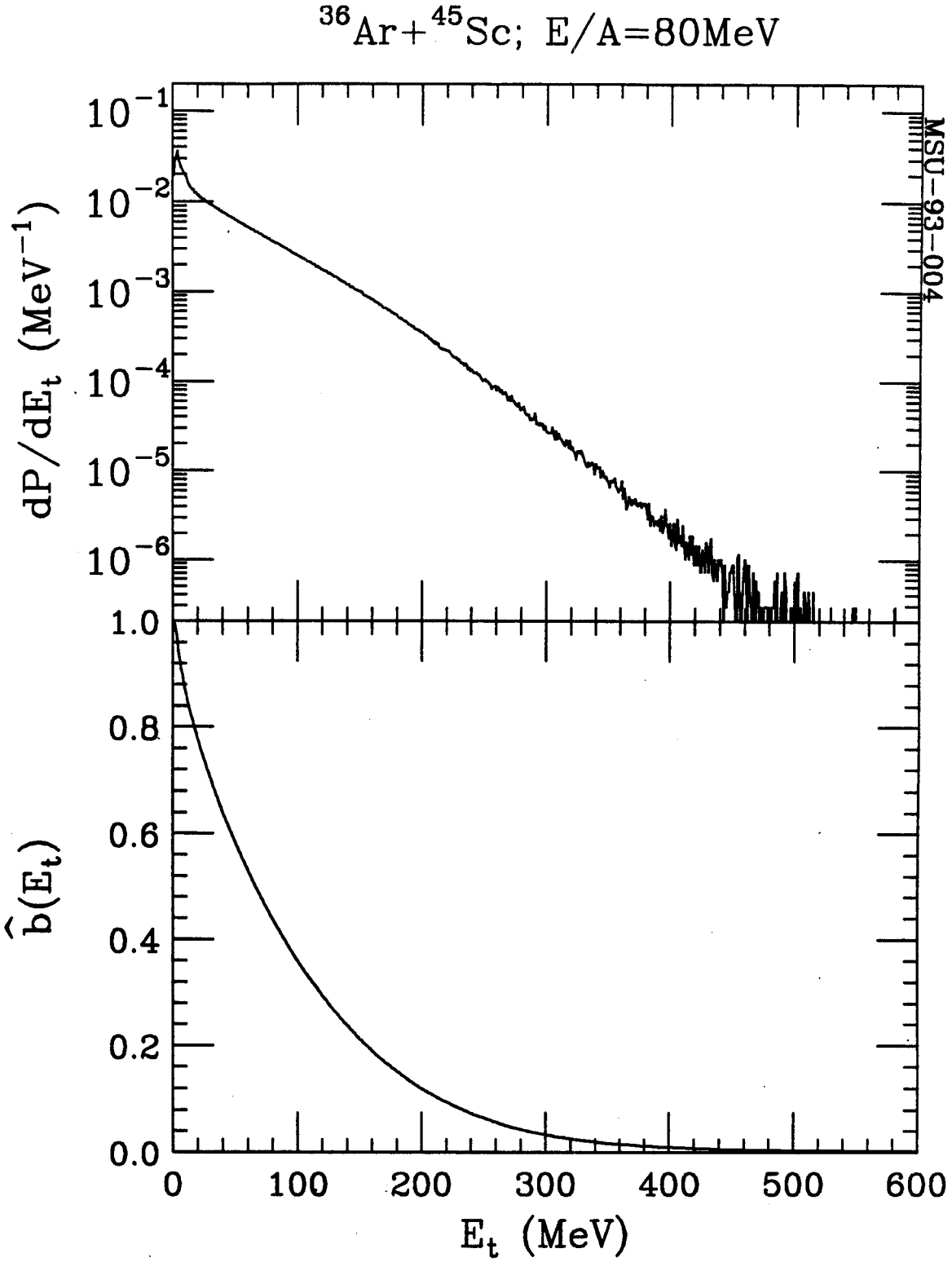

Figure 4.5. The inclusive transverse energy spectrum dP/dE_t is shown in the upper panel. The lower panel shows the average reduced impact parameter scale $\hat{b}(E_t)$ based on this distribution.

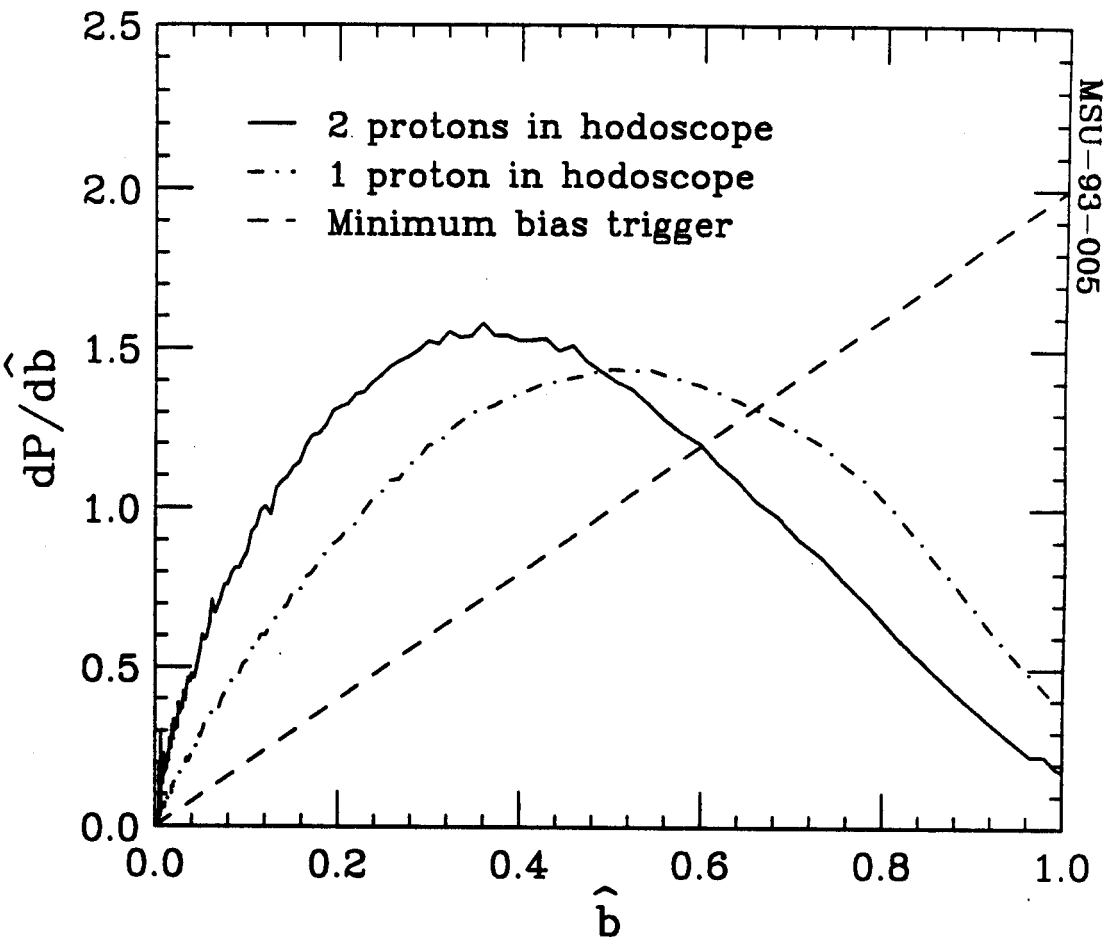

Figure 4.6. Average reduced impact parameter distributions $dP / d\hat{b}(E_t)$ for the three event triggers studied. Curves in this figure correspond to those shown in Figure 4.3.

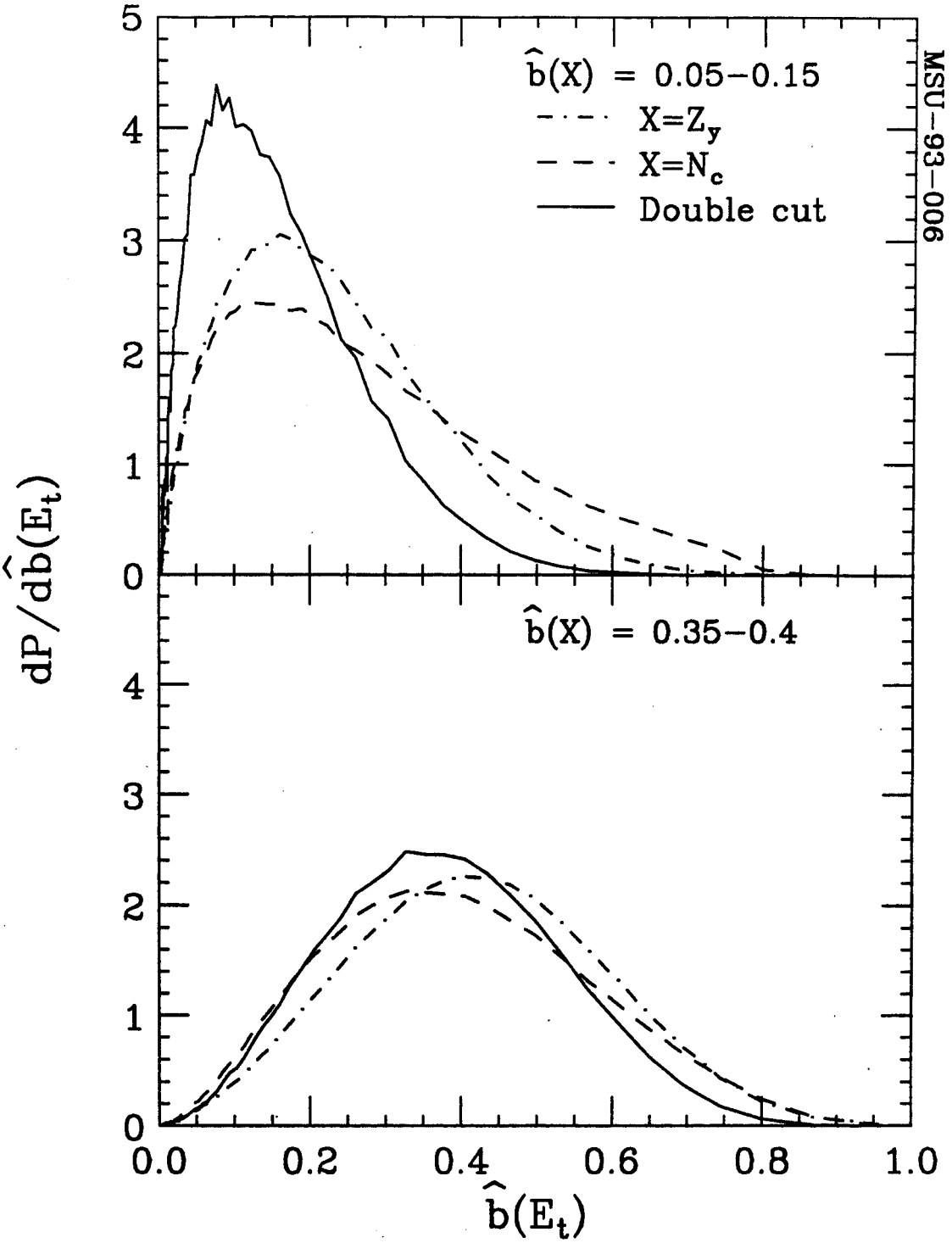

Figure 4.7. Average reduced impact parameter distributions $d\hat{P} / d\hat{b}(E_t)$ for tight centrality cuts on $\hat{b}(X)$, where X=N_C and Z_Y. A double-cut on both observables does not narrow the distribution significantly for the mid-central cut, indicating that the measured width is close to the scale of the intrinsic fluctuations between impact parameter and transverse energy.

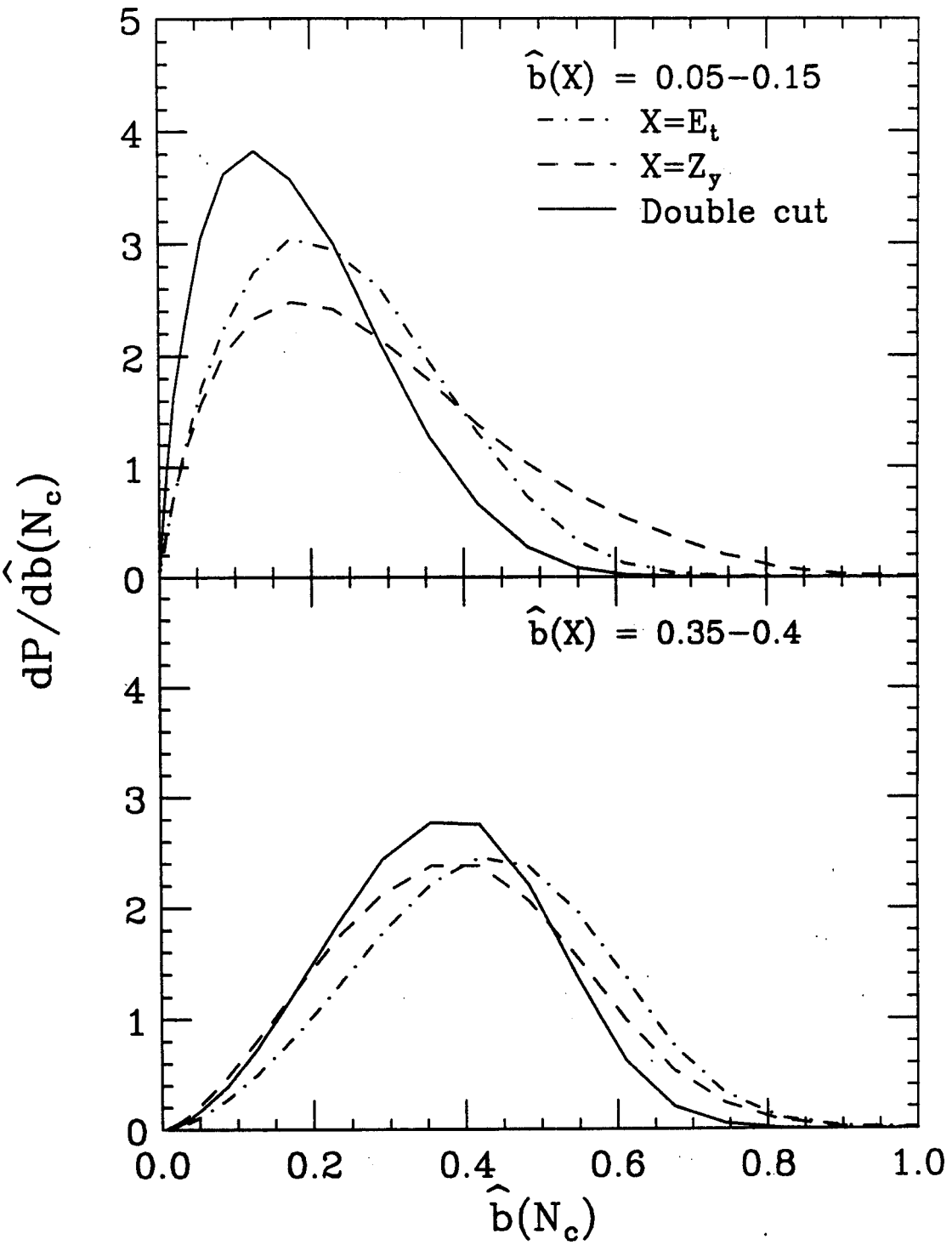

Figure 4.8. Average reduced impact parameter distributions $dP / d\hat{b}(N_c)$ for tight centrality cuts on $\hat{b}(X)$, where X=E_t and Z_y.

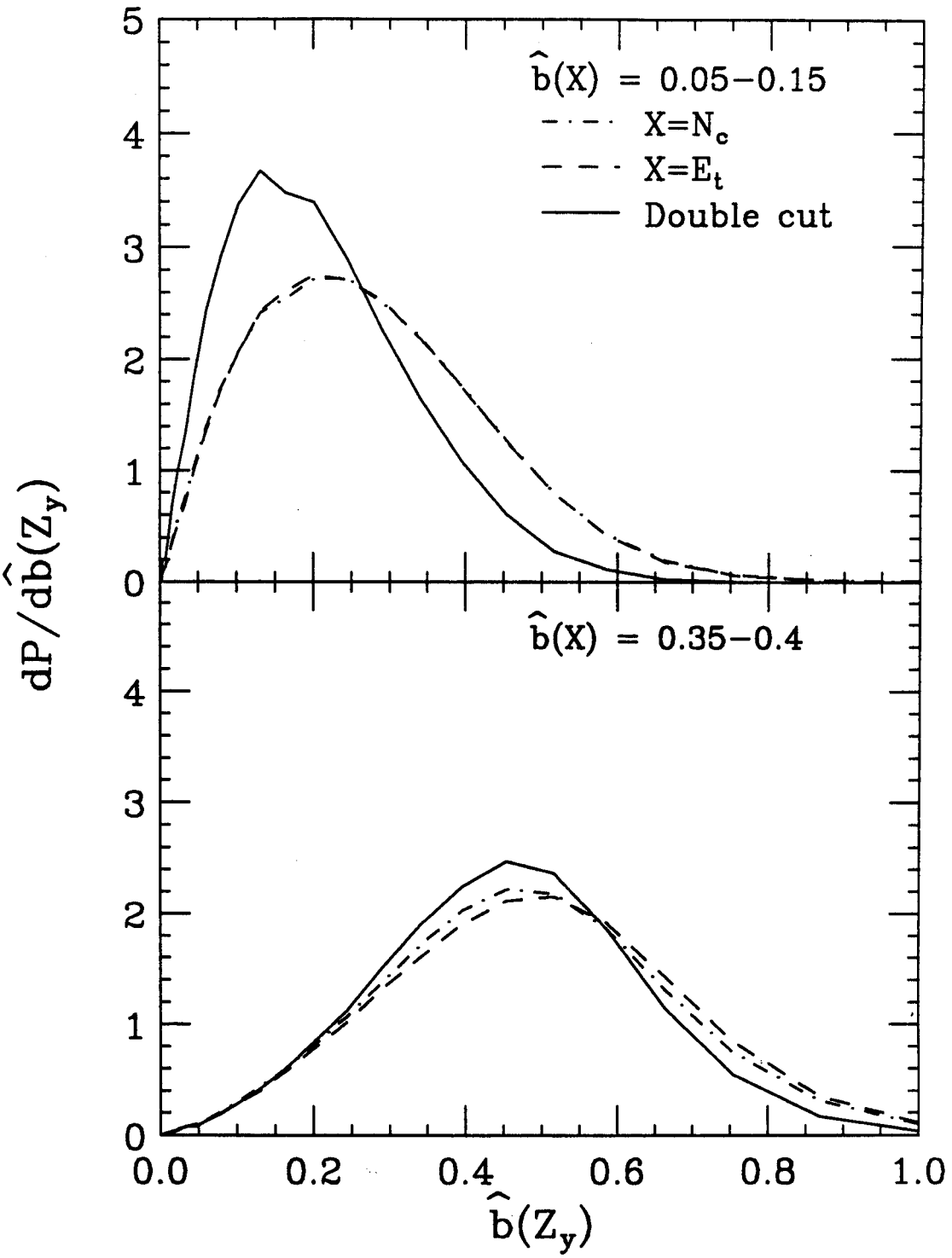

Figure 4.9. Average reduced impact parameter distributions $dP / d\hat{b}(Z_y)$ for tight centrality cuts on $\hat{b}(X)$, where X=E_t and N_C.

Such tests, are complicated by the fact that the very quantity that describes the initial state of the system-- the impact parameter distribution-- is not measured directly. Therefore, before judging the predictive power of a model, one should be as confident as possible that any test is free of the effects of impact parameter selection.

Since an unambiguous method of comparing impact parameter selected data to theoretical predictions does not exist, we discuss below two methods of selecting similar ranges of centrality for data and model events. A transport model based on the Boltzmann-Uehling-Uhlenbeck equation, to which we compare our correlation results in Chapter 6, is used as an example.

4.4.1 The Method of Equivalent Cuts

We want to compare physical quantities constructed from experimental and model events that represent similar regions of centrality. If we cut on E_t in our data, one obvious method of selecting model events would be to cut on the E_t of the event as predicted by the model. Such a procedure assumes that the model correctly describes the relationship between E_t and the impact parameter. We discuss below a procedure to select model events based on a global observable such as E_t.

In Figure 4.10, we compare the total transverse energy spectrum dP/dE_t measured for a minimum bias trigger with the impact-parameter-averaged prediction of the BUU model. To generate dP/dE_t for the BUU, a geometric impact parameter weighting was used ($dP \sim b \cdot db$). For the experimental data, the sum in Equation 4.3 runs over all charged particles and fragments detected in the 4π Array, while for the BUU results, the index is over all emitted nucleons, after passing through the detector acceptance. The E_t distribution predicted by the BUU is shown when the sum in Equation 4.3 runs only over the protons (dot-dashed curve), and when it runs over protons and neutrons (dashed curve).

Although free neutrons are not detected in our experiment, neutrons bound in complex fragments do contribute to the experimental E_t spectrum.

The BUU fails to reproduce the observed E_t spectrum. As mentioned in Chapter 1, the BUU is a theory that describes the time evolution of the single particle phase space distribution function and contains no mechanism for complex fragment formation. Therefore, distributions of global observables sensitive to contributions from complex fragments, such as E_t, N_C, or Z_y, will not be reproduced by the BUU.

From the inclusive E_t distributions shown in Figure 4.10, it is clear that the use of identical E_t cuts on the experimental data and on the BUU events would be rather meaningless. One may, however, define "equivalent" E_t cuts for BUU events and for measured events. We propose a procedure which assumes that, on average, E_t decreases monotonically with increasing impact parameter. The validity of this assumption for the BUU model is illustrated in Figure 4.11, where the contribution to the E_t spectrum from various impact parameter ranges is shown.

Our method then characterizes both data and BUU events according to where the E_t for the event falls in the respective E_t distribution. For example, one could assume that the top 10% of the experimental E_t distribution is produced by the same impact parameters as the top 10% of the theoretical E_t distribution. In practice, this implies that if dP/dE_t and dP'/dE_t are the total transverse energy probability distributions for the BUU and for the data, respectively, then a cut in the data at E_t corresponds to a cut in the BUU at $\hat{E}_t$, where the relationship between E_t and $\hat{E}_t$ is given by

$$\int_{\hat{E}_t}^{\infty} dE_t' \cdot \frac{dP'}{dE_t'} = \int_{E_t}^{\infty} dE_t' \cdot \frac{dP}{dE_t'}. \qquad (4.8)$$

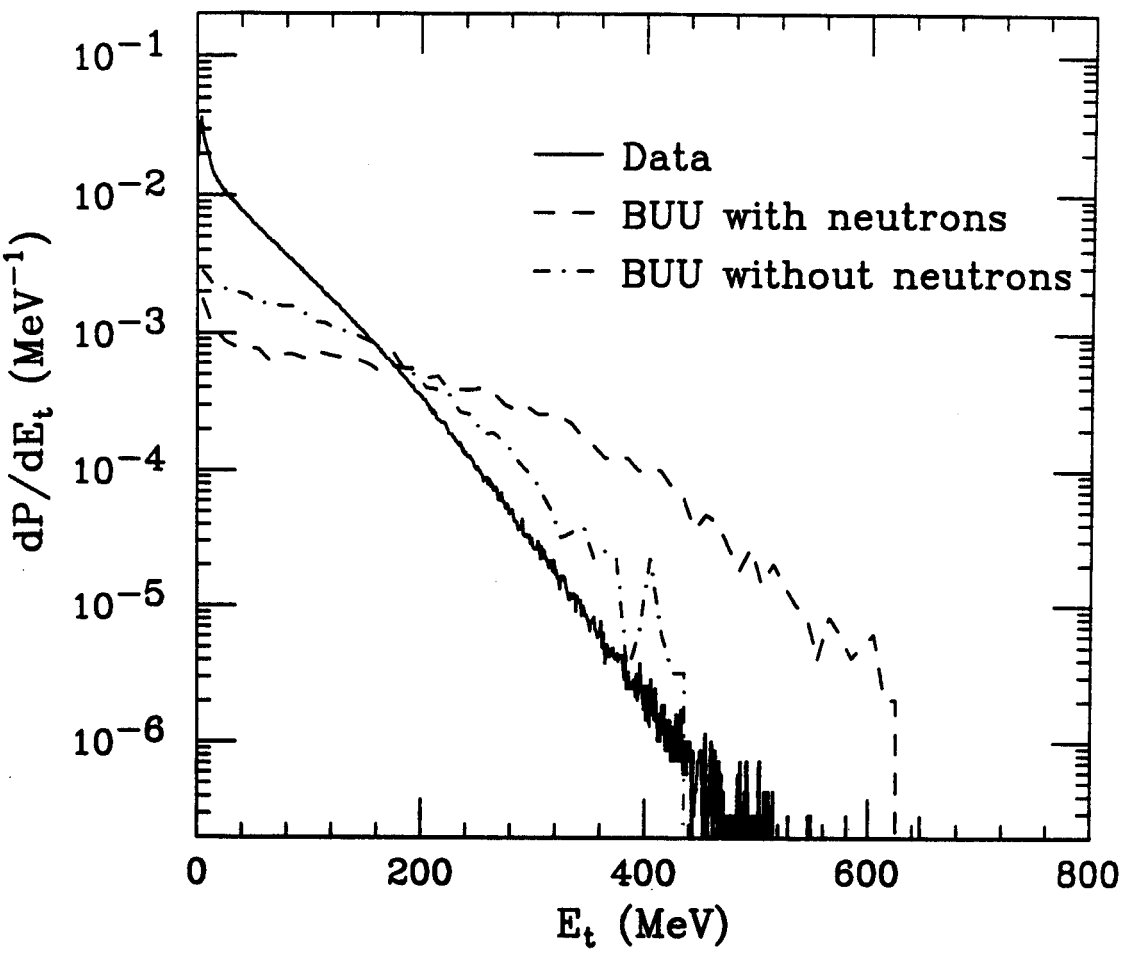

Figure 4.10. Total transverse energy spectrum dP/dE_t measured under a minimum bias trigger in the 4π Array is indicated by the solid line. Also plotted is the prediction of the BUU model, after passing through the detector acceptance of the 4π Array. Dashed and dot-dashed lines indicate calculations in which the definition of E_t (Equation 4.3) includes contributions from all emitted nucleons, and from protons only, respectively. Relative normalization gives equal area for all spectra in the region $E_t \geq 100$ MeV.

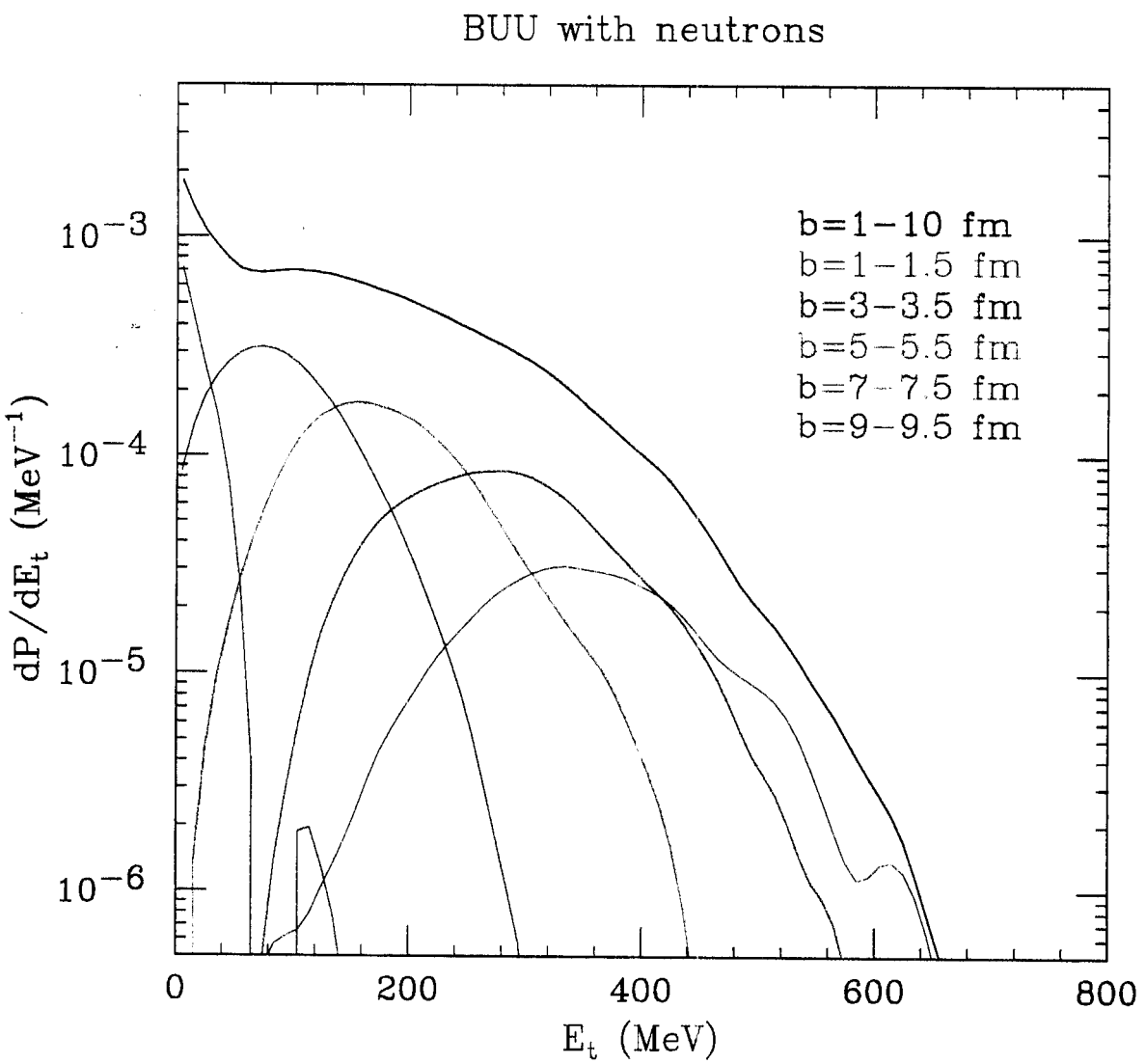

Figure 4.11. Plotted are the contributions to the total E_t spectrum from various ranges of impact parameter as predicted by the BUU when the contribution of neutrons are included. The black curve represents the impact parameter averaged spectrum, while the colored curves show the spectrum for small impact parameter intervals.

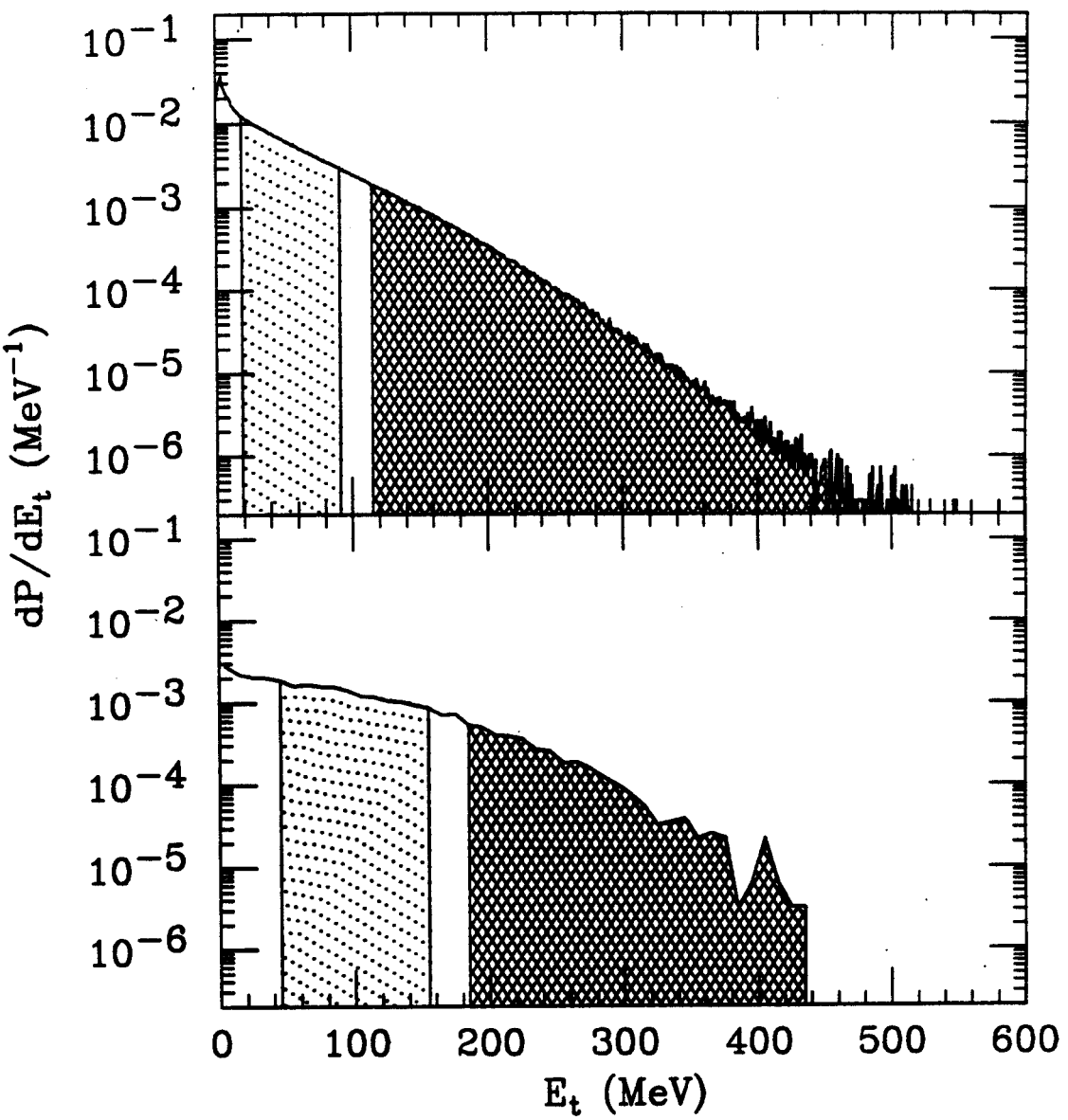

Figure 4.12. Experimental and theoretical inclusive E_t distributions are shown in the upper and lower panels, respectively. "Equivalent" E_t cuts defining central and peripheral events are shown.

Figure 4.12 shows "equivalent" cuts in the experimental and theoretical inclusive E_t distributions for central and peripheral events.

In summary, the procedure for comparing data to model predictions via the methods of equivalent cuts is as follows. First, one generates an ensemble of model events with a geometrical weighting according to impact parameter. Then, experimental events selected according to the E_t cut (E_t^{low}, E_t^{high}) are compared to model events selected from the ensemble according to ($\hat{E}_t^{low}$, $\hat{E}_t^{high}$), where the equivalent cuts are determined by Equation 4.8.

4.4.2 The True Reduced Impact Parameter Distribution

A different event-weighting scheme makes use of the reduced impact parameter scale developed in Section 4.2. In this section, we attempt to extract a realistic "true" reduced impact parameter scale from the data which we may input directly into a dynamical model.

Equation 4.6 defines a one-to-one relationship between the average reduced impact parameter $\hat{b}$ and the transverse energy E_t. Therefore, one may associate a sharp region in $\hat{b}$ with any sharp region in E_t defined by centrality cuts. An example is shown in Figure 4.13, where the upper panel shows the experimental transverse energy distribution when two protons are measured in the hodoscope. The shaded regions indicate the values of E_t that define our "central" and "peripheral" cuts. The center panel shows the average reduced impact parameter distribution that corresponds to this spectrum, calculated through Equation 4.7. Sharp cuts in E_t correspond to sharp cuts in $\hat{b}$, as indicated by the shaded regions in the center panel.

However, it is clear from our discussions in Section 4.3 that while we may postulate a one-to-one relationship between E_t and the *average* value of the impact parameter, event-by-event fluctuations will lead to a broad E_t spectrum even for a single impact parameter. Therefore, association of the $\hat{b}$ distributions

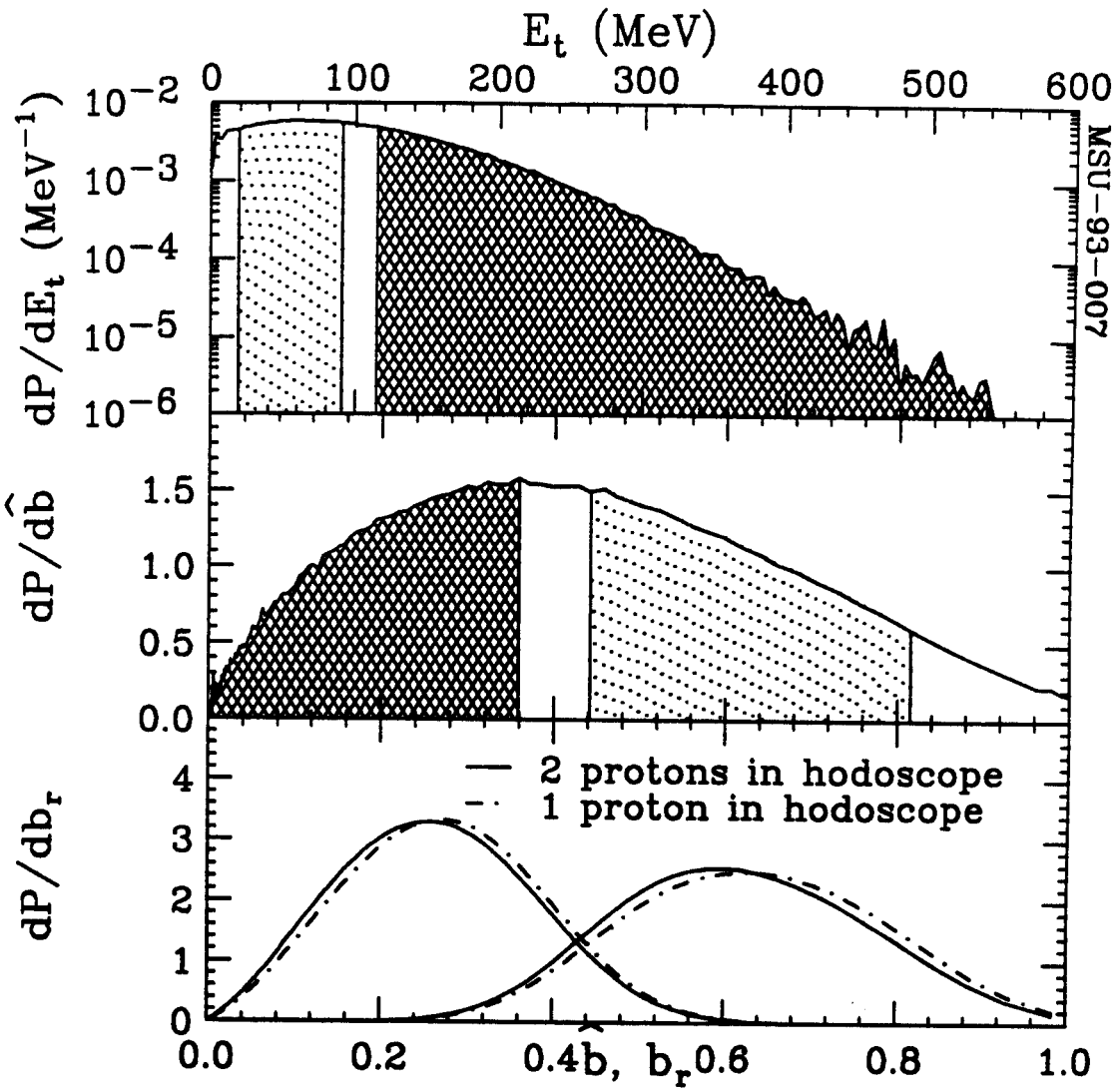

Figure 4.13. The top panel shows the total transverse energy distribution dP/dE_t for events which have two protons in the hodoscope. The cuts we define as "central" (high E_t) and "peripheral" (low E_t) are indicated by the shaded regions . Shown in the center panel are the average reduced impact parameter distribution $dP / d\hat{b}(E_t)$ corresponding to the total transverse energy distribution of the top panel. The bottom panel shows the reduced impact parameter distributions dP/dbr corresponding to the centrality cuts shown in the upper two panels. Solid lines indicate reduced impact parameter distributions for two-proton coincidence events, while dot-dashed lines represent similar distributions for singles proton events.

shown in the center panel of Figure 4.13 with the impact parameter distribution is unrealistic.

To obtain a true reduced impact parameter distribution dP/db_r, it is necessary to fold the effects of the finite widths $\sigma(\hat{b})$ into the impact parameter distribution; we use the widths measured in Section 4.3 for the $\sigma(\hat{b})$. As an ansatz, we take the following expression for the probability that an event with global observable corresponding to average reduced impact parameter $\hat{b}$ was in fact the product of a collision with true reduced impact parameter b_r:

$$\frac{dP_{\hat{b}}(b_r)}{db_r} \sim b_r \cdot e^{-(b_r-\hat{b})^2/2\sigma(\hat{b})^2} \cdot \Theta(1-b_r) \cdot \Theta(b_r). \tag{4.9}$$

For a given cut $E_t^{min} \le E_t \le E_t^{max}$, the reduced impact parameter distribution can be obtained by incorporating the extracted widths $\sigma(\hat{b})$ as follows:

$$\frac{dP}{db_r} = \int_{\hat{b}(E_t^{max})}^{\hat{b}(E_t^{min})} d\hat{b}' \cdot \frac{dP(\hat{b}')}{d\hat{b}'} \cdot \frac{dP_{\hat{b}'}(b_r)}{db_r}. \tag{4.10}$$

The effect of this smearing is illustrated in the bottom panel of Figure 4.13. The solid curves show the distributions of the true reduced impact parameter b_r deduced from the cuts shown in the upper two panels. These distributions represent our best estimate of the distributions of impact parameter for which two protons were measured in the hodoscope. For reference, the dot-dashed curves in the bottom panel correspond to b_r distributions calculated in a similar fashion for proton singles data; a slightly enhanced probability for larger impact parameters is noted in the singles data.

The solid curves in the bottom panel of Figure 4.13 correspond to impact parameter distributions for "central" and "peripheral" events which had two protons in the hodoscope. Hence, these impact parameter distributions have

been selected by the application of double gating conditions, and they may not be used as direct input for model calculations. We assume that in nature, reactions are caused by a geometric weighting of impact parameters, and our two-proton correlation functions are constructed from a select ensemble which produce two protons in the hodoscope detectors. To correctly simulate this experimental scenario in the construction of input impact parameter distributions for dynamical models, only the centrality cut on $\hat{b}(E_t)$ should be applied; the requirement of particles being detected in the hodoscope is implicit in the extraction of the correlation function from BUU events (see Chapters 5 and 6).

In order to construct impact parameter distributions that may be used as input to dynamical calculations, we construct distributions dP/db_r for our two centrality cuts from the *inclusive* E_t distribution, which corresponds to a geometric impact parameter weighting. The distribution of true impact parameters sampled by these two cuts may then be obtained by inserting the geometric distribution, $dP / d\hat{b} = 2\hat{b} / \hat{b}^2_{max}$, into Equation 4.10. The upper panel of Figure 4.14 shows the sharp cuts in average reduced impact parameter corresponding to our central and peripheral definitions. The solid curves in the lower panel of Figure 4.14 show the distributions of true reduced impact parameter deduced from these cuts. These curves may be used to weight events generated by a dynamical model such as the BUU.

Not all events generated by the dynamical model will produce a proton in the hodoscope acceptance. Thus, the impact parameter distributions corresponding to the events that contribute to the correlation function will differ from the "input" impact parameter distributions shown in the lower panel of Figure 4.14. We investigate this effect in Figure 4.15. The solid curves in the figure show the distributions of impact parameters used to weight our BUU calculations. (The distribution representing the central cut is truncated at very

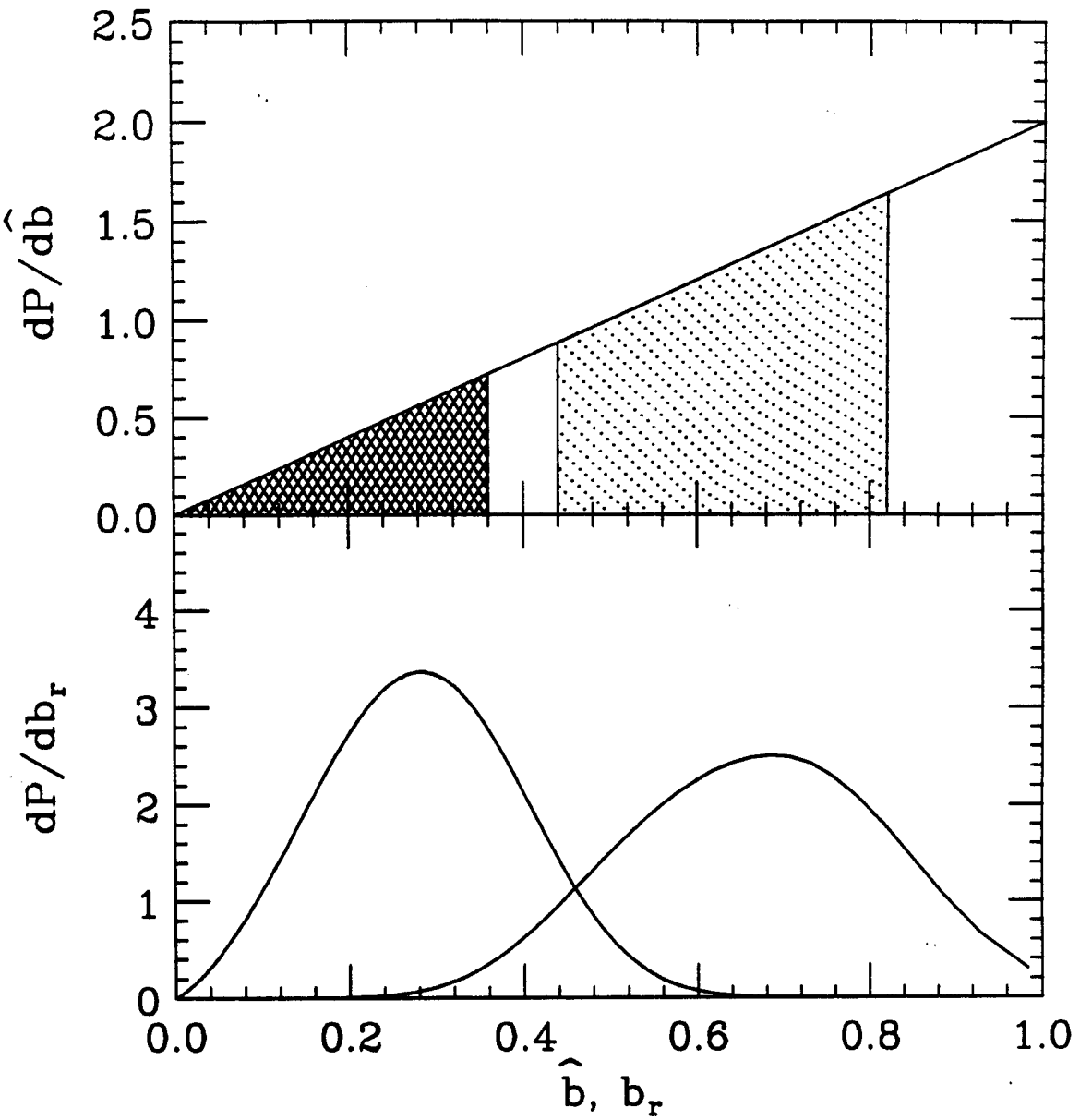

Figure 4.14. The upper panel shows sharp average reduced impact parameter cuts corresponding to the definition of central and peripheral events are indicated for a geometric distribution of impact parameter. The lower panel shows reduced impact parameter distributions dP/db_r corresponding to the centrality cuts indicated above.

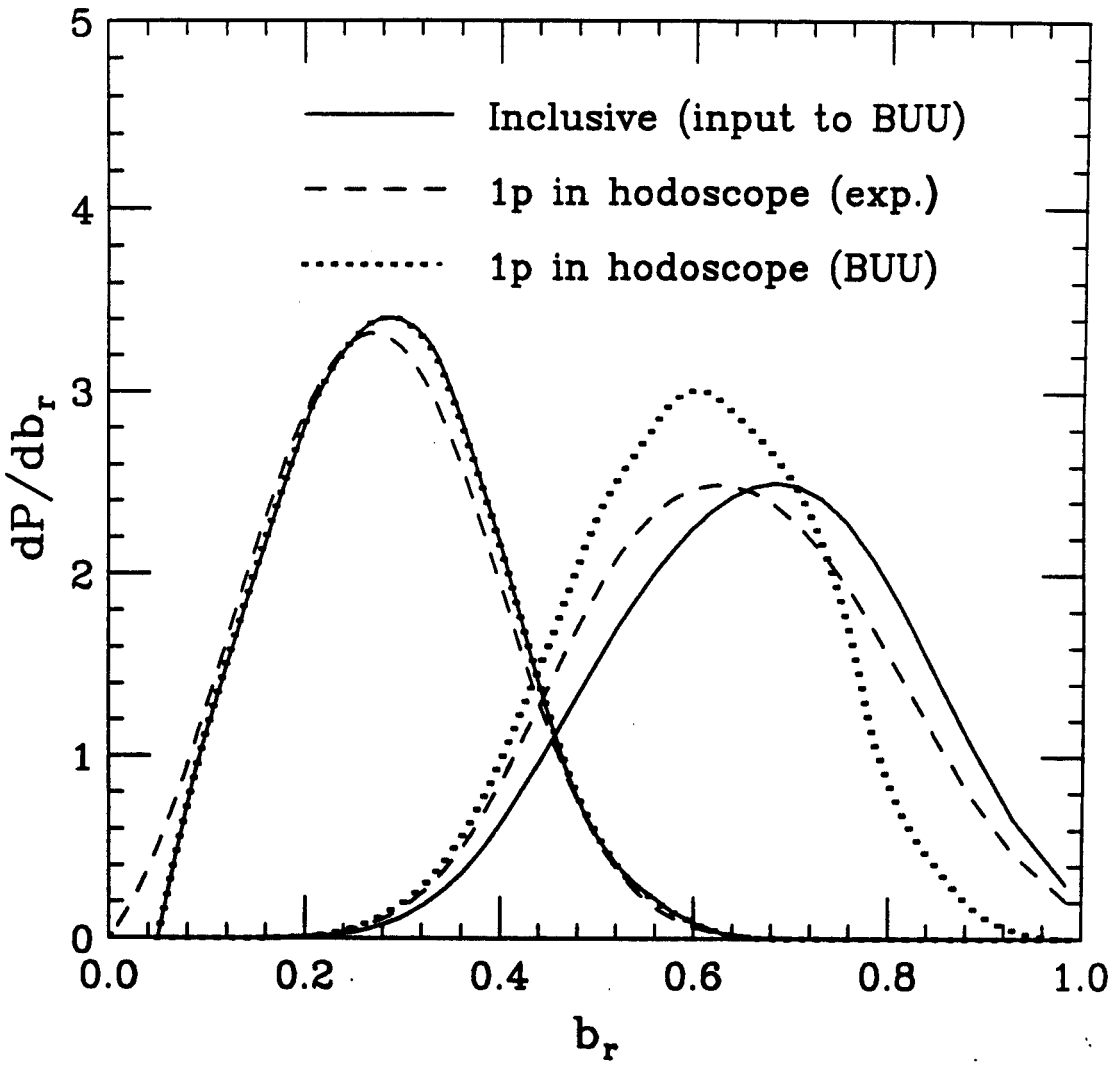

Figure 4.15. Comparison of experimentally reconstructed impact parameter distributions to those used in the BUU calculations. Solid curves show the impact parameter distribution used to weight BUU events (same as bottom panel of Figure 4.14). This distribution is modified by the additional requirement of proton emission towards the hodoscope (dotted curves). The dashed curves show the experimental reduced impact parameter distribution (see Equations 4.9 and 4.10) when a proton is detected in the hodoscope (same as dotted-dashed curve in Figure 4.13).

low impact parameters, since we did not run calculations for very small impact parameters for which the geometric cross section is small.) The dotted curves show the corresponding distributions with the additional requirement of proton emission into the direction of the hodoscope. For the peripheral cut, this requirement produces a shift towards smaller impact parameters. The distributions shown by the dotted curves may be compared to those extracted from our data (dashed curves; they are identical to the dotted-dashed curves in Fig. 6). The overall agreement between these two distributions illustrates the quality of the impact parameter selection and reconstruction procedure used in the present analysis.

To summarize this section, we have two possible methods of comparing the data to a model that requires an impact parameter distribution as an input. One may use "equivalent" E_t-cuts on model and data events, or one may extract reduced impact parameter distributions corresponding to a given cut in a global observable. We consider each in Chapter 6. Finally, we note that the method of "equivalent" E_t cuts is tantamount to defining a relation $\hat{b}'(E_t^{BUU})$ for BUU events as we have done for the data, and to apply the same cuts on $\hat{b}'(E_t^{BUU})$ and on $\hat{b}(E_t^{\exp})$.

Chapter 5 - Two-Proton Correlation Functions

In this chapter, we discuss general aspects of the two-proton correlation function. We discuss what the correlation function can tell us about sources created in nuclear collisions and present the formalism within which correlation functions may be predicted from model results.

Then, we move onto experimental issues. We discuss the construction of the so-called background correlation spectrum. We re-analyze data from a previous study to determine the difference in the correlation function using two popular methods of constructing the background. Finally, we discuss experimental resolution effects. Detector granularity and finite resolution may distort the correlation function. These effects must be accounted for in theoretical correlation functions. For the acceptance of the 56-element hodoscope, resolution effects are shown to be largely negligible in the context of our analysis.

5.1 Relation of the Correlation Function to the Spatio-Temporal Structure of the Source

The Koonin-Pratt formalism provides the theoretical framework in which the two-particle correlation functions is usually understood [Koon 77, Prat 84, Prat 87, Boal 90, Gong 91a]. Below, we present this framework, and then discuss the particular case of the two-proton correlation function. Finally, we discuss the sensitivity of the correlation function to the space-time structure of the proton source with illustrative calculations based upon the Koonin-Pratt formalism.

5.1.1 Koonin-Pratt Formalism

The Koonin-Pratt formalism relates the two-particle correlation function to the single-particle phase-space population density. The formalism has been derived elsewhere using basic assumptions [Koon 77, Prat 84, Prat 87, Gong 91a]. We do not reproduce the derivation here, but discuss the case of correlations between identical particles.

The formalism begins with an emission function g(r,p,t) (often referred to as the "source function"), which represents the probability that a particle with momentum **p** will be emitted at position **r** and time t. Then, the two-particle correlation function may be written as

$$1+R(\mathbf{P},\mathbf{q}) = C(\mathbf{P},\mathbf{q}) = \frac{Y(\mathbf{p}_1,\mathbf{p}_2)}{Y(\mathbf{p}_1)\cdot Y(\mathbf{p}_2)}$$
$$= \frac{\int d^3\mathbf{r}_1 dt_1 d^3\mathbf{r}_2 dt_2 g(\mathbf{r}_1,\mathbf{P}/2,t_1) g(\mathbf{r}_2,\mathbf{P}/2,t_2) \left|\phi(\mathbf{q},\mathbf{r}_1-\mathbf{r}_2-\frac{t_1-t_2}{2\cdot m}\cdot\mathbf{P}\right|^2}{\int d^3\mathbf{r}_1 dt_1 g(\mathbf{r}_1,\mathbf{P}/2,t_1) \bullet \int d^3\mathbf{r}_2 dt_2 g(\mathbf{r}_2,\mathbf{P}/2,t_2)} \quad (5.1)$$

In Equation 5.1, **q** is the momentum of relative motion in the rest frame of the pair, and **P** is the total momentum of the pair. Y(**p**) and Y($\mathbf{p}_1$,$\mathbf{p}_2$) are the single- and two-particle yields. The wavefunction of relative motion for the particle pair, ϕ(**q**,**r**) depends only on the relative phase space coordinates at the time of emission of the second particle.

Several assumptions enter into the derivation of Equation 5.1. Firstly, it is assumed that the particles are emitted independently; the second particle never knew that the first one left. This implies that all two-particle correlations are due to final-state interactions. This is only an approximation since conservation laws place constraints on the independence of the particles [Lync 82]. Furthermore, entrance channel effects [Zhu 91] or correlations in the source itself [Bern 85, Alm 93, Kund 93] may destroy the independence hypothesis.

A second assumption is that the two particles interact only with each other and not with the residue nucleus or with other emitted particles. For pairs of particles with the same charge-to-mass ratio emitted well above the Coulomb barrier, it is reasonable to neglect the residue, since to first order the Coulomb field of the residue does not affect the relative coordinates of the particles. However, three-body Coulomb trajectory calculations indicate that for correlations between heavy fragments [Kim 91, Kim 92, Fox 93, Bowm 93], or even for identical light particles emitted close to the Coulomb barrier [Eraz 91, Gong 92], interactions with the Coulomb field of the residue may be important. Furthermore, many-body Coulomb trajectory calculations [Glas 93] indicate that many-body interactions among emitted heavy fragments are of similar magnitude as two-body effects.

These two assumptions allow a clean separation in the sequence of events. The source, described by $g(\mathbf{r},\mathbf{p},t)$, emits two particles independently. Therefore, the two-particle emission probability may be written as a simple product of the single-particle emission probabilities.

$$\Pi(\mathbf{p}_1,\mathbf{p}_2) = \Pi(\mathbf{p}_1) \cdot \Pi(\mathbf{p}_2). \tag{5.2}$$

Once the second particle is emitted, the interaction between the particles, represented by the relative wavefunction $\phi(\mathbf{q},\mathbf{r})$ is "switched on." This leads to a correlation which destroys the factorability of the *final* probabilities:

$$Y(\mathbf{p}_1,\mathbf{p}_2) \neq Y(\mathbf{p}_1) \cdot Y(\mathbf{p}_2). \tag{5.3}$$

The final important assumption entering into Equation 5.1 is that the source function $g(\mathbf{r},\mathbf{p},t)$ does not vary greatly over a momentum region of the order of $|\mathbf{q}|$. This assumption is appropriate when applied to intermediate

energy heavy ion collisions, since typical momenta (hundreds of MeV/c) are much larger than the values of relative momentum ($\lesssim$ 50 MeV/c) typically of interest in correlation studies.

With this assumption, the need for explicit integration over the initial momenta in Equation 5.1 is eliminated, as the momentum dependence in g may be represented by the average momentum of the pair. Also, by the conservation of momentum, the final and initial average momentum are equal, making any knowledge of the details of the evolution from initial to final momentum unnecessary.

5.1.2 The Two-Proton Wavefunction

The behaviour of the correlation function for a given source configuration depends on the particle pair used, since the two-particle relative wavefunction gives rise to the correlations in Equation 5.1. Here, we discuss briefly the two-proton wavefunction and the physical effects that influence the two-proton correlation function.

In Figure 5.1, the square of the two-proton relative wave function, $|\phi|^2$, is shown as a function of the relative separation $|\mathbf{r}|$ and relative momentum $|\mathbf{q}|$ for the cases $\mathbf{r} \| \mathbf{q}$ and $\mathbf{r} \perp \mathbf{q}$. The relative wavefunction ϕ is determined by three physical effects: the strong nucleon-nucleon interaction, the Coulomb repulsion, and the quantum mechanical requirement of wavefunction antisymmetrization.

To calculate ϕ, the full Coulomb wavefunction [Mess 76] was modified by the contribution from the strong interaction. This modification was determined by solving the Schrödinger equation for the $\ell=0$ and $\ell=1$ partial waves with the Coulomb and the Reid soft-core potential [Reid 68]. Then, the two-proton wavefunction is determined by

$$|\phi(\mathbf{q},\mathbf{r})|^2 = w_1 \cdot \left|{}^1\phi(\mathbf{q},\mathbf{r})\right|^2 + w_3 \cdot \left|{}^3\phi(\mathbf{q},\mathbf{r})\right|^2, \qquad (5.4)$$

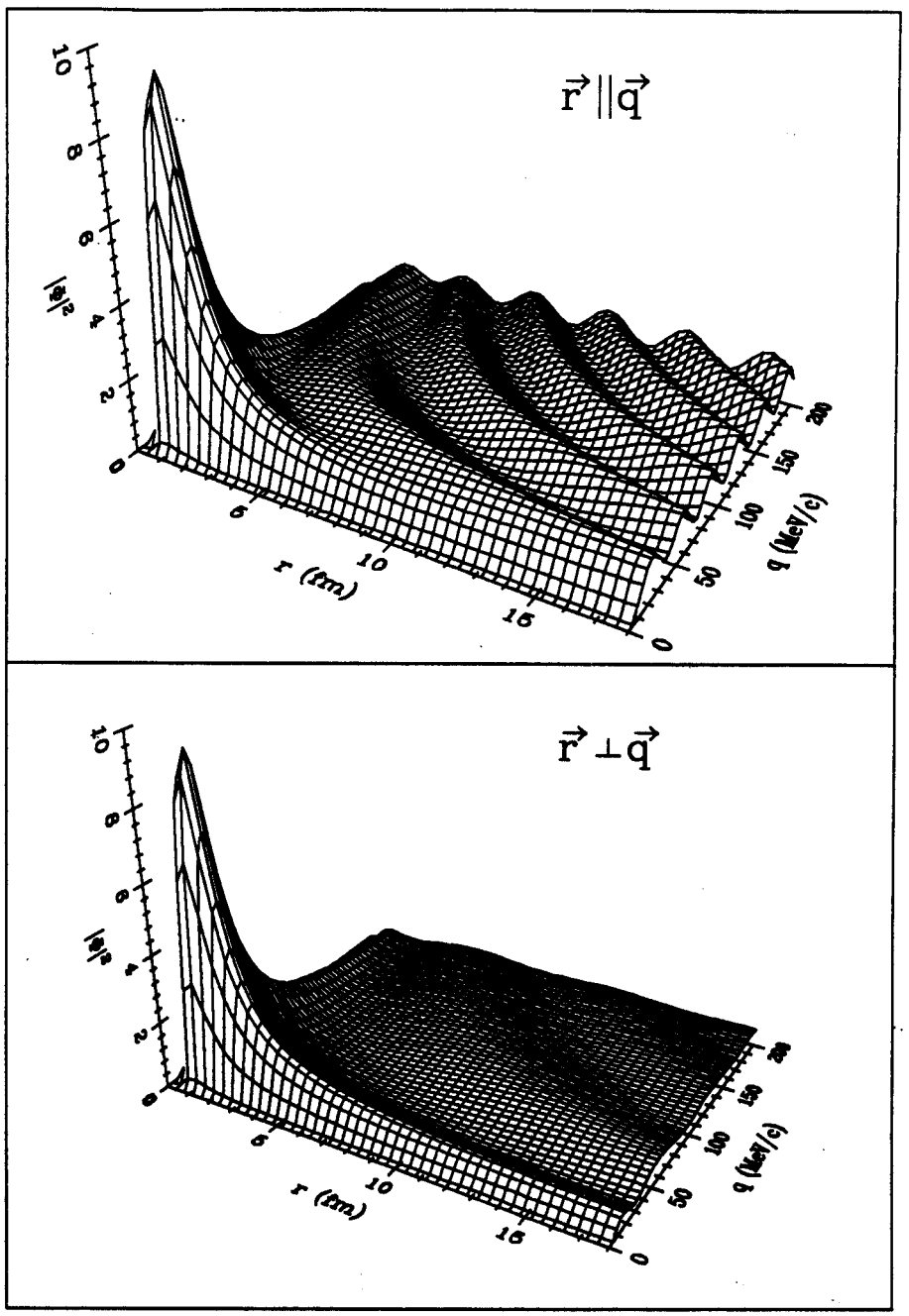

Figure 5.1. The square of the two-proton wavefunction as a function of the relative proton separation in coordinate and momentum space. The top and bottom panels show the wavefunction when **q** and **r** are parallel and perpendicular, respectively.

where $^1\phi(\mathbf{q},\mathbf{r})$ and $^3\phi(\mathbf{q},\mathbf{r})$ are the singlet and triplet spatial two-proton wavefunctions, respectively. We follow the usual assumption that the proton spins are distributed statistically, so the singlet and triplet weighting factors are set to $w_1=1/4$ and $w_3=3/4$. (See, however, [Zhu 91], for a study of ^{3}He breakup, where proton spin correlations from the entrance channel result in a nonstatistical spin distribution of the final state.)

The squared wavefunction for identical non-interacting particles goes as $|\phi(\mathbf{q},\mathbf{r})|^2 \sim 1\pm\cos(2\mathbf{q}\cdot\mathbf{r})$ (where the upper sign applies for bosons and the lower to fermions) due to the quantum mechanical (anti)symmetrization requirement. In this case, the correlation function is just the Fourier transform of the square of the source distribution [Kopy 72, Zajc 92]:

$$1+R(\mathbf{q}) = 1\pm\left|\tilde{g}(\mathbf{q})\right|^2 = 1\pm\int e^{2i\mathbf{q}\cdot\mathbf{r}}d\mathbf{r}\cdot\left\{\int g(\mathbf{R}+\tfrac{1}{2}\mathbf{r})g(\mathbf{R}-\tfrac{1}{2}\mathbf{r})d\mathbf{R}\right\}, \qquad (5.5)$$

where the total momentum dependence has been suppressed for clarity. For spin-1/2 fermions, identical particle interference suppresses the correlation function to 1/2 at $|\mathbf{q}|=0$. The correlation function returns to unity at a relative momentum $q_x\sim 1/R_x$, for a source whose extension in the x-direction is about R_x [Kopy 72]. In principle, then, a measurement of the full 3-dimensional behaviour of 1+R would reveal the size and shape of the emitting source.

The Coulomb repulsion between the two protons also suppresses the correlation function at low relative momentum. The strength of the suppression is greater for small sources. For source functions whose extent is much below the proton Bohr radius of 58 fm, this suppression is largely independent of the relative orientation between $\mathbf{q}$ and $\mathbf{r}$. Therefore, the Coulomb effect obscures shape information carried by the quantum interference by reducing the number of proton pairs at low relative momentum. Worse, the weak directional

dependence that the Coulomb force does contribute to the correlation function *opposes* that of the quantum interference effects [Gong 91a]. With good statistics and tight directional cuts, however, shape information can be recovered, as we discuss below and in Chapter 7.

A near-resonance (corresponding to a phase shift of about 60°) in the strong interaction between the protons provides additional sensitivity to the size of the source. The attractive "^{2}He resonance" causes a bump in the correlation function at q≈20 MeV/c. Because the resonance is s-wave, no directional information is carried by the size of this bump. However, since the strength of the resonance goes roughly as the fraction of proton pairs whose relative position is within this nearly-bound state, the height of the bump provides a good measure of the volume of the system.

5.1.3 Illustrative Calculations

Typically, all three of the physical effects discussed above are important for the correlation function. Here, we present correlation functions corresponding to schematic source functions in order to illustrate the sensitivity of the correlation function for various source sizes and lifetimes.

We parametrize the spatial dependence of the source with a spherical function of Gaussian density profile [Koon 77]. In most comparisons with data, the time dependence of the source function is neglected [Zarb 81, Lync 83, Gust 84, Chen 87a, Chen 87b, Poch 86, Poch 87, Fox 88, Awes 88, Cebr 89, Gong 91b, Zhu 91, Hong 92, Xu 93, Kund 93]:

$$g(\mathbf{r},t,\mathbf{p}) \sim \delta(t)\cdot e^{-(|\mathbf{r}|/r_0)^2}. \qquad (5.6)$$

Besides reducing the number of source parameters to one, a vanishing source lifetime eliminates the $|\mathbf{P}|$ dependence of the correlation function. In Figure 5.2, correlation functions calculated according to Equation 5.1 with the

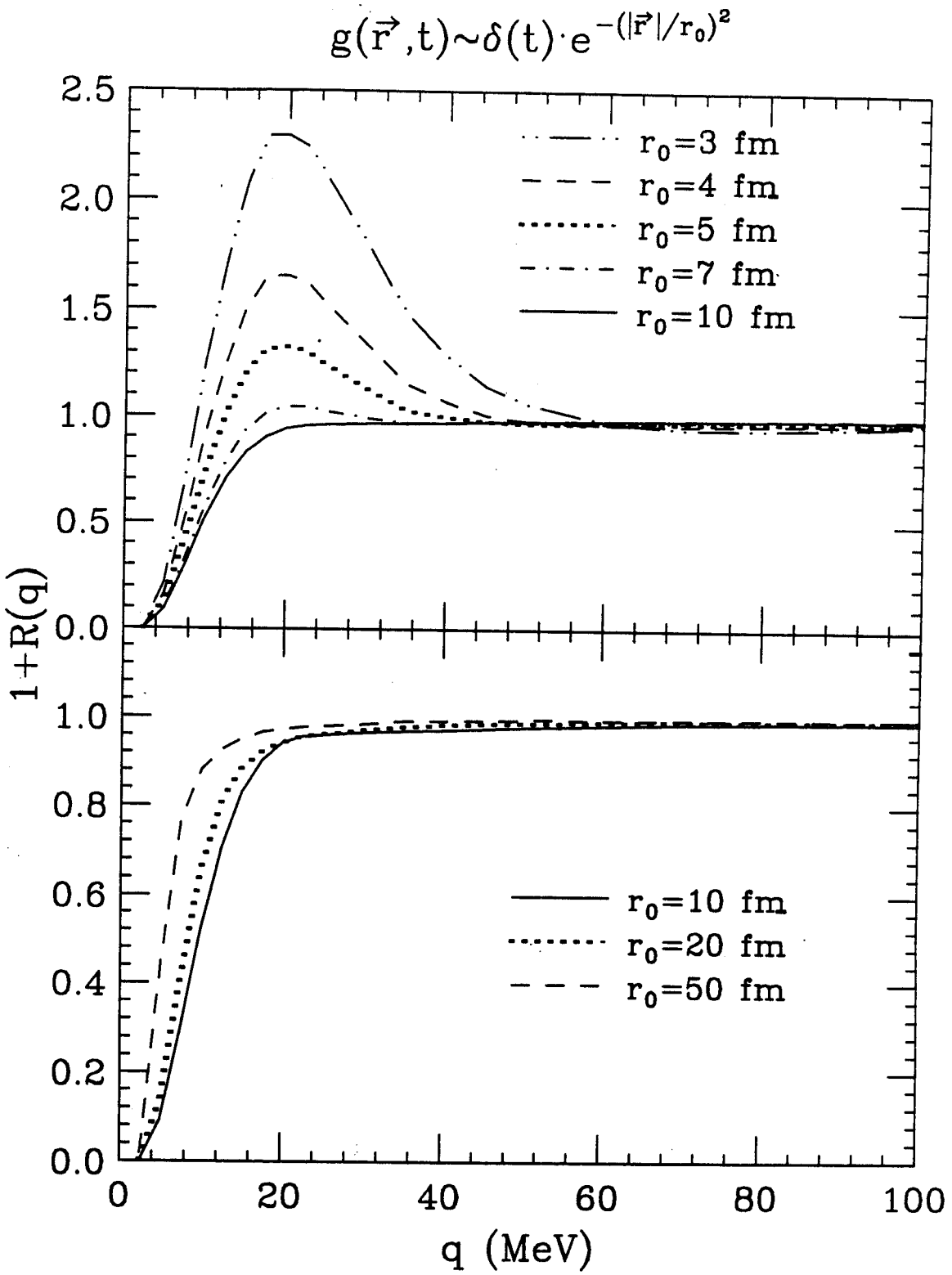

Figure 5.2. Correlation functions corresponding to proton emission from spherical sources with Gaussian density profile and negligible lifetime (Equation 5.6) show a strong source size dependence for smaller sources.

zero-lifetime source parametrization (5.6). For source radius parameters $r_0 \lesssim 7$ fm, the height of the bump at $q \approx 20$ MeV/c provides the best measure of the spatial extent of the source. For larger sources, however, the strong interaction and antisymmetrization effect become negligible [Gong 91a, Gong 91c], and information on the source size is carried by the strength of the Coulomb suppression at low relative momentum.

Although correlation functions similar to those shown in the lower panel of Figure 5.2 have been measured [DeYo 89, DeYo 90, Elma91, Eraz 91, Gong 90c, Gouj 91, Rebr 92], spatial sizes on the order of 50 fm are clearly unphysical for nuclear sources. Finite lifetime effects will increase the apparent size of the source if the parametrization (5.6) is used. In the Koonin-Pratt picture, the interaction between a pair of particles begins when the second particle is emitted. If τ describes the average time delay between the emission of two particles with velocity v, then the average particle separation will be on the order $d \approx |\Delta \mathbf{r} + \mathbf{v} \cdot \tau|$; where $\Delta \mathbf{r}$ is the relative coordinate of the two emission points; i.e. $|\mathbf{r}| \sim r_0$. In this case, a source parametrization with Equation 5.6 will give an overly-large spatial dimension. We now add an exponential time dependence to our source function. To simplify the discussion and concentrate on the spatial aspects of the correlation function sensitivity, we use a thermal energy distribution in the source function:

$$g(\mathbf{r}, t, \mathbf{p}) \sim e^{-(|\mathbf{r}|/r_0)^2} \cdot e^{-t/\tau} \cdot e^{-|\mathbf{p}|^2/2mT}. \qquad (5.7)$$

Here, m is the proton mass and T is the temperature, which we set arbitrarily to 8 MeV, since for tight gates on the total momentum P, the correlation function is insensitive to the details of the energy spectrum.

Figure 5.3 illustrates the interplay between the momenta of emitted protons and the lifetime of the source. In the upper panel, the lifetime parameter τ is varied for a tight total momentum cut P=250-350 MeV/c. The bump in the correlation function damps quickly as the lifetime is increased above about 100 fm/c. Correlation functions corresponding to long time delays between particle emissions are quite similar to those corresponding to spatially large, zero-lifetime sources shown in the bottom panel of Figure 5.2.

Displayed in the lower panel of Figure 5.3 are correlation functions for a fixed lifetime as the total momentum of the pair P is varied. Since these curves are degenerate for a zero-lifetime source, we see that correlations between higher-momentum pairs are more sensitive to lifetime effects. Also, note that for a *fixed* source size and lifetime, the correlation becomes more suppressed as the total momentum of the pair is increased. This is opposite the behaviour observed in correlation measurements [Lync 83, Chen 87a, Chen 87b, Poch 86, Poch 87, Awes 88, Gong 91b, Zhu 91, Lisa 91, Hong 92, Lisa 93a, Lisa 93b], revealing that protons of different energies are emitted from an evolving source, such as a cooling compound nucleus or a hot expanding system [Prat 87]. Thus, the two-proton correlation function may truly serve as a tool to probe the dynamics of a heavy ion collision.

Such an optimistic statement, however, must be taken with a grain of salt. For, although Equation 5.1 unambiguously associates a correlation function with any given source function, inversion of the problem is more difficult. We have seen in Figures 5.2 and 5.3 that the correlation function is affected similarly by an increase in lifetime or in source size. Without further cuts, the correlation function cannot distinguish space and time unambiguously.

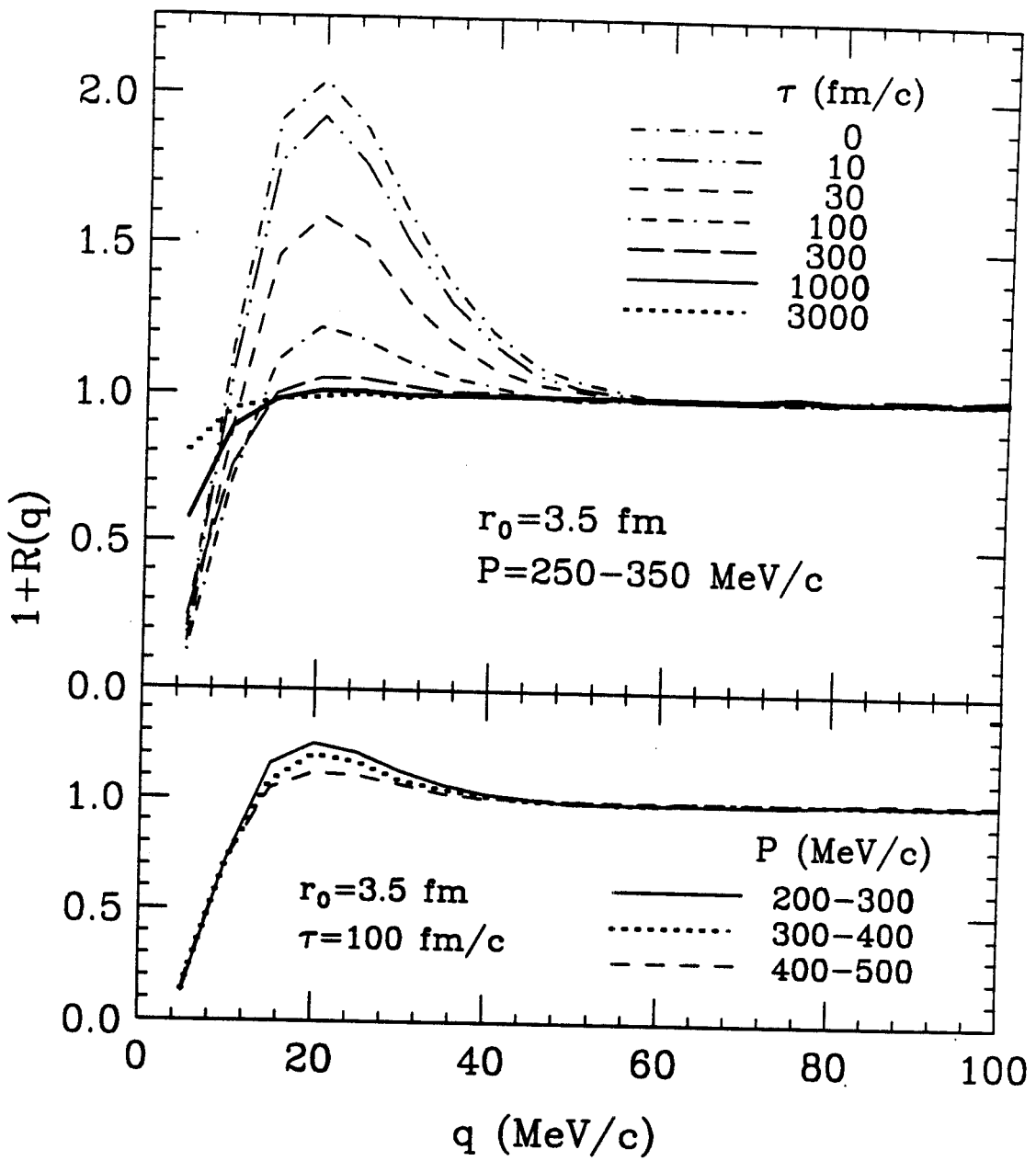

Figure 5.3. The interplay between the momenta of emitted protons and the timescale of emission is illustrated in the two-proton correlation function. The upper panel shows the effect of increasing lifetime for a source described by Equation 5.7, with the parameters indicated, for proton pairs with a fixed total momentum. The bottom panel shows the effect of increasing the total momentum P, when the lifetime is kept fixed.

The convention followed in the literature is to parametrize the source in terms of a zero-lifetime spheres. If such a parametrization leads to an unphysical source size, a finite lifetime is given to the source function. Then, the procedure is to assume some reasonable source size and fit the correlation function by varying the lifetime. In fact, in one study of $^{16}O+^{197}Au$ at E/A=94 MeV, correlation functions measured at forward angles are fit by assuming a negligible lifetime and varying the radius [Chen 87c], while those measured at backward angles assume a radius and vary the lifetime [Ardo 89].

For very large source sizes ($r_0 \gtrsim 20$ fm) or long lifetimes ($\tau \gtrsim 1000$ fm/c) [Gong 91a, Gong 92], the strong interaction and quantum interference effects may safely be ignored in uncut correlation functions, and Coulomb trajectory calculations [DeYo 89, DeYo 90, Elma 91, Eraz 91, Koro 91, Elma 93] are often employed to extract lifetimes on the order of 10^{-20}-10^{-21} s (~300-3000 fm/c) for evaporative sources. Other studies have varied both the size and the lifetime to fit the *shape* of the correlation function for shorter-lived sources [Mach 92].

Accurate lifetime determinations of these types are difficult, since a large change in source parameters leads to a small change in the correlation function. Moreover, for long lifetimes, the correlation function changes only for very low q, where statistics are low (due both to the correlations themselves and to phase space considerations) and where experimental distortion effects are most important; see Section 5.4 below.

Cuts on the direction of the relative momentum **q** with respect to the total momentum **P** have been suggested as a means of independently determining the source size and lifetime [Prat 87, Gong 91a]. Protons emitted from a long-lived source will have a phase space distribution elongated along the direction of the total momentum [Bert 89]; see Figure 1.2. The dimension of the source along the

direction of **P** will be on the order of $|\Delta \mathbf{r} + \mathbf{v} \cdot \tau|$, while typical dimensions perpendicular to **P** will be $|\Delta \mathbf{r}| \sim r_0$. The suppression of the correlation function due to the Pauli suppression will be stronger when **q** is oriented along the short direction of the distribution. Therefore, the longitudinal correlation function ($\mathbf{q} \parallel \mathbf{P}$) will be enhanced as compared to the transverse ($\mathbf{q} \perp \mathbf{P}$). In principle, then, fitting the magnitude of the correlations as well as the difference between longitudinal and transverse correlation functions, would require varying *both* the spatial and the temporal extent of the source.

Schematic calculations of correlation functions cut on $\psi = \mathrm{Cos}^{-1}(\mathbf{P} \cdot \mathbf{q} / |\mathbf{P}| \cdot |\mathbf{q}|)$ are shown in Figure 5.4. The source function is parametrized according to Equation 5.7, with the temperature parameter set to 8 MeV, the radius parameter set to 3.5 fm, and the total momentum of the pair kept between 250 and 350 MeV/c. The longitudinal cut is defined as ψ=0-50°. In the left- and right-hand panels, the transverse cut is defined as ψ=80-90° and ψ=60-90°, respectively. ψ-cut correlation functions for the cuts shown in the right-hand panels are sensitive to lifetime effects for $30 \lesssim \tau \lesssim 300$ fm/c [Gong 91a]. On the other hand, tighter ψ cuts for the transverse correlation function extend the sensitivity to larger lifetimes on the order of 1000 fm/c, raising the hope that ψ-cut correlation functions may be used to measure lifetimes from evaporative sources; see Chapter 7 for further discussion.

5.2 Constructing a Correlation Function for Model Predictions

As discussed above, two-proton correlation functions measure the space-time structure of emitting sources. However, the concept of a "source" is only a mental crutch used to characterize a typical emission pattern. Like physical reality, dynamical models produce individual collisions. The size and shape of proton emitting regions created in each collision depends on the impact parameter and the orientation of the reaction plane; event-by-event fluctuations

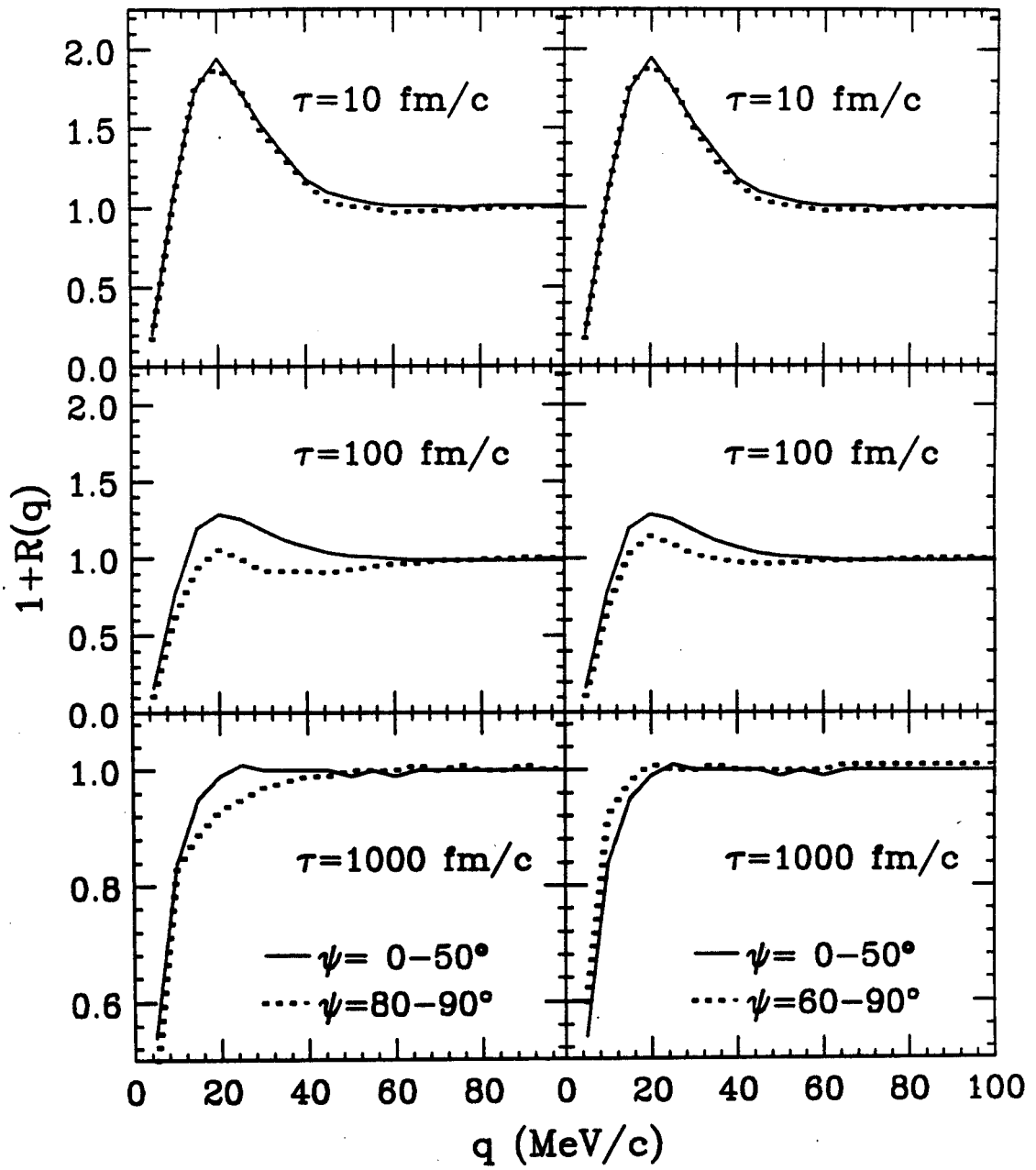

Figure 5.4. Longitudinal (solid lines) and transverse (dotted lines) correlation functions are shown for schematic sources of various lifetime parametrized according to Equation 5.7. Longitudinal cuts correspond to a range ψ=0-50°. In the left- and right-hand panels, transverse cuts correspond to ranges ψ=80-90° and ψ=60-90°, respectively. Details are discussed in the text.

produce variations on top of these dependencies. Therefore, a modified version of Equation 5.1 is used to test model predictions.

The model is used to generate a set of phase space points for different values of impact parameter and reaction plane orientation. We denote the set of phase space points as $(\mathbf{x},\mathbf{p})^{n}_{i\mathbf{b}}$, where $\mathbf{b}$ is the impact parameter vector. The event number n runs from 1 to $N_{\mathbf{b}}$, where $N_{\mathbf{b}}$ denotes the number of events with impact parameter vector $\mathbf{b}$. Finally, i is the particle number in the event (n,$\mathbf{b}$); i=1...$M_{n,\mathbf{b}}$, where $M_{n,\mathbf{b}}$ is the multiplicity of event (n,$\mathbf{b}$). Then, the correlation function is calculated as

$$1+R(q)=$$

$$C\frac{\sum_{\mathbf{b}}\frac{1}{N_{\mathbf{b}}}\sum_{n_1}^{N_{\mathbf{b}}}\sum_{n_2}^{N_{\mathbf{b}}}\sum_{i}^{M_{n_1\mathbf{b}}}\sum_{j}^{M_{n_2\mathbf{b}}}(1-\delta_{ij}\delta_{n_1n_2})\delta_{\Delta}(q-\frac{|p'^{n_1}_{i\mathbf{b}}-p'^{n_2}_{j\mathbf{b}}|}{2})\left|\Phi(x''^{n_1}_{i\mathbf{b}}-x''^{n_2}_{j\mathbf{b}};\frac{|p'^{n_1}_{i\mathbf{b}}-p'^{n_2}_{j\mathbf{b}}|}{2})\right|^2}{\sum_{\mathbf{b}_1}\sum_{\mathbf{b}_2}\sum_{n_1}^{N_{\mathbf{b}_1}}\sum_{n_2}^{N_{\mathbf{b}_2}}\sum_{i}^{M_{n_1\mathbf{b}_1}}\sum_{j}^{M_{n_2\mathbf{b}_2}}(1-\delta_{ij}\delta_{n_1n_2}\delta_{\mathbf{b}_1\mathbf{b}_2})\delta_{\Delta}(q-\frac{|p'^{n_1}_{i\mathbf{b}_1}-p'^{n_2}_{j\mathbf{b}_2}|}{2})} \qquad (5.8)$$

Here, the primed momenta are calculated in the center-of-momentum frame of the proton pair and the double-primed coordinates are calculated in the center-of-momentum frame of the pair at the time of emission of the second particle; Φ is the wavefunction of relative motion between the two protons; $\delta_{\Delta}(q)$ is the "binning function" which is unity for $|q| \le \frac{1}{2}\Delta$ and zero otherwise; C is a constant adjusted such that R(q) vanishes for large q.

In the numerator of Equation 5.8, the summation is "coherent" in impact parameter vector, while in the denominator an "incoherent" sum is performed. This is analogous to the experimental situation. If large ranges in impact parameter are sampled, this distinction between the two summations may lead to so-called "dynamical" correlations [Gong 91b]. Tight centrality cuts in the data

and theory reduce the effects of averaging over the magnitude of the impact parameter $|\mathbf{b}|$.

In principle, tight centrality cuts do not remove all dynamical correlations, since the denominator still averages over the orientation of the reaction plane. Since proton emission is rather isotropic with respect to the reaction plane [Wils 90, Wils 91, Tsan 91], such effects are probably negligible for proton-proton correlations. However, a recent study [Kämp 93] suggests that such effects may be important for correlations between heavy fragments, when larger flow effects exist.

The factor of $(1/N_{\mathbf{b}})$ in the numerator of Equation 5.8 simulates the impact parameter weighting of the experimental correlation function. In the Koonin-Pratt formalism, events with the same **b** are combined to generate the emission function, and then the final state interaction is applied. Therefore, there is a double sum in the numerator in Equation 5.8; this double sum causes the contribution for a given **b** to go as $N_{\mathbf{b}}^2$. The factor of $(1/N_{\mathbf{b}})$ accounts for the fact that in the data, the number of pairs contributing to the numerator for a given **b** is equal to the number of events with that **b**. The denominator needs no such correction factor, as the weighting from the double summation follows that found in the data.

Construction of correlation functions with the "equivalent" E_t technique (see Section 4.4.1) is performed by setting $N_{\mathbf{b}}$ proportional to $|\mathbf{b}|$, consistent with a geometric weighting of impact parameters. The sums in Equation 5.8 are then required to include only those events that have a total transverse energy which falls within the desired cut.

Construction of the correlation function according to the experimentally determined impact parameter distributions (see Section 4.4.2) is performed by

setting $N_{\mathbf{b}}$ proportional to the distributions $dP/d|\mathbf{b}|$ shown in the bottom panel of Figure 4.13.

5.3 Experimental Construction of the Correlation Function

For collisions at fixed impact parameter, the correlation function $1+R(\mathbf{P},\mathbf{q})$ is related to the single- and two-particle yields, $Y(\mathbf{p})$ and $Y(\mathbf{p}_1,\mathbf{p}_2)$ by

$$Y(\mathbf{P},\mathbf{q}) = Y(\mathbf{p}_1,\mathbf{p}_2) = C\cdot(1+R(\mathbf{P},\mathbf{q}))\cdot Y(\mathbf{p}_1)\cdot Y(\mathbf{p}_2) \qquad (5.9)$$

where $\mathbf{p}_1$ and $\mathbf{p}_2$ denote the momenta of the two detected particles, $\mathbf{P}=\mathbf{p}_1+\mathbf{p}_2$ is the total momentum of the proton pair, and $\mathbf{q}$ is the momentum of relative motion in the center of momentum frame of the proton pair. The constant C can be determined from the condition that $R(\mathbf{P},\mathbf{q})=0$ for sufficiently large relative momenta for which modifications of the two-particle phase-space density due to quantum statistics or final-state interactions become negligible.

Since the impact parameter of a subatomic collision cannot be measured with precision, experimental determinations of two-particle correlation functions involve averages over impact parameter. Furthermore, it is virtually impossible to collect sufficient statistics to allow the determination of the full six-dimensional dependence of the correlation function upon $\mathbf{P}$ and $\mathbf{q}$. Hence, implicit integrations are carried out in the constructions of experimental correlation functions. For example, experimental correlation functions are mostly defined according to the relation [Boal 90]:

$$\sum Y(\mathbf{p}_1,\mathbf{p}_2) = \tilde{C}\cdot(1+R(\zeta))\cdot\sum \overline{Y}(\mathbf{p}_1,\mathbf{p}_2) \qquad (5.10)$$

In Equation 5.10, $\overline{Y}(\mathbf{p}_1,\mathbf{p}_2)$ is the "background" yield, $\tilde{C}$ is a normalization constant which ensures proper normalization at large relative momenta, and ζ is the variable for which the explicit dependence of the correlation function is evaluated (the most common and traditional choice is $\zeta=q$). For each

experimental gating condition (representing implicit integrations over a number of variables), the sums on both sides of Equation 5.10 are extended over all energy and detector combinations corresponding to the given bins of ζ. The experimental correlation function is defined in terms of the ratio of these two sums. Comparisons with theoretical results must take this definition into account (see also the discussions of the previous Section and the appendix of [Gong 91b]).

Two different approaches are commonly used for the construction of the background yield. In one approach (referred to as the "singles technique"), the background yield is taken as proportional to the product of the single particle yields, measured with the same external trigger conditions as the true two-particle coincidence yield [Zarb 81, Lync 83, Chit 85, Poch 86, Kyan 86, Chit 86a, Chen 87a, Poch 87, Chen 87b, Awes 88, Gong 90b, Gong 90c, Kim 91, Gong 91b, Zhu 91, Gouj 91, Lisa 93a, Lisa 93b, Lisa 93c, Lisa 93d]

$$\overline{Y}(\mathbf{p}_1,\mathbf{p}_2) \sim Y(\mathbf{p}_1)\cdot Y(\mathbf{p}_2). \tag{5.11}$$

In the other approach (referred to as the "event-mixing technique"), the background yield is generated by mixing particle yields from different coincidence events [Kopy 74, Zajc 84, Gust 84, Dupi 88, Fox 88, DeYo 89, Cebr 89, Rebr 90, DeYo 90, Rebr 92]

$$\overline{Y}(\mathbf{p}_1,\mathbf{p}_2) \sim \sum_{n\neq m}\left\{\delta^3(\mathbf{p}_1-\mathbf{p}_{1,n})\cdot\delta^3(\mathbf{p}_2-\mathbf{p}_{2,m})+\delta^3(\mathbf{p}_2-\mathbf{p}_{1,n})\cdot\delta^3(\mathbf{p}_1-\mathbf{p}_{2,m})\right\}. \tag{5.12}$$

Here, the indices n and m label the n-th and m-th recorded two-particle coincidence events, while $\mathbf{p}_{1,n}$ and $\mathbf{p}_{2,m}$ denote the momenta of particles 1 and 2 recorded in events n and m, respectively. In most analyses, the index n runs over all recorded coincidence events and the index m is varied according to m=n+k, with typically $0<k<1000$.

The main advantage of the event-mixing technique is its simplicity, as no singles measurements are necessary. In some situations, single- and two-particle data could represent different averages of impact parameter. In such cases, the use of the singles technique could lead to serious distortions of the correlation function [Rebr 90] which could complicate comparisons with theoretical predictions. Furthermore, less interesting correlations, resulting for example from phase space constraints due to conservation laws [Knol 80, Lync 82, Lync 83, Tsan 84, Chit 86b, Baue 87, Baue 88], may be suppressed by using the event-mixing technique. However, the event-mixing technique also attenuates the very correlations one wishes to measure [Zajc 84]. The degree of attenuation depends on the phase space acceptance of the experimental apparatus and on the magnitude of the correlations. Quantitative analyses require careful Monte-Carlo simulations. For the extraction of undistorted correlation functions, iterative procedures have been developed [Zajc 84] (for an excellent discussion, see Appendix B of [Mors 90]).

For statistical emission processes in which the emission of a single particle has negligible effect on further emissions, single and two-particle yields should originate from similar regions of impact parameter. In such instances, the singles technique appears to be the preferential choice since it avoids the attenuation of the very correlations one wishes to measure. There are, however, scenarios where the singles technique may become inappropriate. For example, emission to extreme forward angles may have large contributions from breakup reactions in which only one particle is emitted [Rebr 90]. In such instances, single and two-particle detection will select different classes of collisions.

Two-proton correlations generated with the singles technique display a strong dependence on the total energy (or momentum) of the emitted particle pairs [Lync 83, Chen 87c, Poch 86, Poch 87, Awes 88, Gong 90b, Gong 90c, Gong

91b]. In a recent paper [Rebr 90] the issue was raised that this dependence might be an artifact of the singles technique employed for the construction of the experimental correlation function. We address this question and give a quantitative comparison of two-proton correlation functions constructed by the two techniques. For this purpose, we have re-analyzed the high-statistics data of [Gong 90c] and [Gong 91b] taken for the $^{14}N+^{27}Al$ reaction at E/A=75 MeV.

In our event-mixing analysis, we have first projected out "pseudo-singles" spectra from the two-proton yields:

$$\hat{Y}(\mathbf{p}) = \sum_{i,n} \delta^3(\mathbf{p} - \mathbf{p}_{i,n}), \tag{5.13}$$

where $\mathbf{p}_{i,n}$ is the momentum of the i-th proton (i=1,2) detected in the n-th two-proton coincidence event. These pseudo-singles yields were then inserted into Equation 5.11 to generate the background yield. This procedure is equivalent to summing Equation 5.12 over all indices n and (n+m), thus also allowing a contamination of contributions from true coincidences (m=0). In our analysis, this contamination is entirely negligible ($<10^{-6}$). The background constructed via Equations 5.11 and 5.13 provides the maximum statistical accuracy which can be obtained with the event-mixing technique.

Useful insight can be gleaned by comparing true singles and pseudo singles yields. In Figure 5.5, energy spectra are compared for three representative regions of angle covered by the experimental apparatus of [Gong 90c] and [Gong 91b]. In Figure 5.6, angular distributions are compared for three different energy intervals. Clearly, singles and pseudo-singles yields are very similar.

Figure 5.7 gives a comparison of two-proton correlation functions constructed with the two techniques, using the same momentum gates as

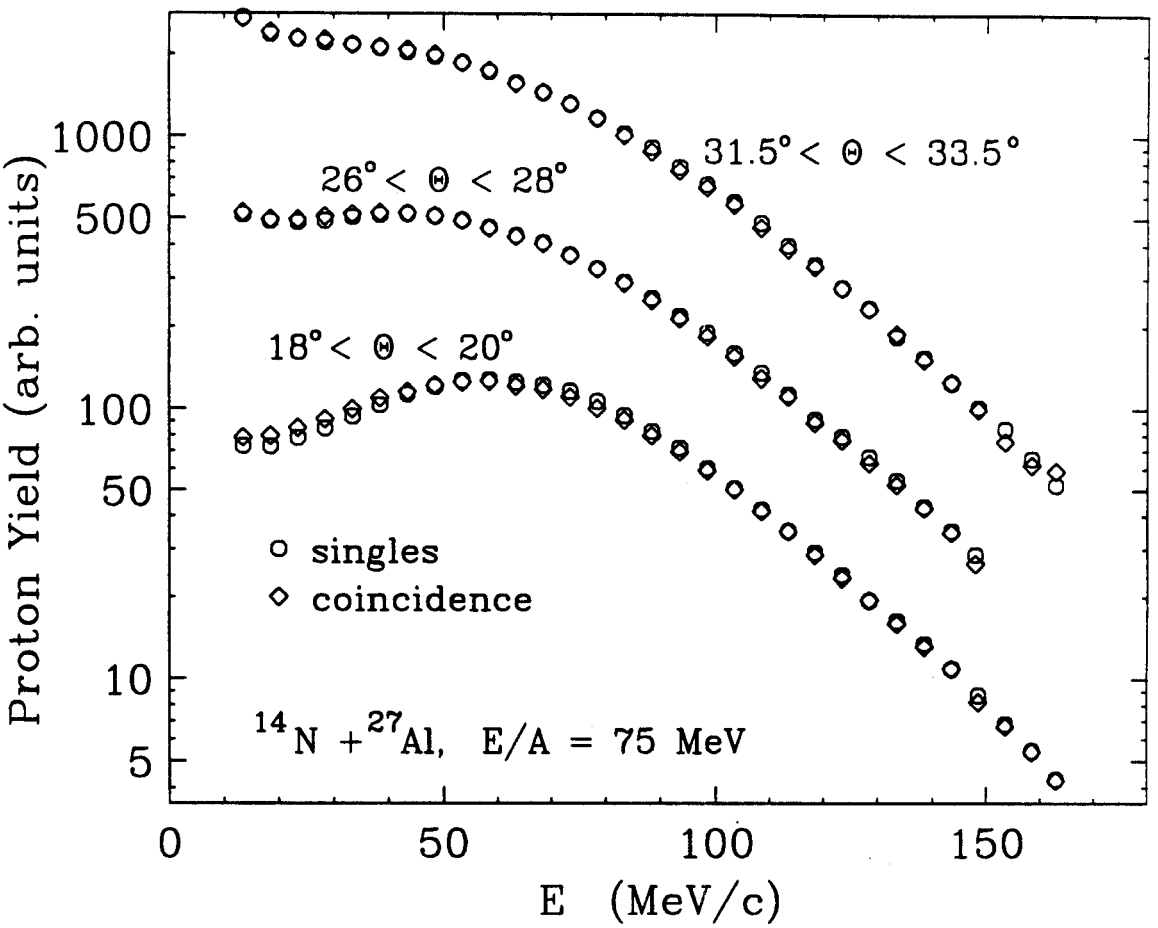

Figure 5.5. Comparison of singles (circles) and pseudo-singles (diamonds) energy spectra measured in [Gong 90c, Gong 91b] for the $^{14}N+^{27}Al$ reaction at E/A=75 MeV. Statistical errors are smaller than the size of the symbols.

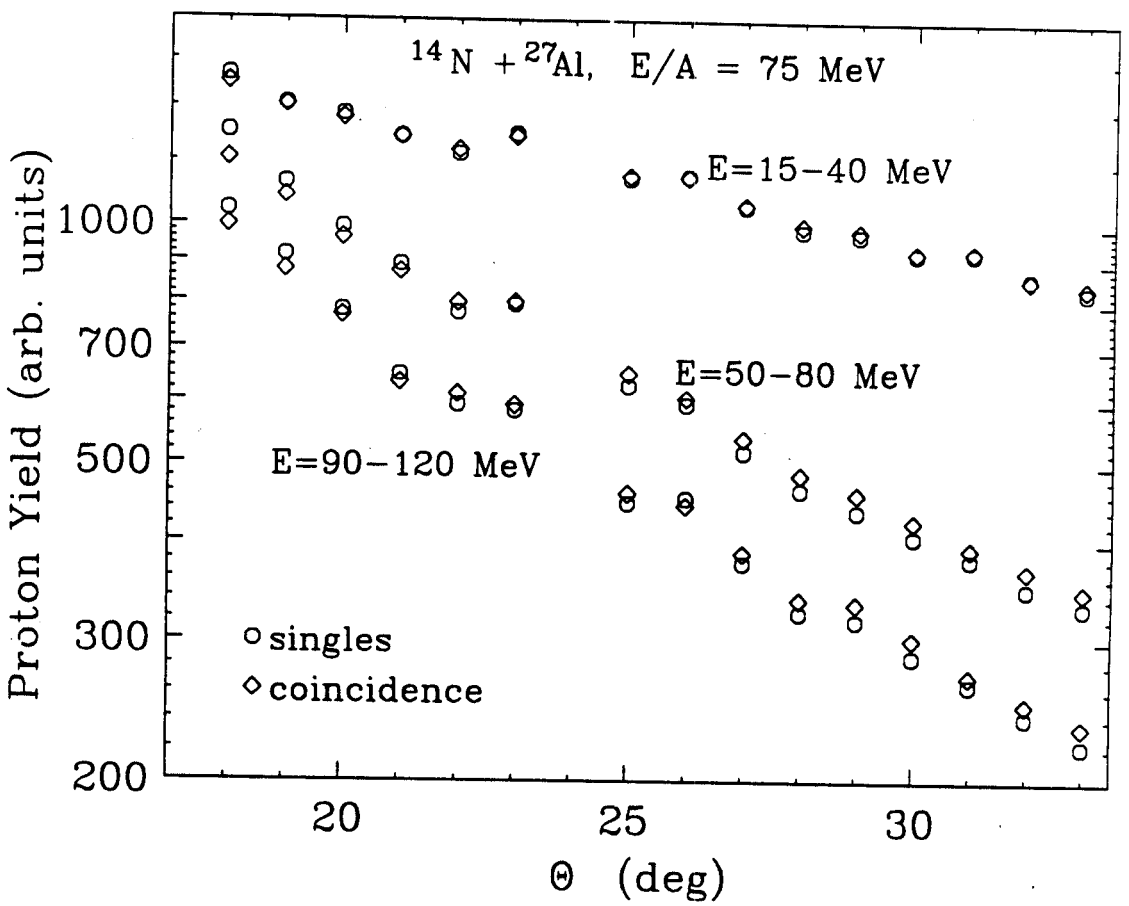

Figure 5.6. Comparisons of singles (circles) and pseudo-singles (diamonds) angular distributions measured in [Gong 90c, Gong 91b] for the ^{14}N+^{27}Al reaction at E/A=75 MeV. Statistical errors are smaller than the size of the symbols.

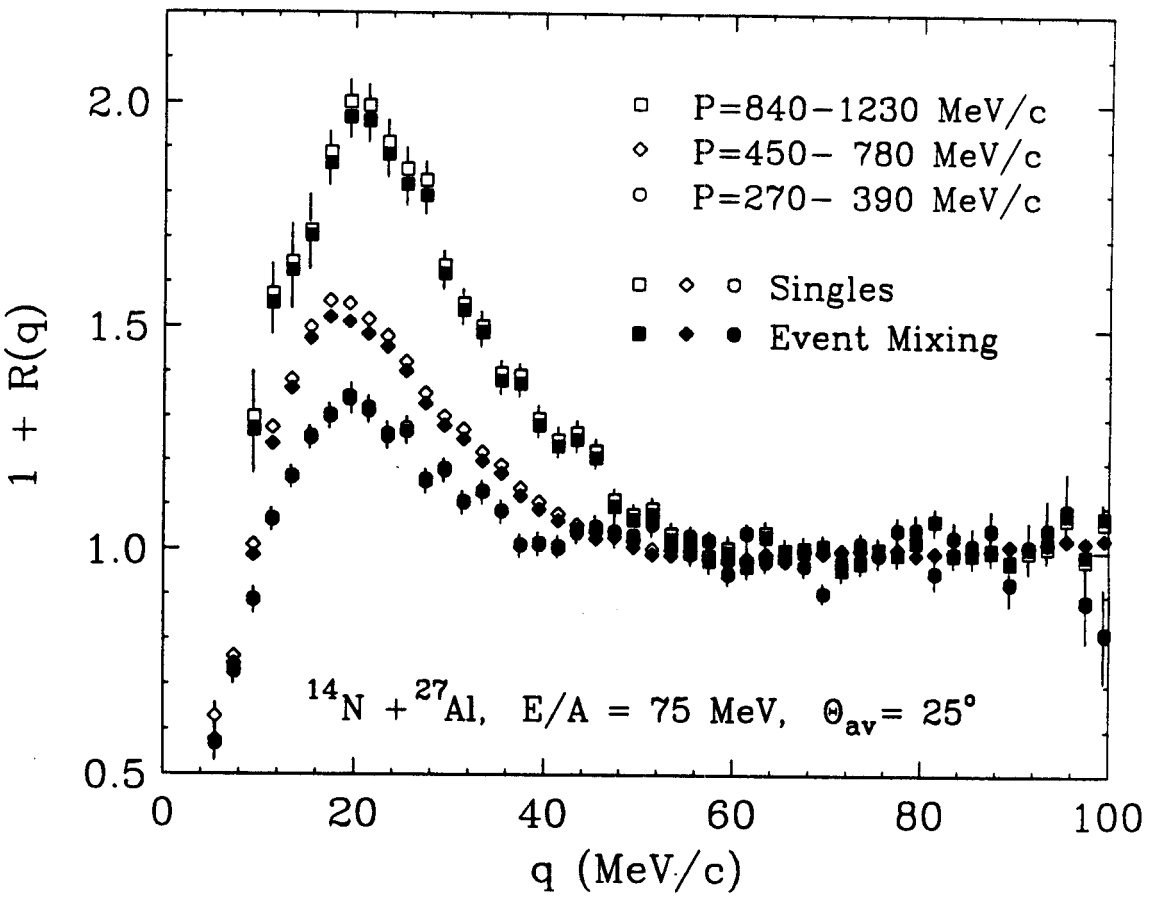

Figure 5.7. Two-proton correlation functions measured [Gong 90c] [Gong 91b] for the $^{14}N+^{27}Al$ reaction at E/A=75 MeV. Open and solid symbols represent correlation functions constructed by the singles and event-mixing techniques, respectively. Momentum cuts are indicated in the figure. Statistical errors (larger than the size of the data points) are shown only for open points. Solid points have errors of same magnitude.

displayed in Figure 14 of [Gong 91b]. Very similar results are obtained by the two techniques. In particular, both techniques give very similar momentum dependencies of the two-proton correlation functions. As expected, the event-mixing technique gives correlation functions which are slightly attenuated in comparison with the singles technique. The differences are small (typically smaller than 5%) and only of marginal statistical significance.

We also explored whether the results were stable with respect to the number of detectors employed in the experiment. In Figure 5.8, we show energy-integrated two-proton correlation functions from data in which the entire hodoscope (top panel), only 23 detectors (center panel), and only 7 detectors (bottom panel) were incorporated into the analysis. (Integration over all outgoing particle energies was performed to ensure good statistical accuracy for the analysis employing only 7 detectors.) Again, the two techniques give rather similar results. Here again, however, correlation functions obtained with the event-mixing technique are slightly attenuated as compared to those constructed with the singles technique, reflecting the presence of "residual" correlations in the background yields constructed from event-mixing analyses [Zajc 84].

In conclusion, the momentum (or energy) dependence of two-proton correlation functions reported in references [Gong 90c] [Gong 91b] can be considered as firmly established. A re-analysis of the data in terms of a background constructed by event-mixing gives correlation functions which are very similar (though slightly attenuated) to those published previously.

Differences between correlation functions constructed via the two techniques must be checked on a case-by-case basis. In our analysis of $^{36}Ar+^{45}Sc$ at E/A=80 MeV, the hodoscope was positioned at 38° in the laboratory. As we discussed in Chapter 4, the region of centrality selected by measuring one proton

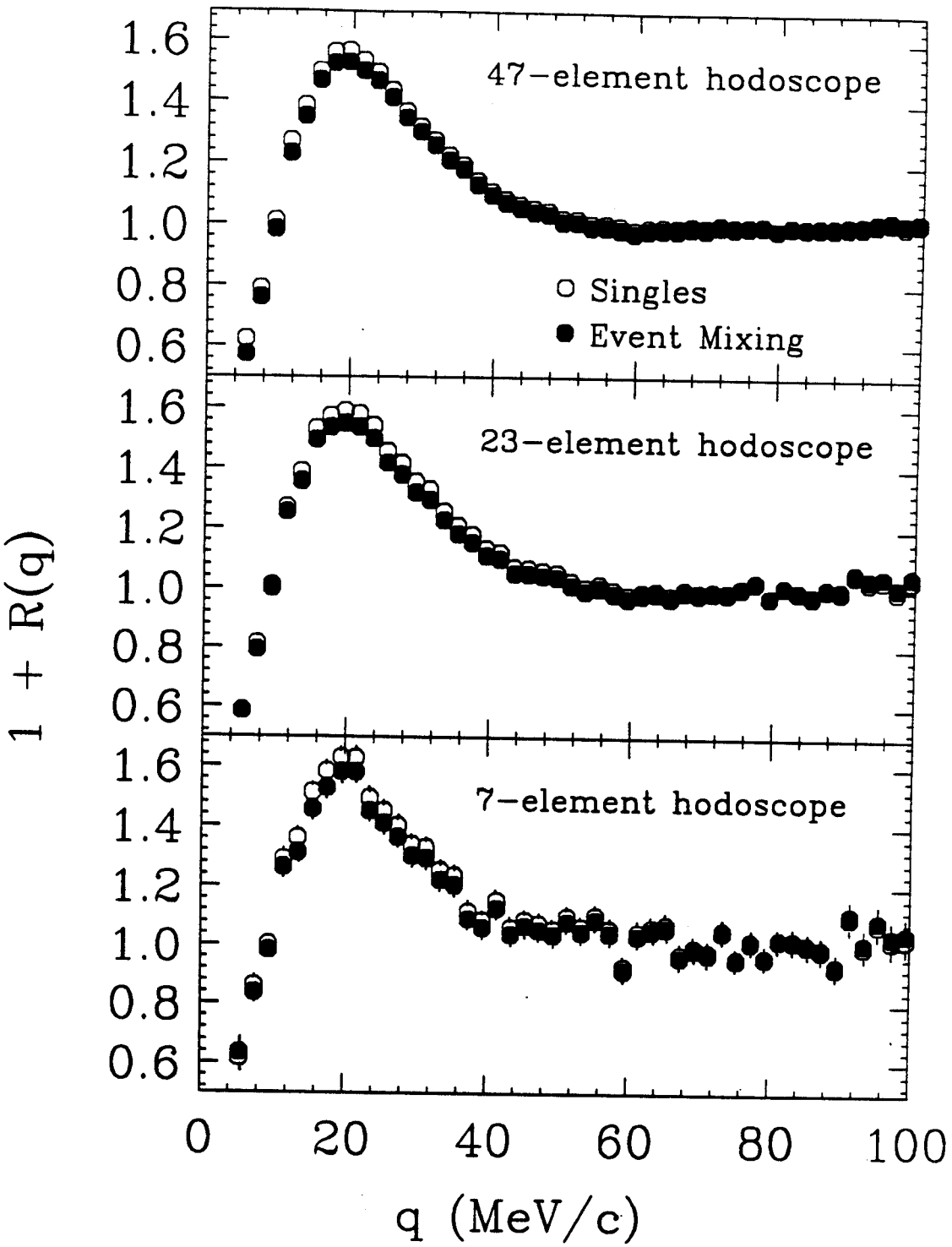

Figure 5.8. Energy-integrated two-proton correlation functions measured [Gong90c] [Gong 91b] for the $^{14}N+^{27}Al$ reaction at E/A=75 MeV. Open and solid symbols represent correlation functions constructed by the singles and event-mixing techniques, respectively. Top, center, and bottom panels represent correlation functions extracted from arrays consisting of 47, 23, and 7 detectors, respectively.

in the hodoscope is very similar to that selected by measuring two. Therefore, as expected, the correlation functions were largely insensitive to the technique used.

In Chapter 7, we re-analyze the data of [Gong 90b] and [Gong 91b] for the reaction $^{129}Xe+^{27}Al$ at E/A=31 MeV. This reverse kinematics system was viewed at 25° in the laboratory frame, where contributions from projectile decay and from fusion residues exist. Therefore, it is somewhat more likely that one- and two-particle events in the hodoscope represent different regions of centrality. Correlation functions constructed with the singles technique differ from those constructed according to the event-mixing technique. The degree to which the event-mixing technique attenuates interesting correlations is proportional to the strength of the correlations. For this system, the correlations are very weak. Therefore, a difference between correlation functions constructed via the singles and event-mixing techniques is attributed to different event class selection, and we use the event-mixing method in our analysis.

5.4 Effects of Finite Resolution

The ability of the correlation function to extract relatively small effects from a large background rests firmly on its insensitivity to single-body phase space and detector acceptance effects. However, experimental uncertainties in the determination of the binning variable (usually the relative momentum) will distort the measured correlation function. Here, we briefly discuss how to account for this effect in calculated correlations, for the hodoscope set-up used in our experiment. We find that finite resolution effects are of minor importance for this case.

It is useful to distinguish the *granularity* of the detector system from the *resolution*. A hodoscope with finite granularity and perfect resolution would consist of infinitesimally small perfect detector elements with a finite spacing between them. In realistic detector systems, finite solid angle coverage and

energy uncertainty lead to nonperfect resolution; **q** is not measured perfectly. The correlation function itself is robust with respect to nonideal granularity, since this is basically a single-particle phase space effect. However, the *degree to which* the finite resolution of the detector distorts the correlation function depends on the granularity. Therefore, calculations which quantify effects of finite resolution should also account for detector granularity.

In Figure 5.9, we show the results of a Monte-Carlo calculation of the resolution of the 56-element hodoscope for four representative cuts in P and $\psi_{lab} = \mathrm{Cos}^{-1}(\mathbf{P}_{lab} \cdot \mathbf{q} / |\mathbf{P}_{lab}| \cdot |\mathbf{q}|)$. Diamonds and circles, respectively, indicate the first and second moments of the quantity $\delta q = q_{real} - q_{meas}$, where q_{real} represents the "true" relative momentum between a pair of protons, and q_{meas} is the relative momentum that the device measures, including all effects of finite granularity and angular and energy resolution. The measured momentum spectrum was averaged over for proper weighting.

The value of the second moment ($\Delta_2 q = (\langle (q_{real} - q_{meas})^2 \rangle)^{0.5}$) indicates the magnitude of resolution effects. Its value is mostly independent of q, but depends on the cut in P and ψ_{lab}. The q-resolution of the hodoscope is dominated by finite solid angle effects (even changing the energy resolution from 1% to 5% does not drastically alter Figure 5.9). Therefore, the resolution for proton pairs for which the relative momentum is parallel to the face of the hodoscope ($\psi_{lab} \approx 90°$) is worse than for those pair whose individual momenta $\mathbf{p}_1$ and $\mathbf{p}_2$ are almost parallel ($\psi_{lab} \approx 0°$). Also, precise measurement of q for more energetic proton pairs (high total momentum P) is more difficult than for less energetic pairs, since a small change in the direction of $\mathbf{p}_1$ or $\mathbf{p}_2$ leads to larger changes in q. In all cases, the resolution is never worse than ±2.5 MeV/c, and, as we see below, is only important for the correlation function at very low q.

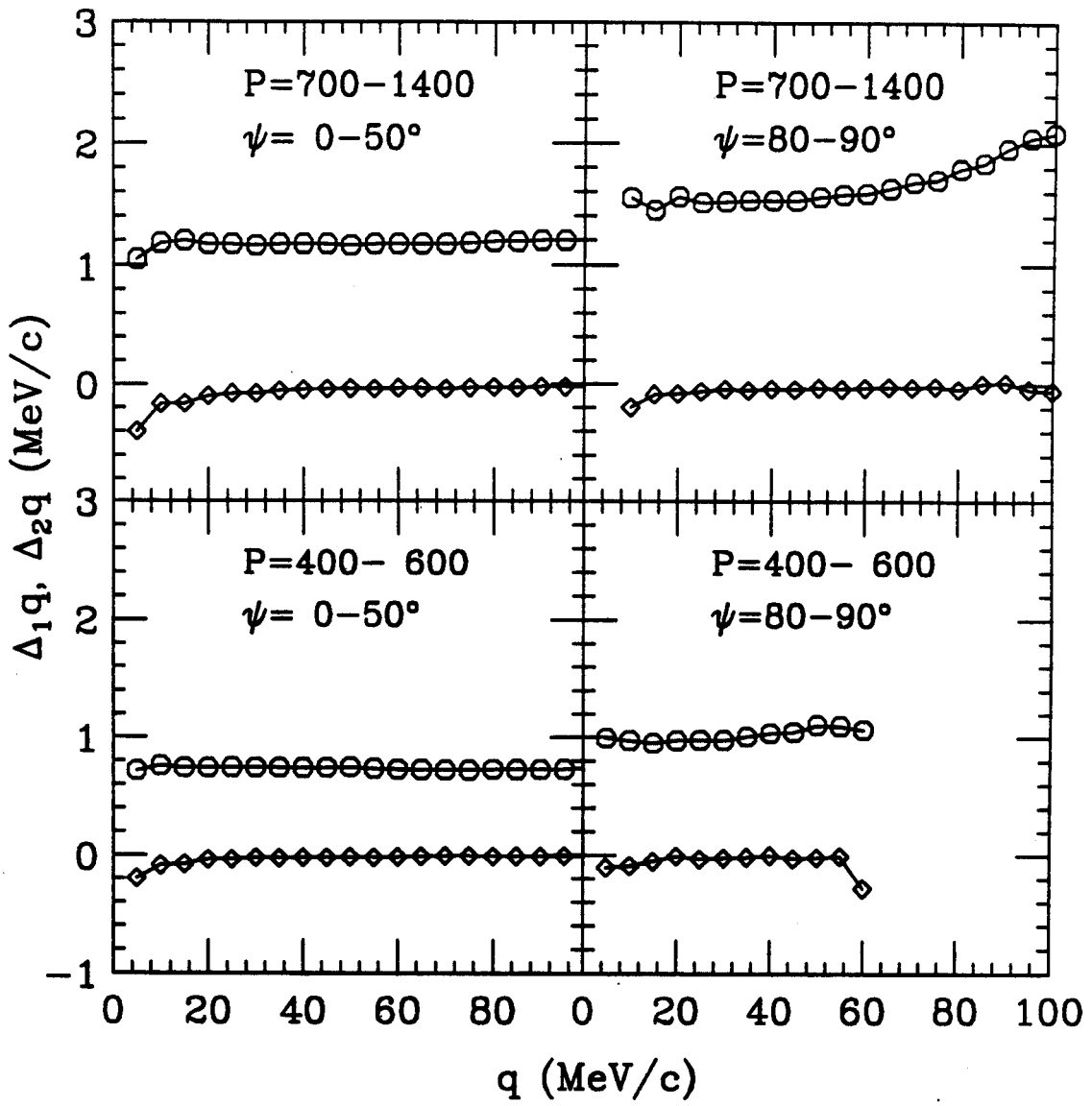

Figure 5.9. The first and second moments of the distribution (q_{real}-q_{meas}) are shown as a function of q_{meas} for representative cuts on P and ψ. Finite resolution effects are quantified by the second moment (indicated by the diamonds), while the first moment (indicated by circles) shows a very small systematic distortion of the value of q. Details are discussed in the text. The distribution for low momentum pairs with q transverse to P stops at q≈60 MeV/c due to the finite solid angular coverage of the hodoscope.

The distributions for the first moment of the distribution ($\Delta_1 q = \langle q_{real} - q_{meas} \rangle$) deserve a comment. Naïvely, we might expect that this quantity should vanish for all q, within statistics. However, $\Delta_1 q$ is slightly smaller than zero for all cuts, especially at low q. This is basically a result of phase space considerations: if $\mathbf{y}=\mathbf{x}+\delta$, where δ is a small random vector, then, on average, $|\mathbf{y}| > |\mathbf{x}|$. Therefore, in addition to the finite precision with which we measure q, finite resolution effects also introduce a systematic distortion of the value of q. This small distortion is significant only for very small values of q, and is well within the overall uncertainty.

Next, we construct correlation functions corresponding to emission from a schematic source function to determine the importance of the finite resolution.

Since resolution effects can depend on the shapes of the singles energy spectra, we parametrize the source function according to

$$g(\mathbf{r},t,\mathbf{p}) \sim e^{-(|\mathbf{r}|/r_0)^2} \cdot e^{-t/\tau} \cdot Y(\mathbf{p}), \tag{5.14}$$

where $Y(\mathbf{p})$ represents the experimentally-determined proton momentum yield. In the data analysis, we assume that the proton hits the center of the detector, and we store the energy spectra with a certain binning width (typically 25 keV). These effects are retained in the $Y(\mathbf{p})$ that enters into Equation 5.14, implicitly accounting for the granularity of the detector.

A set of phase space points $(\mathbf{x},\mathbf{p})_i$ was generated by Monte-Carlo sampling $g(\mathbf{r},t,\mathbf{p})$, and correlation functions were calculated according to a simplified (because we have no impact parameter averaging to deal with) version of Equation 5.8:

$$1+R(q,P,\psi) = \frac{\sum_i \sum_{j \neq i} \delta_{\Delta q} \cdot \delta_{\Delta P} \cdot \delta_{\Delta \psi} \cdot \left| \phi\left(\mathbf{x}_i'' - \mathbf{x}_j''; \frac{|\tilde{\mathbf{p}}_i' - \tilde{\mathbf{p}}_j'|}{2}\right) \right|^2}{\sum_i \sum_{j \neq i} \delta_{\Delta q} \cdot \delta_{\Delta P} \cdot \delta_{\Delta \psi}}. \tag{5.15}$$

Here, $\delta_{\Delta q}$, $\delta_{\Delta P}$, and $\delta_{\Delta \psi}$ are binning functions similar to the function $\delta_{\Delta}(q)$ used in Equation 5.8. As in Equation 5.8, double primes indicate that the spatial separation is calculated at the time of emission of the second proton, and single primes indicate that the relative momentum is calculated in the center of momentum system of the proton pair. Finite resolution effects are accounted for by evaluating the squared wavefunction at $\left|\tilde{\mathbf{p}}_i' - \tilde{\mathbf{p}}_j'\right| / 2$, where $\tilde{\mathbf{p}}$ is the proton momentum after being smeared by detector resolution. So we *bin* the correlation variable according to the binned momenta $\mathbf{p}_i$, but we *weight* the numerator and denominator according to the smeared (or "true") momenta $\tilde{\mathbf{p}}_i$.

Our smearing procedure uses a Gaussian distribution in energy to simulate energy resolution and assumes a uniform hit density over the face of the detector to account for the finite solid angle coverage of each detector element. (This assumes that the angular distribution is flat over the angular range covered by a detector element– a good approximation for our small detectors.) Figures 5.10 and 5.11 show the hit pattern obtained by smearing the energy spectra measured by us (^{36}Ar+^{45}Sc, E/A=80 MeV) and from [Gong 91b] (^{129}Xe+^{27}Al, E/A=31 MeV) with our smearing routine.

Figures 5.12 and 5.13 show the calculated correlation functions for representative cuts in P and ψ_{lab}. Correlation functions calculated with Equation 5.15 with the smearing turned "off" ($\tilde{\mathbf{p}}$=$\mathbf{p}$) represent the undistorted correlations (lines), while those calculated with the smeared momenta (symbols) show the distortion effects of finite resolution. As expected and reported previously [Gong 91b], finite resolution effects are only important for the lowest q-bins; the important peak region (q≈10-40 MeV/c) is relatively free of such effects. Furthermore, as expected from Figure 5.9, the effects are somewhat more pronounced for correlations cut on high total momentum of the pair P.

As a final note to this section, we point out that we have constructed longitudinal and transverse correlation functions with cuts on the relative angle ψ between **P** and **q** as defined in the lab frame. Since **P**, as defined in the lab frame, is normal to the hodoscope face, the relative momentum for pairs contributing to the transverse correlation functions suffer maximum resolution effects due to finite angular resolution. As we discuss in Chapter 7, it is often more appropriate to cut on ψ as defined in a different frame. In such a case, the effect of finite angular resolution will be more equitably distributed among the longitudinal and transverse correlation functions, since **q** will not always be parallel to the hodoscope face for any given ψ-cut. This is illustrated in Figure 5.14, where we show the effects of finite resolution on the correlation function corresponding to a *moving* source (v_{source}=0.18 c) of radius 3 fm and negligible lifetime. The cut on the total momentum of the proton pair as calculated in the laboratory is idendical to that used in Figure 5.13.

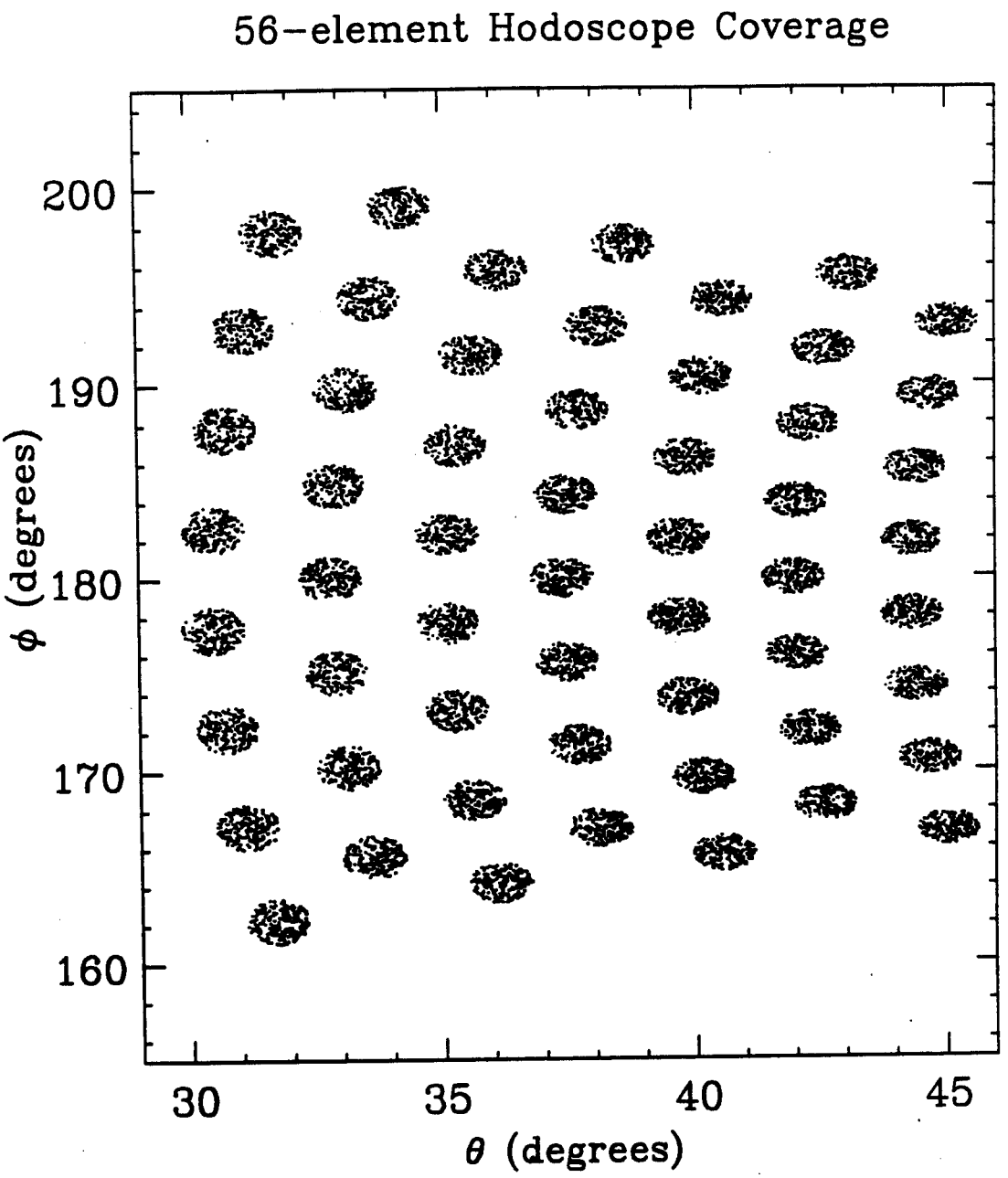

Figure 5.10. A uniform hit pattern over the faces of the detector elements of the 56-element hodoscope was used to quantify finite resolution effects on the correlation function for the $^{36}Ar+^{45}Sc$ measurement.

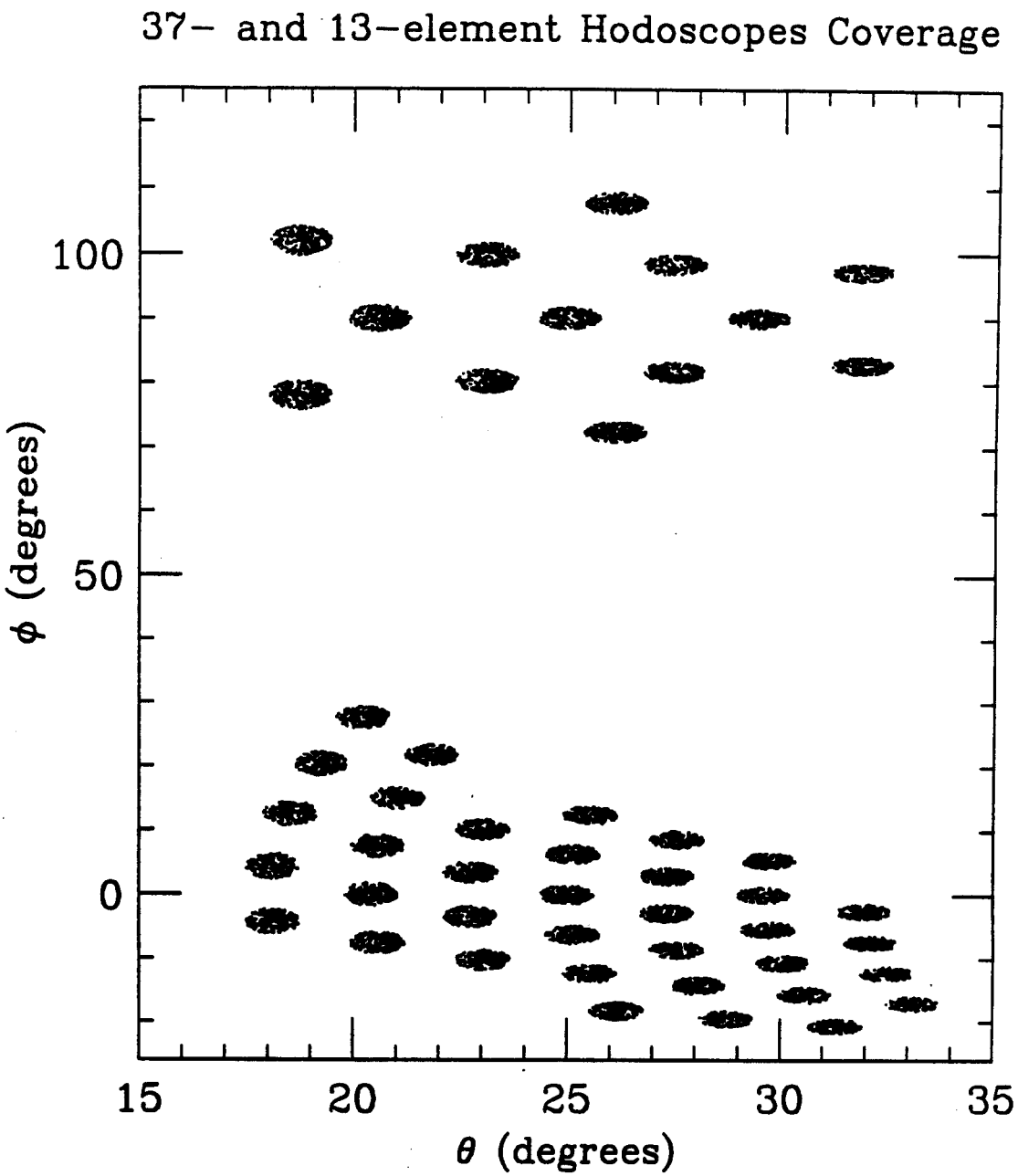

Figure 5.11. A uniform hit pattern over the faces of the detector elements of the (incomplete) 56-element hodoscope and 13-element hodoscope was used to quantify finite resolution effects on the correlation function for the $^{14}N+^{27}Al$ and $^{129}Xe+^{27}Al$ measurements.

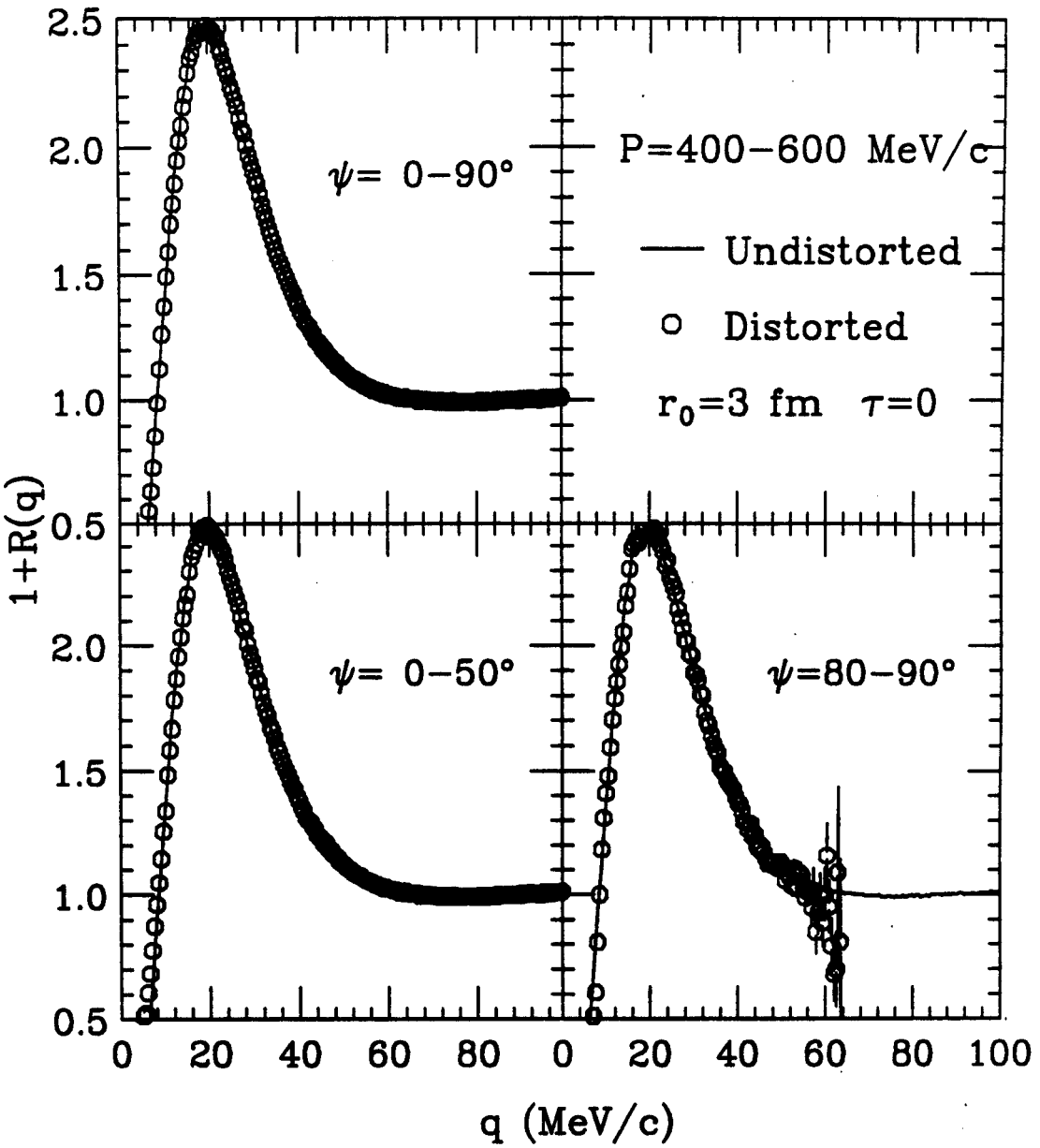

Figure 5.12. Calculated correlation functions for P=400-600 MeV/c. Longitudinal and transverse correlation functions are defined in the laboratory rest frame. Solid lines indicate the "true" or undistorted correlation functions, while symbols indicate the correlation function after accounting for the resolution of the 56-element hodoscope.

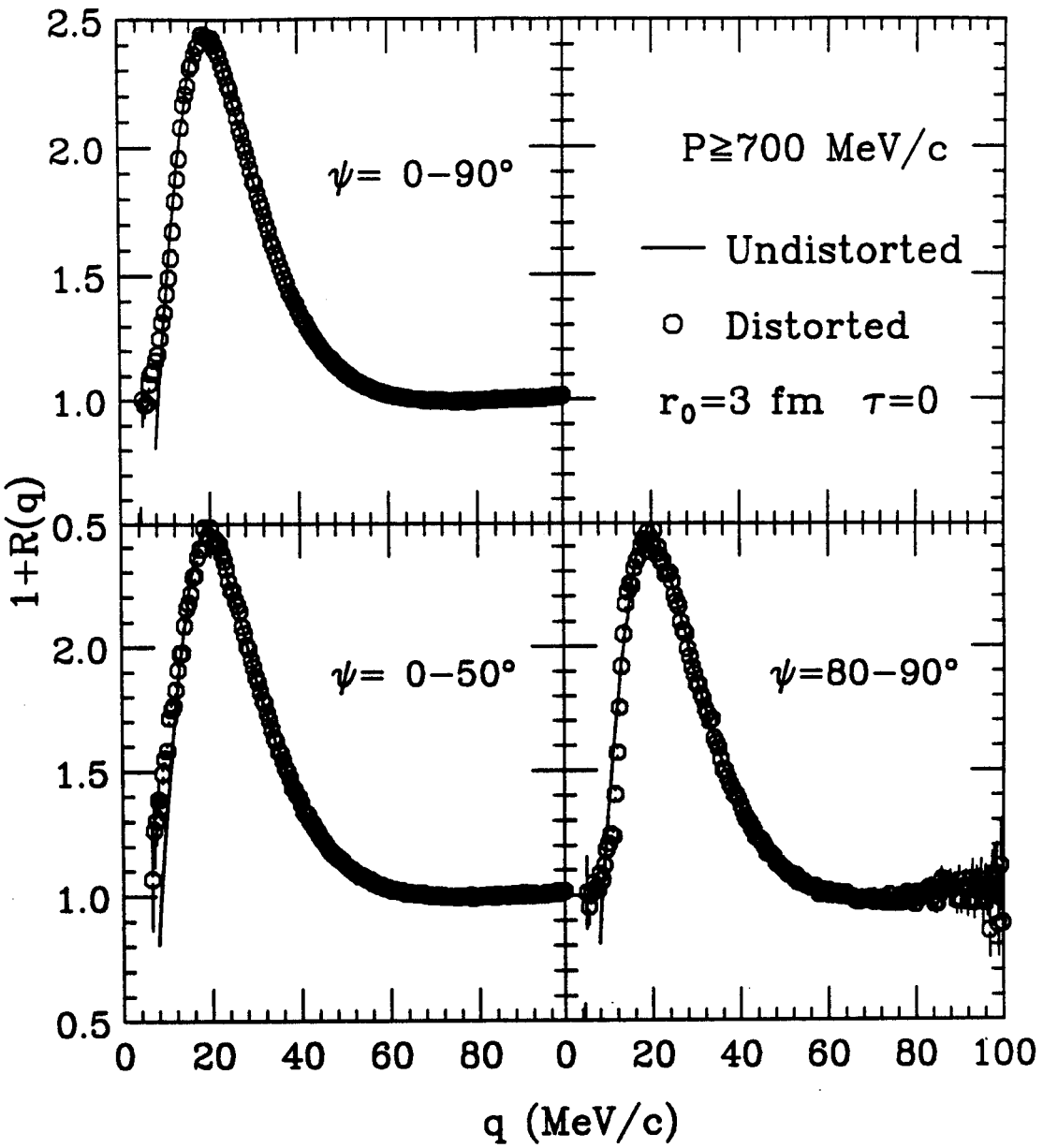

Figure 5.13. Calculated correlation functions for P≥ 700 MeV/c. Longitudinal and transverse correlation functions are defined in the laboratory rest frame. Solid lines indicate the "true" or undistorted correlation functions, while symbols indicate the correlation function after accounting for the resolution of the 56-element hodoscope.

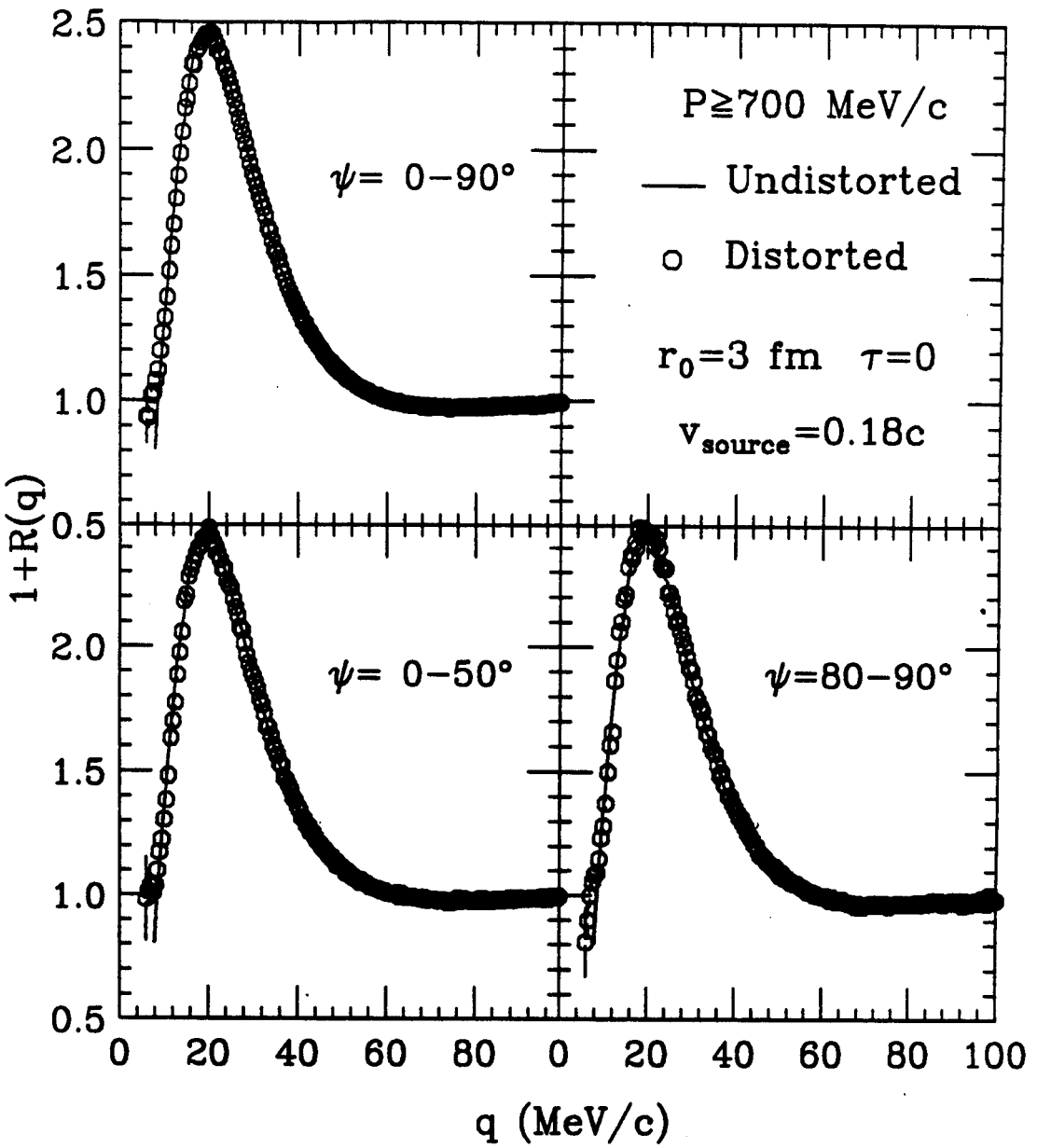

Figure 5.14. Calculated correlation functions for P≥ 700 MeV/c. Longitudinal and transverse correlation functions are defined in a frame moving with β=0.18 in the laboratory. Solid lines indicate the "true" or undistorted correlation functions, while symbols indicate the correlation function after accounting for the resolution of the 56-element hodoscope.

Chapter 6 - Centrality-Cut Proton Data for $^{36}Ar+^{45}Sc$ at E/A=80 MeV; Comparison to BUU

Two proton correlation functions provide a sensitive probe of the space-time extent of the emitting source created in a nuclear collision. The dependence of the correlation function on the total momentum of the pair ($P=|\mathbf{p}_1+\mathbf{p}_2|$) provides valuable information on the evolution of the reaction zone, and may be a method to determine emission and expansion time scales [Boal 86a, Boal 86b, Prat 87, Boal 90, Gong 91a, Baue 92]. Previous measurements of two-proton correlation functions have found stronger correlations at $q\approx 20$ MeV/c for more energetic protons [Lync 83, Poch 86, Chen 87a, Chen 87b, Poch 87, Awes 88, Gong 90, Gong 91b, Zhu 91, Lisa 91, Hong 92], indicating that energetic protons are emitted from smaller sources and/or with shorter characteristic timescales than less energetic protons.

In previous studies [Gong 91a, Baue 92, Zhu 91, Gong 90c, Gong 91b], two-proton correlation functions predicted by the Boltzmann-Uehling-Uhlenbeck (BUU) transport model were seen to be in good agreement with the total momentum dependence observed in the data. In these comparisons of measured and predicted P-dependencies of the correlations, the data were taken without explicit impact parameter selection, and BUU events were weighted geometrically according to impact parameter and filtered through the detector acceptance.

However, BUU calculations of the total momentum dependence of the correlation function show drastically different behavior for central and

peripheral collisions [Gong 91a, Baue 92]. Comparison of these calculations to impact parameter selected data represents a stringent test of the theory and would be interesting.

In this chapter, we present proton data selected by impact parameter filters. We see that differences in the reaction zone evolution for central and peripheral events do not express themselves in the single-proton energy spectra. However, two-proton correlations reveal underlying differences in the source geometry. We present the first study of the total momentum dependence of the two-proton correlation function for different regions of centrality and the first experimental test of the reaction zone evolution predicted by the BUU for impact parameter-selected events. Such a double cut on the data requires higher coincidence statistics than previously available; it provides unique information about reaction zone dynamics in central and peripheral collisions.

6.1 Singles Energy Spectra

Singles proton energy spectra measured in the hodoscope and gated on the centrality conditions defined in Figures 4.13 and 4.14 are shown in Figure 6.1. Filled and open symbols indicate the energy spectra for central and peripheral events, respectively, at the extreme polar angles covered by the hodoscope. The normalization is independent of the polar angle. Clearly, no large difference between central and peripheral events is evident from the singles spectra.

In Figure 6.2, energy spectra predicted by the BUU is compared with the data. BUU events were centrality-selected according to the true reduced impact parameter method (see Section 4.4.2). The relative normalization was chosen to give equal areas for the distributions at θ=30-32° in the region $E_{proton} \geq 50$ MeV. In agreement with the data, no large difference is seen in the singles spectra for the centrality cuts used.

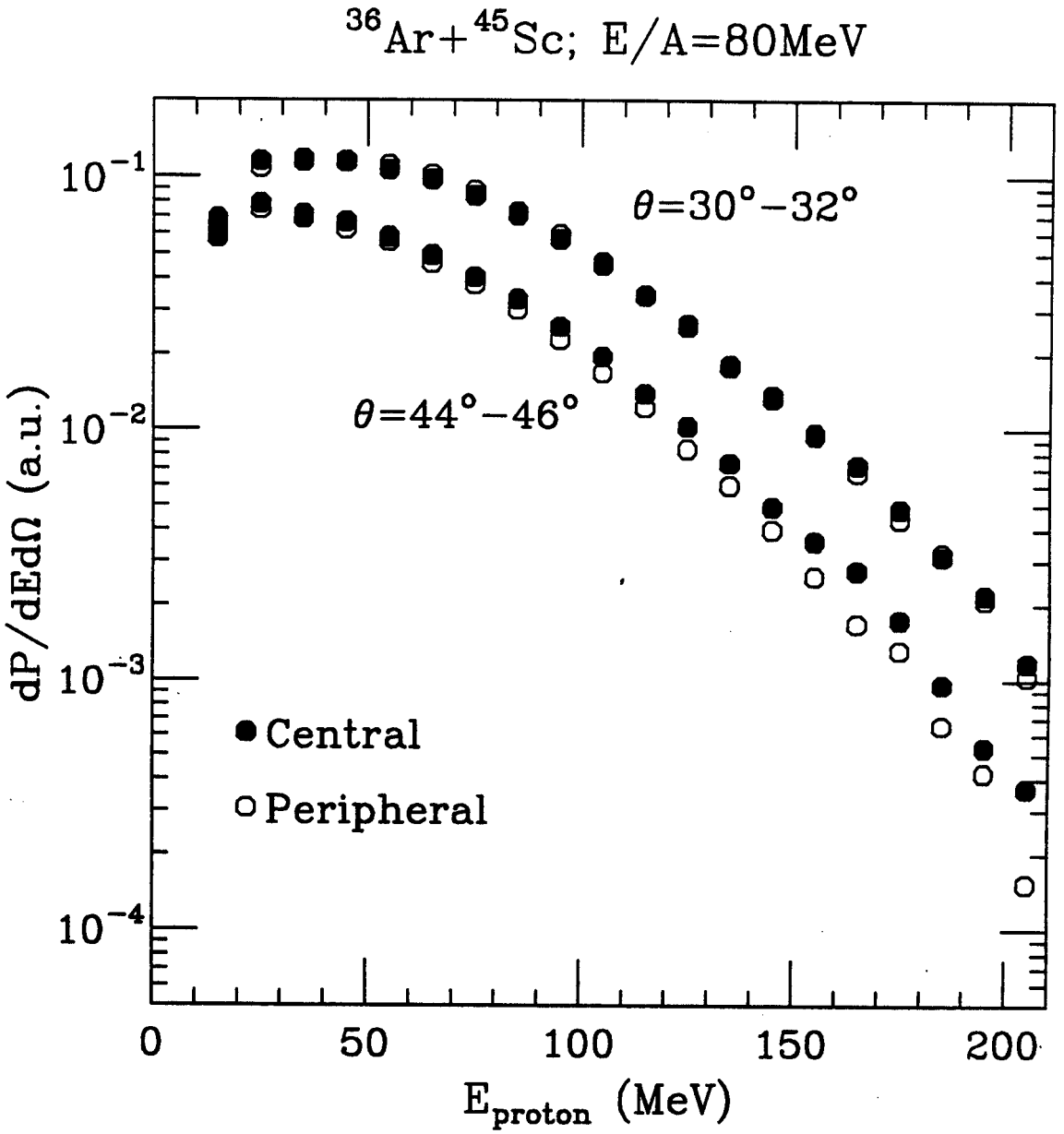

Figure 6.1. Centrality-cut proton energy spectra measured with a singles trigger at two extreme polar angles in the 56-element hodoscope. Spectra for protons emitted from central events (as determined by the total transverse energy measured in the event. See Figures 4.13 and 4.14.) are shown as solid symbols. Spectra corresponding to protons emitted from peripheral events are represented as open symbols.

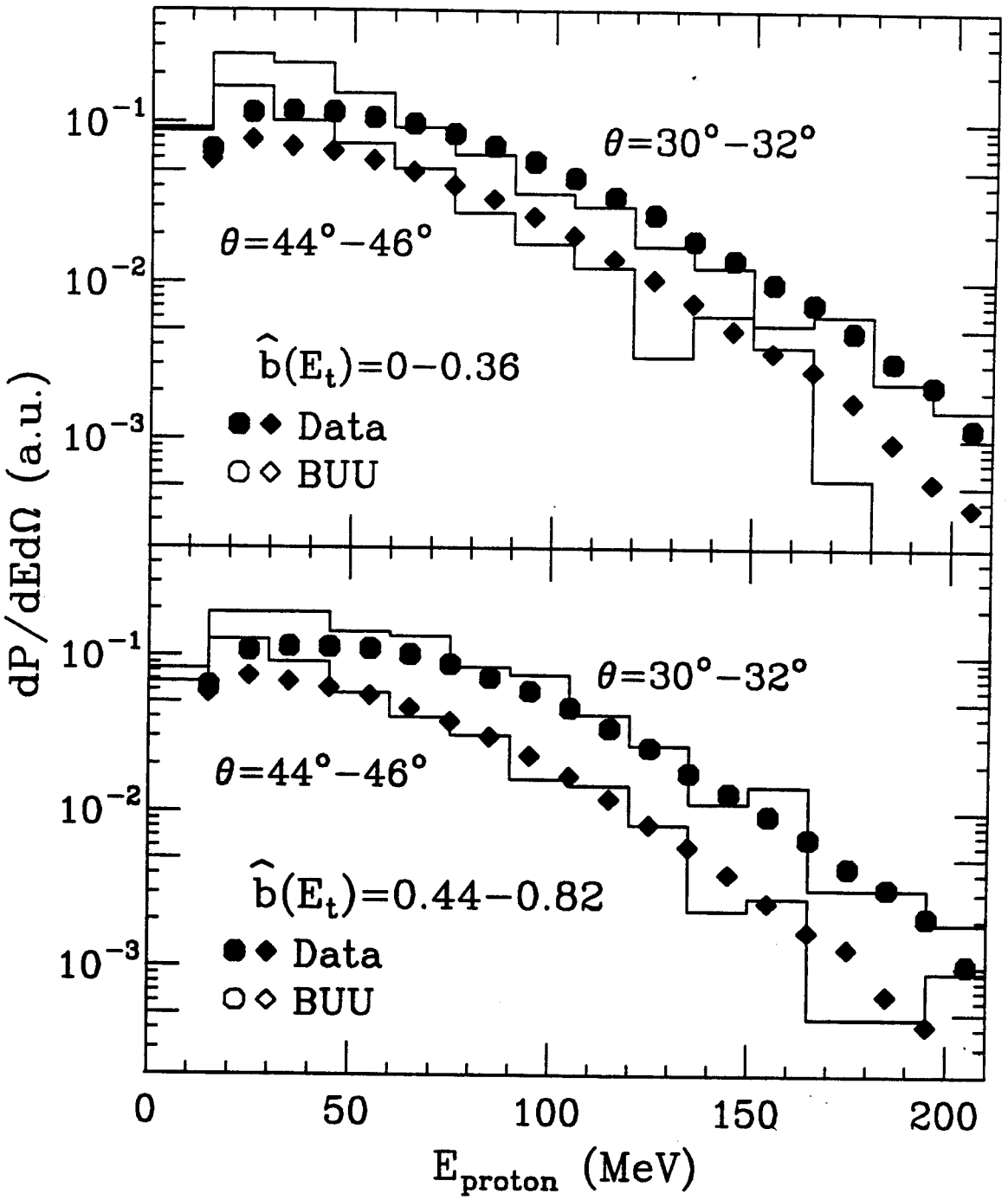

Figure 6.2. Proton energy spectra selected by cuts on $\hat{b}(E_t)$ measured at two extreme polar angles covered by hodoscope detectors are compared to predictions of the BUU. Spectra for central and peripheral events are shown in the upper and lower panels, respectively. Measured and predicted energy spectra are indicated by symbols and histograms, respectively. Relative normalization gives equal area for measured and predicted spectra at θ=30-32° for E_{proton}≥50 MeV.

At energies corresponding to proton emission below or around the Coulomb barrier, the BUU overpredicts the proton yield, but reproduces the spectra well for energies above the Coulomb barrier, in agreement with previous comparisons which did not gate on centrality [Gong 91b]. The BUU's overprediction of the low-energy proton yield has been attributed to the lack of a mechanism for cluster formation [Gong 91b]. In a simple coalescence model picture, clusters may be expected to form in regions of phase space where nucleon population density is high. Thus, more protons will be lost to clusters at low energies than at higher energies, where the phase space density is lower.

6.2 Measured Two-Proton Correlation Functions

The two-proton correlation function is obtained by dividing the two-proton coincident yield by a "background" yield which simulates the phase space population of two non-interacting protons. This background yield is constructed by treating as a pair, two protons measured in different singles events (see Equation 5.11). In this way, the correlation function, usually evaluated as a function of the relative momentum between the proton pair, measures primarily the distortion effects due to the final-state interactions between the protons; single-particle phase space effects largely divide out.

As a check, we have also constructed background yields via the event-mixing technique, in which the background yield is constructed by "mixing" two protons from different coincidence events (see Equation 5.12). Correlation functions constructed via the singles and event-mixing techniques are very similar; differences are on the order of statistical uncertainties, with a slight systematic damping in the correlations observed via the event-mixing technique. This is consistent with previous studies (see Section 5.3). A large discrepancy between results from the two techniques is not expected, since coincidence and singles data sample very similar ranges of impact parameter (see Figure 4.6),

especially after gating on total transverse energy of the event (see bottom panel of Figure 4.13).

Experimentally, the two-proton correlation function 1+R(q) is defined through the relation

$$\sum Y_2(\mathbf{p}_1,\mathbf{p}_2) = N(1+R(q)) \cdot \sum Y_1(\mathbf{p}_1) Y_1(\mathbf{p}_2) \qquad (6.1)$$

where $Y_2(\mathbf{p}_1,\mathbf{p}_2)$ is the measured coincidence yield for two protons with momenta $\mathbf{p}_1$ and $\mathbf{p}_2$, and $Y_1(\mathbf{p})$ is the measured singles yield for a proton with momentum $\mathbf{p}$. The summations are over events selected by the specified gates on E_t and on total momentum $P = |\mathbf{p}_1 + \mathbf{p}_2|$. The correlation function is evaluated as a function of the relative momentum of the proton pair $q = |\mathbf{p}_1 - \mathbf{p}_2|/2$ as measured in the center-of-momentum frame of the pair, and N is a normalization constant set such that R(q)=0 for large q, where final state interactions are believed to be negligible.

Previous studies [Gust 84, Kyan 86, Chen 87a, Chen 87b, Dupi 88] have revealed differences between correlation functions constructed with central and peripheral events, selected by cuts on some global observable. At relatively high incident beam energies (E/A > 50 MeV), it has been observed [Gust 84, Kyan 86, Dupi 88] that peripheral events show a more pronounced maximum in the two-proton correlation function at q≈20 MeV/c than do central events. In this case, a geometric parametrization indicates a smaller emitting source for peripheral events, consistent with a geometric picture of the reaction zone. The opposite trend, however, has been observed in the $^{14}N + ^{197}Au$ system at E/A=35 MeV. In this latter experiment, measurements were performed at angles sufficiently close to the grazing angle that gates on peripheral events selected large contributions from projectile decays. In this experiment, correlations for peripheral collisions were attenuated as compared to those for central collisions, and these data were interpreted in terms of the lifetime of excited projectile

residues and not in terms of a single geometric source size [Chen 87a, Chen 87b, Lync 84].

In Figure 6.3, we display correlation functions corresponding to our centrality cuts (indicated in Figures 4.13 and 4.14) and integrated over pair momentum P. As in Reference [Dupi 88], our measurements of the two-proton correlation function are performed at angles far back of the grazing angle where contributions from projectile decays are small, and our results are qualitatively consistent with the trends previously observed at higher beam energies.

In Figure 6.4, the two-proton correlation function is shown for cuts on the total momentum of the proton pair. For the slowest protons (P=400-520 MeV/c), the peripheral data show an enhanced correlation at q≈20 MeV/c relative to the central data, indicating a smaller implied source size for peripheral collisions. For the fastest protons (P≥880 MeV/c), however, the height of the bump at q≈20 MeV/c is similar if not higher for central as compared to peripheral cuts.

These trends are summarized in Figure 6.5, where the average value of the correlation function in the region q=15-25 MeV/c, $<1+R>_{15\text{-}25MeV/c}$, is plotted against the total momentum of the proton pair for the two centrality cuts. Error bars indicate statistical uncertainties as well as an estimate of the uncertainty due to normalization in the high-q region. For orientation, the right scale gives the radius parameters r_0 calculated in the Koonin formalism [Koon 77] for zero-lifetime spherical sources of Gaussian density profile, $\rho(r) \propto \exp(-r^2/r_0^2)$, which predict the values of $<1+R>_{15\text{-}25MeV/c}$ shown on the left.

Correlation functions from central and peripheral collisions display distinct dependencies on the total momentum P of the proton pair. A decreasing source size (or shorter emission time) for increasing P is indicated for both regions of centrality, with a stronger dependence seen for central collisions. This

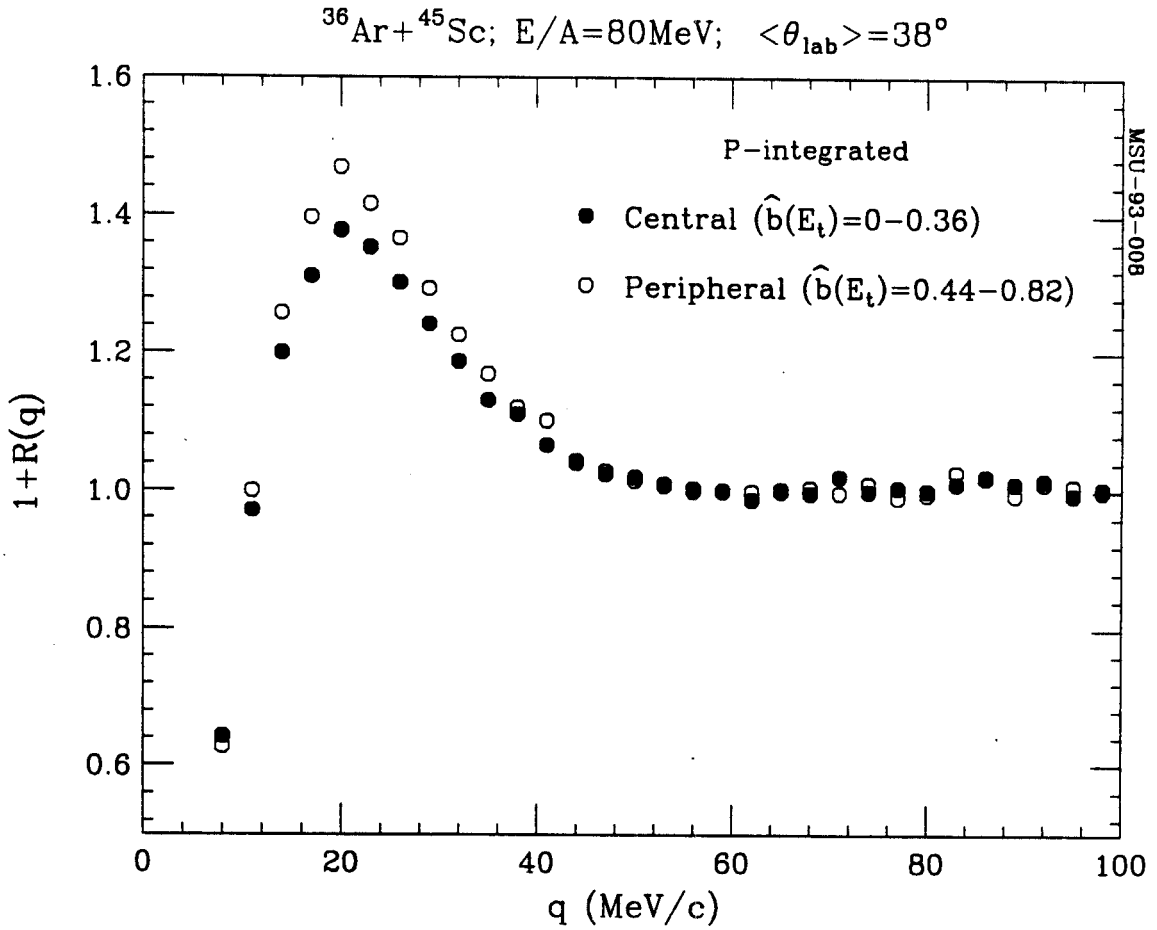

Figure 6.3. Energy-integrated two-proton correlation functions measured in the 56-element hodoscope for the centrality cuts indicated in Figures 4.13 and 4.14. Central events (high E_t) are indicated by solid points, and peripheral events (low E_t) by open points. Statistical errors are smaller than the symbol size.

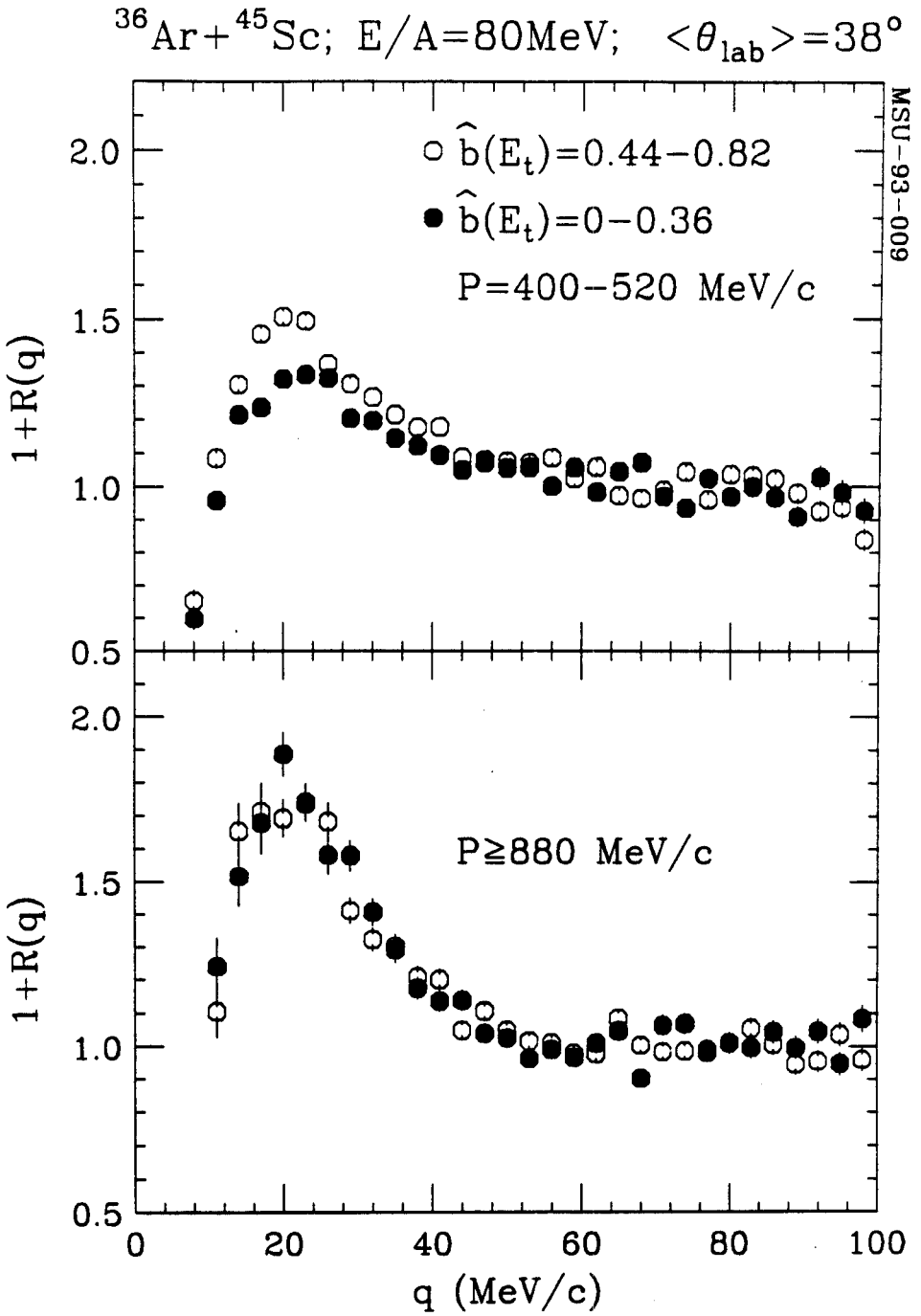

Figure 6.4. Measured two-proton correlation functions for a double cut on the total momentum of the pair $P = |p_1 + p_2|$ and the impact parameter. Centrality cuts are indicated in Figures 4.13 and 4.14. Open and solid points indicate peripheral and central events, respectively. The upper panel shows the correlation function for slow protons, 400 MeV/c $\leq P \leq$ 520 MeV/c. The lower panel shows the correlation function for fast protons, $P \geq$ 880 MeV/c. Statistical errors are indicated when they are larger than the symbol size.

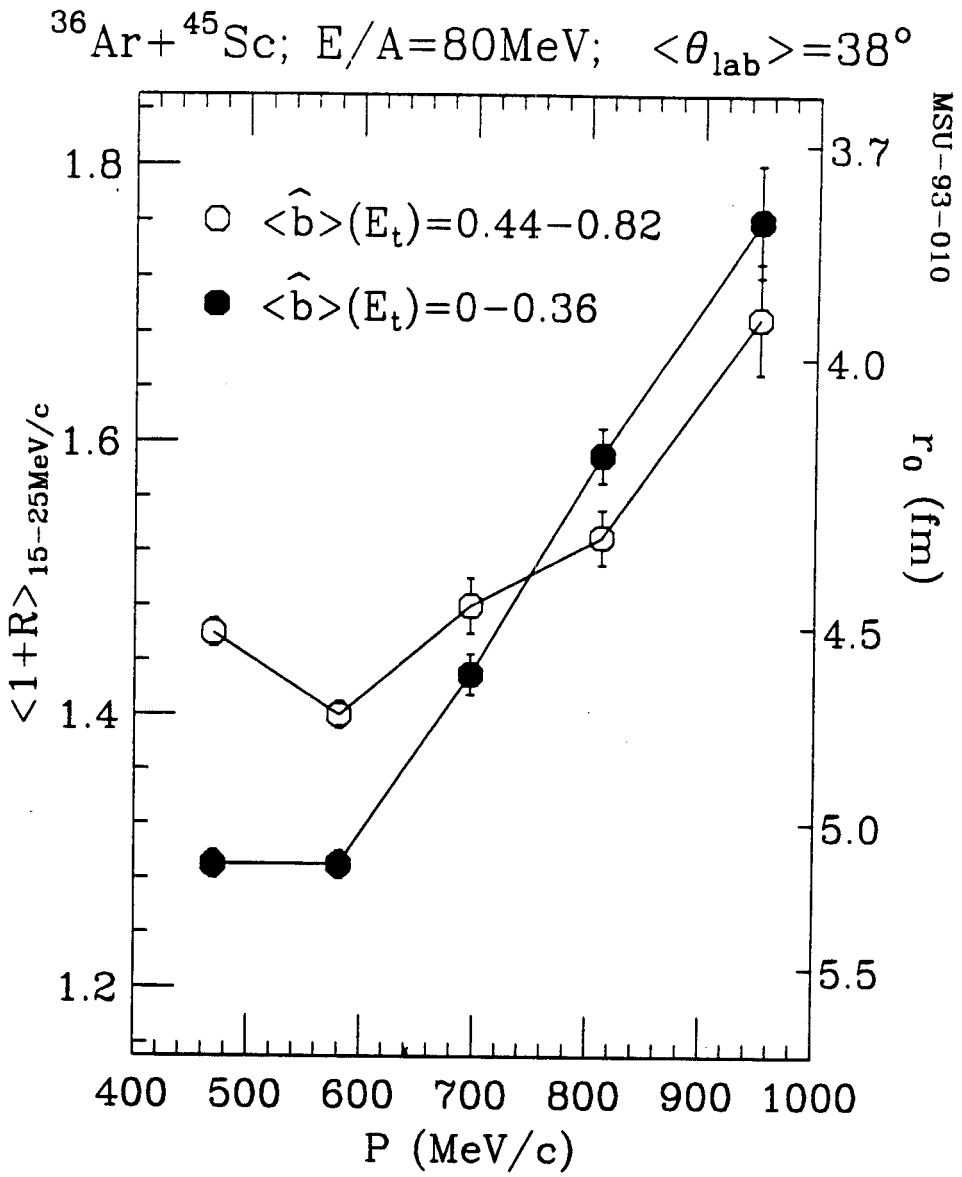

Figure 6.5. The total momentum dependence of the correlation function is summarized by plotting the height of the correlation in the region 15 MeV/c ≤ q ≤ 25 MeV/c as a function of the total momentum P. For reference, on the right-hand axis is indicated the radius of a zero-lifetime spherical source of Gaussian density profile that would produce a correlation of equal magnitude. Solid lines which connect the points for central and peripheral events are drawn to guide the eye. Error bars indicate statistical errors in the region 15 MeV/c ≤ q ≤ 25 MeV/c as well as uncertainties in the height due to uncertainties in normalizing the data at large relative momentum.

may indicate that the effect of source expansion is more prominent in central collisions.

6.3 Comparison of Measured Correlations to BUU Predictions

Interpretation of correlation functions is complicated by the lack of a one-to-one relationship between space-time geometry of the source and the correlation function [Prat 87]. However, any prediction of reaction zone dynamics unambiguously gives rise to a correlation function and its dependence on **P** and **q** [Prat 87]. Therefore, dynamical theories can be tested by comparing the P-dependence of the predicted correlation function to that seen experimentally. Here, we follow the formalism presented in Section 5.2 to construct correlation functions from BUU phase space population predictions.

In this work, we use the BUU model of Bauer [Baue 86, Baue 87, Li 91a, Li 91b, Baue 92] with a stiff equation of state (K = 380 MeV) and the nucleon-nucleon cross section set to its free value. The BUU transport equation was solved via the test particle method [Bert 84], in which many ensembles (or "events") for a given set of initial conditions are run simultaneously. To simulate a geometric distribution of impact parameters, the number of ensembles at a given impact parameter b was set to $N_b = 130 \cdot b$, where b has units of fm. Impact parameters between 1 and 10 fm were run in 0.5 fm steps. In this way, one obtains an ensemble of BUU events representing a geometric distribution of impact parameters. "Central" and "peripheral" subsets of events are chosen from this ensemble according to the methods described in Section 4.4 and below.

The phase-space population distribution was evolved by the BUU in steps of 0.5 fm/c on a spatial grid of dimensions $81 \times 81 \times 161$ fm^3. An unambiguous indication of when and where a particle is emitted is not provided by the BUU; we employed emission criteria similar to those used previously [Gong 91a, Baue

92, Zhu 91, Gong 90c, Gong 91b]: a proton was considered "emitted" if it found itself in a region of local matter density eight times less than that of normal nuclear matter before a time t_{max}=150 fm/c. Following the formalism of Section 5.2, these sets of phase space points were used to construct correlation functions.

Correlation functions for BUU events selected according to impact parameter (Section 4.4.2) were constructed with impact parameter weightings given by the curves in the lower panel of Figure 4.14. They are compared to the data in Figure 6.6. Good agreement between model predictions and observed correlation functions as a function of total pair momentum $P = |\mathbf{p}_1 + \mathbf{p}_2|$ is seen for central events. For peripheral events, the prediction for fast (high P) proton pairs disagrees with the data.

The dependence of the correlation function on total momentum is again summarized in Figure 6.7 where the height of the correlation function at q≈20 MeV/c is plotted against P, for central (upper panel) and peripheral (lower panel) events. Predictions of the BUU model with the impact parameter distributions indicated in Figure 4.14 are shown as open circles connected by dashed lines (they are labeled "$\hat{b}$-selected"). The total momentum dependence of the correlation function for central events, shown in the upper panel, is seen to be reproduced rather well. For peripheral events, the theoretical predictions disagree significantly with measurement.

The heights of correlation functions constructed from sets of BUU events which satisfy "equivalent-E_t" cuts, as described in Section 4.4.1, are shown in Figure 6.7 as the open squares (labeled "E_t-selected"). The "equivalent-E_t" impact parameter selection procedure leads to predictions which are practically equivalent to those obtained via the more elaborate $\hat{b}$-selection procedure, giving confidence to the stability of our results. The insensitivity of the

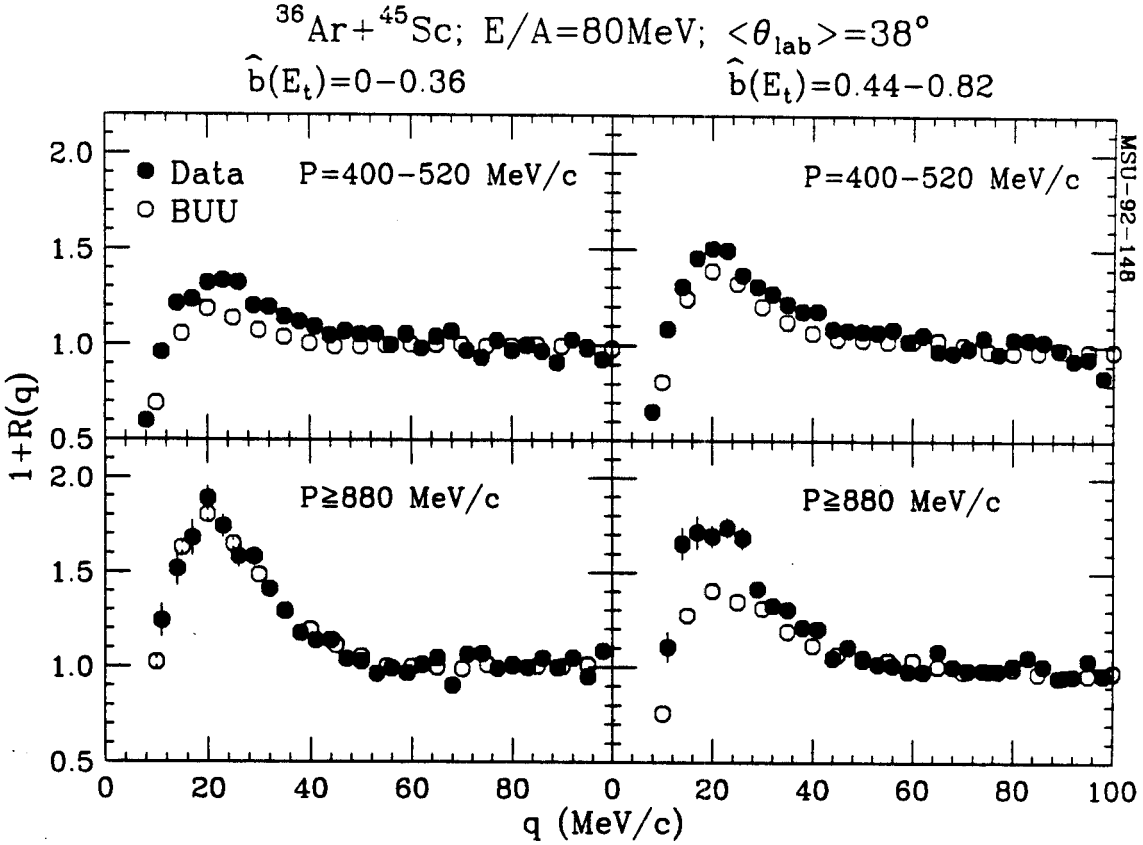

Figure 6.6. Measured two-proton correlation functions for cuts in centrality and total momentum are compared to BUU predictions. Solid symbols represent data. Open symbols are BUU calculations. The upper panels show the correlation function for slow protons (400 MeV/c ≤ P ≤ 520 MeV/c). Lower panels correspond to faster protons (P ≥ 880 MeV/c). Panels on the left- and right-hand sides, respectively, correspond to central and peripheral events. Centrality cuts for the data were based on E_t, as indicated by Figure 4.14. Weighting for BUU events was done according to the reduced impact parameter distributions dP/db_r indicated in the bottom panel of Figure 4.14. Statistical uncertainties are indicated when they are larger than the size of the points.

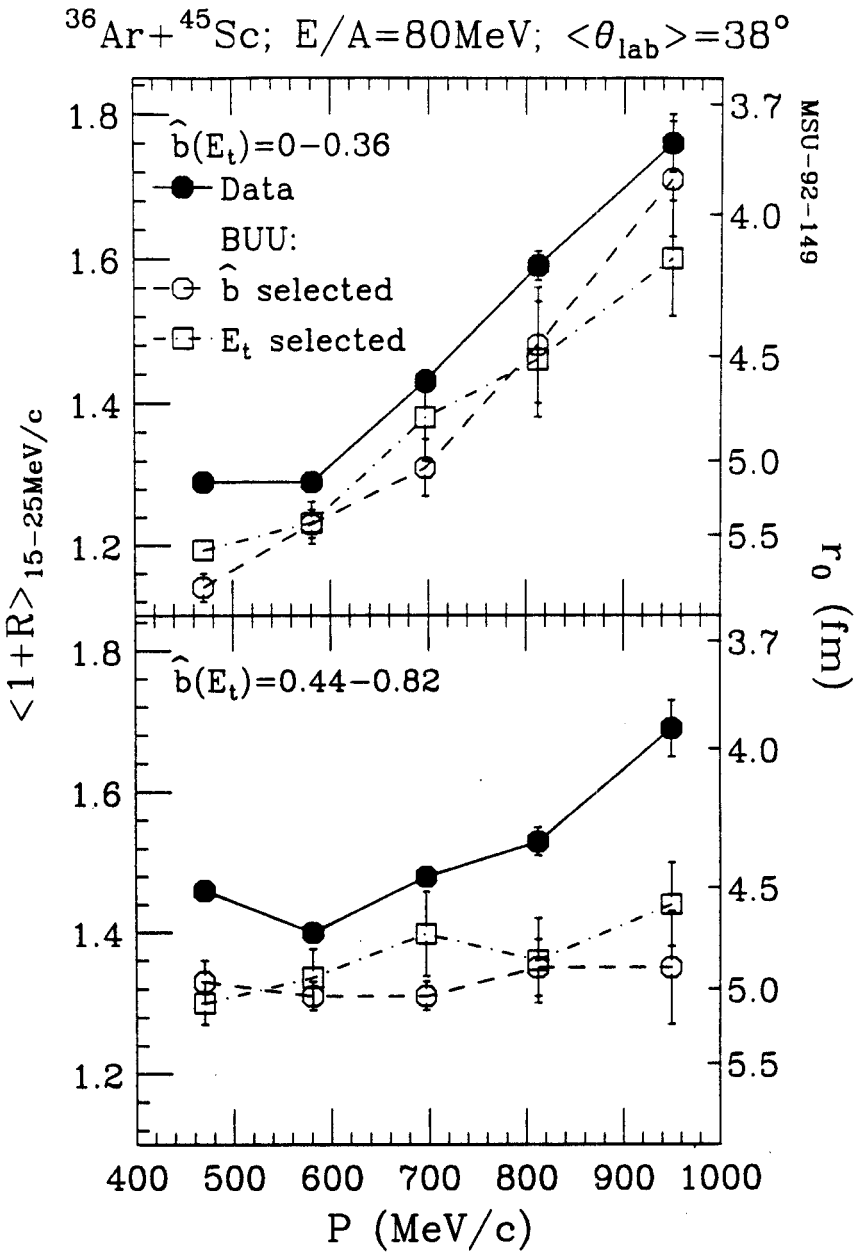

Figure 6.7. The average height of the correlation function in the relative momentum interval 15 MeV/c ≤ q ≤ 25 MeV/c, is plotted against the total momentum of the pair P. For orientation, the right-hand axis indicates the source radius of a zero- lifetime spherical source with a Gaussian density profile that would produce a correlation of equal magnitude. The upper panel displays the data and calculations for central events, and the lower panel provides the comparison for peripheral events. Data are indicated by solid circles, while BUU predictions are indicated by the open symbols. The open circles correspond to BUU results when the event selection is performed according to the dP/db_r distributions shown in the bottom panel of Figure 4.13. The open squares correspond to the selection of events via the "equivalent-E_t" method discussed in the text.

theoretical correlation functions to technical details of the impact parameter weighting method is encouraging.

For central collisions, the BUU describes the total momentum dependence of the correlation function quite well. It is then reasonable to assume that the space-time evolution of the proton-emitting zone generated in central collisions is also fairly well described by the theory. However, the theoretical calculations fail to reproduce the total momentum dependence of the correlation function for peripheral events. While some additional theoretical uncertainties exist, due to ambiguities in the criteria for where and when a particle is emitted, the discrepancies for peripheral collisions may indicate that the present model is incomplete in its description of peripheral collisions and that it may be deficient in its description of surface effects.

Chapter 7 - Longitudinal and Transverse Correlation Functions; Finite Lifetime Effects

As discussed in Section 5.1.3, the spatial and temporal extent of a proton-emitting source may be independently determined through differences between longitudinal and transverse correlation functions. However, previous studies [Zarb 81, Awes 88, Gong 90c, Rebr 92] have failed to observe such differences. (A weak signal of marginal statistical significance was reported in [Gouj 91]. However, in this study, longitudinal and transverse correlation functions were normalized independently, an incorrect procedure, as discussed in [Gong 91b] and below.) In this chapter, we discuss the main difficulty in extracting signals of finite lifetime from the correlation function and present the first clearly observed differences between longitudinal and transverse correlation functions for two systems with very different emission time scales: a hot, rapidly evolving nuclear zone and a slowly cooling compound nucleus.

The experimental two-proton correlation function is defined according to

$$1 + R(\mathbf{q}) = C \cdot \frac{N_{coinc}(\mathbf{q})}{N_{back}(\mathbf{q})}, \tag{7.1}$$

where $N_{coinc}(\mathbf{q})$ represents the yield of coincident proton pairs with relative momentum $\mathbf{q}$. The background yield, $N_{back}(\mathbf{q})$, is constructed using either the singles or the event-mixing technique. Two-proton correlation functions were

constructed with cuts on the relative angle between the total momentum of the pair and the momentum of relative motion, $\psi = \mathrm{Cos}^{-1}(|\mathbf{P}\cdot\mathbf{q}|/|\mathbf{P}|\cdot|\mathbf{q}|)$.

The normalization constant C in Equation 7.1, adjusted such that R(q) vanishes for large q, should be determined independently of the angle ψ. This may be understood through the following simple reasoning. At $|\mathbf{q}|=0$, cuts on the relative orientation of **q** and **P** become degenerate, and the normalizations for longitudinal and transverse correlation functions are by definition identical. Since the normalization constant is independent of $|\mathbf{q}|$, this same constant must apply for all q and ψ values. Thus, there is no *a priori* justification for separately normalizing longitudinal and transverse correlation functions, and doing so may produce misleading results [Gong 91b].

We should point out, however, that differences in the assymtotic behaviour of the longitudinal and transverse correlation functions may arise from other physical effects. As discussed in Section 5.2 and [Gong 91b], impact parameter and reaction plane averaging may lead to "dynamical" azimuthal correlations that distort the large-q behaviour of the correlations. Such effects cannot be normalized away and must be accounted for by a reaction model or else be considered part of the intrinsic uncertainty.

We are interested in the low-q behaviour of the correlation function, where such distortion effects should be small. Indeed, as we see below, for the systems we study, such effects are unimportant.

7.1 The Importance of Identifying the Source Frame

Proton emission from a long-lived source will lead to a phase space distribution elongated in the direction of total momentum [Prat 87, Bert 89, Gong 91a]. For such distributions, the suppression of the correlation function at low q due to the Pauli principle is less important for proton pairs whose relative momentum is oriented along the direction of the total momentum, and cuts on ψ

will reveal finite lifetime effects in the correlation function. However, the relative orientation of **P** and **q** is a function of rest frame (since **P** depends on the rest frame, but **q**– at least in the nonrelativistic limit– does not). In order to see the effects of finite lifetime, therefore, it is important that the angle ψ is constructed in the frame of the emitting source [Rebr 92, Lisa 93c, Lisa 93d].

The problem of identifying finite-lifetime effects is illustrated in Figure 7.1. The figure depicts phase space distributions in the laboratory rest frame of protons emitted with fixed velocity $\mathbf{v}_{p,lab}$ towards the detector at $\theta_{lab} = 38°$ for a source at rest in the laboratory (part a) and for a source at rest in the center-of-momentum frame of the system $^{36}Ar+^{45}Sc$ at E/A=80 MeV ($v_{source} = 0.18c$, part b). We assumed a spherical source of 7 fm diameter and 70 fm/c lifetime emitting protons of momentum 250 MeV/c in the laboratory.

For emission from a source at rest, the phase space distribution of particles moving with a fixed velocity $\mathbf{v}_{p,lab} = \mathbf{v}_{emit}$ towards the detector exhibits an elongated shape [Prat 87, Bert 89, Gong 91b] oriented parallel to $\mathbf{v}_{p,lab}$. A source of lifetime τ appears elongated in the direction of the proton momentum by an incremental distance $\Delta\mathbf{s} \approx \mathbf{v}_{emit} \cdot \tau = \mathbf{v}_{p,lab} \cdot \tau$. Correlation functions for relative momenta $\mathbf{q} \perp \mathbf{v}_{p,lab}$ reflect a stronger Pauli-suppression, and hence a reduced maximum at $q \approx 20$ MeV/c, than those for $\mathbf{q} \parallel \mathbf{v}_{p,lab}$ [Prat 87, Bert 89, Gong 91a, Gong 91b].

Previous analyses [Zarb 81, Awes 88, Gong 90b, Gong 91b, Gouj 91] compared the shapes of correlation functions selected by cuts on the relative angle $\psi_{lab} = \mathrm{Cos}^{-1}(\mathbf{q}\cdot\mathbf{P}/qP)$ between **q** and $\mathbf{P} = \mathbf{p}_1 + \mathbf{p}_2 \approx 2m\mathbf{v}_{p,lab}$, where $\mathbf{p}_1$ and $\mathbf{p}_2$ are the laboratory momenta of the two protons and **q** is the momentum of relative motion. Such analyses are optimized to detect lifetime effects of sources stationary in the laboratory system, but they can fail to detect lifetime effects for moving sources. For the specific case illustrated in Figure 7.1b, the source

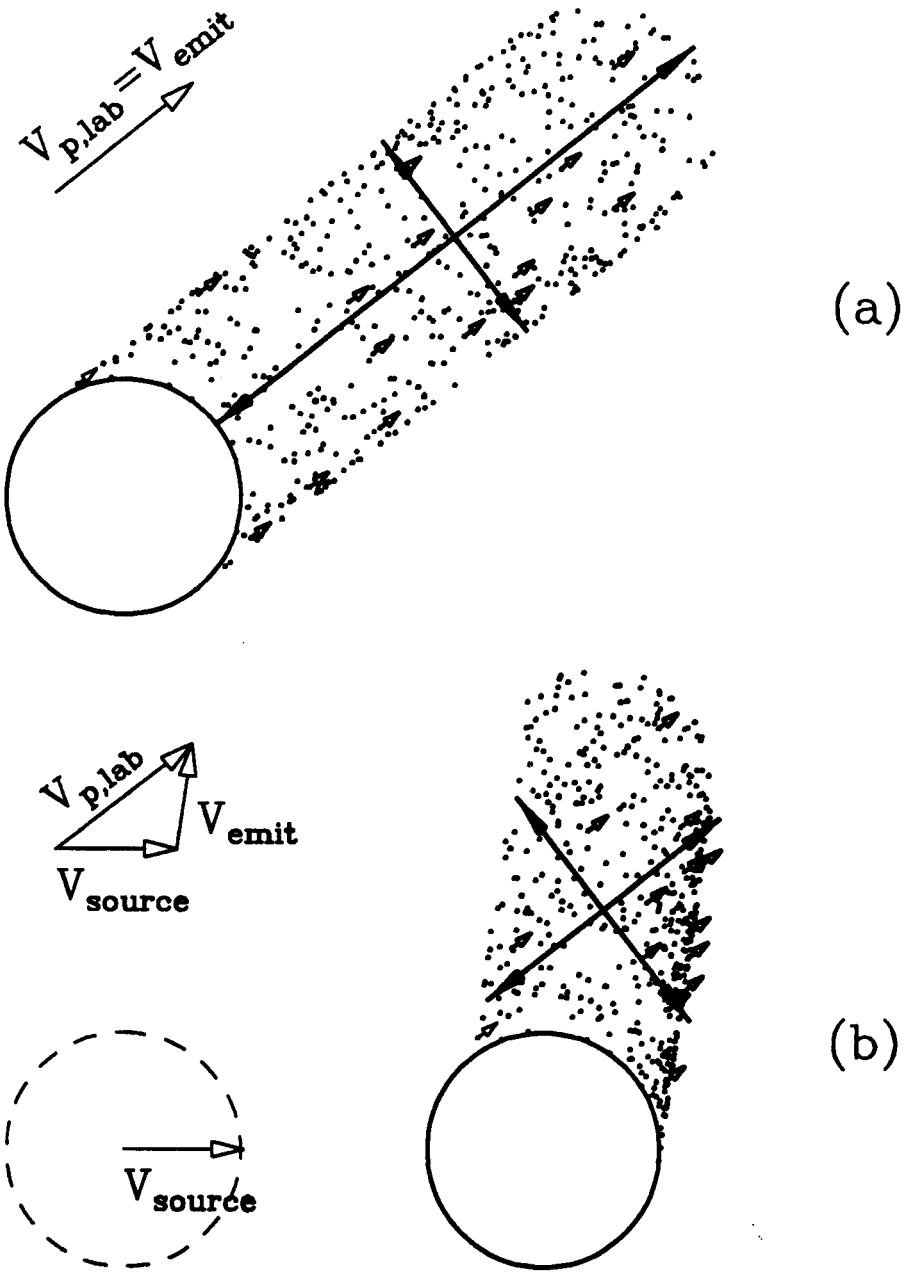

Figure 7.1. Schematic illustration of phase space distributions at a time t = 70 fm/c, seen by a detector at θ_{lab} = 38°, for a spherical source of radius r = 3.5 fm and lifetime τ = 70 fm/c emitting protons of momentum 250 MeV/c. Part a) Source at rest in the laboratory. Part b) Source moves with v_{source} = 0.18c. In the distributions shown, the laboratory velocities of the protons ($v_{p,lab}$) are depicted by small arrows and the directions perpendicular and parallel to $v_{p,lab}$ are depicted by large double-headed arrows. In parts (a) and (b), $v_{p,lab}$ is kept constant, and v_{emit} is different. Therefore, the elongations along v_{emit} are different.

dimensions parallel and perpendicular to $v_{p,lab}$ are very similar, and no significant differences are expected for the corresponding longitudinal and transverse correlation functions.

For a source of known velocity, the predicted lifetime effect is detected most clearly if longitudinal and transverse correlation functions are selected by cuts on the angle $\psi_{source} = \mathrm{Cos}^{-1}(\mathbf{q'}\cdot\mathbf{P'}/q'P')$, where the primed quantities are defined in the rest frame of the source. (In the rest frame of the source, the phase space distribution is always elongated in the direction of v_{emit}. Hence, in Figure 7.1b, the source dimensions should be compared in directions parallel and perpendicular to v_{emit}.) Such analyses can only be carried out for emission from well characterized sources [Rebr 92, Lisa 93c, Lisa 93d]. In the following, we corroborate these qualitative arguments by our experimental data.

7.2 Determination of the Source Lifetime in Central ^{36}Ar+^{45}Sc Collisions at E/A=80 MeV

Cuts on ψ were applied to the centrality-gated two-proton correlation functions measured for the ^{36}Ar+^{45}Sc system at E/A=80 MeV in an attempt to identify the effects of a finite lifetime. Since typical emission timescales may differ for protons with different energies, cuts were also made on the total momentum of the proton pair. Very good statistics is required to perform such multi-dimensional cuts on the impact parameter, total momentum, and angle ψ between **P** and **q**: in all, about 1.6 million "good" proton pairs were measured in the present experiment.

In a symmetric system like the one under consideration, the source velocity may take on many values, depending on the impact parameter. For very central collisions, we assume stopping of projectile and target. The protons would then be emitted from a hot source moving in the lab with the center-of-momentum velocity of the system. For peripheral collisions, the linear

momentum transfer may be incomplete, and the source velocity may vary significantly from event to event. Furthermore, many proton sources— for example "target-like," "projectile-like," and "participant" sources— with different velocities and lifetimes may be created in a single peripheral collision. For peripheral collisions, then, more sophisticated methods may be required to extract the signatures of finite lifetime.

Figure 7.2 shows experimental longitudinal and transverse two-proton correlation functions for central $^{36}Ar + ^{45}Sc$ collisions at E/A = 80 MeV selected by appropriate cuts on the total transverse energy detected in the 4π Array. In a geometrical picture (see Section 4.2), the applied cuts correspond to reduced impact parameters of $b/b_{max} = 0 - 0.36$. Longitudinal (solid points) and transverse (open points) correlation functions were defined by cuts on the angle $\psi = \mathrm{Cos}^{-1}(\mathbf{q}\cdot\mathbf{P}/qP) = 0°\text{-}50°$ and 80°-90°, respectively. (The normalization constant C in Equation 7.1 is independent of ψ.) To maximize lifetime effects and reduce contributions from the very early stages of the reaction, the coincident proton pairs were selected by a low-momentum cut on the total laboratory momentum, P = 400-600 MeV/c. The top panel shows correlation functions for which the angle ψ was defined in the center-of-momentum frame of projectile and target ($\psi = \psi_{source}$); for central collisions of two nuclei of comparable mass, this rest frame should be close to the rest frame of the emitting source. The bottom panel shows correlation functions for which the angle ψ was defined in the laboratory frame ($\psi = \psi_{lab}$).

Consistent with the qualitative arguments presented in Figure 7.1, a clear difference between longitudinal and transverse correlation functions is observed for cuts on ψ_{source} (top panel of Figure 7.2), but not for cuts on ψ_{lab} (bottom panel of Figure 7.2). The clear suppression of the transverse correlation function

with respect to the longitudinal correlation function observed in the top panel in Figure 7.2 is consistent with expectations for emission from a source of finite lifetime [Prat 87, Gong 91a, Gong 91b, Bert 89]. The solid and dashed curves in the top panel of Fig. 2 depict calculations for emission from a spherical Gaussian source of radius parameter $r_0 = 3.5$ fm and lifetime $\tau = 70$ fm/c, see also Equation 7.2 below. The data in Figure 7.2 represent the first clear experimental evidence of this predicted lifetime effect.

For a more quantitative analysis, we performed calculations assuming a simple family of sources of lifetime τ and spherically symmetric Gaussian density profiles, moving with the center-of-momentum frame of reference. Energy and angular distributions of the emitted protons were selected by randomly sampling the experimental yield $Y(\mathbf{p})$. Specifically, the single particle emission functions [Gong 91a, Gong 91b] were parametrized as

$$g(r,p,t) \propto \exp(-r^2/r_o^2 - t/\tau) \cdot Y(p). \qquad (7.2)$$

In Equation 7.2, $\mathbf{r}$, $\mathbf{p}$, and t refer to the rest frame of the source. Phase-space points generated in the rest frame of the source were Lorentz boosted into the laboratory frame, and the two-proton correlation function was obtained by convolution with the two-proton relative wavefunction, see Section 5.2 or [Prat 87, Gong 91a, Gong 91b] for details.

Transverse and longitudinal correlation functions were calculated for the range of parameters $r_0 = 2.5$ - 6.0 fm and $\tau = 0$ - 150 fm/c. For each set of parameters, the agreement between calculated and measured longitudinal and transverse correlation functions was evaluated by determining the value of χ^2/ν (chi-squared per degree of freedom) in the peak region, q = 15 - 30 MeV/c. A contour plot of χ^2/ν as a function of r_0 and τ is given in Figure 7.3. Good agreement between calculations and data is obtained for a source with a

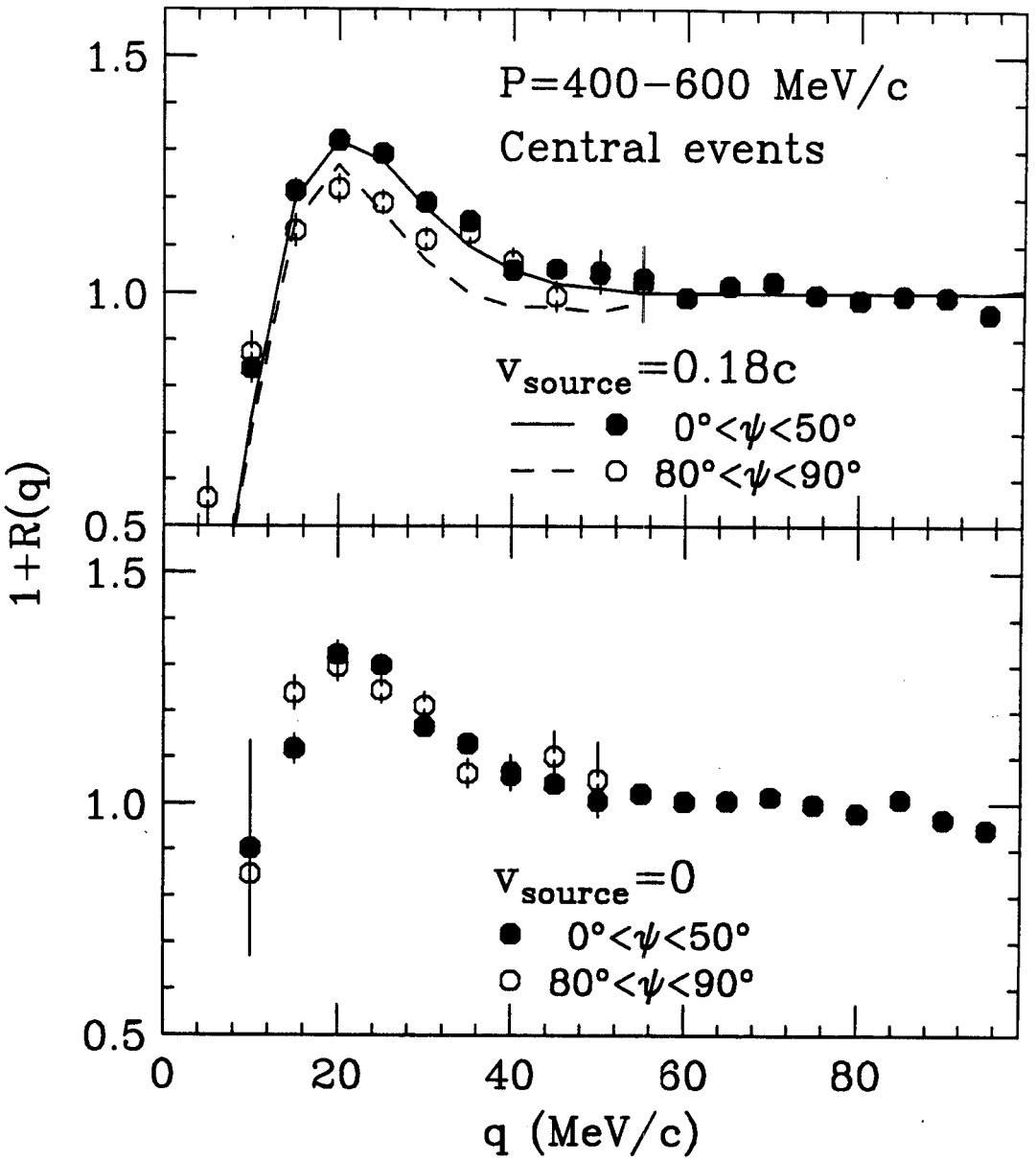

Figure 7.2. Measured longitudinal and transverse correlation functions for protons emitted in central $^{36}Ar + ^{45}Sc$ collisions at E/A = 80 MeV. The correlation functions are shown for proton pairs of total laboratory momenta P=400-600 MeV/c detected at $\langle\theta_{lab}\rangle$=38°. Longitudinal and transverse correlation functions (solid and open points, respectively) correspond to $\psi = \mathrm{Cos}^{-1}(\mathbf{q}\cdot\mathbf{P}/qP)$ = 0° - 50° and 80° – 90°, respectively, where P is defined in the rest frame of the presumed source. Upper panel- v_{source} = 0.18c. Solid and dashed curves represent longitudinal and transverse correlation functions predicted for emission from a Gaussian source with r_0 = 4.7 fm and τ = 25 fm/c, moving with v_{source} = 0.18c. Lower panel- v_{source} = 0.

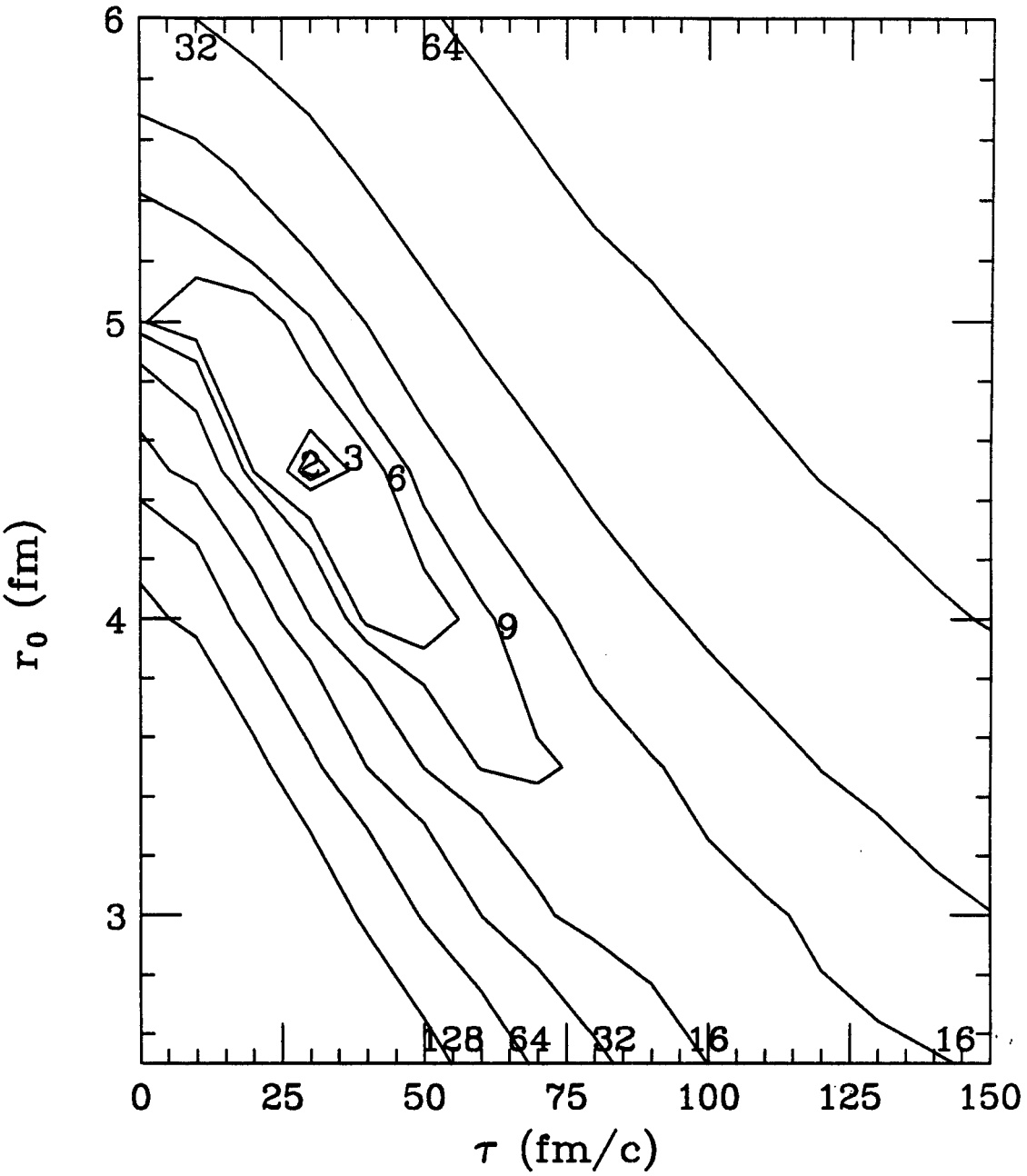

Figure 7.3. Contour diagram of χ^2/ν (chi-squared per degree of freedom) determined by comparing theoretical correlations functions to the data shown in the upper panel of Figure 7.2. The fit was performed in the peak region of the correlation function, q = 15-30 MeV/c. Details are discussed in the text.

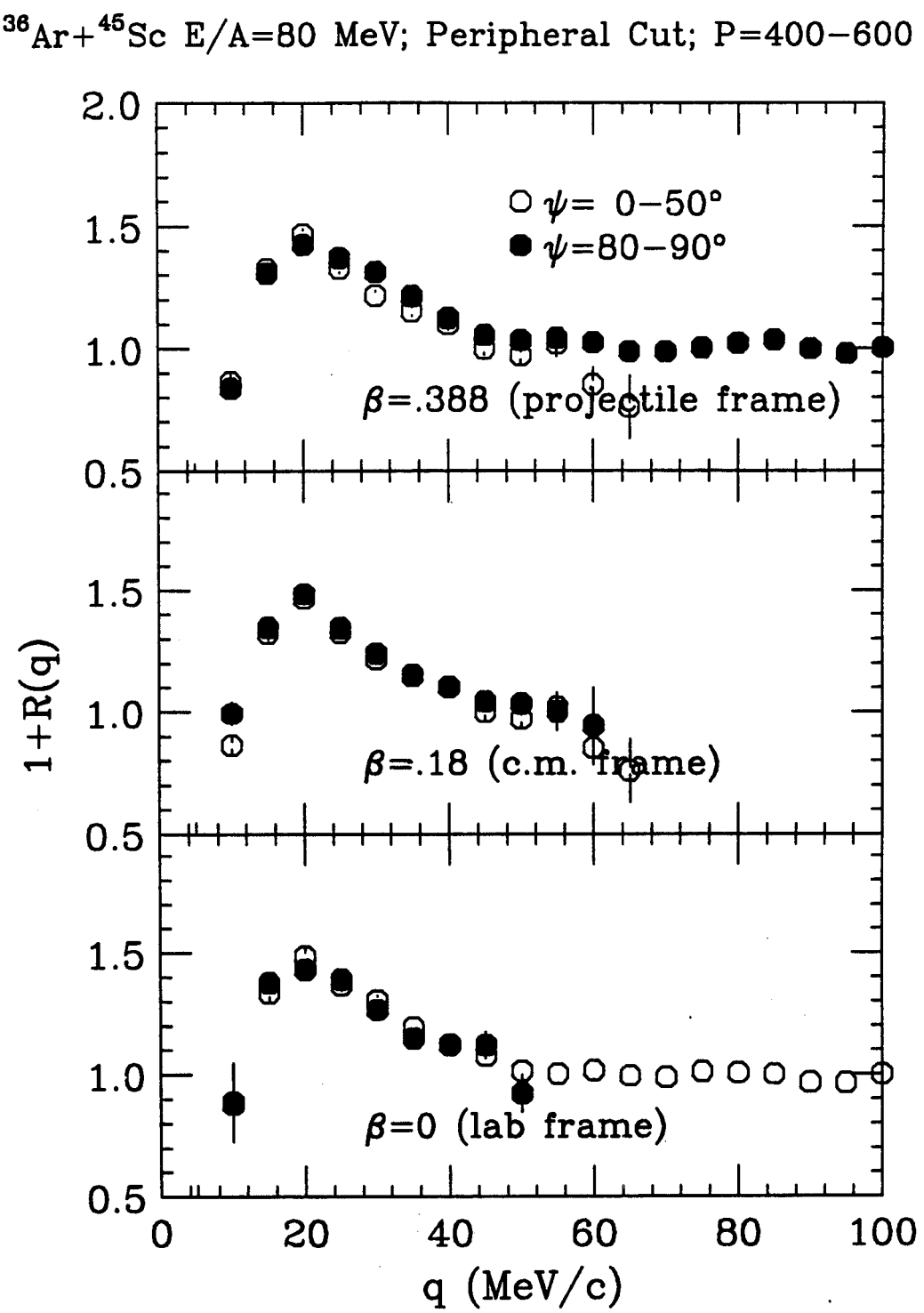

Figure 7.4. Longitudinal (solid symbols) and transverse (open symbols) correlation functions constructed for protons emitted from peripheral events with total pair momentum P=400-600 MeV/c. Cuts were performed on the angle ψ as constructed in the projectile, center-of-momentum of the ^{36}Ar+^{45}Sc system, and the laboratory frame.

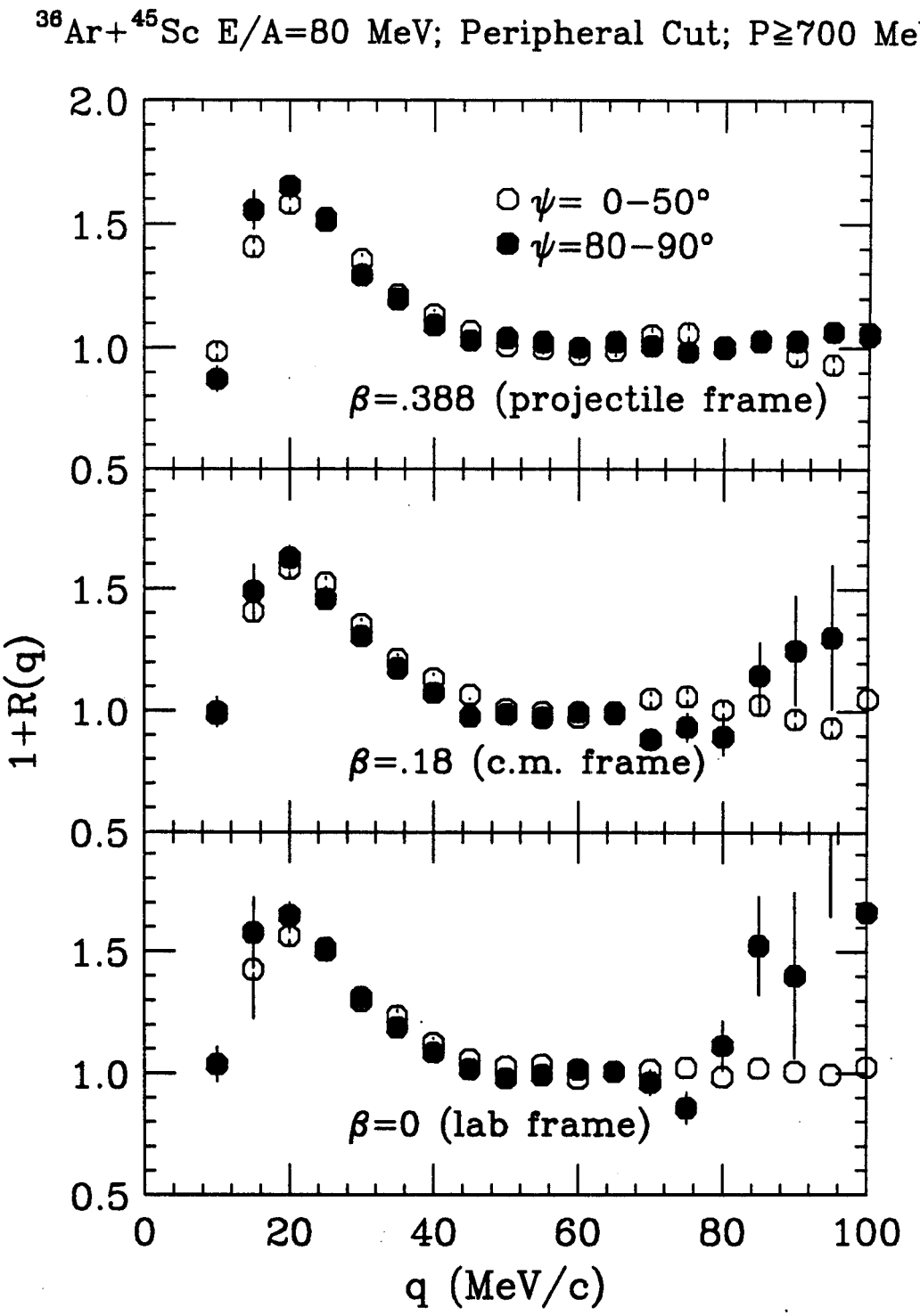

Figure 7.5. Longitudinal (solid symbols) and transverse (open symbols) correlation functions constructed for protons emitted from peripheral events with total pair momentum P≥700 MeV/c. Cuts were performed on the angle ψ as constructed in the projectile, center-of-momentum of the ^{36}Ar+^{45}Sc system, and the laboratory frame.

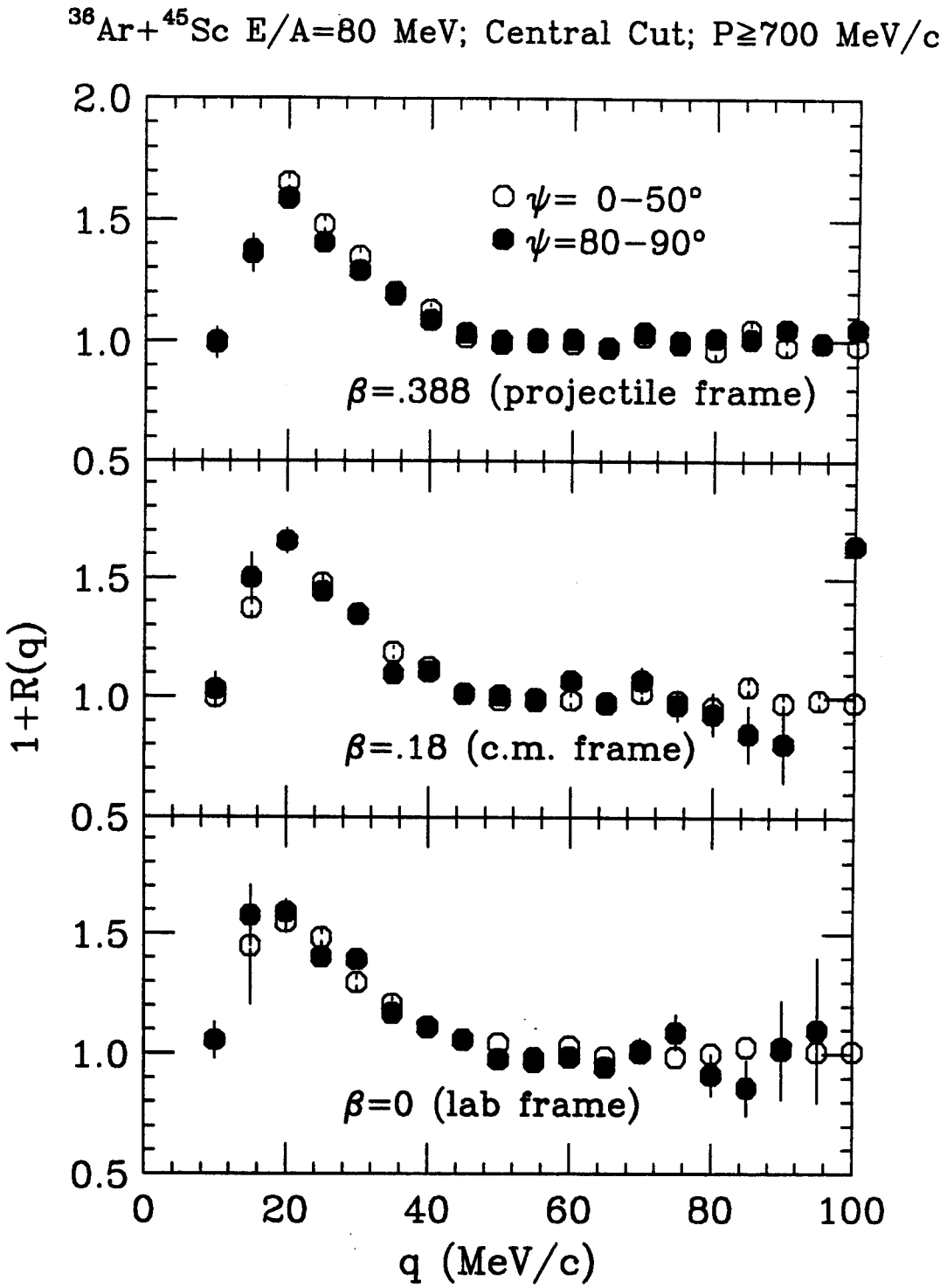

Figure 7.6. Longitudinal (solid symbols) and transverse (open symbols) correlation functions constructed for protons emitted from central events with total pair momentum P≥700 MeV/c. Cuts were performed on the angle ψ as constructed in the projectile, center-of-momentum of the ^{36}Ar+^{45}Sc system, and the laboratory frame.

Gaussin radius of about 4.5 fm and a lifetime of about 25-40 fm/c. It is gratifying to note that these extracted emission timescales are consistent with those predicted by BUU transport calculations [Li 91a, Li 91b], which are expected to apply here.

Clean characterization of a relatively well-defined source frame appears crucial. Figures 7.4 and 7.5 shows longitudinal and transverse correlation functions constructed for peripheral collisions, where ψ is defined in the projectile frame, the center-of-momentum frame of the $^{36}Ar + ^{45}Sc$ system, and the laboratory frame. Two-proton correlation functions selected by theperipheral cut do not exhibit any differences between longitudinal and transverse correlation functions, irrespective of the assumed rest frame. Indeed, for such collisions no single unique source velocity may exist, and more sophisticated analysis techniques may be necessary to exploit directional dependencies of two-proton correlation functions.

More interestingly, even for central collisions no significant difference between longitudinal and transverse correlation functions was observed for protons selected by cuts on large total momenta, $P \geq 700$ MeV/c. In Figure 7.6, we show these correlation function assuming the same source frames as discussed above. The degeneracy of the longitudinal and transverse correlation functions for this cut suggests that these very energetic protons are emitted on a very fast time scale and/or at such an early stage of the reaction where the concept of emission from a single source does not apply.

In conclusion to this section, we have measured the lifetime of the source of intermediate-energy protons in central Ar+Sc collisions at E/A=80 MeV. Consistent with dynamical models, a lifetime of about 30 ± 10 fm/c was

extracted. Such emission timescales are consistent with the creation of a deconfined nuclear gas [Prat 87].

7.3 Determination of the Source Lifetime in $^{129}Xe+^{27}Al$ Collisions at E/A=31 MeV

Extraction of finite lifetime effects in the measurement discussed in the previous section was possible because central events could be selected, for which the assumption of emission from a unique source may be reasonable. Previous measurements of longitudinal and transverse correlation functions were performed without impact parameter selection. Here, we discuss a re-analysis of previously-measured high statistics two-proton coincidence data for the inverse kinematics reaction $^{129}Xe+^{27}Al$ at E/A=31 MeV [Gong 90b, Gong 91b]. For this reaction, ambiguities of the emitting source velocities should be relatively small; the likely source velocities range from $\beta = 0.209$ (for complete fusion reactions) to $\beta = 0.251$ (for emission from excited projectile fragments) [Gong 91b]. We will show that clear differences between longitudinal and transverse correlation functions exist when the appropriate angular cuts are made in the compound nucleus rest frame. These differences become largely washed out when the angular cuts are made in the laboratory rest frame as was done in Reference [Gong 91b].

In the experiment of [Gong 91b], an ^{27}Al target of areal density 5.6 mg/cm^2 was irradiated by a ^{129}Xe beam at E/A = 31 MeV from the K1200 cyclotron of the National Superconducting Cyclotron Laboratory. Light particles were detected by two arrays of ΔE-E telescopes consisting of 300-400 μm-thick silicon detectors backed by 10-cm-long CsI(Tl) or NaI(Tl) detectors. An array of 37 Si-CsI(Tl) telescopes was centered at polar and azimuthal lab angles of $\theta = 25°$ and $\phi = 0°$. Each telescope covered a solid angle of $\Delta\Omega = 0.37$ msr with a nearest-neighbor spacing of $\Delta\theta = 2.6°$. Centered at $\theta = 25°$ and $\phi = 90°$ was an array of 13

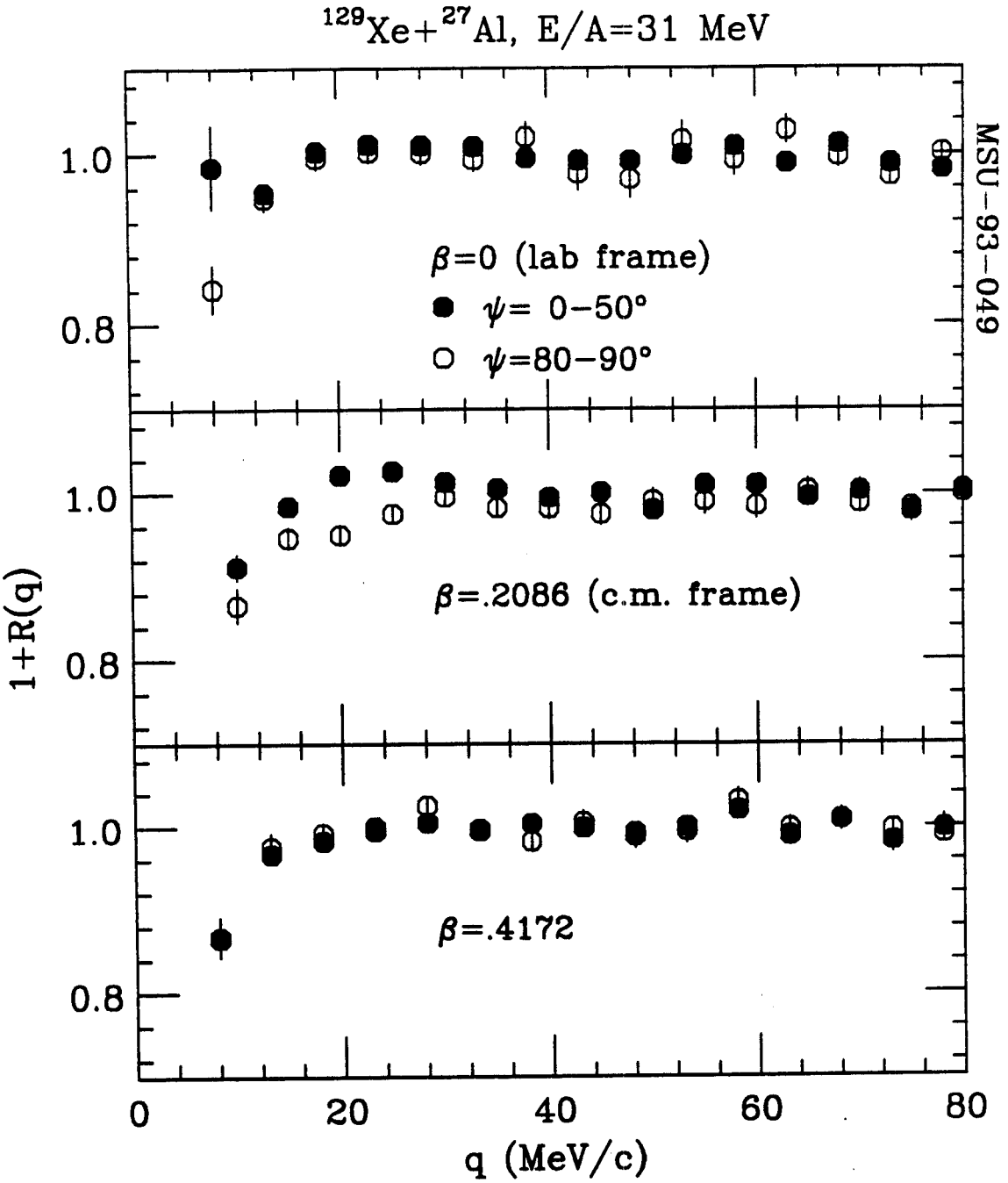

Figure 7.7. Longitudinal (filled circles) and transverse (open circles) two-proton correlation functions for the reaction ^{129}Xe + ^{27}Al at E/A=31 MeV. Angular cuts in the upper panel were constructed in the laboratory frame of reference, and in rest frames moving in the lab with β = 0.2086 (center panel) and β=.4172 (bottom panel). The cut on the total momentum of the proton pair was P ≥ 480 MeV/c.

Si-NaI(Tl) telescopes, each covering $\Delta\Omega$ = 0.5 msr of solid angle with a nearest-neighbor spacing of $\Delta\theta$ = 4.4°. Proton energy resolution was on the order of 1%. More experimental details can be found in References [Gong 91b, Gong 91c].

In order to eliminate small differences in the shapes of the single- and two-proton inclusive energy spectra, the background yield, $N_{back}(\mathbf{q})$ in Equation 7.1, is constructed using the event-mixing technique (see Section 5.3). Differences in the single- and two-proton inclusive energy spectra could, for example, arise from different relative contributions from decays of projectile and fusion residues.

Also, in order to minimize the effects of proton interaction with the heavy residue, which are not accounted for in the Koonin-Pratt formalism, we study correlation functions only for particle emission above the Coulomb barrier of the compound system.

As in the search for lifetime effects in the Ar+Sc system, it is important that the angle ψ is constructed in the frame of the emitting source. This is illustrated inFigure 7.7. The individual panels of the figure show longitudinal (ψ = 0° - 50°, filled symbols) and transverse (ψ = 80° - 90°, open symbols) two-proton correlation functions selected by the cut on the total laboratory momentum P≥480 MeV/c. For the top, center and bottom panels, the angle ψ was defined in the laboratory system (β = 0), the center-of-momentum frame of projectile and target (i.e. the rest frame of the compound nucleus, β = 0.209), and a rest frame moving with twice the velocity of the center-of-momentum system (β = 0.417). Consistent with the results of References [Gong 90b, Gong 91b], no significant differences between longitudinal and transverse correlation functions are observed when ψ is defined in the laboratory rest frame. When the angle ψ is defined in the rest frame of the compound nucleus, however, significant differences between longitudinal and transverse correlation functions emerge.

They disappear again when ψ is defined in a rest frame moving with twice the speed of the compound nucleus.

The identification of lifetime effects from differences between longitudinal and transverse correlation functions can be difficult, if not impossible, for data containing a broad distribution of source velocities. Fortunately, for the present reaction, the range of source velocities is relatively narrow [Gong 91b], thus allowing the study of lifetime effects without further event characterization. In the following, we will use a simple parametrization of the source function to illustrate the sensitivity of the present data to the average spatial dimension and lifetime of the emitting system.

The Koonin-Pratt formalism (Section 5.1.1) allows the construction of the two-proton correlation function from the single-particle emission function $g(\mathbf{r},t,\mathbf{p})$, which is a function of the space-time emission coordinates $\mathbf{r}$ and t, as well as the momentum $\mathbf{p}$ [Prat 87, Gong 91a, Gong 91b] of the emitted particles. In our schematic calculations, we parametrize the source in terms of surface emission from a sphere of sharp radius R and with an exponential lifetime τ [Kim 92]. Energy and angular distributions of the emitted protons were obtained by sampling the experimental yield $Y(\mathbf{p})$. In the rest frame of the source, the source function was parametrized as

$$g(\mathbf{r},t,\mathbf{p}) \sim \delta(|\mathbf{r}|-R)\cdot\theta(\mathbf{r}\cdot\mathbf{p})\cdot\frac{\mathbf{r}\cdot\mathbf{p}}{|\mathbf{r}|\cdot|\mathbf{p}|}\cdot Y(\mathbf{p})\cdot\exp(-t/\tau)\ , \qquad (7.3)$$

where $\theta(x)$ is the unit step function which vanishes for $x<0$, and $\delta(x)$ is the delta function which vanishes for $x\neq 0$. The source was assumed to be at rest in the center-of-momentum system, and the emitted particles were then boosted into the laboratory rest frame ($\beta = 0.2086$). Longitudinal and transverse correlation

functions for a given R and τ were constructed according to the Koonin-Pratt formalism [Gong 91a].

For a given parameter set R and τ, the agreement between measured and calculated correlation functions was quantified by the value of χ^2/ν (chi-squared per degree of freedom) evaluated in the region q=10-40 MeV/c, where the measured difference between longitudinal and transverse correlation functions is most pronounced and where distortions due to detector resolution are small [Gong 91b]. Contour plots of χ^2/ν as a function of the parameters R and τ are shown in Figure 7.8 for the two cuts on the total momentum of the emitted proton pairs, P≥480 MeV/c and P≥580 MeV/c. The best agreement between measured and calculated correlation functions is obtained for source radii of R = 3 - 4 fm; the extracted emission times are τ = 1700± 200 fm/c and 1200± 200 fm/c for the momentum cuts P ≥ 480 MeV/c and P ≥ 580 MeV/c, respectively. (Uncertainties in extracted lifetimes are estimated from χ^2/ν values.) Calculated longitudinal and transverse correlation functions giving the best fit to the data are shown as solid and dashed curves in Figure 7.9.

The extracted source radius is smaller than that of the compound nucleus. The reason for such a small source radius is not fully understood. It may reflect an artifact of the present schematic source parametrization which neglects anisotropies of emission resulting from angular momentum effects. It is interesting, however, that the extracted average emission time scale decreases slightly as the total momentum threshold is increased. Such a dependence is expected [Prat 87, Gong 91a] for emission from a cooling compound nucleus.

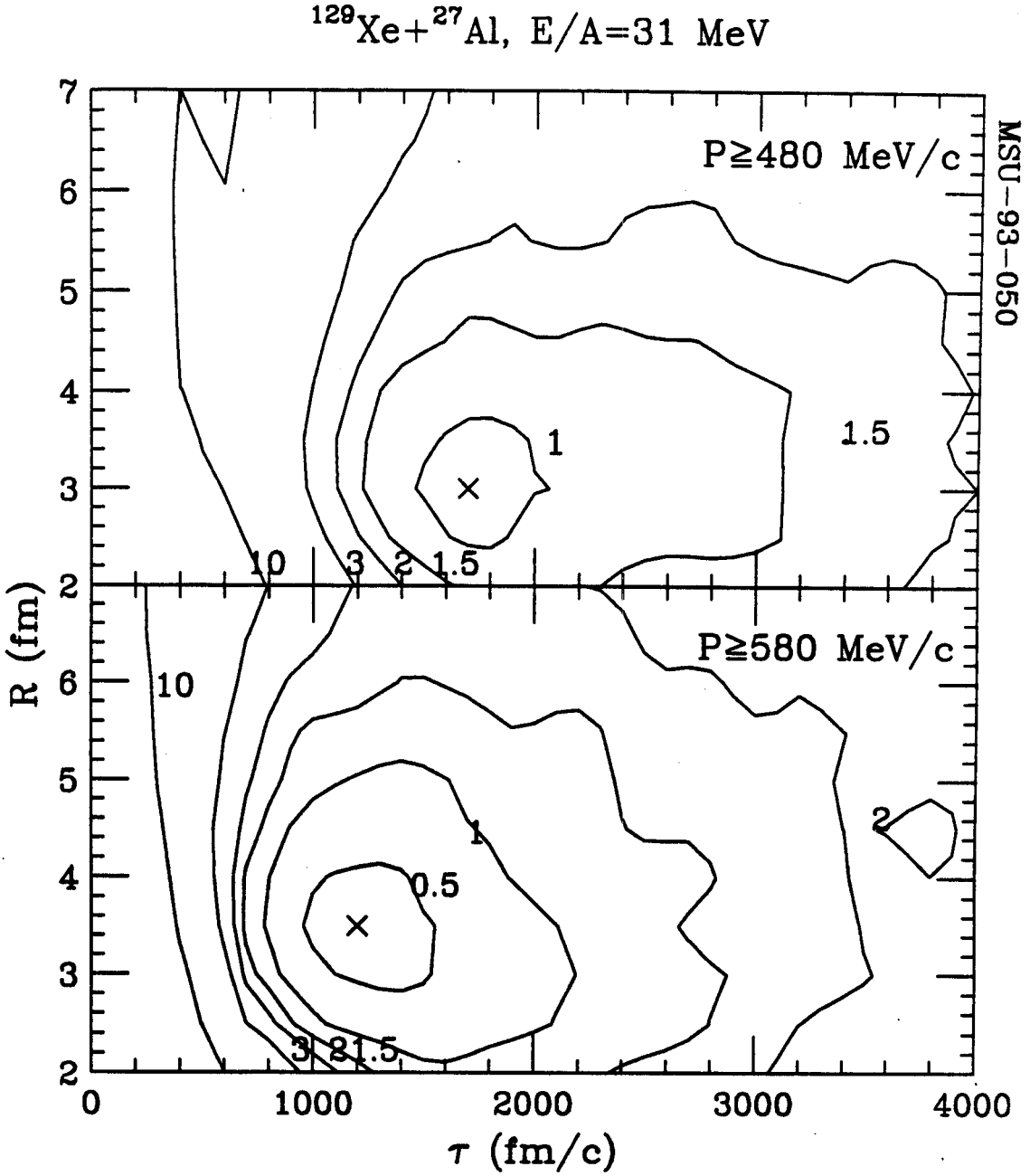

Figure 7.8. Contour plots of χ^2/ν (chi-squared per degree of freedom) evaluated by comparing measured longitudinal and transverse correlation functions (over the range of 10 MeV/c ≤ q ≤ 40 MeV/c to those predicted for emission from a schematic source with radius and lifetime parameters R and τ. The upper and lower panels compare correlation functions constructed from pairs with P≥480 MeV/c and P≥580 MeV/c, respectively. X's mark parameter sets used for calculated correlation functions shown in Figure 7.9.

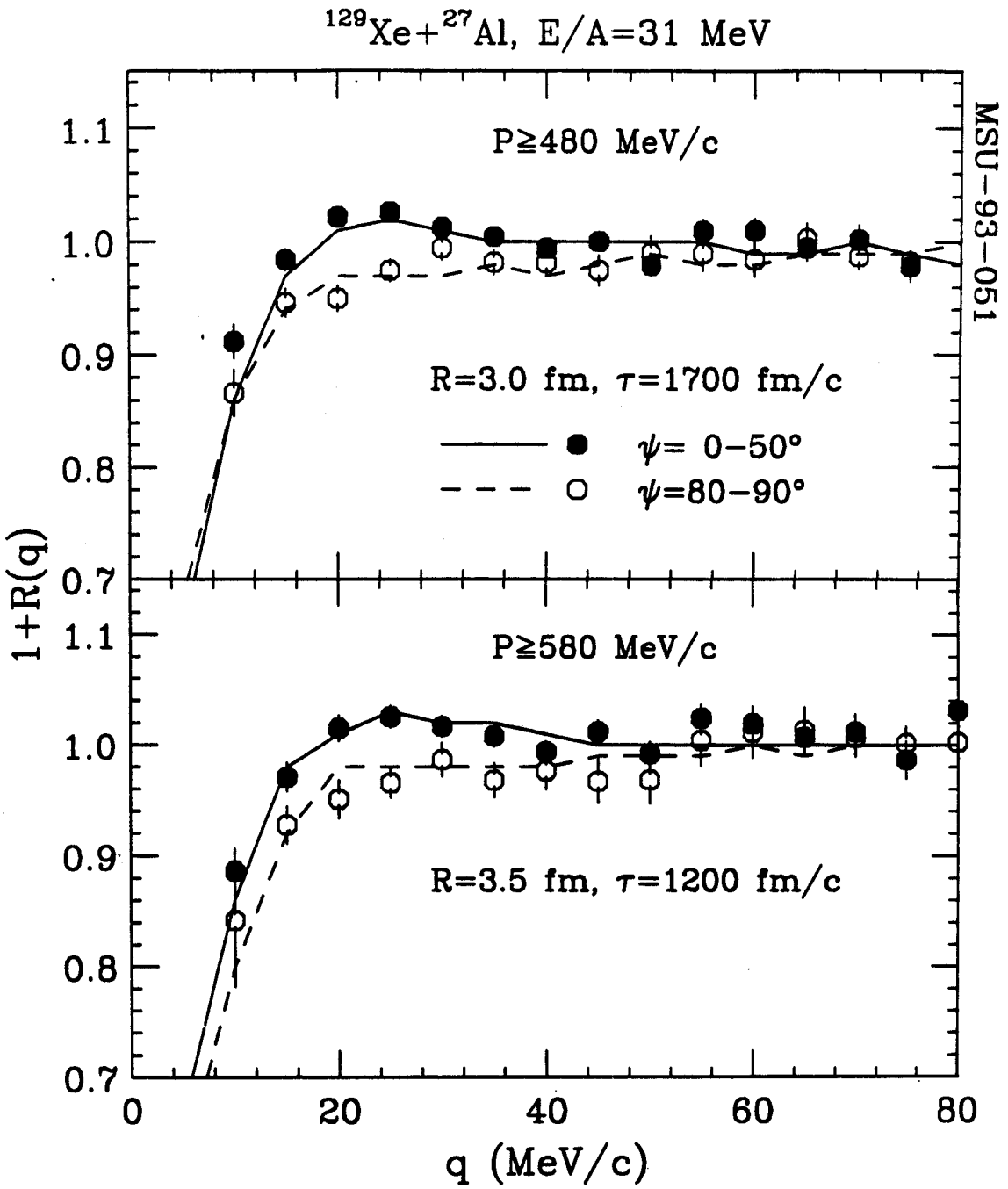

Figure 7.9. Longitudinal (filled circles) and transverse (open circles) two-proton correlation functions for the reaction ^{129}Xe + ^{27}Al at E/A=31 MeV, evaluated in the center-of-momentum frame of the projectile and target. Top and bottom panels show data for cuts on the total momentum of the proton pair of P ≥ 480 MeV/c and P ≥ 580 MeV/c, respectively. Solid and dashed curves show calculations of longitudinal and transverse correlation functions using the source parametrization of Equation 7.3 with the parameters given in the figure.

Chapter 8 - Summary and Conclusions

In this work, we have used the technique of two-proton intensity interferometry to explore the space-time structure of emitting sources created in intermediate energy heavy ion collisions. We have discussed the Koonin-Pratt formalism, the theoretical framework which relates the two-proton correlation function to the phase space population density. In the context of this formalism, schematic calculations were presented that illustrated how the two-proton correlation function may provide a "snapshot" of the proton configuration at the time of proton emission.

The two-proton correlation function is sensitive to the spatial separation of emitted protons due to final state interactions and quantum statistical effects. An attractive S-wave resonance in the strong nuclear interaction leads to a pronounced bump in the correlation function at q≈20 MeV/c. Sources with small spatial and temporal extent produce larger bumps, while sources with large spatial dimensions ($r \gtrsim 10$ fm) or long lifetimes ($c\cdot\tau \gtrsim 10$ fm) lead to no bump at all. The Coulomb repulsion produces a minimum at q=0, with smaller or shorter-lived sources producing stronger minima.

A directional dependence in the quantum statistical suppression of the correlation function due to the Pauli principle allows independent extraction of source size and lifetime. Appropriate cuts on the relative orientation between the total and relative momentum of the proton pair define the longitudinal and transverse correlation functions. The overall magnitude of the correlations

indicates the space-time extent of the source, while the difference between longitudinal and transverse correlations reveals its lifetime. If the rest frame of the emitting source is identified and if sufficiently tight cuts are performed, lifetimes on the order of $\tau \sim$ 30-3000 fm/c may be extracted. This range of emission timescales cover those expected for proton emission from a hot nuclear gas, as well as from cooling nuclear systems in the liquid state.

Single- and two-proton yields at $\langle\theta_{lab}\rangle$=38° were measured with a high resolution hodoscope in coincidence with charged particles detected in the MSU 4π Array. Two-proton correlation functions were constructed from the yields measured in the hodoscope, and information about the impact parameter of the event was obtained from the total transverse energy measured in the 4π Array. Central and peripheral collisions were characterized by high and low values of the total transverse energy, respectively.

Correlation functions for both central and peripheral events exhibited stronger bumps at q≈20 MeV/c when proton pairs with high total momentum were selected. Statistical and dynamical models of heavy ion collisions associate more energetic particles with the early stages of the collision. Using such associations as a guide, we conclude that the proton-emitting source created in the collisions increases in size and/or emission timescale as the reaction evolves. The total momentum dependence was observed to be stronger for collisions with high total transverse energy than for those with low total transverse energy, indicating a significant difference in the evolution of central and peripheral collisions.

A dynamical model based on the Boltzmann-Uehling-Uhlenbeck (BUU) transport equation was used to generate phase space distributions for protons emitted from ^{36}Ar+^{45}Sc collisions at various impact parameters. Following the Koonin-Pratt formalism, we calculated two-proton correlation functions for

central and peripheral events. The total momentum dependence of the experimental correlations was well reproduced by the predicted correlation functions for central events, indicating that the model describes the reaction evolution well. For peripheral collisions, however, the total momentum dependence was underpredicted by the model. This discrepancy may be due to inadequacies in the model's description of nuclear surface effects.

The issue of impact parameter selection was examined in detail. In particular, reduced impact parameter scales were constructed for three different global observables, each of which presumably gives an indication of the impact parameter. The impact parameter resolution associated with cuts on each of these observables was approximately evaluated. Next, we developed two different methods of realistically incorporating experimental impact parameter cuts into theoretical calculations. In the construction of impact parameter selected correlation functions for the BUU theory, the two methods gave almost identical results, giving us confidence that the observed discrepancy between experimental and theoretical correlations functions for peripheral events is not due to incorrect impact parameter selection.

Next, we studied the use of longitudinal and transverse correlation functions as a tool in a search for finite lifetime effects. We discussed the importance of clear identification of the rest frame of the emitting source. Then, we examined the longitudinal and transverse correlation functions for two systems for which the source velocity is reasonably well-determined.

For central $^{36}Ar+^{45}Sc$ collisions, it is reasonable to assume that the proton-emitting source moves with the center-of-momentum velocity of the system. We found that if this source velocity was assumed, tight cuts on $\psi = \mathrm{Cos}^{-1}(\mathbf{q}\cdot\mathbf{P}/qP)$ revealed the effect of a finite emission timescale on the order of 25-40 fm/c. Such timescales are consistent with those predicted by the BUU model, and may

indicate the formation of a nuclear system in the gaseous state. Improper choice of the assumed source rest frame obscured the lifetime effect. Correlation functions for protons emitted from peripheral collisions, for which there may exist no unique source frame, did not show a lifetime effect.

We also reanalyzed proton coincidence data for the reaction $^{129}Xe+^{27}Al$ at E/A=31 MeV, for which the spread of possible source velocities is small. Assuming that the source velocity was the center-of-momentum velocity of the system, we observed differences between longitudinal and transverse correlation functions consistent with emission timescales on the order of ~1500 fm/c, and source radii on the order of 3 fm. Furthermore, more energetic protons were associated with shorter emission timescales. These results are consistent with statistical proton emission from a hot cooling residue, analogous to the evaporation from a cooling liquid drop.

APPENDIX

Appendix A - Raw and Physics Tape Formats

Raw data taken on-line in our experiment followed the 4π Array formatting standard, which is itself a variant of the NSCL formatting standard. Off-line, we created "physics tapes," which contained calibrated data in a somewhat streamlined format.

Below, we briefly record the data formats of the raw and physics tapes for completeness. Details of the raw tape format may be found in the 4π L'User's Guide [Winf 91].

A.1 Raw Tape Format

The 4π data acquisition system organizes data into "buffers" of 4096 16-bit words, in accordance with the NSCL standard. The first 16 words of each buffer constitute a "header" containing information about the buffer, such as the buffer sequence number and number of valid words in the buffer.

The readout scheme of the 4π Array electronics imposes a unique structure onto the raw data format. This is due to the use of ECLine readout of ADCs and QDCs, as well as to the front end system used.

All valid data from an entire module (FERA or Silena ADC) is read out at once in zero-suppressed mode via an ECLine front panel interface. The use of FERA Drivers (LeCroy model #4301) to read out groups of modules mandated the grouping of modules that used a common gate. Therefore, all FERA's that digitize Forward Array "slow" signals constituted a group and were read out sequentially. Other groups were then read out in sequence. Consequently, the

various elements of data concerning one detector– fast, slow, and time (or ΔE, E, and time for a hodoscope detector)– do not appear near each other in the raw data buffer, and decoding of module header words is required to "relink" the data.

A second feature of the raw buffer in the 4π format arises due to the front end system used, the so-called "FERA Faucet System," designed by Michael Maier at the NSCL. In each event, data is loaded from the ECL data bus into a 512 kB memory array, which sits in a VME crate with the front end slave and master CPU's. Before loading data from an event, a special word is loaded into the memory to separate data from different events. When the memory becomes nearly full, its contents are packaged by the slave cpu into small "FERA Faucet (FF) buffers," each of which has its own 16-word header, as well as a two-word trailer to mark the end of the FF buffer. These FF buffers are then inserted into the 8 kB NSCL buffers. Although usually a NSCL buffer will contain only one FF buffer, in principle it may contain several, each with its own header and trailer. Therefore, the number of FF buffers is indicated in the NSCL buffer header.

The data format is indicated in Figure A.1. Events are separated by the hexadecimal word 'FFFF'. Each module has a header, followed by one or more data words. The crate and slot number of each module is encoded in each module header, and the channel number is encoded in each data word. A simple map links each data word with a detector signal component.

The buffer type, indicated by the second word in the buffer header, follows the NSCL standard and is useful for uniform processing of control information, such as begin-of-run markers.

A.2 Physics Tape Format

Calibrated data was written to tape in a simpler format designed to maximize analysis efficiency. The buffer header follows the NSCL standard, and

4π event separators were employed. The more natural order of the data reduces the need for cumbersome arrays necessary for data reorganization and encourages the use of a simpler program architecture.

Our physics tape format is shown in Figure A.2. Each detector that fired carries 3 or 5 words of data, depending on whether it was an element in the 4π Array or the 56-element hodoscope.

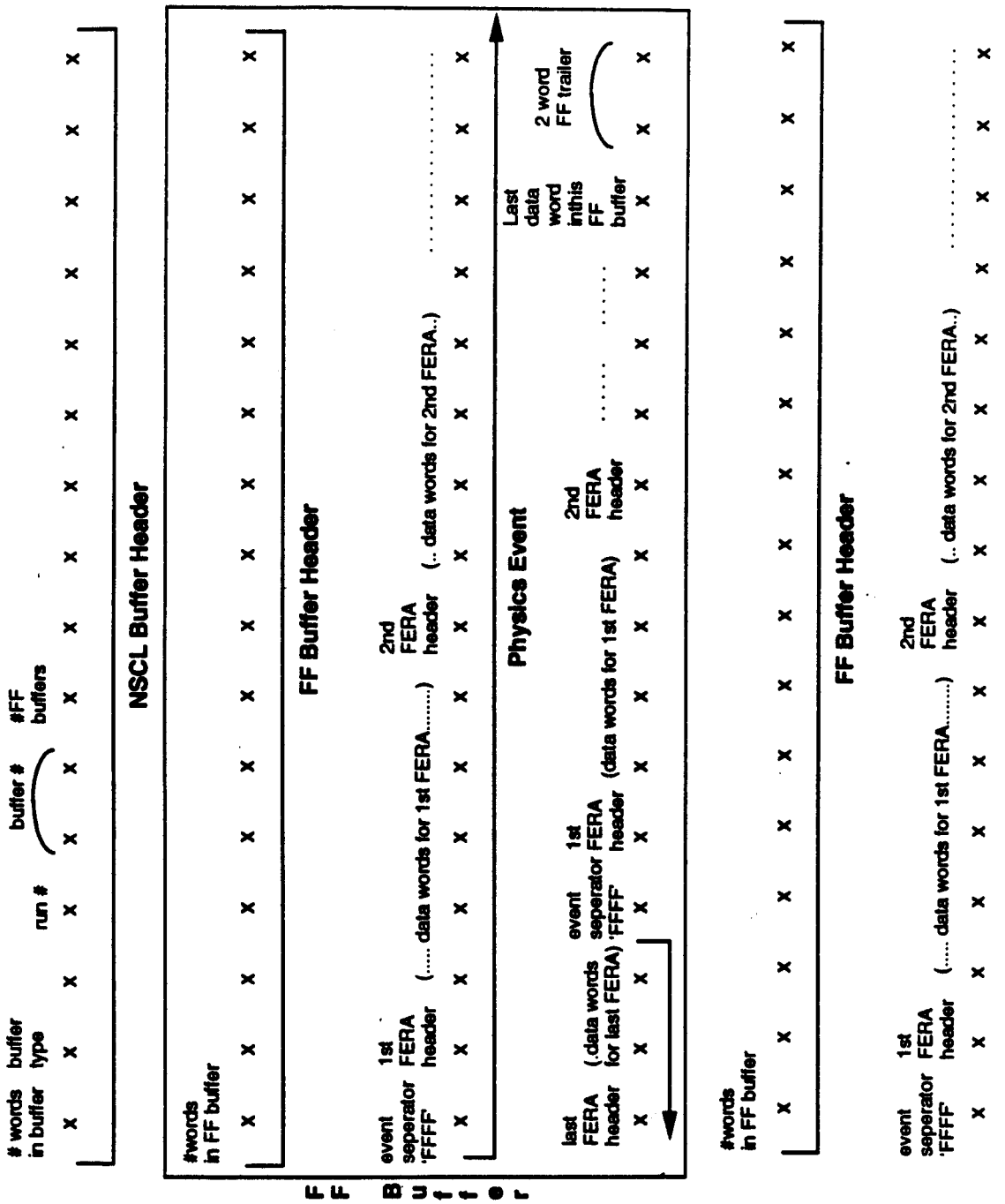

Figure A.1. The data format of the uncalibrated "raw" tapes shows a hierarchical structure. Data words are indicated by x's. These are grouped into physics events, FF buffers, and NSCL buffers.

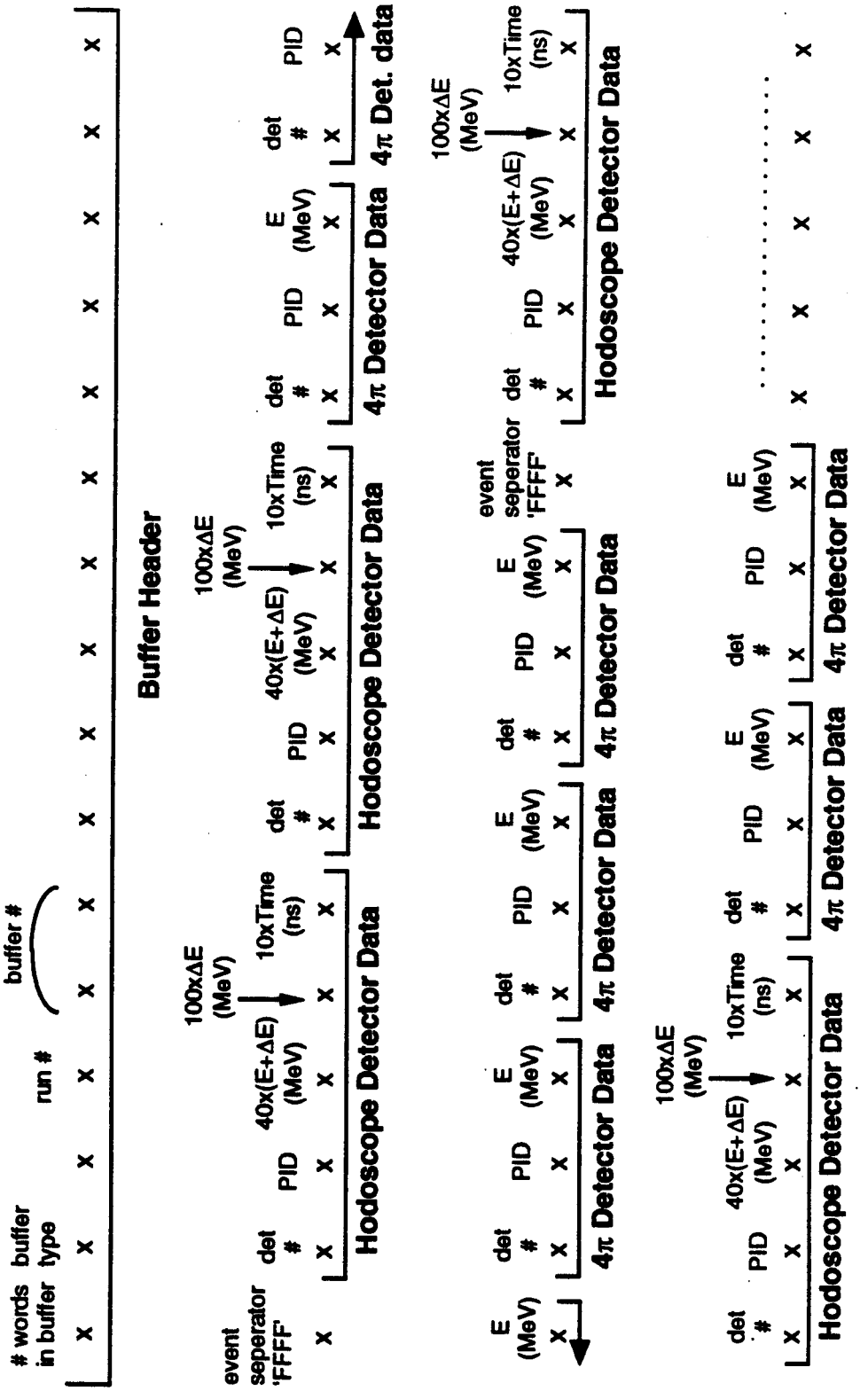

Figure A.2. The data format of calibrated "physics" tapes follows a more natural structure. Data for detector elements are grouped together.

LIST OF REFERENCES

List of References

[Aich 85] J. Aichelin and G. Bertsch, Phys. Rev. **C31**, 1730 (1985)

[Aich 86] J. Aichelin, Phys. Rev. **C33**, 537 (1986)

[Ajze 86] F. Ajzenberg-Selove, Nucl. Phys. **A449**, No. 1, 86 (1986)

[Alm 93] T. Alm, G. Röpke, and M. Schmidt, Phys. Lett. **B301**, 170 (1993)

[Ardo 89] D. Ardouin, F. Lautrido, D. Durand, D. Goujdami, F. Guilbault, C. Lebrun, A. Péghaire, J. Québert, and F. Saint-Laurent, Nucl. Phys. **A495**, 57c (1989).

[Awes 88] T.C. Awes, R.L. Ferguson, F.E. Obenshain, F. Plasil, G.R. Young, S. Pratt, Z. Chen, C.K. Gelbke, W.G. Lynch, J. Pochodzalla, H.M. Xu, Phys. Rev. Lett. **61**, 2665 (1988).

[Baue 86] W. Bauer, G.F. Bertsch, W. Cassing, and U. Mosel, Phys. Rev. **C34**, 2127 (1986).

[Baue 87] W. Bauer, Nucl. Phys. **A471**, 604 (1987)

[Baue 88] W. Bauer, G.D. Westfall, D. Fox, and D. Cebra, Phys. Rev. **C37**, 664 (1988)

[Baue 92] W. Bauer, C.K. Gelbke, and S. Pratt, Ann. Rev. Nucl. Part. Sci. **42**, 77 (1992).

[Bern 85] M.A. Bernstein, W.A. Friedman, W.G. Lynch, C.B. Chitwood, D.J. Fields, C.K. Gelbke, M.B. Tsang, T.C. Awes, R.L. Ferguson, F.E. Obenshain, F. Plasil, R.L. Robinson, and G.R. Young, Phys. Rev. Lett. **54**, 402 (1985)

[Bert 84] G.F. Bertsch, H. Kruse, and S. Das Gupta, Phys. Rev. **C29**, 673 (1984).

[Bert 89] G.F. Bertsch, Nucl. Phys. **A498**, 173c (1989).

[Boal 86a] D.H. Boal and J.C. Shillcock, Phys. Rev. **C33**, 549 (1986).

[Boal 86b] D.H. Boal and H. DeGuise, Phys. Rev. Lett. **57**, 2901 (1986).

[Boal 90] D.H. Boal, C.K. Gelbke, and B.K. Jennings, Rev. Mod. Phys. **62**, 553 (1990).

[Bowm 91] D.R. Bowman, G.F. Peaslee, N. Carlin, R.T. de Souza, C.K. Gelbke, W.G. Gong, Y.D. Kim, M.A. Lisa, W.G. Lynch, L. Phair, M.B. Tsang, C. Williams, N. Colonna, K. Hannold, M.A. McMahan, G.J. Wozniak, L.G. Moretto, and W.A. Friedman, Phys. Rev. Lett. **67**, 1527 (1991).

[Bowm 93] D.R. Bowman, G.F. Peaslee, N. Carlin, R.T. de Souza, C.K. Gelbke, W.G. Gong, Y.D. Kim, M.A. Lisa, W.G. Lynch, L. Phair, M.B. Tsang, C. Williams, N. Colonna, K. Hannold, M.A. McMahan, G.J. Wozniak, and L.G. Moretto, Phys. Rev. Lett. **70**, 3534 (1993).

[Cebr 89] D.A. Cebra, W. Benenson, Y. Chen, E. Kashy, A. Pradhan, A. Vander Molen, G.D. Westfall, W.K. Wilson, D.J. Morrissey, R.S. Tickle, R. Korteling, and R.L. Helmer, Phys. Lett. **227B**, 336 (1989).

[Cebr 90] D. Cebra, Ph.D. Thesis, Department of Physics, Michigan State University (1990).

[Chen 87a] Z. Chen, C.K. Gelbke, J. Pochodzalla, C.B. Chitwood, D.J. Fields, W.G. Lynch, and M.B. Tsang, Phys. Lett. **B186**, 280 (1987).

[Chen 87b] Z. Chen, C.K. Gelbke, J. Pochodzalla, C.B. Chitwood, D.J. Fields, W.G. Gong, W.G. Lynch, and M.B. Tsang, Nucl. Phys. **A473**, 564 (1987).

[Chen 87c] Z. Chen, C.K. Gelbke, W.G. Gong, T.D. Kim, W.G. Lynch, M.R. Maier, J. Pochodzalla, M.B. Tsang, F. Saint-Laurent, D. Ardouin, H.

Delagrange, H. Doubre, J. Kasagi, A. Kyanowski, A. Péghaire, J. Péter, E. Rosato, G. Bizard, F. Lefèbvres, B. Tamain, J. Québert, and Y.P. Viyogi, Phys. Rev. **C36**, 2297 (1987).

[Chit 85] C.B. Chitwood, J. Aichelin, D.H. Boal, G. Bertsch, D.J. Fields, C.K. Gelbke, W.G. Lynch, M.B. Tsang, J.C. Shillcock, T.C. Awes, R.L. Ferguson, F.E. Obenshain, F. Plasil, R.L. Robinson, and G.R. Young, Phys. Rev. Lett. **54**, 302 (1985).

[Chit 86a] C.B. Chitwood, C.K. Gelbke, J. Pochodzalla, Z. Chen, D.J. Fields, W.G. Lynch, R. Morse, M.B. Tsang, D.H. Boal, and J.C. Shillcock, Phys. Lett **172B**, 27 (1986).

[Chit 86b] C.B. Chitwood, D.J. Fields, C.K. Gelbke, D.R. Klesch, W.G. Lynch, M.B. Tsang, T.C. Awes, R.L. Ferguson, F.E. Obenshain, F. Plasil, R.L. Robinson, and G.R. Young, Phys. Rev. **C34**, 858 (1986).

[de So 91] R.T. de Souza, L. Phair, D.R. Bowman, N. Carlin, C.K. Gelbke, W.G. Gong, Y.D. Kim, M.A. Lisa, W.G. Lynch, G.F. Peaslee, M.B. Tsang, H.M. Xu, F. Zhu, and W. Friedman, Phys. Lett. **B268**, 6 (1991).

[DeYo 89] P.A. DeYoung, M.S. Gordon, Xiu qin Lu, R.L. McGrath, J.M. Alexander, D.M. de Castro Rizzo, and L.C. Vaz, Phys. Rev. **C39**, 128 (1989).

[DeYo 90] P.A. DeYoung, C.J. Gelderloos, D. Kortering, J. Sarafa, K. Zienert, M.S. Gordon, B.J. Fineman, G.P. Gilfoyle, X. Lu, R.L. McGrath, D.M. de Castro Rizzo, J.M. Alexander, G. Auger, S. Kox, L.C. Vaz, C. Beck, D.J. Henderson, D.G. Kovar, and M.F. Vineyard, Phys. Rev. **C41**, R1885 (1990).

[Dupi 88] P. Dupieux, J.P. Alard, J. Augerat, R. Babinet, N. Bastid, F. Brochard, P. Charmensat, N. De Marco, H. Fanet, Z. Fodor, L. Fraysse, J. Girard, P. Gorodetzky, J. Gosset, C. Laspalles, M.C. Lemaire, D. L'Hôte, B. Lucas, J. Marroncle, G. Montarou, M.J. Parizet, J. Poitou, D. Qassoud, C. Racca, A. Rahmani, W. Schimmerling, and O. Vallete, Phys. Lett. **B200**, 17 (1988).

[Elma 91] A. Elmaani, N.N. Ajitanand, J.M. Alexander, R. Lacey, S. Kox, E. Liatard, F. Merchez, T. Motobayashi, B. Noren, C. Perrin, D. Rebreyend, Tsan Ung Chan, G. Auger, and S. Groult, Phys. Rev. **C43**, R2474 (1991)

[Eraz 91] B. Erazmus, N. Carjan, and D. Ardouin, Phys. Rev. C44, 2663 (1991).

[Feyn 65] R. Feynman, "The Character of Physical Law", 130, MIT Press, Cambridge, MA, 1965

[Fox 88] D. Fox, D.A. Cebra, J. Karn, C. Parks, A. Pradhan, A. Vander Molen, J. van der Plicht, G.D. Westfall, W.K. Wilson, and R.S. Tickle, Phys. Rev. **C38**, 146 (1988).

[Fox 93] D. Fox, R.T. de Souza, L. Phair, D.R. Bowman, N. Carlin, C.K. Gelbke, W.G. Gong, Y.D. Kim, M.A. Lisa, W.G. Lynch, G.F. Peaslee, M.B. Tsang, and F. Zhu, Phys. Rev. **C47**, R421 (1993).

[Frie 83] W.A. Friedman and W.G. Lynch, Phys. Rev. **C28**, 16 (1983).

[Fuch 90] H. Fuchs and H. Homeyer, Contribution to CORRINE 90, International Workshop on Particle Correlations and Interferometry in Nuclear Collisions, D. Ardouin, editor, World Scientific 1990.

[Glas 93] T. Glasmacher, C.K. Gelbke, and S. Pratt, submitted to Phys. Lett. **B**, (1993).

[Gold 60] G. Goldhaber, S. Goldhaber, W. Lee, and A. Pais, Phys. Rev. **120**, 300 (1960).

[Gong 88] W.G. Gong, Y.D. Kim, G. Poggi, Z. Chen, C.K. Gelbke, W.G. Lynch, M.R. Maier, T. Murakami, M.B. Tsang, H.M. Xu, and K. Kwiatkowski, Nucl. Instr. and Meth. **A268**, 190 (1988).

[Gong 90a] W.G. Gong, N. Carlin, C.K. Gelbke, and R. Dayton, Nucl. Instr. and Meth. **A287**, 639 (1990).

[Gong 90b] W.G. Gong, C.K. Gelbke, N. Carlin, R.T. de Souza, Y.D. Kim, W.G. Lynch, T. Murakami, G. Poggi, D. Sanderson, M.B. Tsang, H.M. Xu, D.E. Fields, K. Kwiatkowski, R. Planeta, V.E. Viola, Jr., S.J. Yennello, and S. Pratt, Phys. Lett. **B246**, 21 (1990).

[Gong 90c] W.G. Gong, W. Bauer, C.K. Gelbke, N. Carlin, R.T. de Souza, Y.D. Kim, W.G. Lynch, T. Murakami, G. Poggi, D. Sanderson, M.B. Tsang, H.M. Xu, S. Pratt, D.E. Fields, K. Kwiatkowski, R. Planeta, V.E. Viola, Jr., and S.J. Yennello, Phys. Rev. Lett. **65**, 2114 (1990).

[Gong 91a] W.G. Gong, W. Bauer, C.K. Gelbke, and S. Pratt, Phys. Rev. **C43**, 781 (1991).

[Gong 91b] W.G. Gong, C.K. Gelbke, W. Bauer, N. Carlin, R.T. de Souza, Y.D. Kim, W.G. Lynch, T. Murakami, G. Poggi, D. Sanderson, M.B. Tsang, H.M. Xu, D.E. Fields, K. Kwiatkowski, R. Planeta, V.E. Viola, Jr., S.J. Yennello, and S. Pratt, Phys. Rev. **C43**, 1804 (1991).

[Gong 91c] W.G. Gong, Ph.D. Thesis, Department of Physics, Michigan State University (1991)

[Gong 92] W.G. Gong, Y.D. Kim, and C.K. Gelbke, Phys. Rev. **C45**, 863 (1992)

[Gouj 91] D. Goujdami, F. Guilbault, C. Lebrun, D. Ardouin, H. Dabrowski, S. Pratt, P. Lautridou, R. Boisgard, J. Québert, and A. Péghaire, Z. Phys. **A339**, 293 (1991).

[Gust 84] H.A. Gustafsson, H.H. Gutbrod, B. Kolb, H. Loehner, B. Ludewigt, A.M. Poskanzer, T. Renner, H. Riedesel, H.G. Ritter, A. Warwick, F. Weik, and H. Wieman, Phys. Rev. Lett **53**, 544 (1984).

[Hanb 54] R. Hanbury Brown and R.Q. Twiss, Phil. Mag. **45**, 663 (1954)

[Harv 62] B.G. Harvey, J. Cerney, R.H. Pehl, and E. Rivet, Nucl. Phys. **39**, 160 (1962).

[Hong 92] X. Hongfei, Z. Wenlong, Z. Yongtai, G. Zhongyan, H. Xiaoqing, L. Guanhua, Z. Jianqun, Y. Shizhi, Z. Youxiong, W. Zhiyong, and F. Enjie, Chin. J. Nucl. Phys. **14**, 214 (1992)

[Kämp 93] B. Kämpfer, R. Kotte, J. Mösner, W. Neubert, D. Wohlfarth, J.P. Alard, Z. Basrak, N. Bastid, I.M. Belayev, Th. Blaich, A. Buta, R. Čaplar, C. Cerruti, N. Cindro, J.P. Coffin, P. Dupieux, J. Erö, Z.G. Fan, P. Fintz, Z. Fodor, R. Freifelder, L. Fraysse, S. Frolov, A. Gobbi, Y. Grigorian, G. Guillaume, N. Herrmann, K.D. Hildenbrand, S. Hölbling, O. Houari, S.C. Jeong, M. Jorio, F. Jundt, J. Kecskemeti, P. Koncz, Y. Korchagin, M. Krämer, C. Kuhn, I. Legrand, A. Lebedev, C. Maguire, V. Manko, T. Matulewicz, G. Mgebrishvili, D. Moisa, G. Montaru, I. Montbel, P. Morel, D. Pelte, M. Petrovici, F. Rami, W. Reisdorf, A. Sadchikov, D. Schüll, Z. Seres, B. Sikora, V. Simion, S. Smolyankin, U. Sodan, K. Teh, R. Tezkratt, M. Trzaska, M.A. Vasiliev, P. Wagner, J.P. Wessels, T. Weinold, Z. Wilhelmi, A.L. Zhilin, submitted to Phys. Rev. C (1993)

[Kim 91] Y.D. Kim, R.T. de Souza, D.R. Bowman, N. Carlin, C.K. Gelbke, W.G. Gong, W.G. Lynch, L. Phair, M.B. Tsang, F. Zhu, and S. Pratt, Phys. Rev. Lett. **67**, 14 (1991)

[Kim 92] Y.D. Kim, R.T. de Souza, C.K. Gelbke, W.G. Gong, and S. Pratt, Phys. Rev. **C45**, 387 (1992)

[Knol 80] J. Knoll, Nucl. Phys. **A343**, 511 (1980)

[Koon 77] S.E. Koonin, Phys. Lett. **70B**, 43 (1977).

[Kopy 72] G.I. Kopylov and M.I. Podgoretskii, Sov. J. Nucl. Phys. **15**, 219 (1972).

[Kopy 74] G.I. Kopylov, Phys. Lett. **B50**, 472 (1974)

[Koro 91] M. Korolija, D. Shapira, N. Cindro, J. Gomez del Campo, H.J. Kim, K. Teh, and J. Y. Shea, Phys. Rev. Lett. **67**, 572 (1991)

[Kund 93] G.J. Kunde, J. Pochodzalla, E. Berdermann, B. Berthier, C. Cerruti, C.K. Gelbke, J. Hubele, P. Kreutz, S. Leray, R. Lucas, U. Lynen, U. Milkau, C. Ngô, C.H. Pinkenburg, G. Raciti, H. Sann, and W. Trautmann, Phys. Rev. Lett. **70**, 2545 (1993)

[Kyan 86] A. Kyanowski, F. Saint-Laurent, D. Ardouin, H. Delagrange, H. Doubre, C. Grégoire, W. Mittig, A. Péghaire, J. Péter, Y.P. Viyogi, B. Zwieglinski, J. Québert, G. Bizard, F. Lefèbvres, B. Tamain, J. Pochodzalla, C.K. Gelbke, W. Lynch, and M. Maier, Phys. Lett. **B181**, 43 (1986).

[Li 91a] B.A. Li and W. Bauer, Phys. Rev. **C44**, 450 (1991).

[Li 91b] B.A. Li, W. Bauer, and G.F. Bertsch, Phys. Rev. **C44**, 2095 (1991).

[Li 93a] T. Li, W. Bauer, D. Craig, M. Cronqvist, E. Gualtieri, S. Hannuschke, R. Lacey, W.J. Llope, T. Reposeur, A.M. Vander Molen, G.D. Westfall, W.K. Wilson, J.S. Winfield, J. Yee, S.J. Yennello, A. Nadasen, R.S. Tickle, and E. Norbeck, Phys. Rev. Lett. **70**, 1924 (1993).

[Li 93b] T. Li, W. Bauer, D. Craig, M. Cronqvist, E. Gualtieri, S. Hannuschke, R. Lacey, W.J. Llope, T. Reposeur, A.M. Vander Molen, G.D. Westfall, W.K. Wilson, J.S. Winfield, J. Yee, S.J. Yennello, A. Nadasen, R.S. Tickle, and E. Norbeck, submitted to Phys. Rev. **C** (1993).

[Lisa 91] M.A. Lisa, W.G. Gong, C.K. Gelbke, and W.G. Lynch, Phys. Rev. **C44**, 2865 (1991).

[Lisa 93a] M.A. Lisa, C.K. Gelbke, W. Bauer, P. Decowski, W.G. Gong, E. Gualtieri, S. Hannuschke, R. Lacey, T. Li, W.G. Lynch, C.M. Mader, G.F. Peaslee, T. Reposeur, A.M. Vander Molen, G.D. Westfall, J. Yee, and S.J. Yennello, Phys. Rev. Lett. **70**, 3709 (1993).

[Lisa 93b] M.A. Lisa, C.K. Gelbke, W. Bauer, P. Decowski, W.G. Gong, E. Gualtieri, S. Hannuschke, R. Lacey, T. Li, W.G. Lynch, C.M. Mader, G.F. Peaslee, T. Reposeur, A.M. Vander Molen, G.D. Westfall, J. Yee, and S.J. Yennello, Submitted to Phys. Rev. **C** (1993).

[Lisa 93c] M.A. Lisa, C.K. Gelbke, P. Decowski, W.G. Gong, E. Gualtieri, S. Hannuschke, R. Lacey, T. Li, W.G. Lynch, G.F. Peaslee, T. Reposeur,

S. Pratt, A.M. Vander Molen, G.D. Westfall, J. Yee, and S.J. Yennello, Submitted to Phys. Rev. Lett. (1993).

[Lisa 93d] M.A. Lisa, W.G. Gong, C.K. Gelbke, N. Carlin, R.T. de Souza, Y.D. Kim, W.G. Lynch, T. Murakami, G. Poggi, M.B. Tsang, H.M. Xu, K. Kwiatkowski, V.E. Viola, Jr., and S.J. Yennello, Submitted to Phys. Lett. **B**, (1993).

[Lync 82] W.G. Lynch, L.W. Richardson, M.B. Tsang, R.E. Ellis, C.K. Gelbke, and R.E. Warner, Phys. Lett. **108B**, 274 (1982)

[Lync 83] W.G. Lynch, C.B. Chitwood, M.B. Tsang, D.J. Fields, D.R. Klesch, C.K. Gelbke, G.R. Young, T.C. Awes, R.L. Ferguson, F.E. Obenshain, F. Plasil, R.L. Robinson, and A.D. Panagiotou, Phys. Rev. Lett. **51**, 1850 (1983).

[Lync 84] W.G. Lynch, C.B. Chitwood, M.B. Tsang, D.J. Fields, D.R. Klesch, C.K. Gelbke, G.R. Young, T.C. Awes, R.L. Ferguson, F.E. Obenshain, F. Plasil, R.L. Robinson, and A.D. Panagiotou, Phys. Rev. Lett. **52**, 2302 (1984).

[Mach 92] H. Machner, M. Palarczyk, H.W. Wilschut, M. Nolte, and E.E. Koldenhof, Phys. Lett **B280**, 16 (1992)

[Mess 76] A. Messiah, "Quantum Mechanics," Volume 1, North Holland Publishing Company, Amsterdam (1976)

[Mors 90] R. Morse, Ph.D. Thesis, Department of Physics, Massachusetts Institute of Technology, (1990)

[Ogil 91] C.A. Ogilvie, J.C. Adloff, M. Begemann-Blaich, P. Bouissou, J. Hubele, G. Imme, I. Iori, P. Kreutz, G.J. Kunde, S. Leray, V. Lindenstruth, Z. Liu, U. Lynen, R.J. Meijer, U. Milkau, W.F.J. Müller, C. Ngô, J. Pochodzalla, G. Raciti, G. Rudolf, H. Sann, A. Schüttauf, W. Seidel, L. Stuttge, W. Trautmann, and A. Tucholski, Phys. Rev. Lett. **67**, 1214 (1991).

[Peas 93] G.F. Peaslee, W. Bauer, D.R. Bowman, N. Carlin, R.J. Charity, M. Chartier, J. Dinius, D. Fox, W.A. Friedman, C.K. Gelbke, D.O.

Handzy, W.C. Hsi, G.J. Kunde, M-C. Lemaire, M.A. Lisa, W.G. Lynch, U. Lynen, C.M. Mader, L. Phair, J. Pochodzalla, H. Sann, C. Schwarz, L.G. Sobotka, R.T. de Souza, S.R. Souza, W. Trautmann, M.B. Tsang, G. Van Buren, and C. Williams, submitted to Phys. Rev. **C**, rapid communications (1993)

[Phai 92] L. Phair, D.R. Bowman, C.K. Gelbke, W.G. Gong, Y.D. Kim, M.A. Lisa, W.G. Lynch, G.F. Peaslee, R.T. de Souza, M.B. Tsang, and F. Zhu, Nucl. Phys. **A548**, 489 (1992).

[Poch 86] J. Pochodzalla, C.B. Chitwood, D.J. Fields, C.K. Gelbke, W.G. Lynch, M.B. Tsang, D.H. Boal, and J.C. Shillcock, Phys. Lett. **B174**, 36 (1986).

[Poch 87] J. Pochodzalla, C.K. Gelbke, W.G. Lynch, M. Maier, D. Ardouin, H. Delagrange, H. Doubre, C. Grégoire, A. Kyanowski, W. Mittig, A. Péghaire, J. Péter, F. Saint-Laurent, B. Zwieglinski, G. Bizard, F. Lefèbvres, B. Tamain, J. Québert, Y.P. Viyogi, W.A. Friedman, and D.H. Boal, Phys. Rev. **C35**, 1695 (1987).

[Prat 84] S. Pratt, Phys. Rev. Lett. **53**, 1219 (1984).

[Prat 87] S. Pratt and M.B. Tsang, Phys. Rev. **C36**, 2390 (1987).

[Rebr 90] D. Rebreyend, S. Kox, J.C. Gondrand, B. Khelfaoui, F. Merchez, B. Norén, and C. Perrin, Proceedings of the International Workshop on Particle Correlations and Interferometry in Nuclear Collisions, Le Cellier, France, 1990, edited by D. Ardouin (World Scientific, Singapore, 1990), p. 93

[Rebr 92] D. Rebreyend, F. Merchez, B. Norén, E. Andersen, M. Cronqvist, J.C. Gondrand, H.A. Gustafsson, B. Jäger, B. Jakobsson, B. Khelfaoui, S. Kox, A. Kristainsson, G. Lövhöiden, S. Mattson, J. Mistretta, A. Oskarsson, C. Perrin, M. Rydehell, Ö. Skeppstedt, T.F. Thorsteinsen, M. Westenius, and L. Westerberg, Phys. Rev. **C46**, 2387 (1992).

[Reid 68] R.V. Reid, Jr., Ann. Phys. (N.Y.)**50**, 411 (1968).

[Schw 93] C. Schwarz, W.G. Gong, N. Carlin, C.K. Gelbke, Y.D. Kim, W.G. Lynch, T. Murakami, G. Poggi, R.T. de Souza, M.B. Tsang, H.M. Xu, D.E. Fields, K. Kwiatkowski, V.E. Viola, Jr., and S.J. Yennello, accepted for publication in Phys. Rev. **C**, (1993)

[Shim 79] T. Shimoda, M. Ishihara, and K. Nagatani, Nucl. Instr. and Meth. **165**, 261 (1979).

[Swen 87] L. S. Swenson, Jr. Physics Today **40**, 24 (May, 1987)

[Tsan 84] M.B. Tsang, W.G. Lynch, C.B. Chitwood, D.J. Fields, D.R. Klesch, C.K. Gelbke, G.R. Young, T.C. Awes, R.L. Ferguson, F.E. Obenshain, F. Plasil, and R.L. Robinson, Phys. Lett. **148B**, 265 (1984).

[Tsan 91] M.B. Tsang, R.T. de Souza, Y.D. Kim, D.R. Bowman, N. Carlin, C.K. Gelbke, W.G. Gong, W.G. Lynch, L. Phair, and F. Zhu, Phys. Rev. **C44**, 2065 (1991).

[Tsan 93] M.B. Tsang, W.C. Hsi, D.R. Bowman, C.K. Gelbke, M.A. Lisa, G.F. Peaslee, G.J. Kunde, M.L. Begemann-Blaich, T. Hofmann, J. Hubele, J. Kempter, P. Kreutz, W.D. Kunze, V. Lindenstruth, U. Lynen, M. Mang, W.F.J. Müller, M. Neumann, B. Ocker, C.A. Ogilvie, J. Pochodzalla, F. Rosenberker, H. Sann, A. Schüttauf, V. Serfling, J. Stroth, W. Trautmann, A. Tucholski, A. Wörner, E. Zude, B. Zwieglinski, G. Raciti, G. Imme, R.J. Charity, L.G. Sobotka, I. Iori, A. Moroni, R. Scardoni, A. Ferrero, W. Seidel, Th. Blaich, L. Stuttge, A. Cosmo, W.A. Friedman, and G. Peilert, submitted to Phys. Rev. Lett. (1993)

[West 82] G.D. Westfall, B.V. Jacak, N. Anantaraman, M.W. Curtin, G.M. Crawley, C.K. Gelbke, B. Hasselquist, W.G. Lynch, D.K. Scott, M.B. Tsang, M.J. Murphy, T.J.M. Symons, R. Legrain, and T.J. Majors, Phys. Lett. **116B**, 118 (1982)

[West 85] G.D. Westfall, J.E. Yurkon, J. van der Plicht, Z.M. Koenig, B.V. Jacak, R. Fox, G.M. Crawley, M.R. Maier, and B.E. Hasselquist, Nucl. Instr. and Meth. **A238**, 347 (1985).

[Wils 90] W.K. Wilson, W. Benenson, D.A. Cebra, J. Clayton, S. Howden, J. Karn, T. Li, C.A. Ogilvie, A. Vander Molen, G.D. Westfall, J.S. Winfield, and A. Nadasen, Phys. Rev. **C41**, R1881 (1990).

[Wils 91] W.K. Wilson, Ph.D. Thesis, Department of Physics, Michigan State University (1991).

[Winf 91] J. Winfield, editor, "L'User's Guide to the MSU 4π Array", (unpublished), Original Version November 1989, Revised January 1991.

[Xu 93] Nu Xu, for the E814 Collaboration: Brookhaven National Laboratory, GSI, McGill University, University of New Mexico, University of Pittsburg, SUNY at Stony Brook, University of São Paulo, Wayne State University, Yale University, at *Heavy Ion Physics at AGS* (HIPAGS), Cambridge, USA, (1993).

[Zajc 84] W.A. Zajc, J.A. Bisterlich, R.R. Bossingham, H.R. Bowman, C.W. Clawson, K.M. Crowe, K.A. Frankel, J.G. Ingersoll, J.M. Kurk, C.J. Martoff, D.J. Murphy, J.O. Rasmussen, J.P. Sullivan, E. Yoo, O. Hashimoto, M. Koike, W.J. McDonald, J.P. Miller, and P. Truöl, Phys. Rev. **C29**, 2173 (1984)

[Zajc 92] W.A. Zajc, "A Pedestrian's Guide to Interferometry," (1992) (to appear in Proceedings of the NATO Advanced Study Institiute on Particle Production in Hightly Excited Matter, Lucca, Italy, H. Gutbrod and J. Rafelski, ed.)

[Zarb 81] F. Zarbaksh, A.L. Sagle, F. Brochard, T.A. Mulera, V. Perez-Mendez, R. Talaga, I. Tanihata, J.B. Carroll, K.S. Ganezer, G. Igo, J. Oostens, D. Woodard, and R. Sutter, Phys. Rev. Lett. **46** 1268 (1981).

[Zhu 91] F. Zhu, W.G. Lynch, T. Murakami, C.K. Gelbke, Y.D. Kim, T.K. Nayak, R. Pelak, M.B. Tsang, H.M. Xu, W.G. Gong, W. Bauer, K. Kwiatkowski, R. Planeta, S. Rose, V.E. Viola, Jr., L.W. Woo, S. Yennello, and J. Zhang, Phys. Rev. **C44**, R582 (1991).